SCALE-UP OF PRECIPITATION PROCESSES

Rudolf Zauner
Dipl.-Ing., 1994

A thesis submitted to the University of London
for the Degree of Doctor of Philosophy

Ramsay Memorial Laboratory
of Chemical Engineering
University College London
Torrington Place
London WC1E 7JE

June 1999

ABSTRACT

This thesis concerns the scale-up of precipitation processes aimed at predicting product particle characteristics. Although precipitation is widely used in the chemical and pharmaceutical industry, successful scale-up is difficult due to the absence of a validated methodology. It is found that none of the conventional scale-up criteria reported in the literature (equal power input per unit mass, equal tip speed, equal stirring rate) is capable of predicting the experimentally observed effects of the mixing conditions on kinetic rates and particle characteristics. As a result of high gradients in the supersaturation field during precipitation, particularly in the feed zone, high local gradients in the nucleation rate are to be expected.

In this thesis, a compartmental mixing model (Segregated Feed Model SFM) linked to the population balance is proposed for scaling up both continuous and semibatch precipitation processes, and is validated with experiments on different scales.

Experiments were carried out using two chemical systems (calcium oxalate CaC_2O_4 and calcium carbonate $CaCO_3$), varying the residence time/feed time, feed concentration, feed point position, impeller type, feed tube diameter and stirring rate in geometrically similar reactors ranging from 0.3 to 30 l.

A new procedure is introduced in order to solve the inverse problem for determination of the kinetic parameters for nucleation, growth, disruption and agglomeration from the particle size distributions obtained in the continuous laboratory-scale experiments. This method, where the kinetic rates were extracted separately and sequentially from the particle size distribution, was found to be a reliable alternative to the conventional simultaneous estimation of all kinetic parameters from the distribution.

Using the kinetic parameters extracted from the laboratory-scale experiments, the population balance is solved within the Segregated Feed Model. The local mixing parameters also required for solving the SFM are obtained from a sliding mesh Computational Fluid Dynamics (CFD) model. These are used to specify the different micromixing and mesomixing conditions in the feed and bulk zones of the reactor.

The model accurately predicts the mean size, coefficient of variation and nucleation rate on different scales for different process and mixing conditions in both

continuous and semibatch mode of operation. Furthermore, the model confirms the observed greater effect of mixing on product particle characteristics in semibatch than in continuous operation. This is thought to be due to direct mixing of the feed solution in semibatch operation with the other component already present in the reactor.

The methodology proposed here for the scale-up of precipitation processes is very versatile and computationally efficient. It combines the advantages of both a CFD and a population balance approach without having to solve the equations together, which is currently still impracticable due to the excessive computational demand and simulation time required.

ACKNOWLEDGEMENTS

The author wishes to express his gratitude to the following:

Professor Alan Jones for his excellent supervision and encouragement in which he provided the right balance between guidance and freedom that I needed during the course of my research.

Professor John Mullin for sharing his extensive experience and for his inspiration and invaluable comments on so many different aspects of crystallization.

Dr Janusz Wójcik for his assistance with the experimental equipment.

Dr Vinca Grethe for organising a research visit to the Institut für Mechanische Verfahrenstechnik und Umweltverfahrenstechnik at the Technical University of Clausthal, Germany, where part of this research was carried out within the EU Training and Mobility of Researchers (TMR) programme.

Sarah Bailey, Alan Craig, John Graham, Julian Perfect, Martin Town and Martyn Vale for their invaluable help with managing the technical and computational side of the project.

My friends and colleagues in the department, who shared in my joy and despair.

The EPSRC, the Oberösterreichische Landesregierung and the European Union for the provision of grants and scholarships.

My family for their constant support and encouragement throughout my studies, without which this work would not have been possible.

Belinda, for being there when I needed you.

TABLE OF CONTENTS

TITLE PAGE 1

ABSTRACT 2

ACKNOWLEDGEMENTS 4

TABLE OF CONTENTS 5

LIST OF FIGURES AND TABLES 10

1 INTRODUCTION 19

2 PRINCIPLES OF PRECIPITATION 27

2.1 INTRODUCTION 28

2.2 THE DRIVING FORCE IN CRYSTALLIZATION AND PRECIPITATION 28

2.3 PRECIPITATION KINETICS 29

2.3.1 NUCLEATION 29

2.3.1.1 PRIMARY NUCLEATION 30

2.3.1.2 SECONDARY NUCLEATION 31

2.3.2 GROWTH 32

2.3.3 AGGLOMERATION 33

2.3.4 DISRUPTION 35

2.3.5 SECONDARY CHANGES OF THE PRECIPITATE 36

2.4 MIXING AND PRECIPITATION 37
2.4.1 INTRODUCTION 37
2.4.2 MIXING EQUIPMENT 37
2.4.2.1 STIRRED TANK 37
2.4.2.2 TEE-MIXER 43
2.4.2.3 JET MIXER 44
2.4.2.4 STATIC MIXERS 44

3 THE POPULATION BALANCE 45

3.1 DERIVATION OF THE POPULATION BALANCE 46
3.2 MOMENT TRANSFORMATION OF THE POPULATION BALANCE 48
3.3 POPULATION BALANCE FOR THE MIXED-SUSPENSION MIXED-PRODUCT-REMOVAL (MSMPR) CRYSTALLIZER 48
3.4 POPULATION BALANCE MODELLING INCLUDING AGGLOMERATION AND DISRUPTION KINETICS 52
3.4.1 INTRODUCTION 52
3.4.2 ANALYTICAL SOLUTION OF THE POPULATION BALANCE 53
3.4.3 NUMERICAL SOLUTION OF THE POPULATION BALANCE 54
3.4.4 DISCRETIZATION METHODS 54
3.4.4.1 DISCRETIZATION METHOD OF GELBARD *ET AL.* 54
3.4.4.2 DISCRETIZATION METHOD OF HOUNSLOW 54
3.4.4.3 DISCRETIZATION METHOD OF KUMAR AND RAMKRISHNA 56
3.4.5 SOLUTION METHODS 57
3.4.5.1 FORTRAN PROGRAMMING 57
3.4.5.2 SPEEDUP PROGRAMMING 58
3.5 RESULTS 58
3.5.1 CASE 1: PRECIPITATION OF CALCIUM CARBONATE 58
3.5.2 CASE 2: PRECIPITATION OF CALCIUM OXALATE 60

4	DETERMINATION OF THE PRECIPITATION KINETICS	62
4.1	INTRODUCTION	63
4.2	PHYSICAL PROPERTIES OF THE SYSTEMS UNDER INVESTIGATION	63
4.2.1	CALCIUM OXALATE CaC_2O_4	63
4.2.2	CALCIUM CARBONATE $CaCO_3$	64
4.3	KINETIC STUDIES IN THE LITERATURE	65
4.4	PARAMETER ESTIMATION	66
4.5	EXPERIMENTAL CONDITIONS	69
4.6	EXPERIMENTAL SET-UP	70
4.7	EXPERIMENTAL PROCEDURE	74
4.8	REPRODUCIBILITY	76
4.9	RESULTS	77
4.9.1	MORPHOLOGY	77
4.9.2	MEAN SIZE AND COEFFICIENT OF VARIATION	82
4.9.3	PRECIPITATION KINETICS OF CALCIUM OXALATE	86
4.9.4	PRECIPITATION KINETICS OF CALCIUM CARBONATE	100
4.10	DETERMINATION OF THE SHAPE FACTOR	100
4.11	DESIGN OF EXPERIMENTS (DOE)	102
4.12	CONCLUSIONS	112
5	MIXING, MIXING MODELS AND COMPUTATIONAL FLUID DYNAMICS (CFD)	115
5.1	INTRODUCTION	116
5.2	MACROMIXING AND MACROMIXING MODELS	116
5.3	MESOMIXING AND MICROMIXING	118
5.4	MESOMIXING AND MICROMIXING MODELS	119

5.5 SEGREGATED FEED MODEL (SFM) 121
5.5.1 INTRODUCTION 121
5.5.2 EXTREME CASES OF MIXING 123
5.5.3 SFM APPLIED TO CONTINUOUS PRECIPITATION 124
5.5.4 SFM APPLIED TO SEMIBATCH PRECIPITATION 127
5.5.5 GENERAL MODEL RESULTS 129
5.6 COMBINED MACROMIXING AND MICROMIXING MODELS 133
5.7 DETERMINATION OF MIXING TIMES USING COMPUTATIONAL FLUID DYNAMICS (CFD) 134
5.7.1 INTRODUCTION 134
5.7.2 ELEMENTS OF A CFD CODE 134
5.7.3 SIMULATIONS OF THE FLUID DYNAMICS IN A STIRRED TANK 135
5.7.4 CALCULATION OF LOCAL MICROMIXING TIMES 137
5.7.5 GRID GENERATION 138
5.7.6 SOLVER OPTIONS 138
5.7.7 RESULTS 139

6 SCALE-UP OF CONTINUOUS PRECIPITATION – EXPERIMENTAL AND MODELLING RESULTS 150
6.1 INTRODUCTION 151
6.2 EXPERIMENTAL SET-UP AND PROCEDURE 151
6.3 EXPERIMENTAL CONDITIONS 153
6.4 EXPERIMENTAL AND MODELLING RESULTS 154
6.4.1 MORPHOLOGY 154
6.4.2 DETERMINATION OF THE MESOMIXING TIME CONSTANT 155
6.4.3 SMALL-SCALE RESULTS 155
6.4.4 RESULTS ON DIFFERENT SCALES 158

7 SCALE-UP OF SEMIBATCH PRECIPITATION – EXPERIMENTAL AND MODELLING RESULTS 166

7.1 INTRODUCTION 167

7.2 EXPERIMENTAL SET-UP AND PROCEDURE 167

7.3 EXPERIMENTAL CONDITIONS 168

7.4 EXPERIMENTAL AND MODELLING RESULTS 169

7.4.1 MORPHOLOGY 169

7.4.2 SMALL-SCALE RESULTS 174

7.4.3 RESULTS FOR CALCIUM OXALATE ON DIFFERENT SCALES 181

7.4.4 RESULTS FOR CALCIUM CARBONATE ON DIFFERENT SCALES 190

8 SCALE-UP RECOMMENDATIONS, CONCLUSIONS AND FURTHER RESEARCH 197

8.1 SCALE-UP RECOMMENDATIONS 198

8.2 CONCLUSIONS 203

8.3 FURTHER RESEARCH 207

NOMENCLATURE 210

REFERENCES 216

APPENDIX 231

LIST OF FIGURES AND TABLES

LIST OF FIGURES

Figure 2.1	Kinetic processes during precipitation	29
Figure 2.2	Mechanisms of nucleation (after Mullin, 1993)	30
Figure 2.3	Continuous precipitation reactor	38
Figure 2.4	Semibatch precipitation reactor	39
Figure 2.5	Batch precipitation reactor	39
Figure 2.6	Feed points close to one another and to impeller	40
Figure 2.7	Feed points remote from one another and close to impeller	40
Figure 2.8	Feed points close to one another and remote from impeller	41
Figure 2.9	Feed points remote from one another and from impeller	41
Figure 2.10	Tee-mixer	43
Figure 2.11	Jet mixer	44
Figure 3.1	Particle size distribution of an MSMPR crystallizer	50
Figure 3.2	Population density distribution of calcium carbonate	60
Figure 3.3	Population density distribution of calcium oxalate	61
Figure 4.1	Experimental set-up: Continuous laboratory-scale precipitation reactor	71
Figure 4.2	300 ml draft tube baffled (DTB) reactor	72
Figure 4.3	Calibration curve for calcium-ion selective electrode	74
Figure 4.4	Calcium ion concentration vs. dimensionless time	75
Figure 4.5	Reproducibility of laboratory experiments	77
Figure 4.6	Light microscope picture of calcium oxalate precipitate	78
Figure 4.7	Agglomerate of calcium oxalate (SEM)	79
Figure 4.8	Intergrowth of particles (SEM)	79

Figure 4.9	Agglomeration and disruption effects (SEM)	79
Figure 4.10	Twinned particle (SEM)	79
Figure 4.11	Single particle of calcium carbonate (SEM)	80
Figure 4.12	Agglomeration of particles (SEM)	80
Figure 4.13	Loose agglomerate of calcium carbonate (SEM)	81
Figure 4.14	Compact agglomerate of calcium carbonate (SEM)	81
Figure 4.15	Transformation of vaterite into calcite	82
Figure 4.16	Vaterite and calcite after 24 hours	82
Figure 4.17	Volume mean diameter vs. residence time for calcium oxalate	83
Figure 4.18	Volume mean diameter vs. specific power input for calcium oxalate	84
Figure 4.19	Coefficient of variation vs. residence time for calcium oxalate	85
Figure 4.20	Volume mean diameter vs. specific power input for calcium carbonate	85
Figure 4.21	Number density distribution calculated using concentrations and activities	88
Figure 4.22	Growth rate vs. stirrer speed	89
Figure 4.23	Growth rate vs. residence time	90
Figure 4.24	Growth rate vs. supersaturation	91
Figure 4.25	Nucleation rate vs. residence time	92
Figure 4.26	Nucleation rate vs. stirrer speed	93
Figure 4.27	Nucleation rate vs. supersaturation	94
Figure 4.28	Particle size distribution for disruption experiment (ε = 2.7 W/kg)	95
Figure 4.29	Disruption kernel vs. power input	96

Figure 4.30	Prediction quality of various agglomeration kernels	97
Figure 4.31	Agglomeration rate vs. shear rate	98
Figure 4.32	Measured surface and volume based mean sizes	101
Figure 4.33	Experimental sphericity for calcium oxalate	102
Figure 4.34	Number mean size L_{10} – experimental results vs. designed experiments	109
Figure 4.35	Number mean size L_{10} – experimental results and DOE predictions for intermediate conditions	110
Figure 4.36	Volume mean size L_{43} – experimental results vs. designed experiments	111
Figure 4.37	Particle size distribution at different stirrer speeds (300 ml reactor, 500 to 2000 rpm, 0.04M, 7.5 min, od)	114
Figure 5.1	Residence time distribution in the 300 ml reactor	117
Figure 5.2	Segregated feed model (SFM)	122
Figure 5.3	Time-dependence of the second moment m_2	129
Figure 5.4	Time-dependence of number mean size	130
Figure 5.5	Time-dependence of the particle size distribution	131
Figure 5.6	Dependence of the nucleation rate on the mixing conditions	132
Figure 5.7	Two-dimensional projection of Figure 5.6	132
Figure 5.8	Example of a combined macro-meso-micromixing model	133
Figure 5.9	Geometry and velocity field in a draft tube baffled (DTB) reactor equipped with a propeller (4.3 l, 100 rpm)	140
Figure 5.10	Geometry and velocity field in baffled reactor equipped with a Rushton turbine (1 l, 500 rpm)	141
Figure 5.11	Geometry and velocity field in baffled reactor equipped with a 45°-pitched blade turbine (1 l, 500 rpm)	142

Figure 5.12	Geometry and velocity field in baffled reactor equipped with a marine-type impeller (propeller) (1 l, 500 rpm)	143
Figure 5.13	Local energy dissipation in baffled reactor equipped with a Rushton turbine (1 l, 461 rpm)	145
Figure 5.14	Local energy dissipation in baffled reactor equipped with a Rushton turbine (5 l, 351 rpm)	146
Figure 5.15	Local energy dissipation in baffled reactor equipped with a Rushton turbine (25 l, 250 rpm)	147
Figure 5.16	Local energy dissipation in baffled reactor equipped with a Rushton turbine (1 l, 100 rpm)	148
Figure 6.1	Experimental set-up for continuous scale-up experiments	151
Figure 6.2	Dimensions of the 4.3 l and 12 l large-scale DTB reactors	152
Figure 6.3	Residence time distribution of the 12 l reactor, 100 rpm	153
Figure 6.4	Calcium oxalate precipitate from large-scale experiment (12 l, 250 rpm, 0.01M, 11 min, od)	155
Figure 6.5	Experimental and SFM results for the number mean size (300 ml, 500 to 2000 rpm, 0.04M, 7.5 min, id and od)	156
Figure 6.6	Experimental and SFM results for the nucleation rate (300 ml, 500 to 2000 rpm, 0.04M, 7.5 min, id and od)	157
Figure 6.7	Particle size distribution (300 ml, 500 rpm, 0.04M, 7.5 min, id)	158
Figure 6.8	Scale-up of continuous calcium oxalate precipitation: Volume mean size L_{43} (300 ml, 4.3 l and 12 l; 0.04M, 7.5 min, id)	160
Figure 6.9	Scale-up of continuous calcium oxalate precipitation: Volume mean size L_{43} (300 ml, 4.3 l and 12 l; 0.01M, 11 min, od)	161
Figure 6.10	Scale-up of continuous calcium oxalate precipitation: Coefficient of variation c.v. (300 ml, 4.3 l and 12 l; 0.01M, 11 min, od)	163

Figure 6.11	Scale-up of continuous calcium oxalate precipitation: Nucleation rate B^0 (300 ml, 4.3 l and 12 l; 0.04M, 7.5 min, id)	164
Figure 6.12	Scale-up of continuous calcium oxalate precipitation: Growth rate G (300 ml, 4.3 l and 12 l; 0.04M, 7.5 min, id)	165
Figure 7.1	Experimental set-up for semibatch precipitation experiments	167
Figure 7.2	Semibatch reactor with Rushton turbine (dimensions in appendix A7.1)	168
Figure 7.3	Twinned calcium oxalate crystal	170
Figure 7.4	Calcium oxalate agglomerate	170
Figure 7.5	Calcium carbonate (calcite) agglomerate	171
Figure 7.6	Detail of the edges and faces of a calcite crystal	172
Figure 7.7	Calcite crystal (directly precipitated)	172
Figure 7.8	Calcite crystal with dissolving vaterite crystal	173
Figure 7.9	Fully transformed calcite agglomerate	173
Figure 7.10	Particle size vs. specific energy input for different impeller types (CaOx, 40 min feed time, feed point position close to the impeller, total concentration 0.008M)	174
Figure 7.11	Particle size vs. stirrer speed for different impeller types (CaOx, 40 min feed time, feed point position close to the impeller, total concentration 0.008M)	175
Figure 7.12	Mean particle size vs. specific energy input for different feed tubes (CaOx, Rushton turbine, 40 min feed time, feed point position close to the impeller, total concentration 0.008M)	176
Figure 7.13	Mean particle size vs. specific energy input for different feed rates (CaOx, Rushton turbine, feed point position close to the impeller, total concentration 0.008M)	177
Figure 7.14	Mean particle size vs. specific energy input for different	

feed point positions (f.p.p.) (CaOx, Rushton turbine, 40 min feed time, total concentration 0.008M) 178

Figure 7.15 Mean particle size vs. specific power input for different feed point positions ($CaCO_3$, Rushton turbine, 40 min feed time, total concentration 0.04M) 179

Figure 7.16 Particle size vs. specific power input for different feed concentrations (CaOx, Rushton turbine, 40 min feed time, feed point position close to the impeller) 180

Figure 7.17 Particle size vs. specific power input for different feed volume ratios (CaOx, Rushton turbine, 40 min feed time, feed point position close to the impeller, total concentration 0.008M) 181

Figure 7.18 Mean particle size for reference conditions (CaOx, Rushton turbine, 40 min feed time, feed point position close to the impeller, total concentration 0.008M) 182

Figure 7.19 Mean particle size for marine-type impeller (CaOx, 40 min feed time, feed point position close to the impeller, total concentration 0.008M) 183

Figure 7.20 Mean particle size for feed point position close to surface (CaOx, Rushton turbine, 40 min feed time, 0.008M) 184

Figure 7.21 Mean particle size for high feed rate (CaOx, Rushton turbine, feed point position close to the impeller, total concentration 0.008M) 185

Figure 7.22 Total number of particles for reference conditions (CaOx, Rushton turbine, 40 min feed time, feed point position close to the impeller, total concentration 0.008M) 186

Figure 7.23 Total number of particles for marine-type impeller (CaOx, Rushton turbine, 40 min feed time, feed point position close to the impeller, total concentration 0.008M) 187

Figure 7.24	Number density of nuclei for reference conditions (CaOx, Rushton turbine, 40 min feed time, feed point position close to the impeller, total concentration 0.008M)	188
Figure 7.25	Number density of nuclei for marine-type impeller (CaOx, 40 min feed time, feed point position close to the impeller, total concentration 0.008M)	189
Figure 7.26	Mean particle size for reference conditions ($CaCO_3$, Rushton turbine, 40 min feed time, feed point position close to the impeller, total concentration 0.04M)	190
Figure 7.27	SEM micrograph of vaterite and calcite	191
Figure 7.28	Total number of particles for reference conditions ($CaCO_3$, Rushton turbine, 40 min feed time, feed point position close to the impeller, total concentration 0.04M)	192
Figure 7.29	Number density of nuclei for reference conditions ($CaCO_3$, Rushton turbine, 40 min feed time, feed point position close to the impeller, total concentration 0.04M)	193
Figure 7.30	Coefficient of variation for reference conditions ($CaCO_3$, Rushton turbine, 40 min feed time, feed point position close to the impeller, total concentration 0.04M)	194
Figure 7.31	SEM micrograph of vaterite and calcite (100 rpm)	195
Figure 7.32	SEM micrograph of vaterite and calcite (500 rpm)	196
Figure 8.1	Scale-up with constant stirrer speed (continuous precipitation)	199
Figure 8.2	Scale-up with constant stirrer speed (semibatch precipitation)	199
Figure 8.3	Scale-up with constant tip speed (continuous precipitation)	200
Figure 8.4	Scale-up with constant tip speed (semibatch precipitation)	201
Figure 8.5	Scale-up methodology	206

LIST OF TABLES

Table 3.1	Relative errors of discretization methods	59
Table 4.1	Solubility products of calcium oxalate hydrates at 25°C (Garside *et al.*, 1982)	63
Table 4.2	Solubility products of calcium oxalate hydrates at 37°C (Nancollas and Gardner, 1974)	64
Table 4.3	Solubility products of calcium carbonate polymorphs at 25°C Ohtaki (1998)	65
Table 4.4	Treatment combinations in DOE	104
Table 4.5	Levels of factors (input parameters)	105
Table 4.6	Yates' algorithm (Part 1)	106
Table 4.7	Yates' algorithm (Part 2)	107
Table 4.8	Influence of the input parameters and interactions on the response variables (properties)	112
Table 6.1	Experimental conditions for large-scale continuous experiments	154
Table 6.2	Experimental and DOE results for the number mean size (0.7 W/kg, 0.04M, 7.5 min, id)	159
Table 6.3	Experimental and DOE results for the number mean size (0.7 W/kg, 0.01M, 11 min, od)	159
Table 7.1	Experimental conditions for semibatch experiments (CaOx)	169
Table 7.2	Experimental conditions for semibatch experiments ($CaCO_3$)	169

CHAPTER 1

INTRODUCTION

Introduction

Chemical engineers deal with industrial processes in which mass, heat, momentum transfer and chemical reactions take place. As these rate processes are scale-dependent, *i.e.* their behaviour differs on different scales, one important task for chemical engineers is to find a reliable way to model or design industrial-scale processes using information obtained from a smaller scale. This concept is known as "scale-up".

Bisio and Kabel (1985) define scale-up as

> *the successful start-up and operation of a commercial size unit whose design and operating procedures are in part based upon experimentation and demonstration at a smaller scale of operation.*

Historical overview

The desire to gain information about a large-scale process by first carrying out tests on models has existed for a long time. As far back as the 16th century, Leonardo da Vinci wrote (from Johnstone and Thring, 1957)

> *Vitruvius says that small models are of no avail for ascertaining the effects of large ones; and I here propose to prove that this conclusion is a false one.*

Later, Galileo Galilei investigated the strength of mechanical parts of different sizes and drew conclusions about the scale-up (Galilei, 1638). In the 17th century, Isaac Newton wrote about the concept of "mechanical similarity" (Newton, 1687). Developing these thoughts on similarity, Froude and Reynolds published their results on hydrodynamic similarity (from Zlokarnik, 1985). In 1915 Lord Rayleigh's publication *The principle of similitude* appeared, on which modern dimensional analysis is based (Rayleigh, 1915). At the same time Buckingham (1914) introduced the Π theorem which states that a physical problem can always be described in dimensionless form. The objective of dimensional analysis is to express the behaviour of a physical system with a minimum number of independent variables and in such a way that it is unaffected by changing the units of measurement (Johnstone and Thring, 1957).

Since that time, the concept of dimensional analysis has been applied to chemical engineering problems and has given valuable insights into process design and scale-up.

Scale-up in chemical engineering is frequently a very difficult task, however, as a variety of factors can influence the quantity and quality of the final product of a process. Hence successful scale-up requires the utilisation of a wide range of technical skills and thorough understanding of the problem under study (Bisio and Kabel, 1985). Both technical and economic aspects have to be taken into account. Time and money can thus restrict the scale-up procedure, while calculated risks have to be taken in design and construction. The financial uncertainties resulting from the risks have to be compared with the additional expense necessary for a deeper insight into the process.

For many processes, such as precipitation, there is a lack of understanding as to what role certain physical and chemical processes play in scale-up, and so they are scaled up empirically or by trial and error.

Scale-up procedure

As a first step, the development of a large-scale chemical reactor or mass transfer equipment usually involves determining rate and selectivity expressions from the analysis of laboratory data. Parameters and kinetic models are thus obtained from these laboratory-scale data. The experiments have to be designed in such a way that the physical and chemical processes taking place in the reactor can be clearly understood; only then is it possible to understand how the process is influenced by various parameters. If, for example, a chemical reaction is the rate-determining step in a process, the reactor volume is likely to be crucial for scale-up, whereas in a process with heat transfer limitation, the surface-to-volume ratio could have a significant impact on the outcome of the scale-up study (Zlokarnik, 1991).

As it is not always possible to gain sufficient insight into a process using only laboratory-scale data, a pilot plant of a scale between laboratory and commercial scale can help to scale up a chemical or physical process successfully (Sie and Krishna, 1998). Using pilot plant data, more reliable scale-up can be achieved, and it is possible to produce a product in such a quantity that it can serve market research purposes and

therefore help to determine the capacity of the commercial unit. In addition, by using pilot plant data the scale-up ratio and thus the risk of errors in design can be reduced. The scale-up ratio is defined as

$$\text{scale - up ratio} = \frac{\text{large} - \text{scale production rate}}{\text{small} - \text{scale production rate}} \qquad (1.1)$$

and is usually within a range from 10 to 1000 for scale-up from laboratory scale to the pilot plant unit and within a range from 10 to 1500 for scale-up from pilot plant units to commercial plants, depending on the process and system involved.

Ohsol (1973) gives an overview of typical scale-up ratios and recommends a scale-up ratio of 20 to 200 for the scale-up laboratory → pilot plant and 20 to 250 for the scale-up pilot plant → commercial plant for processes involving liquid reactants. For processes that are notoriously difficult to scale up, such as processes involving kinetic mechanisms that are not fully understood or are very difficult to investigate, pilot plants of different sizes may be necessary in order to decrease the scale-up ratio in steps between different scales.

In the simplest case, geometric, dynamic, kinematic, thermal and/or chemical similarity can be maintained with scale-up. Similarity on different scales is fulfilled when the dimensionless groups (*e.g.* Reynolds number, Sherwood number, Damköhler number) have the same value on different scales.

In most scale-up situations, however, total similarity on different scales cannot be established, as it is difficult or even impossible to maintain constancy in *all* the dimensionless groups that characterise the process. In these cases, a trade-off between different dimensionless groups has to be found, with groups being "weighted" differently according to their expected influence on the process. Scale-up then loses its theoretical base and becomes empirical. Deviation from similarity on different scales can have significant consequences and, if the process is poorly understood, result in failure (Dickey, 1993).

Alternatively, a mathematical model can be developed which accounts for the underlying physical and chemical processes considered important for scale-up. Therefore, the process mechanisms have to be clearly understood and the model must

not contain any phenomenological or unknown scale-dependent parameters, as it is not then suitable for quantitative scale-up predictions.

Scale-up of crystallization and precipitation processes

Scale-up of crystallization, precipitation and mixing-controlled processes is not a new problem in chemical engineering. Collating the most important findings will serve as a starting point for further investigations.

Contradictory scale-up criteria for both crystallization and precipitation have been reported in the literature (see later). One explanation for the variety of scale-up rules is the impossibility of keeping all dimensionless groups constant when precipitation and crystallization processes are scaled up. For example, scale-up with a constant Reynolds number leads to different local Damköhler numbers and therefore different reaction and precipitation rates, whereas scale-up with constant specific power input leads to a different flow pattern and therefore different meso- and macromixing in the reactor.

As far as scale-up of crystallization is concerned, secondary nucleation seems to play a crucial role (Garside and Jancic, 1979). Green *et al.* (1996) sum up the difficulties arising during crystallizer scale-up, and also show the limitations of Computational Fluid Dynamics (CFD) simulations in solving the problem. Ploß *et al.* (1986) studied the scale-up of MSMPR crystallizers, and observed that the nucleation and growth rates on different scales are the same if suspension density, specific power input and residence time are held constant with scale-up. However, they were unable to make any predictions as to how mixing can influence the crystal size distribution. Qian *et al.* (1987) observed that scale-up with constant tip speed of the impeller leads to equal nucleation rates on different scales. Kramer *et al.* (1996) performed a scale-up to industrial scale (970 l), and point out the importance of attrition kinetics since the attrition fragments initiate nuclei formation and therefore secondary nucleation in the crystallizer.

These contradictory results of scale-up criteria for crystallization processes show the difficulties in scaling up crystallization. Even more complications occur with precipitation as the reaction and precipitation rates are likely to be mixing-limited. This

mixing limitation can occur on the macroscale (macromixing limitation), mesoscale (mesomixing limitation) or microscale (micromixing limitation), or any combination of these.

The influence of mixing on product quality and scale-up has been studied by a number of authors. Rice and Baud (1990) used constant specific power input as a scale-up criterion and found that this criterion can only be used for certain feed point locations. Moreover, they state that a localisation of the reaction zone with scale takes place. To avoid this effect, the authors suggest changing the ratio of impeller to tank diameter. Bourne and Dell'Ava (1987) studied micromixing effects on different scales using competitive-consecutive azo coupling reactions in order to determine the segregation index and therefore obtain a measure of micromixing. They "excluded" any meso- and macromixing effects by feeding the reagents with feed rates which were much smaller than the circulation rate, and confirmed that constant specific power input is a suitable scale-up criterion for these micromixing-controlled conditions. Mersmann and Laufhütte (1985), too, suggest scale-up with constant specific power input for micromixing-limited processes. The authors also provide an overview of scale-up rules for mixing processes involving suspensions.

In contrast to the authors mentioned above, Bourne and Yu (1994) found that scale-up with constant specific power input in the semibatch mode of operation is not suitable for parallel reaction systems. They explained the variance of the segregation index on different scales by the fact that the trajectory of the reaction zone and the spatial distribution of the power dissipation vary with scale even for homologous feed points. These effects are modelled using an experimental flow model. Wang and Mann (1992) showed that for mixing-limited consecutive-competitive reaction systems, scale-up with constant tip speed leads to an increase in segregation with scale-up and therefore unsatisfactorily large-scale predictions. Tipnis *et al.* (1994) state that the single most important factor for scale-up is feed blending, which is influenced by the chemical species concentrations, the feed flow rates, the impeller geometry and the feed pipe locations. The authors give no hard and fast rules for scale-up; however, a procedure is suggested with various scale-up criteria ranging from constant blending time to constant specific power input. Oldshue (1983 and 1985) shows that the maximum impeller zone

macroscale shear rate increases while the average impeller zone macro-scale shear rate decreases upon scale-up. This leads to further complications on scale-up as the flow regime depends very much on the shear rate distribution in the reactor. Choplin and Villermaux (1994) investigated mixing phenomena in polymer reactors, and concluded that successful scale-up is possible if only one of the multistep mixing mechanisms is controlling. For example, if the engulfment process is limiting, micromixing can be scaled up based on constant power input per unit volume. For mesomixing limitation, a scale-up with constant tip speed is suggested.

Unfortunately, none of the publications mentioned above deals with the scale-up of precipitation processes. Publications concerning the scale-up of precipitation are very sparse in the literature, although its importance has been emphasised by the chemical and pharmaceutical industry (Krei and Buschmann, 1998).

Houcine *et al.* (1997) investigated the influence of mixing conditions on the precipitation of calcium oxalate on a 20 l pilot scale; however, the authors did not relate their results to other scales. Momonaga *et al.* (1992) introduced a mixing-dependent scale-up factor based on equal power input per unit volume on different scales. They scaled up the batch precipitation process of methyl α-methoxyimino acetoacetate, but did not carry out a study of the precipitation kinetics. Mahajan and Kirwan (1996) investigated micromixing and scale effects of the precipitation of Lovastatin in a two-impinging-jets (TIJ) precipitator. By means of the geometry of the TIJ mixer, it is possible to achieve very short micromixing times in the range of the induction time and therefore ensure homogeneous supersaturation throughout the reactor before nucleation starts. A scale-up criterion based on the Damköhler number (ratio of characteristic micromixing time constant to characteristic reaction time constant) is proposed.

In conclusion, various scale-up criteria for the scale-up of precipitation processes have been proposed in the literature. Scale-up with constant specific power input can be applied to micromixing-limited processes, scale-up with constant tip speed, on the other hand, can be successfully used for mesomixing-controlled processes where the shear rate distribution in the reaction zone is essential. If macromixing plays a decisive role, scale-up with constant stirrer speed has to be considered. Problems occur, however, if

more than one of these mixing processes controls the mixing quality and therefore the process. This is generally the case in precipitation processes due to the very fast reaction kinetics, and therefore all these conventional scale-up criteria fail.

In this research, a methodology based on a hybrid CFD-mixing model is introduced for scaling up continuous and semibatch precipitation processes from laboratory scale to pilot scale which can simultaneously account for micro-, meso- and macromixing effects. The method developed efficiently combines the advantages of CFD and a population balance approach including nucleation, growth, agglomeration and disruption kinetics. Chapter 2 introduces the principles of precipitation, and is followed by a detailed analysis of the population balance in Chapter 3, where different discretization and solving methods are compared. Chapter 4 discusses the determination of nucleation, growth, agglomeration and disruption kinetics of calcium oxalate and calcium carbonate from experimental data. Furthermore, an alternative to finding all the kinetic constants simultaneously is introduced. Principles of mixing and mixing models in Chapter 5 cover macromixing, mesomixing, micromixing and their mathematical description. In the same chapter, the Segregated Feed Model (SFM) is chosen for modelling the influence of mixing on the precipitation process. In addition, Computational Fluid Dynamics (CFD) is used to determine the parameters necessary to describe the diffusive and convective mass transfer in the SFM. The experimental and modelling results of scale-up of continuous precipitation are compared in Chapter 6, while in Chapter 7 semibatch precipitation processes are scaled up. Chapter 8 concludes the thesis with scale-up recommendations, conclusions and suggestions for further research.

CHAPTER 2

PRINCIPLES OF PRECIPITATION

2.1 INTRODUCTION

Precipitation is widely used in the chemical and pharmaceutical industry, for example in the production of fine chemicals, pigments, catalysts, photochemicals and pharmaceuticals. With the new fields of nanoscale science and nanotechnology, its importance as a unit operation has further increased in recent years.

Precipitation can be regarded as rapid crystallization with high supersaturation levels obtained by mixing two compounds that subsequently react. Nucleation rates are very high due to high supersaturation levels, and the particle size is small compared with conventional crystallization. Agglomeration and mixing often determine the crystal size distribution and hence influence the properties of the final product to a significant extent. In *Precipitation* Söhnel and Garside (1992) present a good summary of the state of the art of precipitation and a thorough collection of experimental data.

2.2 THE DRIVING FORCE IN CRYSTALLIZATION AND PRECIPITATION

The concise explanations regarding the thermodynamics of solutions given in *Handbook of Industrial Crystallization* (Myerson, 1993) and *The Formation and Properties of Precipitates* (Walton, 1979), and the description of the crystalline state (Mullin, 1993), provide a basic insight into the principles of particle formation from solution.

At this stage only *supersaturation, i.e.* the driving force in the precipitation process, will be mentioned, which relates the concentration to the equilibrium solubility c^*, to the solubility product K_{sp} or to the activity product K_{ap}. Several expressions are common for the supersaturation.

Relative supersaturation:

$$S = \frac{c}{c^*} \text{ and} \tag{2.1}$$

$$S_{sp} = \left(\frac{c_A^{\nu_A} c_B^{\nu_B}}{K_{sp}} \right)^{\frac{1}{\nu_A+\nu_B}} \text{ or } S_{ap} = \left(\frac{c_A^{\nu_A} c_B^{\nu_B}}{K_{ap}} \right)^{\frac{1}{\nu_A+\nu_B}} \tag{2.2}$$

$$\sigma = \frac{c - c^*}{c^*} = S - 1 \tag{2.3}$$

Concentration difference:

$$\Delta c = c - c^* \tag{2.4}$$

As the local and overall levels of supersaturation determine the precipitation rates and therefore the properties of the precipitate, supersaturation is of crucial importance in every precipitation process.

2.3 PRECIPITATION KINETICS

Kinetic parameters are used to describe the events of growth (growth rate), birth and death (nucleation rate, agglomeration and disruption kernel) of a precipitation process. The interplay of these parameters and their dependence on supersaturation, hydrodynamics and mixing determine the crystal size distribution (Figure 2.1).

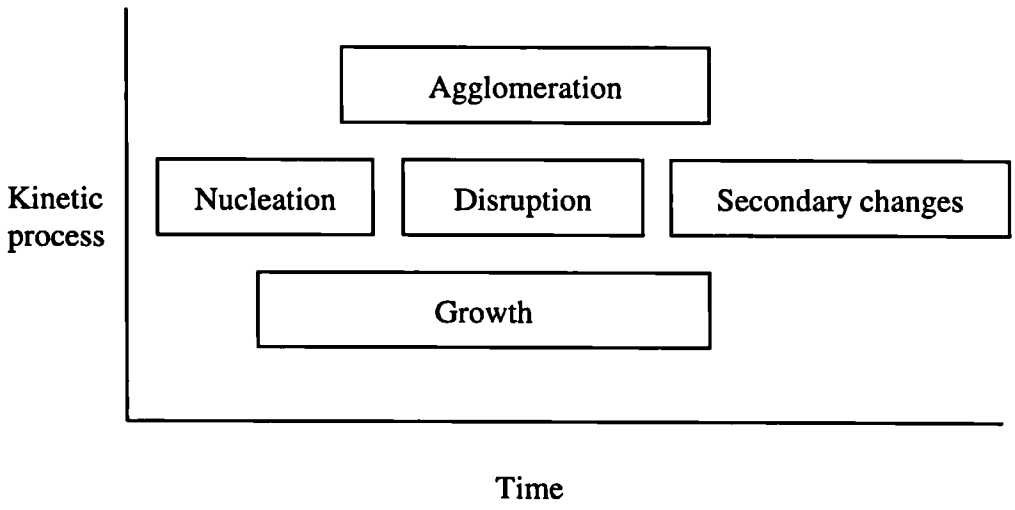

Figure 2.1 Kinetic processes during precipitation

2.3.1 NUCLEATION

According to the mechanism (Figure 2.2), nucleation can be divided into

- **primary nucleation** (nucleation without crystalline matter)
  - ➢ homogeneous nucleation (spontaneous nucleation from solution)

- heterogeneous nucleation (induced by foreign particles)

- **secondary nucleation** (induced by crystals).

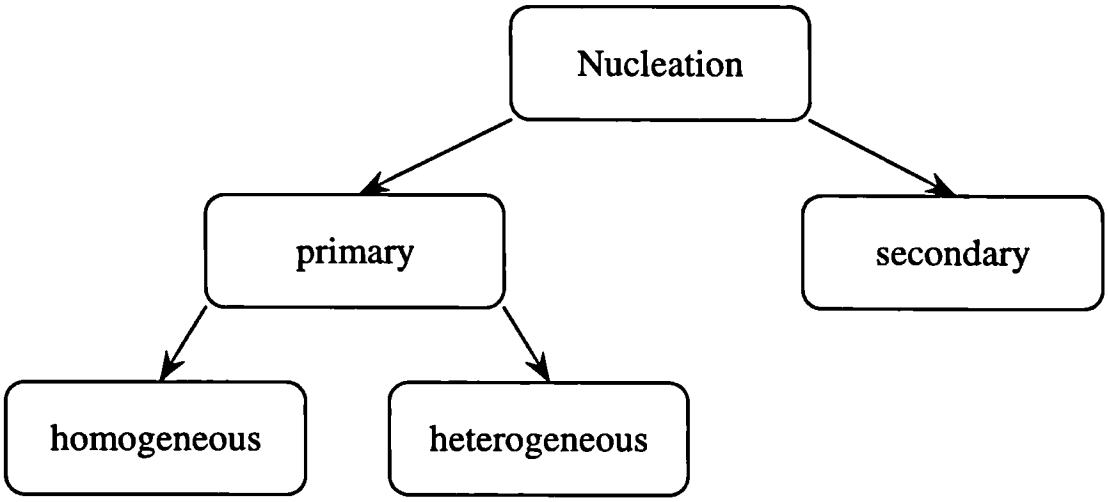

Figure 2.2 Mechanisms of nucleation (after Mullin, 1993)

2.3.1.1 PRIMARY NUCLEATION

Homogeneous nucleation

The process of homogeneous nucleation is determined by the formation of stable nuclei in a supersaturated solution. It is not yet known how the crystalline lattice is built up and whether the formation of clusters plays a crucial role. Part of the nuclei redissolves without achieving stability.

Gibbs considers the change of free energy during homogeneous nucleation, which leads to the classical nucleation theory and to the Gibbs-Thompson relationship (Mullin, 1993)

$$B^0_{hom} = A_{hom} \exp\left[-\frac{16\pi\gamma^3 v^2}{3k^3T^3(\ln S)^2}\right] \qquad (2.5).$$

Empirical power laws of the following form are often assumed for homogeneous nucleation:

$$B^0_{hom} = A_{1,hom}\sigma^a \qquad (2.6).$$

The time interval which elapses between the creation of the supersaturation and the time when nuclei are actually detected is known as induction time t_{ind}. This time span is a measure of the nucleation rate. However, it is very difficult to make predictions about the range of the induction time or even to measure it. Furthermore, the experimentally determined values for induction times depend on the detection method (*e.g.* turbidity, refractive index) applied. In general, the induction time is given by the expression

$$t_{ind} = A_{ind} S^{-n} \qquad (2.7).$$

Heterogeneous nucleation

Heterogeneous nucleation is induced by foreign nuclei or surfaces present in the solution and becomes significant at lower supersaturation levels. However, it is often difficult to distinguish between homogeneous and heterogeneous nucleation. In analogy to homogeneous nucleation, heterogeneous nucleation can be described by means of a relationship similar to Equation (2.5) (Söhnel and Garside, 1992)

$$B^0_{het} = A_{het} \exp\left[-\frac{16\pi\gamma^3 v^2 f(\varphi)}{3k^3T^3(\ln S)^2}\right] \qquad (2.8)$$

with the factor $f(\varphi)$ accounting for the decreased energy barrier to nucleation due to a foreign solid phase. Furthermore,

$$B^0_{het} = A_{1,het}\sigma^b \qquad (2.9)$$

represents an empirical relationship between heterogeneous nucleation and the level of supersaturation.

2.3.1.2 SECONDARY NUCLEATION

Crystals already present in the solution induce secondary nucleation. Nucleation takes place at a low supersaturation level and is mainly influenced by the prevailing hydrodynamic conditions and the suspension density, since the crystal-agitator, crystal-crystal and crystal-wall contacts are the main causes of this nucleation process. As secondary nucleation kinetics depend on the suspension density M_T and on hydrodynamics, the secondary nucleation rate becomes (Mullin, 1993)

$$B^0_{sec} = A_{sec}(\varepsilon) M_T^i \sigma^j \qquad (2.10).$$

Detailed descriptions of both primary and secondary nucleation can be found in *Crystallization* (Mullin, 1993), *Precipitation* (Söhnel and Garside, 1992) and *Crystallization Technology Handbook* (Mersmann, 1995).

2.3.2 GROWTH

In addition to nucleation, the growth of crystals is another dominant kinetic process which takes place in a supersaturated solution. Several crystal growth models have been proposed to describe the growth process.

- **Diffusion-reaction model (Berthoud, 1912)**

In this model, growth is seen as a mass transfer process

$$\frac{dm}{dt} = k_m A(c - c^*) \tag{2.11}$$

which can be divided into two stages, *i.e.*

diffusion $$\frac{dm}{dt} = k_d A(c - c_I) \tag{2.12}$$

and reaction $$\frac{dm}{dt} = k_r A(c_I - c^*)^r \tag{2.13}$$

with the concentration in the interface c_I. The elimination of c_I leads to

$$\frac{dm}{dt} = k_g A(c - c^*)^g \tag{2.14}.$$

Therefore, using the definition of supersaturation given in Equation (2.3),

$$G \propto \sigma^g \tag{2.15}$$

is obtained.

- **Surface integration models**

Several theories of crystal growth by surface integration have been developed and successfully applied to model crystal growth (Mullin, 1993).

Continuous growth model

The integration of growth units on a rough surface takes place where their energy demand for orientation is lowest.

$$G \propto \sigma \tag{2.16}$$

Birth and spread (B+S) model (O'Hara and Reid, 1973)

It is assumed that the formation and growth of nuclei and occurs on a smooth surface.

$$G \propto \sigma^{\frac{5}{6}} \exp\left(-\frac{A_3}{\sigma}\right) \tag{2.17}$$

Burton-Cabrera-Frank (BCF) model (Burton, Cabrera and Frank, 1951)

The BCF model is based on the assumption that growth occurs along screw dislocations.

$$G \propto \sigma^2 \tanh\left(\frac{A_4}{\sigma}\right) \tag{2.18}$$

Growth mechanisms are described in detail in *Precipitation* (Söhnel and Garside, 1992), *Crystallization* (Mullin, 1993) and *Handbook of Industrial Crystallization* (Myerson, 1993).

2.3.3 AGGLOMERATION

High supersaturation levels and therefore the rapid formation of huge numbers of nuclei increase the tendency of the particles to aggregate (particles held together with weak cohesive forces) and to agglomerate (particles held together with strong interparticle forces) in the solution (Wachi and Jones, 1992).

In general, two types of aggregation can be distinguished (Smoluchowski, 1916), *i.e.*

perikinetic aggregation in static fluids where the particles are in Brownian motion

$$D^3(t) = A_1 + B_1 t \tag{2.19}$$

and ***orthokinetic aggregation*** for agitated systems

$$\log D(t) = A_2 + B_2 t \tag{2.20}.$$

The prevailing mechanism in precipitation is usually orthokinetic agglomeration. However, Equation (2.20) is only valid to a limited extent until a maximum

agglomerate size is reached. Perikinetic agglomeration becomes important for very small particles ($L < 0.2$ µm) (Söhnel and Garside, 1992).

In the population balance, agglomeration can be considered in the birth and death terms B_{aggl} and D_{aggl} using an agglomeration rate K_{aggl}. Various expressions for the agglomeration kernel β_{aggl} are suggested in the literature. Many of these kernels have a sound theoretical basis, but others are purely empirical. Some of the kernels which are of significance for precipitation in a stirred tank are listed below.

Constant aggregation kernel

The agglomeration process is described here using a size-independent agglomeration kernel. As this is the simplest function for a kernel, the particle size distributions observed can often be approximated only insufficiently.

$$K_{aggl} = \beta_{aggl} \neq f(L_u, L_v) \tag{2.21}$$

Smoluchowski kernel (Smoluchowski, 1916)

As early as 1916, Smoluchowski showed that aggregation of spherical particles in a laminar shear field can be expressed as

$$K_{aggl}(L_u, L_v) = \frac{4}{3} Sh[L_u + L_v]^3 = \beta_{aggl}[L_u + L_v]^3 \tag{2.22}$$

with the shear rate Sh and the particle sizes L_u and L_v of the aggregating particles.

In an analogous way, aggregation due to the diffusion of particles in eddies in a turbulent flow regime can be expressed as

$$K_{aggl}(L_u, L_v) = kU[L_u + L_v]^3 = \beta_{aggl}[L_u + L_v]^3 \tag{2.23}$$

with U as the velocity gradient of the fluid in turbulent motion (Low, 1975). As the aggregation rate increases with the volume of the particle, it is more likely that a large particle is involved in an aggregation event than a small particle.

Thompson kernel (Thompson, 1968)

This empirical formulation of a kernel is given as

$$K_{aggl}(L_u, L_v) = C_A E_i \frac{(u-v)^2}{u+v} = \beta_{aggl} \frac{\left[L_u^3 - L_v^3\right]^2}{L_u^3 + L_v^3} \tag{2.24}$$

with the collection efficiency E_i and the aggregation parameter C_A. Hartel *et al.* (1986) and Hartel and Randolph (1986) successfully modelled the agglomeration kinetics of calcium oxalate with this kernel.

In a mixed system, such as a stirred tank, the rate of agglomeration additionally depends on the shear field and therefore on the energy dissipation ε in the tank. Furthermore, the degree of supersaturation S in a solution plays an important role in precipitation systems as the higher the supersaturation, the "stickier" the particles and the more readily they agglomerate (Mullin, 1993). This leads to a general formulation of the agglomeration rate

$$K_{aggl}(L_u, L_v, \varepsilon, S) = \beta_{aggl} \varepsilon^p S^q f(L_u, L_v) \qquad (2.25)$$

where both the energy dissipation and the level of supersaturation are accounted for using a power law function.

2.3.4 DISRUPTION

Fluid-particle or particle-particle interactions can lead to disruption, *i.e.* a reduction in particle size by particle splitting or surface erosion (Jones *et al.*, 1996). As with aggregation, a disruption rate K_{disr} is used for modelling. Various suggestions about the size-dependence of this rate have been made, but the function most often used in modelling breakage and disruption processes has the form

$$K_{disr}(L_u, L_v) = \beta_{disr}[L_u + L_v]^3 \qquad (2.26).$$

With this form of the disruption kernel, the disruption rate is proportional to the particle volume. This assumption of the disruption rate dependence on particle volume was theoretically validated by Synowiec *et al.* (1993), who proved that a third-order dependence on the particle size (and therefore a proportionality on particle volume) can be explained by the dominant disruption mechanism of turbulent crystal-shear forces.

In addition, the disruption rate is a function of the degree of supersaturation prevailing in the reactor. High supersaturation results in high growth rates and rigid agglomerates and thus reduces breakage (Wojcik and Jones, 1998a). Moreover, the rate of disruption increases with increased power input. Therefore, the disruption rate becomes

$$K_{disr}(L_u, L_v, \varepsilon, S) = \beta_{disr} \varepsilon^r S^s f(L_u, L_v) \qquad (2.27).$$

A further complication in the breakage process is that, depending on the breakage mechanism, a breakage event can lead to

- two daughter particles of the same or almost the same size (particle splitting)
- two daughter particles of very different sizes (attrition or abrasion)
- a number of daughter particles (multiple breakage).

In order to describe these different mechanisms, various breakage functions have been proposed (Hill and Ng, 1995 and 1996). For precipitation processes, a breakage function of the form

$$b(v, x_k) = \frac{6}{x_k}\left[4\left(\frac{v}{x_k}\right)^2 - 4\left(\frac{v}{x_k}\right) + 1\right] \qquad (2.28),$$

with $b(v,x_k)$ being the discretized number fraction of particles broken from size v into size interval x_k, seems particularly suitable as both attrition - with a high probability - and particle splitting - with a low probability - are accounted for.

2.3.5 SECONDARY CHANGES OF THE PRECIPITATE

Recrystallization

Due to the instantaneous character of the kinetics involved in the early stages of precipitation, it is frequently not the thermodynamically most stable polymorph which is obtained but the kinetically favoured metastable form of the precipitate. However, if the crystals are left in the solution for a sufficient amount of time, they may change their morphology by recrystallizing into a more stable form.

Ostwald ripening

Small crystals suspended in their own mother liquor tend to dissolve and be deposited on larger crystals. The reason for this behaviour is the tendency of the system to achieve a stage with minimum overall Gibbs energy. The dependence of solubility on size can be written as

$$\ln\left[\frac{c(r)}{c^*}\right] = \frac{2\gamma v}{vRTr} \qquad (2.29)$$

and states that smaller particles have a higher solubility than larger particles. However, this effect only becomes significant for size $r < 1$ μm.

Secondary changes were not considered in this research as the samples were withdrawn from the precipitation reactor immediately after the experiment had finished. Therefore, the crystals did not have sufficient time to ripen, age or recrystallize.

2.4 MIXING AND PRECIPITATION

2.4.1 INTRODUCTION

An important feature that distinguishes precipitation and reactive crystallization from conventional crystallization, *i.e.* cooling and evaporative crystallization, is the occurrence of steep local gradients in the supersaturation field. As the degree of supersaturation is the single most important factor determining the precipitation rates, its distribution throughout the reactor is vital for the particle size distribution of the final product.

Due to the short induction periods and high nucleation rates observed during precipitation, mixing can become a controlling factor for the precipitation rates. This chapter gives a short overview of mixing equipment and methods, while Chapter 5 discusses mixing models and mixing theory in detail.

2.4.2 MIXING EQUIPMENT

2.4.2.1 STIRRED TANK

The most common type of mixed reactor used in chemical engineering is the stirred tank. One or more impellers transfer energy from the outside to the contents of the reactor, usually a liquid or suspension (Harnby *et al.*, 1985).

As different types of impeller produce different flow fields, the flow characteristics in a vessel may vary considerably. The flow field produced by a Rushton turbine is characterised by a high local power dissipation in the impeller zone with the discharge stream of the impeller being mainly radial. By contrast, a marine-type impeller produces a fairly uniform energy distribution throughout the vessel. The discharge stream is mainly axial due to the angled blades. A 45°-pitched blade turbine produces a

discharge stream and a flow pattern between that of a radial impeller (Rushton turbine) and an axial impeller (marine-type impeller).

Stirred tanks are often equipped with a number of baffles to increase the mixing intensity by avoiding gross vortexing. The flow field produced by an axial impeller can be further controlled by the use of a draft tube. If correctly designed, the draft tube "divides" the upflowing and downcoming parts of the liquid, thus providing essential advantages for the isokinetic and representative withdrawal of samples and product streams.

Depending on the mode of operation, stirred tanks are used for continuous, semibatch and batch precipitation.

Continuous precipitation in a stirred tank

Two feed solutions A and B enter the reactor, while the product solution is withdrawn simultaneously (Figure 2.3).

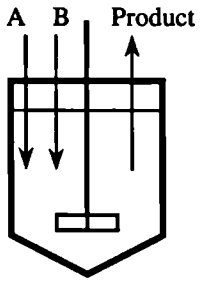

Figure 2.3 Continuous precipitation reactor

The precipitation rates of a continuously operated precipitation reactor under steady state are independent of time. However, unintended seeding, accumulation of impurities and the fact that cleaning is difficult to carry out without a complete shutdown often outweigh this advantage.

Semibatch precipitation in a stirred tank

One feed solution A is already present in the reactor, while the other feed solution B is added to the vessel (Figure 2.4).

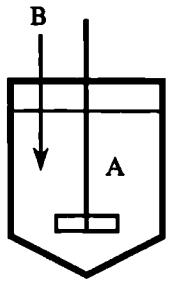

Figure 2.4 Semibatch precipitation reactor

Although semibatch reactors are simple to operate and to control, the level of supersaturation and therefore the rates change during the precipitation process. Semibatch precipitation is often used in the pharmaceutical industry where very low levels of impurities and rapid cleaning of the reactor are essential.

Batch precipitation in a stirred tank

Both feed solutions A and B are added simultaneously, but no product is withdrawn (Figure 2.5).

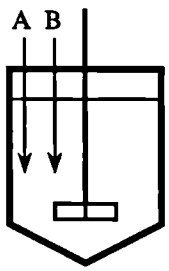

Figure 2.5 Batch precipitation reactor

Batch precipitation in its strictest sense implies that the reactor is empty before it is gradually filled as the feed solutions A and B are fed into the reactor. Under these conditions, mixing during the first part of the process would be insufficient as the impeller must have a clearance from the tank bottom. The mixing conditions will thus not be clearly specified and it may be difficult to reproduce the results. One way to avoid starting with an empty reactor is to partly fill the reactor with saturated solution or solvent and then feed the feed solutions into the reactor.

In addition to the influence of the mode of operation, the positioning of the feed tubes also has a significant effect on the particle size distribution of the precipitated product. The crucial importance of the feed point position in mixing-controlled systems is shown for four different cases of continuous or batch precipitation with two feed tubes. The same considerations can be applied to semibatch precipitation. In this case, however, only one feed tube is used and the number of different possibilities is reduced.

Case 1

Feed points are close to one another and close to the impeller (Figure 2.6).

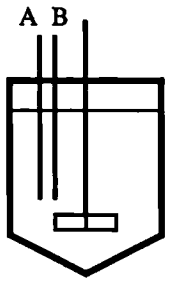

Figure 2.6 Feed points close to one another and to impeller

This set-up leads to

- uniform distribution of the feed solutions
- direct mixing of the two feed streams.

Case 2

Feed points are remote from one another but close to the impeller (Fig. 2.7).

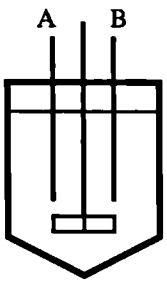

Figure 2.7 Feed points remote from one another and close to impeller

This set-up leads to

- uniform distribution of the feed solutions
- indirect mixing of the two feed streams via the bulk.

Case 3

Feed points are close to one another in a zone remote from the impeller (Figure 2.8).

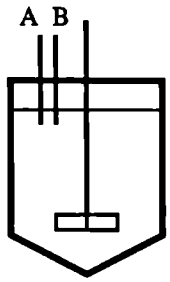

Figure 2.8 Feed points close to one another and remote from impeller

This set-up leads to

- high local concentrations of the feed solutions
- direct mixing of the two feed streams.

Case 4

Feed points are remote from one another and in a zone remote from the impeller (Figure 2.9).

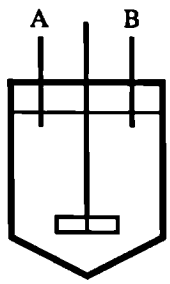

Figure 2.9 Feed points remote from one another and from impeller

This set-up leads to

- high local concentrations of the feed solutions
- indirect mixing of the two feed streams via the bulk.

As mentioned above, the supersaturation field is crucial for the rates in a precipitation reactor. In Case 1 and Case 2, high local levels of supersaturation can be avoided by adding the feed solutions close to the impeller, whereas in Case 3 and Case 4, excessive nucleation around the feed points is to be expected due to high local supersaturation levels.

Power input in a stirred tank

The power input for Newtonian liquids mixed in a stirred tank cannot be obtained from first principles as the reactor geometry, impeller and baffles coupled with the fluid dynamics become a very complex problem. From dimensional analysis, however, it has been found that

$$\frac{P}{\rho N^3 {d_s}^5} = f\left(\frac{\rho N {d_s}^2}{\mu}, \frac{N^2 d_s}{g}\right) \tag{2.30}$$

with the power number Po

$$Po = \frac{P}{\rho N^3 {d_s}^5} \tag{2.31}$$

and the Reynolds number Re

$$Re = \frac{\rho N {d_s}^2}{\mu} \tag{2.32}$$

and the Froude number Fr

$$Fr = \frac{N^2 d_s}{g} \tag{2.33}$$

and therefore

$$Po = f(Re, Fr) \tag{2.34}.$$

If the reactor is equipped with baffles, the effect of the Froude number Fr can be ignored and the relationship (2.34) simplified to

$$Po = f(Re) \qquad (2.35).$$

The Po versus Re curves, the power curves, have been published for many different geometrical set-ups (Harnby *et al.*, 1985). It was found that the power number in the turbulent regime ($Re > 6\times10^3$) approaches a constant value.

From the power number Po, the actual power input P into the reactor is calculated according to

$$P = Po\rho N^3 d_s^5 \qquad (2.36)$$

and the power input per unit mass ε to

$$\varepsilon = \frac{Po\rho N^3 d_s^5}{m_{susp}} \qquad (2.37).$$

If no suitable power curve is available or the geometric set-up is unique, the power curve $Po = f(Re)$ can be determined by measuring the torque T and the speed N over a range of stirrer speeds. The power input P is calculated as

$$P = \omega T = 2\pi NT \qquad (2.38).$$

The fluid dynamic parameters (Reynolds number Re, tip speed v_{tip} and specific energy dissipation ε_{avg}) for different mixing conditions are listed in Appendix A2.1.

2.4.2.2 TEE-MIXER

Tee-mixers are often used to pre-mix feed solutions A and B before they enter the actual reactor (Figure 2.10). By changing the flow rate of the feed solutions or the

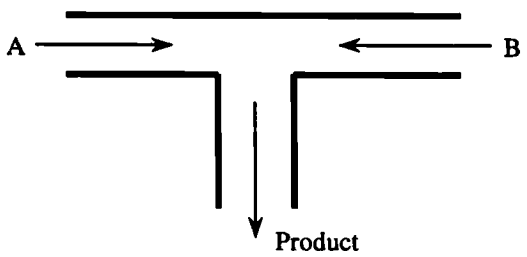

Figure 2.10 Tee-mixer

geometry of the Tee-mixer, it is possible to vary the mixing conditions. In general, Tee-mixers lead to very high degrees of supersaturation and consequently high nucleation rates due to the highly localised mixing of the concentrated feed solutions.

Marmo *et al.* (1996) and Mahajan and Kirwan (1996) investigated mixing and precipitation in Tee-mixers and two-impinging-jets (TIJ) mixers, respectively.

2.4.2.3 JET MIXER

In the semibatch mode of operation, a jet mixer can be used to achieve the desired mixing effect as the momentum transferred from the high-velocity jet B to the bulk phase A causes the mixing (Figure 2.11). Jet mixers are simple in construction and do not include any moving parts.

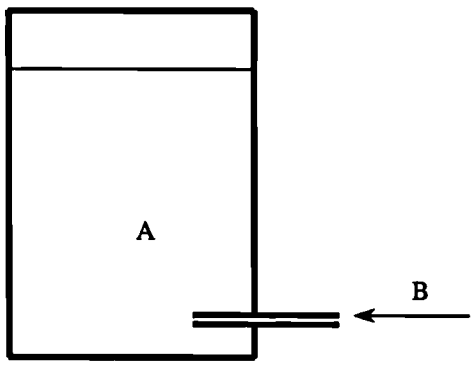

Figure 2.11 Jet mixer

2.4.2.4 STATIC MIXERS

Static mixers function in a similar way to packings in mass transfer units, such as distillation columns and absorption towers. The static mixing elements force the liquid flow to change its direction frequently and thereby mix with neighbouring parts of the liquid. This form of mixing, however, is usually not suitable for precipitation processes because the precipitate tends to stick to the solid surfaces, grow on the mixing elements and subsequently block the fluid flow.

A concise description of mixing equipment can be found in Oldshue (1983) and in Harnby *et al.* (1985).

CHAPTER 3

THE POPULATION BALANCE

3.1 DERIVATION OF THE POPULATION BALANCE

During the course of precipitation, individual particles may nucleate, grow, agglomerate or break and leave the precipitation reactor in the continuous mode of operation. The mathematical framework used to describe this process is called the population balance.

The concept of population balances for agglomerative processes based on the conservation of probability in a mechanical system was introduced by Hulburt and Katz (1964). They derived their mathematical model from statistical mechanics and applied it to processes involving both growth and agglomeration.

Randolph and Larson (1988) investigated in detail the modelling of crystal size distributions using population balances and developed the mixed-suspension mixed-product-removal (MSMPR) model for continuous crystallizers.

In general, the population balance of a system is derived from a number-continuity equation.

The population balance in a defined volume can be stated as

Accumulation = Input - Output + Net generation.

Therefore, in the Lagrangian framework the population balance can be written as

$$\frac{d}{dt}\int_{V_1} n dV = \int_{V_1} (B-D) dV \tag{3.1}$$

with V_1 as an arbitrarily chosen subvolume. $n(\boldsymbol{x})$ represents the population density at location $\boldsymbol{x}\,(x,y,z)$ and is defined as

$$n(\boldsymbol{x}) = \frac{dN(\boldsymbol{x})}{dt} \tag{3.2}$$

and B and D are the birth and death rate, respectively. The first term can be written as

$$\frac{d}{dt}\int_{V_1} n dV = \int_{V_1}\left[\frac{\partial n}{\partial t} + \nabla\left(\frac{d\boldsymbol{x}}{dt} n\right)\right] dV \tag{3.3}$$

$$\text{with } \frac{d\boldsymbol{x}}{dt} = \boldsymbol{v} = \boldsymbol{v}_i + \boldsymbol{v}_e \tag{3.4}$$

and the population balance becomes

$$\int_{V_1}\left[\frac{\partial n}{\partial t} + \nabla(\boldsymbol{v}_i n) + \nabla(\boldsymbol{v}_e n) + D - B\right] dV = 0 \tag{3.5}$$

with the internal velocity v_i and the external velocity v_e. In this context the internal co-ordinate space specifies the condition(s) of the particle, while the external co-ordinate space refers to the position of the particle in the physical space. The internal velocity therefore describes the change of particle size or particle volume and the external velocity the fluid velocity in the reactor.

As the subvolume V_1 was arbitrary, it must be independent of the volume integration, leading to

$$\frac{\partial n}{\partial t}+\nabla(vn)-B+D=0 \qquad (3.6).$$

This equation is analogous to the continuity equation derived for the conservation of mass in a continuum

$$\frac{\partial \rho}{\partial t}+\nabla(v\rho)=0 \qquad (3.7).$$

The general equation (3.6) can be used when particles are distributed along both internal and external co-ordinate space. For most precipitation and crystallization problems, however, it is sufficient to know only the distribution of particles in the internal phase space. The system is considered to be fully backmixed with inputs and outputs Q_k and population densities n_k. The population balance for this simplified case can be derived from the general population balance with the form

$$\int_V \left[\frac{\partial n}{\partial t}+\nabla(v_e n)+\nabla(v_i n)+D-B\right]dV=0 \qquad (3.8).$$

As n, B and D are only functions of time and internal co-ordinates, these terms can be easily integrated

$$\frac{\partial n}{\partial t}+\nabla(v_i n)+D-B+\frac{1}{V}\int_{V_1}\nabla(v_e n)dV=0 \qquad (3.9)$$

with

$$\frac{1}{V}\int_{V_1}\nabla(v_e n)dV=n\frac{d(\log V)}{dt}+\sum_k \frac{Q_k n_k}{V} \qquad (3.10)$$

where Q_k and n_k are the flow rate and population density respectively of the flows incoming and outgoing, and using the internal velocity expressed in terms of the crystal growth rate

$$\nabla v_i n=\frac{\partial(Gn)}{\partial L} \qquad (3.11)$$

the *macrodistributed population balance* (3.12) can be derived

$$\frac{\partial n}{\partial t}+\frac{\partial (Gn)}{\partial L}+n\frac{d(\log V)}{dt}=B-D-\sum_k \frac{Q_k n_k}{V} \qquad (3.12).$$

This equation describes the change of population in a well-mixed system and is often used to model crystallization and precipitation processes.

3.2 MOMENT TRANSFORMATION OF THE POPULATION BALANCE

Using the moment transformation of the population balance, it is possible to reduce the dimensionality of the population balance to that of the transport equations. Though the mathematical effort to solve the population balance may therefore decrease considerably, a moment transformation always leads to a loss of information about the distribution of the variables with the particle size or any other internal co-ordinate.

The *micromoment population balance* is derived from the general population balance (Lagrangian framework) and can be written as

$$\frac{\partial m_j}{\partial t}+\nabla v_e m_j = 0^j B^0 + jGm_{j-1}+\overline{B}-\overline{D} \qquad (3.13)$$

with $j = 0,1,2,...$ and the j-th moment m_j defined as

$$m_j=\int_0^\infty nL^j dL \qquad (3.14).$$

The micromoment population balance (3.13) averages the internal co-ordinate (*i.e.* the particle properties) in moments but accounts for their local variations. The *macromoment population balance* (3.15) is an ordinary differential equation (time dependence only) and can be obtained from the macrodistributed population balance:

$$\frac{dm_j}{dt}+m_j\frac{d(\log V)}{dt}=0^j B^0 + jGm_{j-1}+\overline{B}-\overline{D}-\sum_k \frac{Q_k n_k}{V} \qquad (3.15).$$

3.3 POPULATION BALANCE FOR THE MIXED-SUSPENSION MIXED-PRODUCT-REMOVAL (MSMPR) CRYSTALLIZER

To start with the simplest case, the population balance concept will be applied to an ideal MSMPR crystallizer. The MSMPR model is analogous to the continuous stirred

tank reactor (CSTR) model in reaction engineering. The following assumptions lead to the basic definition of an MSMPR crystallizer:

- continuous steady state of operation
- well-mixedness
- no agglomeration or disruption
- crystal growth rate independent of crystal size
- no classified withdrawal of the product
- no seed crystals in the feed.

Two different approaches used to derive the basic equations of an MSMPR crystallizer will be shown below.

In the first approach, the population balance (3.12) is considered

$$\frac{\partial n}{\partial t}+\frac{\partial (Gn)}{\partial L}+n\frac{d(\log V)}{dt}=B-D-\sum_k \frac{Q_k n_k}{V}.$$

The following simplifications can be made:

$\frac{\partial n}{\partial t}=0$	steady state
$n\frac{d(\log V)}{dt}=0$	constant volume
$B=0, D=0$	no agglomeration, no breakage
$\frac{\partial (Gn)}{\partial L}=G\frac{dn}{dL}$	size-independent growth
$\sum_k \frac{Q_k n_k}{V}=\frac{Qn}{V}=\frac{n}{\tau}$	mixed suspension discharge
$\tau=\frac{V}{Q}$	residence time.

The population balance of an MSMPR crystallizer that meets the criteria mentioned above therefore has the form

$$G\frac{dn}{dL}+\frac{n}{\tau}=0 \qquad (3.16).$$

The same result can be obtained using the following approach:

for a time interval Δt and a size range $\Delta L=L_2-L_1$ the population balance has the form

$$n_1 G_1 V \Delta t = n_2 G_2 V \Delta t + Q\bar{n}\Delta L \Delta t \tag{3.17}$$

(crystals entering = crystals leaving by growth + removal of crystals).

This leads to

$$V(n_2 G_2 - n_1 G_1) = -Q\bar{n}\Delta L \tag{3.18}$$

and for $\Delta L \rightarrow 0$ the population balance becomes

$$V\frac{d(Gn)}{dL} = -Qn \tag{3.19}.$$

With G ≠ G(L) $$G\frac{dn}{dL} + \frac{n}{\tau} = 0 \tag{3.20}$$

the same result as above is obtained.

With the population density of nuclei n^0 the integration of

$$G\frac{dn}{dL} + \frac{n}{\tau} = 0 \tag{3.21}$$

gives $$n = n_0 exp\left(-\frac{L}{G\tau}\right) \tag{3.22}$$

which characterises the crystal size distribution of an MSMPR crystallizer (Figure 3.1).

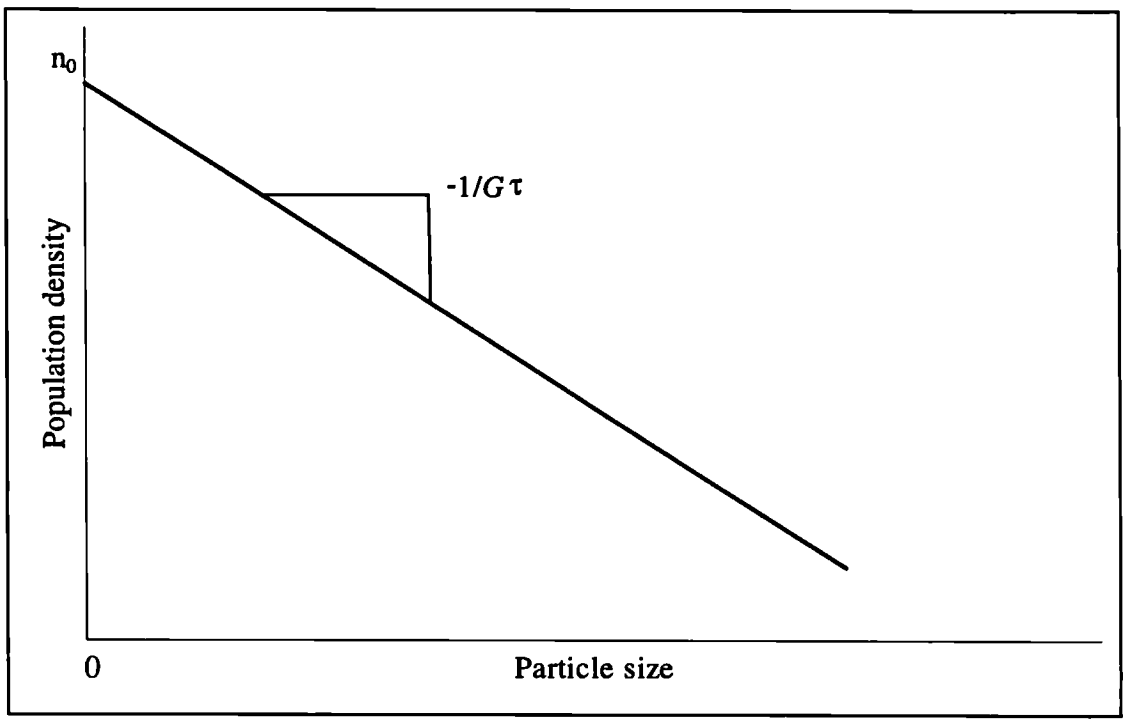

Figure 3.1 Particle size distribution of an MSMPR crystallizer

The nucleation rate B^0 is defined as

$$B^0 = \left.\frac{dN}{dt}\right|_{L\to 0} \tag{3.23}$$

and the growth rate as

$$G = \frac{dL}{dt} \tag{3.24}$$

with
$$\left.\frac{dN}{dt}\right|_{L\to 0} = \left.\frac{dN}{dL}\right|_{L\to 0} \frac{dL}{dt} \tag{3.25}$$

B^0 for MSMPR conditions becomes

$$B^0 = n_0 G \tag{3.26}.$$

Next, the **moments** of the crystal size distribution can be defined as:

Zeroth moment of the distribution

Number of crystals in the considered volume

$$m_0 = N_T = \int_0^\infty n(L)dL = n_0 G\tau \tag{3.27}$$

First moment of the distribution

Cumulative length

$$m_1 = L_T = \int_0^\infty Ln(L)dL = n_0 (G\tau)^2 \tag{3.28}$$

Second moment of the distribution

Specific surface area

$$m_2 k_a = A_T = k_a \int_0^\infty L^2 n(L)dL = 2k_a n_0 (G\tau)^3 \tag{3.29}$$

Third moment of the distribution

Specific mass of crystals

$$m_3 k_v \rho_c = M_T = k_v \rho_c \int_0^\infty L^3 n(L)dL = 6k_v \rho_c n_0 (G\tau)^4 \tag{3.30}.$$

Furthermore, for MSMPR conditions the **characteristic lengths** can be calculated from the moments. For example:

Number mean size $\quad L_{10} = G\tau \tag{3.31}$

Volume mean size $L_{43} = 4G\tau$ (3.32).

3.4 POPULATION BALANCE MODELLING INCLUDING AGGLOMERATION AND DISRUPTION KINETICS

3.4.1 INTRODUCTION

Processes in which, in addition to growth and nucleation, agglomeration occurs as a consequence of aggregation and disruption can also be mathematically described by means of population balances. From the macrodistributed form of the population balance

$$\frac{\partial n}{\partial t} + \frac{\partial (Gn)}{\partial L} + n\frac{d(\log V)}{dt} = B - D - \sum_k \frac{Q_k n_k}{V} \tag{3.33}$$

with the assumption that the growth rate G is not a function of the particle size (McCabe's ΔL-law), with a constant crystallizer volume and a crystal-free inlet flow (no seeding) the population balance becomes

$$\frac{\partial n}{\partial t} + G\frac{\partial n}{\partial L} = B_{aggl} + B_{disr} - D_{aggl} - D_{disr} - \frac{n}{\tau} \tag{3.34}$$

with the birth terms for agglomeration and disruption

$$\begin{aligned} B_{aggl} + B_{disr} &= \frac{L^2}{2}\int_0^L \frac{K_{aggl} n(L_u) n(L_v) dL_u}{L_v^2} \\ &+ \int_{L_v}^{\infty} K_{disr} S'(L_u, L_v) n(L_u) n(L_v) dL_u \end{aligned} \tag{3.35}$$

and the death terms for agglomeration and disruption

$$D_{aggl} + D_{disr} = n(L)\int_0^{\infty} K_{aggl} n(L_u) dL_u + K_{disr} n(L) \tag{3.36}$$

and the residence time $\tau = \frac{V}{Q}$.

The population balance therefore represents a partial integro-differential equation that can only be solved analytically in specific cases (Ramkrishna, 1985). It is thus necessary to search for numerical solution strategies that solve the population balance rapidly and accurately in order to model precipitation processes and estimate kinetic parameters.

3.4.2 ANALYTICAL SOLUTION OF THE POPULATION BALANCE

One specific case in which the population balance can be solved analytically is described by Hostomský (1987). He solves the steady-state population balance for agglomeration and nucleation only (no growth) and assumes size-independent agglomeration, *i.e.* $K_{aggl} = \beta_{aggl}$ = const. Hostomský considers the population balances for particles containing i primary particles and derives a set of i non-linear equations, which are solved with repeated substitution.

The accuracy of the solution obtained depends on the number i of primary particles, since Hostomský uses an approximation for a factorial expression. The solution is therefore not totally analytical, but gives an error of 3.8% and 1.3% for $i = 10$ and $i = 30$, respectively.

The population density distribution is obtained by converting the original volume density distribution into a number density distribution, and has the form

$$n(L) = \frac{3}{2}\left(\frac{2a+1}{\pi}\right)^{\frac{1}{2}} \frac{1}{\beta_{aggl}\tau}\left(\frac{2a}{2a+1}\right)^{\left(\frac{L}{L_0}\right)^3} \frac{L_0^{3/2}}{L^{5/2}} \qquad (3.37)$$

with $$a = \beta_{aggl} B^0 \tau^2 \qquad (3.38)$$

as an aggregation parameter and L_0 for the size of the primary particles.

As mentioned above, this equation is not derived in a purely analytical way and is only valid when

- no growth takes place: $G = 0$
- agglomeration is size-independent: $K_{aggl} = \beta_{aggl}$ = const.
- no disruption takes place.

According to Hostomský, the distribution can be approximated with a power law for high values of a, *i.e.* for crystallization processes with high nucleation rates (*e.g.* precipitation),

$$n(L) = n(L_0)\left(\frac{L}{L_0}\right)^{-\frac{5}{2}} \qquad (3.39).$$

3.4.3 NUMERICAL SOLUTION OF THE POPULATION BALANCE

The numerical methods for solving population balances can be divided into the following groups:

Method of classes

Calculates the number of particles in length- or volume-discretized size classes.

Method of finite differences

Estimates differential quotients at different points.

Method of moments

Reduces dimensionality, but impracticable for too many size-dependent mechanisms (Hulburt and Katz, 1964).

Method of orthogonal collocation

Transforms the population balance into a set of linear differential equations by decomposing the number density function in a set of orthogonal functions.

Only the most widespread method, *i.e.* the method of classes, will be considered below. Various solution procedures have been proposed, according to different methods of discretization.

3.4.4 DISCRETIZATION METHODS

3.4.4.1 DISCRETIZATION METHOD OF GELBARD *ET AL.*

Originally derived for aerosol kinetics, Gelbard and Seinfeld (1978) and Gelbard *et al.* (1980) were the first to propose a solution for the population balance of a size-dependent agglomerative process. In their model only one property, for example number *or* mass but not both, can be conserved. Furthermore, their technique is computationally very time-consuming because of the need to evaluate a large number of double integrals.

3.4.4.2 DISCRETIZATION METHOD OF HOUNSLOW

Hounslow *et al.* (1988) solve the population balance by discretizing the particle volume in a geometrical grid, *i.e.* $v_{i+1} = 2\ v_i$ and $L_{i+1} = 2^{1/3}\ L_i$ with the particle volume v and the particle size L. As the fact that the grid cannot be chosen freely may be limiting, in a subsequent paper Litster *et al.* (1995) published a generalised version for a grid with $v_{i+1} = v_i^{1/q}$ (q is an integer). However, Litster's formulation does not always conserve

mass and number of the particles and thus only the original method with the geometrical grid will be considered below.

With regard to agglomeration, Hounslow *et al.* (1988) and Hounslow (1990a and b) distinguish four different mechanisms that change the population in a size range, and consider them separately. Nucleation of particles is assumed to occur to the extent of B^0 in the first class. For growth, the two adjacent classes to each class are taken into account.

Using this method, the zeroth moment (number) and the third moment (mass) are conserved properly, the latter, however, only after introducing a correction factor. The final set of equations has the form

$$\frac{dN_i}{dt} = \left(\frac{dN_i}{dt}\right)_{nucl} + \left(\frac{dN_i}{dt}\right)_{growth} + \left(\frac{dN_i}{dt}\right)_{aggl} - \frac{N_i - N_{i,in}}{\tau} \tag{3.40}$$

with

$$\left(\frac{dN_i}{dt}\right)_{nucl} = \begin{cases} B^0 & i=1 \\ 0 & i \neq 1 \end{cases} \tag{3.41}$$

$$\left(\frac{dN_1}{dt}\right)_{growth} = \frac{G}{L_1}\left[\left(b_g + c_g r\right)N_1 + c_g N_2\right] \tag{3.42}$$

$$\left(\frac{dN_i}{dt}\right)_{growth} = \frac{G}{L_i}\left(a_g N_{i-1} + b_g N_i + c_g N_{i+1}\right) \tag{3.43}$$

$$a_g = \frac{2r}{(1+r)(r^2-1)} \tag{3.44}$$

$$b_g = \frac{2}{1+r} \tag{3.45}$$

$$c_g = -\frac{2r}{(1+r)(r^2-1)} \tag{3.46}$$

$$r = \frac{L_{i+1}}{L_i} = 2^{1/3} \tag{3.47}$$

$$\left(\frac{dN_i}{dt}\right)_{aggl} = N_{i-1}\sum_{j=1}^{i-2} 2^{j-i+1} K_{aggl} N_j + \frac{1}{2} K_{aggl} N_{i-1}^2$$

$$- N_i \sum_{j=1}^{i-1} 2^{j-i} K_{aggl} N_j - N_i \sum_{j=i}^{i_{max}} K_{aggl} N_j \tag{3.48}.$$

3.4.4.3 DISCRETIZATION METHOD OF KUMAR AND RAMKRISHNA

In contrast to Hounslow (1990a and b), Kumar and Ramkrishna (1996a and b) present a solution to population balance problems of agglomeration processes without restricting the choice of the grid of the discretized length scale. Furthermore, two arbitrarily chosen properties can be preserved. In the case of preservation of the zeroth and third moments (number and mass respectively), the equations for a purely agglomerative process can be written in the following form:

$$\left(\frac{dN_i}{dt}\right)_{aggl} = \sum_{\substack{j,k \\ x_{i-1}\le(x_j+x_k)\le x_{i+1}}}^{j\ge k} \left(1-\frac{1}{2}\delta_{j,k}\right)\eta K_{aggl}N_jN_k - N_i\sum_{k=1}^{i_{max}} K_{aggl}N_k \quad (3.49)$$

with
$$\eta = \begin{cases} \dfrac{x_{i+1}-v}{x_{i+1}-x_i} & , x_i \le v \le x_{i+1} \\ \dfrac{v-x_{i-1}}{x_i-x_{i-1}} & , x_{i-1} \le v \le x_i \end{cases} \quad (3.50)$$

and x_i as the representative volume of the ith size range and v as the particle volume.

Moreover, according to Kumar and Ramkrishna (1996a and b) disruption can be accounted for with

$$\left(\frac{dN_i}{dt}\right)_{disr} = \sum_{k=i}^{i_{max}} n_{i,k}K_{disr}N_k - K_{disr}N_i \quad (3.51)$$

with
$$n_{i,k} = \int_{x_i}^{x_{i+1}} \frac{x_{i+1}-v}{x_{i+1}-x_i} b(v,x_k)dv + \int_{x_{i-1}}^{x_i} \frac{v-x_{i-1}}{x_i-x_{i-1}} b(v,x_k)dv \quad (3.52).$$

For binary breakage the breakage function $b(v,x_k)$ becomes

$$b(v,x_k) = \frac{2}{x_k} \quad (3.53)$$

and the weighting matrix

$$n_{i,k} = \frac{x_{i+1}-x_{i-1}}{x_k} \quad (3.54).$$

Using the parabolic attrition function

$$b(v,x_k) = \frac{6}{x_k}\left[4\left(\frac{v}{x_k}\right)^2 - 4\left(\frac{v}{x_k}\right)+1\right] \quad (3.55)$$

which was proposed by Hill and Ng (1995) and is based on an empirical form suggested by Austin *et al.* (1976) and Klimpel and Austin (1984), the weighting matrix becomes

$$\begin{aligned} n_{i,k} = & \left(\frac{x_i}{x_{i+1}-x_i} + \frac{x_i}{x_i - x_{i-1}} \right) \left[6\left(\frac{x_i}{x_k}\right)^3 - 8\left(\frac{x_i}{x_k}\right)^2 + 3\left(\frac{x_i}{x_k}\right) \right] \\ & - \left(\frac{x_{i+1}}{x_{i+1}-x_i} + \frac{x_{i-1}}{x_i - x_{i-1}} \right) \left[8\left(\frac{x_i}{x_k}\right)^3 - 12\left(\frac{x_i}{x_k}\right)^2 + 6\left(\frac{x_i}{x_k}\right) \right] \\ & + \frac{x_{i+1}}{x_{i+1}-x_i} \left[2\left(\frac{x_{i+1}}{x_k}\right)^3 - 4\left(\frac{x_{i+1}}{x_k}\right)^2 + 3\left(\frac{x_{i+1}}{x_k}\right) \right] \\ & + \frac{x_{i-1}}{x_i - x_{i-1}} \left[2\left(\frac{x_{i-1}}{x_k}\right)^3 - 4\left(\frac{x_{i-1}}{x_k}\right)^2 + 3\left(\frac{x_{i-1}}{x_k}\right) \right] \end{aligned} \qquad (3.56).$$

Both breakage functions were checked for consistency using

$$\int_0^{x_k} b(v, x_k)\,dv = 2 \qquad (3.57)$$

for the number of particles formed per breakage event.

Nucleation and growth are modelled as described in 3.4.4.2.

3.4.5 SOLUTION METHODS

The sets of non-linear ordinary differential equations obtained by discretization were solved using two different strategies, *i.e.*

- FORTRAN90 programming including routines from the NAG Routines Library
- flowsheet-orientated programming with the software package SpeedUp©.

3.4.5.1 FORTRAN PROGRAMMING

The set of differential equations was solved using the NAG subroutine D02EAF which is particularly suitable for stiff systems of first-order ordinary differential equations (ODEs). This variable-order, variable-step method implements the Backward Differentiation Formulae (BDF) and is of an explicit type (Schuler, 1996). The ODEs are integrated over a time range of ten residence times, assuming that after that time steady state has been achieved. Subroutines calculate values for the change of

population due to nucleation, growth, agglomeration and disruption. The population density of each class is calculated from the number of particles in each size class.

3.4.5.2 SPEEDUP© PROGRAMMING

SpeedUp© is an equation-based software tool which enables the user to run steady-state, dynamic, parameter estimation and optimisation problems. The user is not required to provide an algorithm for solving the equations, but only to specify them in a model. SpeedUp© then converts sets of equations into blocks and solves these decomposed blocks separately. The numerical routines provided for integrating ODEs are a modified Gear's integrator, a Euler integrator and a fourth order Range-Kutta integrator. Sets of linear and non-linear equations (steady state) are solved with a Newton algorithm. A choice can thereby be made between the two methods of calculating the elements of the Jacobian matrix each time or estimating them by an update method.

3.5 RESULTS

In order to compare the accuracy of the discretization methods of Hounslow (1990a and b) and Kumar and Ramkrishna (1996a and b), the population balances for two different cases are discussed below. For both cases a constant agglomeration kernel $K_{aggl} = \beta_{aggl} = \text{const.}$ is assumed and disruption is only accounted for in the precipitation of calcium oxalate (Case 2).

3.5.1 CASE 1: PRECIPITATION OF CALCIUM CARBONATE

For the continuous precipitation of calcium carbonate from equimolar solutions of $Ca(NO_3)_2$ and Na_2CO_3, Hostomský and Jones (1991) found that under most conditions investigated the real growth rate (in contrast to the apparent growth rate) can be ignored. In this case an analytical solution to the population balance as presented by Hostomský (1987) and described in Chapter 3.4.2 can be obtained. According to Hostomský and Jones (1991), experiment 4, the following conditions were chosen:

$$\tau = 0.0833 \text{ h}$$

$$B^0 = 1.98 \times 10^{17} \text{ 1/m}^3\text{h}$$

$\beta_{aggl} = 1.68 \times 10^{-10}$ m^3/h

$L_0 = 0.5$ µm.

Figure 3.2 shows a comparison of the results of the two discretization methods. It can be seen that compared with the analytical solution, Hounslow's discretization method (using both SpeedUp© and FORTRAN-BDF) leads to the highest errors - as one would expect due to the coarse grid. The solution of Ramkrishna's discretization is shown for two different grids ($r = 1.6$ and $r = 1.3$). The finer grid ($r = 1.3$) approximates the analytical solution very accurately. However, due to the large number of size classes necessary to cover a reasonable size-range (58 classes for $r = 1.3$ in comparison to 22 classes for $r = 2.0$), the computation time is substantially higher than for the other grids.

All discretization methods approximate the analytical solution very well up to a size of 50 µm and lead to an overprediction of particles in the range greater than 50 µm. This leads, in particular, to errors in the mass balance, as can be seen from the following calculations. The error in the mass balance is assumed to be proportional to the error in the prediction of the third moment of the distribution according to

$$c_{in} - c_{out} = k_v m_3 \frac{\rho_c}{MW} \qquad (3.58).$$

The errors for the third moment, calculated in the size range from 0.5 µm to 80 µm, are listed in Table 3.1.

Discretization method	m_3 [µm^3/m$^3 \times 10^{16}$]	Rel. error
Analyt. solution	0.219	-
Ramkrishna $r = 1.3$	0.240	0.032
Ramkrishna $r = 1.6$	0.266	0.072
Ramkrishna $r = 1.8$	0.285	0.101
Hounslow	0.301	0.125

Table 3.1 Relative errors of different discretization methods

Another conclusion that can be drawn from the results in Figure 3.2 is that the calculated values are independent of the method of numerical solution. The steady-state SpeedUp© simulation gives the same population density distribution for Hounslow's discretization method as the program with the NAG routine using the Backward Differentiation Formulae (BDF). Consequently, only computational efficiency and convenience for data handling need to be taken into account when choosing the most suitable method. Due to its better versatility, FORTRAN programming was chosen as the most appropriate solution method.

As far as the method of discretization is concerned, Ramkrishna's discretization with the medium-fine grid $v_{i+1} = 1.6v_i$ seems to be a reasonable compromise between computational efficiency and mathematical accuracy.

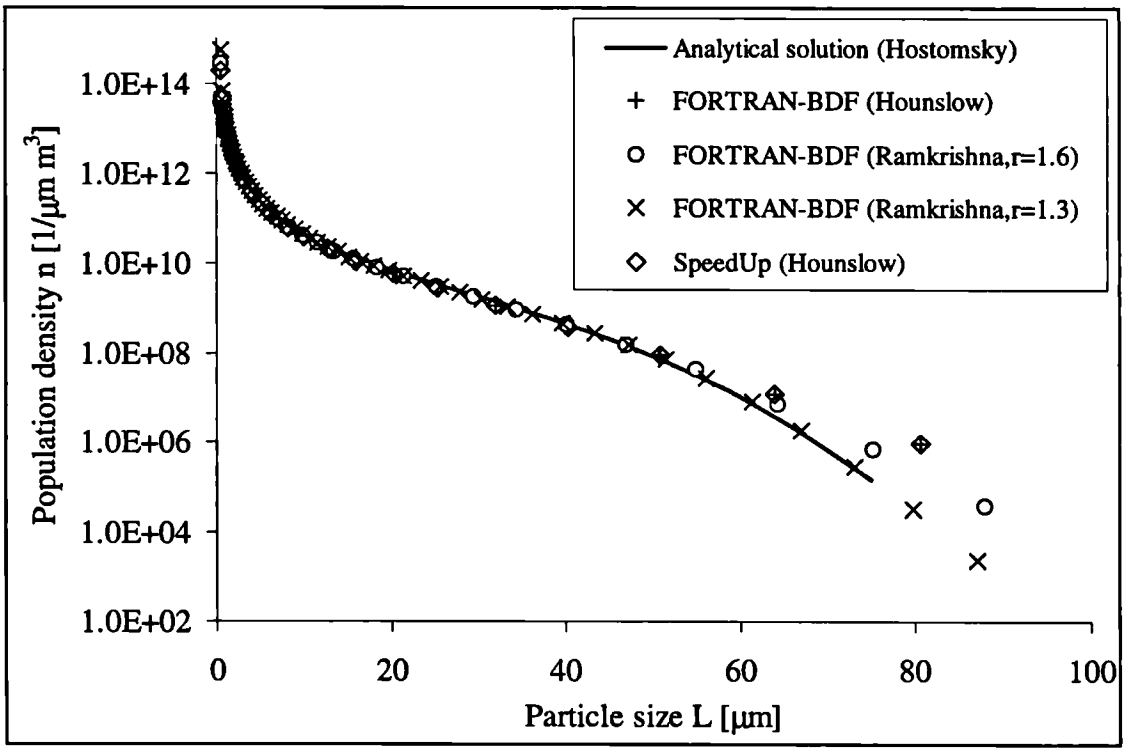

Figure 3.2 Population density distribution of calcium carbonate

3.5.2 CASE 2: PRECIPITATION OF CALCIUM OXALATE

Even though it is a well-known fact that agglomeration occurs during the precipitation of calcium oxalate, no reliable data for nucleation, growth, agglomeration

and disruption could be found in one source. Therefore, more than one literature source of data is used to estimate the expected rates. From Kavanagh (1992), Hartel and Randolph (1986), Bramley *et al.* (1996a and b) and Garside *et al.* (1982) the following precipitation parameters were estimated:

$\tau = 0.1$ h

$B^0 = 2.0\times10^{12}$ 1/m^{3}h

$\beta_{aggl} = 1.0\times10^{-10}$ m^3/h (size-independent)

$\beta_{disr} = 20$ 1/h (size-independent)

$G = 50$ µm/h

$L_0 = 0.5$ µm.

The population density is modelled with and without disruption (Figure 3.3). Using the FORTRAN90 program including the NAG routine for the integration of the differential equation system, both the agglomeration and the disruption kernels are set to be size-independent. A strong influence of the disruption process on the size distribution can be seen, leading to a bimodality in the distribution curve.

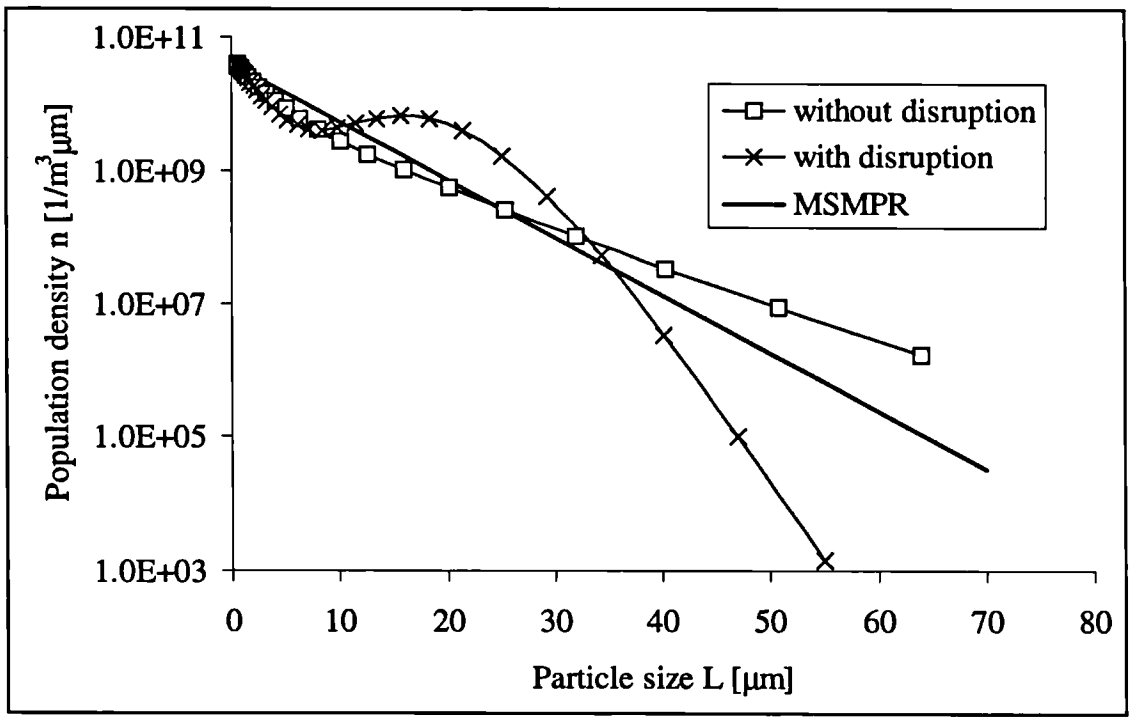

Figure 3.3 Population density distribution of calcium oxalate

CHAPTER 4

DETERMINATION OF THE PRECIPITATION KINETICS

4.1 INTRODUCTION

Reliable kinetic data are of paramount importance for successful scale-up. Most data found in the literature were determined assuming MSMPR conditions and did not account for agglomeration and breakage of particles. Therefore, in the present study laboratory-scale experiments will be carried out under a range of different conditions and the kinetic parameters for nucleation, growth, agglomeration and breakage calculated from the particle size distributions obtained. Furthermore, the morphology and shape factors of the crystals will be determined, and the suitability of "designed experiments" for reducing the number of experiments will be investigated.

4.2 PHYSICAL PROPERTIES OF THE SYSTEMS UNDER INVESTIGATION

4.2.1 CALCIUM OXALATE CaC_2O_4

Calcium oxalate can be precipitated from reacting supersaturated solutions of calcium chloride $CaCl_2$ and sodium oxalate $Na_2C_2O_4$. According to the process conditions, three different hydrates are formed:

- Calcium oxalate monohydrate $CaC_2O_4 \times H_2O$ (COM) monoclinic
- Calcium oxalate dihydrate $CaC_2O_4 \times 2H_2O$ (COD) tetragonal
- Calcium oxalate trihydrate $CaC_2O_4 \times 3H_2O$ (COT) triclinic.

At 25°C COM is the stable hydrate, whereas COD and COT are metastable. Garside *et al.* (1982) observed only COT in their MSMPR experiments at 9°C, while at 37°C (body temperature) calcium oxalate precipitated fully as COM. In the range between 20°C and 30°C a mixture of the hydrates is likely. The authors report the following thermodynamic solubility products K_{sp} at 25°C:

Hydrate	K_{sp} [mol^2 l^{-2}×10^{-9}]
COM	2.0
COD	3.7
COT	5.3

Table 4.1 Solubility products of calcium oxalate hydrates at 25°C (Garside *et al.*, 1982)

and at 37°C Nancollas and Gardner (1974) report:

Hydrate	K_{sp} [$mol^2\ l^{-2} \times 10^{-9}$]
COM	2.51
COT	8.20

Table 4.2 Solubility products of calcium oxalate hydrates at 37°C (Nancollas and Gardner, 1974)

Physical properties of calcium oxalate (Mullin, 1993)

Density of COM: $\rho_{COM} = 2200\ kg/m^3$

Molecular weight of calcium oxalate $MW_{CaOx} = 146.1\ g/mol$

Molecular weight of calcium chloride: $MW_{CaCl2} = 111.0\ g/mol$

Molecular weight of sodium oxalate: $MW_{Na2Ox} = 134.0\ g/mol$

4.2.2 CALCIUM CARBONATE $CaCO_3$

About 7% of the earth's crust is limestone or marble, which are naturally precipitated calcium carbonate (Tai and Chen, 1998). In the chemical industry, calcium carbonate is produced in large quantities for fillers for plastics, paper and rubber.

Calcium carbonate can be precipitated from reacting supersaturated solutions of calcium chloride $CaCl_2$ and sodium carbonate Na_2CO_3. According to the process conditions (temperature, pH, supersaturation), different polymorphs are formed.

Calcium carbonate polymorphs

Calcium carbonate can exist in three different polymorphs:

- rhombohedron calcite
- rosette aragonite
- spherical or hexagonal-plate vaterite.

Additionally, amorphous calcium carbonate can be formed.

As pointed out by Ohtaki (1998), calcite is the stable polymorph at room temperature. The author reports the following solubility products:

Polymorph	K_{sp} [$mol^2\ l^{-2} \times 10^{-9}$]
Calcite	3.31
Aragonite	4.57
Vaterite	12.30

Table 4.3 Solubility products of calcium carbonate polymorphs at 25°C (Ohtaki, 1998)

Physical properties of calcium carbonate (Mullin, 1993)

Density of calcium carbonate $\rho_{CaCO3} = 2710\ kg/m^3$

Molecular weight of calcium carbonate $MW_{CaCO3} = 100.1\ g/mol$

Molecular weight of calcium chloride: $MW_{CaCl2} = 111.0\ g/mol$

Molecular weight of sodium carbonate: $MW_{Na2CO3} = 106.0\ g/mol$

4.3 KINETIC STUDIES IN THE LITERATURE

Nancollas and Gardner (1974) observed that crystal growth of COM is surface-reaction controlled, independent of the temperature. Supersaturation is related to crystal growth using a second order power law. In the experimental studies of Gardner and Nancollas (1975) the growth kinetics of calcium oxalate trihydrate showed a second order dependence on the supersaturation. Neither temperature nor stirrer speed was found to have an influence on the kinetics.

Tomazic and Nancollas (1979) studied the dissolution kinetics of different hydrates at various temperatures and found that the process is diffusion-controlled. Gardner and Nancollas (1975) came to the same conclusion for monohydrate. Garside *et al.* (1982) investigated the effect of temperature on the precipitation kinetics and the hydrate distribution in an MSMPR precipitation reactor. The importance of temperature for the distribution of hydrates has already been mentioned briefly above, but the authors also suggest that solution-mediated processes and therefore kinetic rather than thermodynamic factors govern the formation of different hydrates.

Nielsen and Toft (1984) compared the growth kinetics of various sparingly soluble salts. The influence of ion concentrations on crystal growth is shown in isotach

diagrams, where lines connect points of equal growth rates. For calcium oxalate monohydrate, as for most of the substances investigated, growth kinetics are calculated using a parabolic rate law.

Brecevic *et al.* (1986) investigated growth and dissolution kinetics of calcium oxalate hydrates and suggest that the transformation process of the unstable phases to the monohydrate is solution-mediated. Brecevic and Kralj (1989) carried out batch precipitation experiments and found a strong dependence of the crystal size distribution and hydrate distribution on the mode of mixing and feed concentration. Hartel *et al.* (1986) studied the precipitation kinetics of calcium oxalate in a mininucleator and a Couette flow aggregator under MSMPR conditions, and modelled the results using a population balance model. With this arrangement, it was possible to separate the effects of nucleation and growth from those of aggregation and disruption. The authors varied the initial oxalate concentration and the rotational speed in the Couette flow aggregator, and found an increase in aggregation rate with increasing supersaturation and an increase in disruption with higher rotational speeds.

Brown *et al.* (1991) used turbidity measurements and microscopic studies to investigate homogeneous and heterogeneous nucleation of calcium oxalate monohydrate. As one would expect, only the latter occurred at low initial levels of supersaturation. In addition, initial supersaturation and measured lag-times were correlated. Kavanagh (1992) analysed experimental procedures from a medical point of view and suggested studying the kinetics of human kidney stone formation in an MSMPR reactor because of the constant level of supersaturation in steady-state operation. Bramley *et al.* (1996a and b) included agglomeration in their kinetic considerations and observed a strong dependence of the kinetic parameters on the oxalate concentration and stirrer speed in their batch experiments.

4.4 PARAMETER ESTIMATION

The aim of the parameter estimation is to deduce the growth rate G, nucleation rate B^0, disruption kernel β_{disr} and agglomeration kernel β_{aggl} from the experimental particle size distribution.

However, it is notoriously difficult to solve this so-called inverse problem. Muralidar and Ramkrishna (1986) describe a procedure for obtaining agglomeration frequencies from measured size distributions without the kinetic processes of nucleation, growth and disruption. The authors point out that even if the experimental data are very accurate, it is not always possible to estimate the aggregation frequency satisfactorily and to distinguish between different mechanisms.

It is even more difficult to estimate not just one but four parameters simultaneously from a particle size distribution. The errors are likely to be unacceptably high and it might be impossible to distinguish between the mechanisms involved. A new technique has thus been developed to sequentially obtain the kinetic parameters nucleation rate, growth rate, agglomeration kernel and disruption kernel from experimental results.

Theoretical considerations and alternative approach

Equation of moments

The equation of moments (Randolph and Larson, 1988) for a well-mixed crystallizer

$$\frac{dm_j}{dt} + m_j \frac{d(\log V)}{dt} = jGm_{j-1} + 0^j B^0 - \sum_k \frac{Q_k m_{j,k}}{V} + \overline{B} - \overline{D} \quad (4.1)$$

with $j = 0, 1, 2, 3, \ldots$ can be manipulated in such a way that the growth and nucleation kinetics can be determined without estimation or approximation.

Growth and nucleation

Assuming steady state, size-independent growth and conservation of the third moment (mass) in the agglomeration and disruption process, *i.e.*

$$\frac{dm_j}{dt} + m_j \frac{d(\log V)}{dt} = 0 \quad (4.2)$$

and $\overline{B}_3 = \overline{D}_3 = 0$,

the following equation for $j = 3$ is obtained:

$$0 = 3Gm_2 - \frac{m_3}{\tau} \quad (4.3).$$

Therefore, when the moments of the distribution are known, it is possible to calculate the growth rate G

$$G = \frac{m_3}{3m_2\tau} \tag{4.4}$$

Furthermore, from the relationship

$$n_0 = \frac{B^0}{G} \tag{4.5}$$

the nucleation rate B^0 can be calculated as

$$B^0 = n_0 G \tag{4.6}$$

with n_0 obtained from the intercept of the experimental distribution with the abscissa at $L = 0$.

Test data

Kinetic data used:

$G = 50\ \mu m$

$B^0 = 2\times10^{12}\ 1/m^3h$

$\beta_{aggl} = 10^{-10}\ m^3/h$

$\beta_{disr} = 20\ 1/h$.

Using these data, the number density distribution and the moments were calculated. From the moments, the kinetic data for growth and nucleation were estimated as $G = 49.6\ \mu m$ and $B^0 = 1.97\times10^{12}\ 1/m^3h$. These data correspond very well to the original rates. The errors for the nucleation rate and the growth rate due to the discretization procedure are 1.5% and 0.8% respectively. This method can therefore be considered suitable for calculating growth and nucleation rates directly from the moments of the distribution.

Disruption kernel

The evaluation of the disruption kernel was carried out in "disruption experiments", where an initial particle size distribution was stirred for a certain time and the change in the distribution then analysed. The solution was saturated so that negligible growth, agglomeration and nucleation occurred and therefore all changes in

the particle size distribution could be attributed to attrition and breakage. By fitting the population balance model for disruption to the experimental disruption data, the disruption kernel was estimated. The experiments were carried out at different stirrer speeds, and the dependence of the disruption kernel on the specific power input could thus be analysed.

Agglomeration kernel

As the last kinetic parameter to be determined, the agglomeration kernel was calculated using all the kinetic data already known. The number density distribution of the population balance model was fitted to the number density distributions of the continuous experiments and the sum of least squares of the population balance model and the experimental data minimised iteratively.

4.5 EXPERIMENTAL CONDITIONS

In order to investigate the precipitation kinetics and the parameters influencing the kinetic processes, experiments were carried out under the following conditions.

Calcium oxalate:

3 feed concentrations

0.01M	initial supersaturation $S_{init,\overline{CP}} = 99.8$
0.04M	$S_{init,\overline{CP}} = 399.2$
0.10M	$S_{init,\overline{CP}} = 998.0$

3 residence times

2 min

7.5 min

11 min

5 stirrer speeds

250 rpm

500 rpm

1000 rpm

1500 rpm

2000 rpm

2 feed point positions

inside draft tube: *id*

outside draft tube: *od*

Temperature: 37°C = 310.15 K

Calcium carbonate:

Feed concentration

0.10M $S_{init,\overline{AP}} = 998.0$

2 residence times

5 min

10 min

4 stirrer speeds

250 rpm

500 rpm

1000 rpm

2000 rpm

feed point position

inside draft tube: *id*

Temperature: 25°C = 298.15 K

4.6 EXPERIMENTAL SET-UP

The experiments for the determination of the precipitation kinetics were carried out using the set-up shown in Figure 4.1.

Reactor

The glass reactor (1) (300 ml, D = 65 mm) is equipped with a polyethylene draft tube and four baffles (Figure 4.2) which lead to a flow pattern which is geometrically similar to that of the larger scale draft tube baffled (DTB) reactors. The contents are stirred using a three-blade marine-type propeller (5) which pumps the suspension upwards in the annulus and downwards inside the draft tube.

The product withdrawal pipe is located in the annulus half-way up the draft tube where the vector of the circulation velocity of the suspension and that of the withdrawal velocity of the product point in the same direction. This arrangement ensures low classification effects. Moreover, the feed tubes and withdrawal tube can be exactly positioned in the reactor and scaled up with high accuracy which would appear to be of fundamental importance for the supersaturation profile of the reaction plumes and subsequently for nucleation and growth.

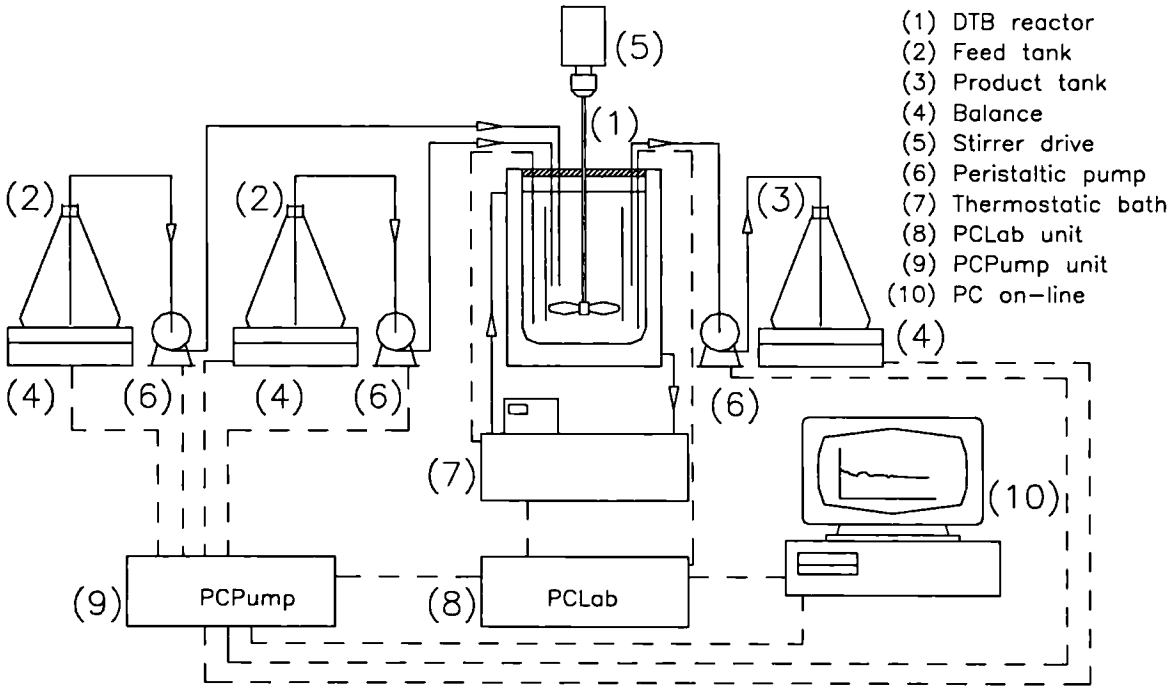

Figure 4.1 Experimental set-up: Continuous laboratory-scale precipitation reactor

PCPump unit

The feeding and withdrawal of solution and product from the feed tanks (2) and withdrawal tank (3), respectively, is established by peristaltic pumps (6) controlled by a Spectrum PCPump unit (9). Balances (4) connected to the PCPump system are used to determine the speed of the pumps and therefore the desired feed and withdrawal rates. This technique ensures high accuracy and a constant residence time.

PCLab unit

A Spectrum PCLab unit (8) controls the temperature in the reactor and measures process variables on-line. The reactor jacket is thermostated by either cooling or heating water, according to the desired reactor temperature, using a Haake thermostatic bath (7). The PCLab unit also enables the user to measure and record the pH, ion concentrations and other user-defined quantities in the reactor. A temperature-compensated pH electrode (BDH Gelplas) is used for measuring the pH. The calcium ion concentration is measured using a calcium ion selective electrode (EDT Instruments, QSE 310) and a Calomel reference electrode (BDH Glass+). Temperature, pH and calcium concentration over time are displayed on-line on a computer screen, data files are stored automatically and any interruptions during operation are recorded.

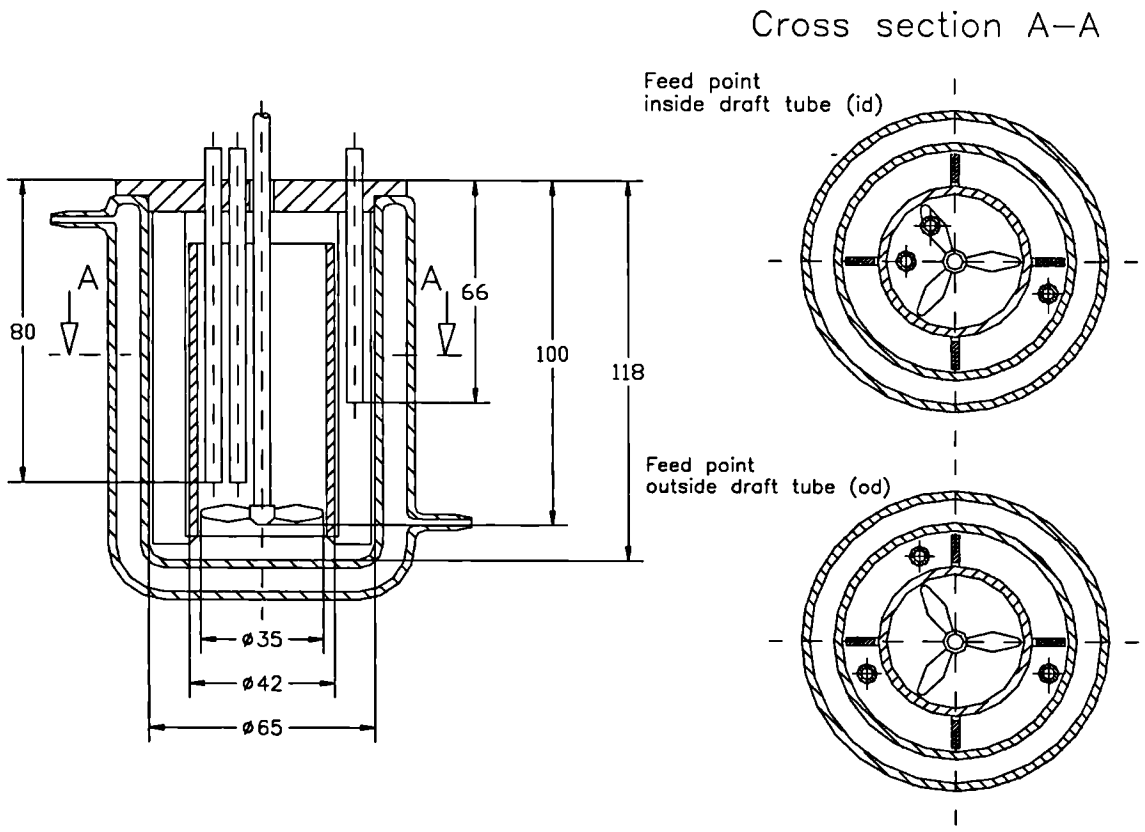

Figure 4.2 300 ml draft tube baffled (DTB) reactor

Tubing

According to the desired flow rate, silicon tubes with a bore in the range from 0.5 to 8 mm can be used to feed or withdraw solutions. If the flow rate cannot be achieved with a single pump head, up to four pump heads can be connected in parallel to the PCPump unit.

Coulter Counter

The particle size distribution is determined with a Coulter Counter Multisizer II. The Coulter Counter determines the number and size of particles suspended in a conductive liquid by monitoring the electric current between two electrodes immersed in the conductive liquid on either side of a small aperture, through which the suspension of particles is forced to flow. When a particle passes through the aperture, the impedance between the electrodes changes and produces an electric pulse with a magnitude proportional to the particle volume.

The aperture tube chosen for the measurements (100 μm) enables the user to measure particles in the range from 1.9 to 60 μm in size. In order to avoid secondary changes of the precipitate during the particle sizing, a suitable electrolyte has to be found which, on the one hand, fulfils the conductivity criteria necessary to detect particles as they pass through the orifice, and on the other does not dissolve particles. A saturated solution of calcium oxalate with 3% by weight sodium chloride proved to be suitable. The electrolyte is filtered twice through 0.1 μm Whatman cellulose nitrate membrane filters in order to achieve low background counts of particles already present in the electrolyte. A dispersant specially designed for Coulter Counter measurements is added to avoid aggregation of the particles during the measurement. The calibration of the aperture tube is carried out using a 9.7 μm latex calibration standard and repeated monthly.

In order to minimise statistical errors, the measurements are carried out for at least 20,000 particles counted by the analyser. The concentration of the sample is chosen in such a way that the saturation index of the Coulter Counter is below 10%, ensuring that the particles pass through the orifice one by one.

4.7 EXPERIMENTAL PROCEDURE

Calibration of the ion-selective electrode and peristaltic pumps

The pH electrode is calibrated with buffer solutions of pH 7 and pH 9.2. The calcium selective electrode (EDT Instruments, QSE 310) is calibrated with standard solutions of calcium chloride in the concentration range from 5×10^{-5}M to 10^{-1}M. Figure 4.3 shows the calibration chart. The minimum and maximum flow rate calibration of the peristaltic pumps is carried out using a calibration program provided by the PCPump supplier Spectrum.

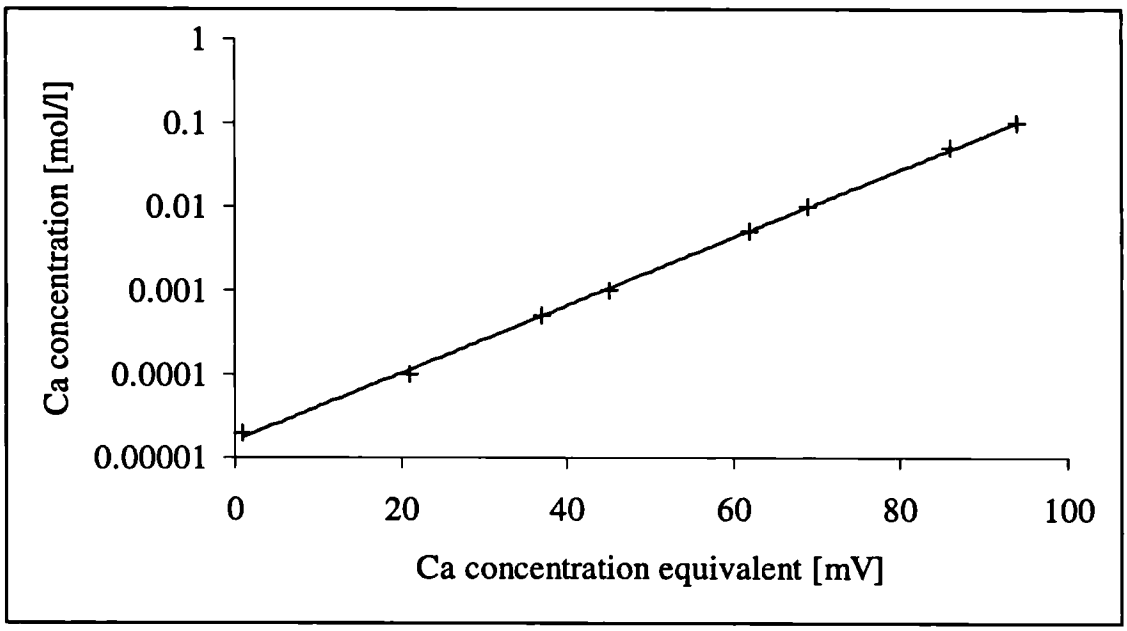

Figure 4.3 Calibration curve for calcium-ion selective electrode

Running of experiments

For the preparation of the feed stock solutions, analar grade reagents (Fisher Scientific International Company) and deionised water with a conductivity of less than 0.5 µS/cm are used. To ensure that aliquot amounts of feed solutions are added and to avoid instabilities in the flow rates, it is necessary to fill all the tubes with solution before the experiment is started.

The stirrer is switched on and adjusted to a speed between 250 and 2000 rpm. The main process parameters such as temperature, feed rates and the duration of an experiment can be chosen in a set-up menu before the experiment is started. The pumps of the PCPump unit will not start to pump solution into the reactor until the desired reactor temperature has been reached. The vessel and jacket temperature, the pH and the calcium ion concentration can be monitored on-line. A typical plot of the calcium ion concentration over time is given in Figure 4.4.

In order to ensure that steady state was reached when taking samples to determine the crystal size distribution (CSD), the calcium ion concentration in the liquid phase, and therefore the supersaturation in the reactor, was monitored continuously.

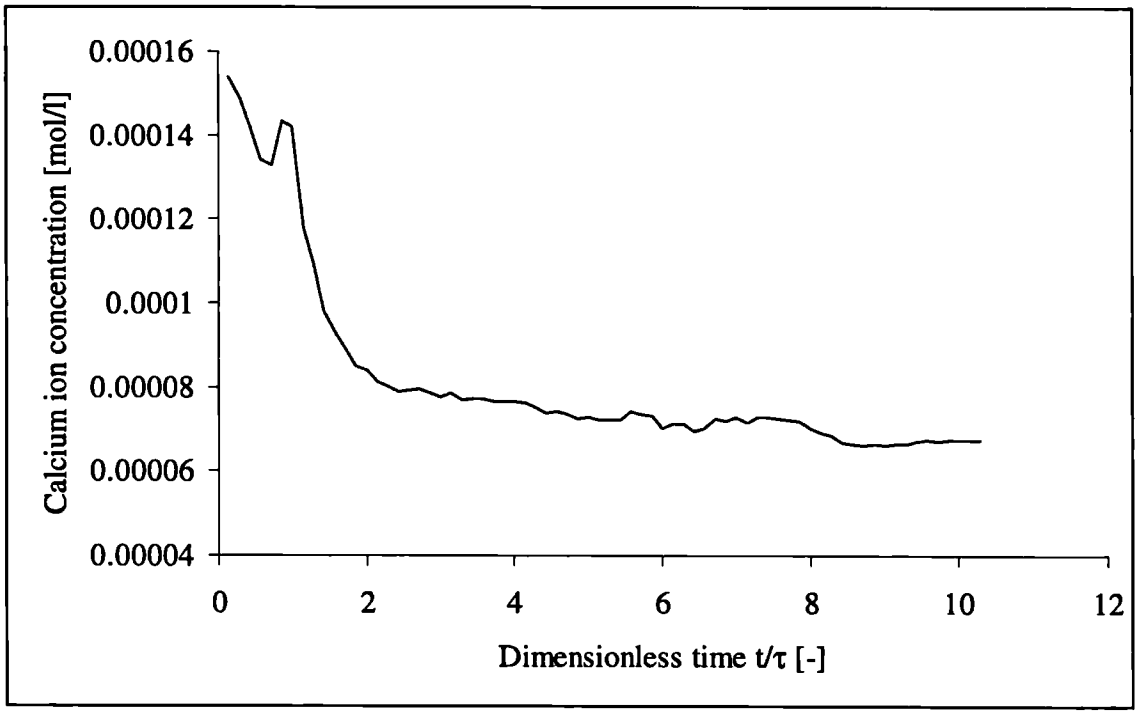

Figure 4.4 Calcium ion concentration vs. dimensionless time

It was observed that steady-state conditions occurred after seven to twelve residence times, depending on the residence time and feed concentration. In general, steady state was reached earlier at high concentrations and long residence times. This can probably be explained by the fact that in these cases slight fluctuations in the feed

rate and suspension density have a lower impact on the overall performance of the reactor.

Sampling and analysing the crystal size distribution

After about ten residence times, a probe of 2 to 10 ml - according to the solid concentration - is taken and analysed in the Coulter Counter. The measurements with the particle size analyser were performed at least twice and generally showed very good reproducibility. In some measurements, blockage of the aperture tube occurred and subsequently led to inaccurate results in the small size range. These measurements were discarded and the particle size distribution determined again without blockage. The results were obtained in text files with the number of particles in the channels and the upper diameter of each channel. The files were converted into EXCEL files and the number density distribution calculated.

Furthermore, after achieving steady state, samples for observation under the light microscope and the scanning electron microscope (SEM) were taken from the reactor contents.

To investigate particles smaller than 1.9 μm in size, measurements were carried out with a Malvern Zeta Sizer, which measures the diffusion speed of particles moving under Brownian motion. The results of the measurements showed no reproducibility, however. One reason for this could be that the larger particles influence the random motion of the smaller particles, as the upper size limit up to which this technique can be applied is determined by the onset of sedimentation and can be estimated to be 5 μm. These results are not therefore taken into account in the subsequent analysis of crystal size distribution (CSD) data.

4.8 REPRODUCIBILITY

The reproducibility of the experiments was generally very high, as is shown by the plots of the crystal size distributions (CSDs) of different runs in Figure 4.5. The runs were performed on different days and with different feed stock solutions under identical

conditions. The reproducibility of the CSD is very high which is especially important in terms of parameter estimation where the kinetic parameters are extracted from CSD data.

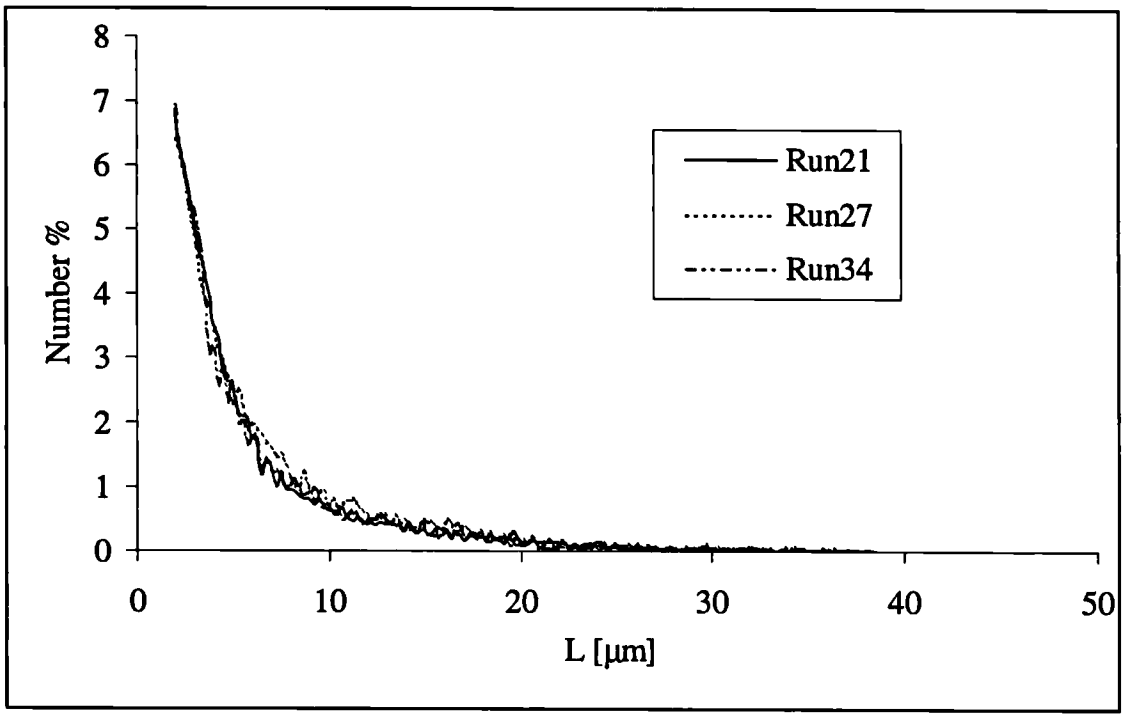

Figure 4.5 Reproducibility of laboratory experiments

4.9 RESULTS

4.9.1 MORPHOLOGY

The morphology of the crystals precipitated was investigated using both light and scanning electron microscopes, and the formation of different hydrates and polymorphs was monitored. The magnification obtained with the light microscope Olympus IX50 was within a range from 100 to 400. Particles were sampled during and after the experiments and analysed visually; in addition, pictures were recorded with a video camera module (CCD) attached to the microscope and transferred to a PC. Furthermore, investigations were carried out using the scanning electron microscope

(SEM) JOEL JSM-820. The SEM is capable of magnifications of up to 20,000 for particles in the size range obtained by precipitation, with a far better depth of field than the light microscope.

Calcium oxalate

Figure 4.6 shows a picture of calcium oxalate, taken with the video camera under a magnification of 200 for 0.01M feed solutions, 7.5 min residence time, 2000 rpm stirrer speed and the feed point inside the draft tube. From this picture, it can be clearly seen that single particles and aggregated (loosely bond) or agglomerated (cemented) particles are obtained. However, the depth of field and magnification of the picture are not sufficient to determine whether the larger particles are formed due to loose bonds, cementation or intergrowth.

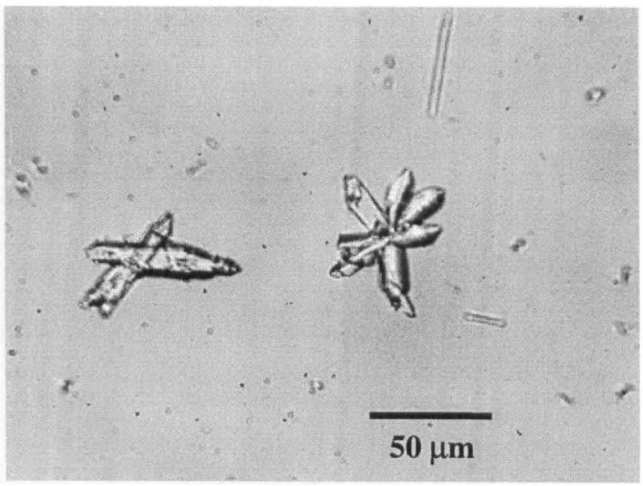

Figure 4.6 Light microscope picture of calcium oxalate precipitate

Figure 4.7 shows a 1800-fold magnification of precipitated calcium oxalate obtained under 0.01M feed solutions, 11 min residence time, 1000 rpm stirrer speed and the feed point outside the draft tube. The picture which was taken under the SEM gives a three-dimensional impression of the particles and suggests that particles not only

aggregate but also grow into each other. Further magnification of 10,000 in Figure 4.8 shows a site at which two particles have actually grown into each other.

Figure 4.9 depicts an agglomerate at 4500-fold magnification (0.01M feed solutions, 7.5 min residence time, 1500 rpm stirrer speed and the feed point inside the draft tube). Particles have grown into each other and therefore form stable agglomerates. On the right-hand side of the picture, signs of particle disruption are visible.

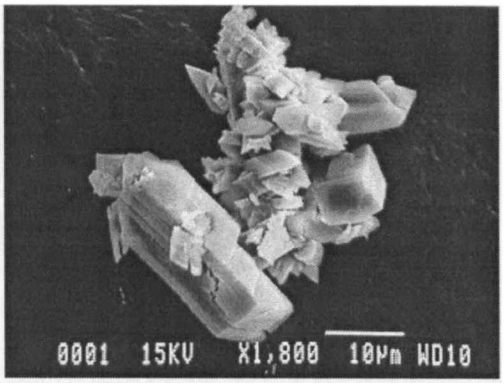

Figure 4.7 Agglomerate of calcium oxalate (SEM)

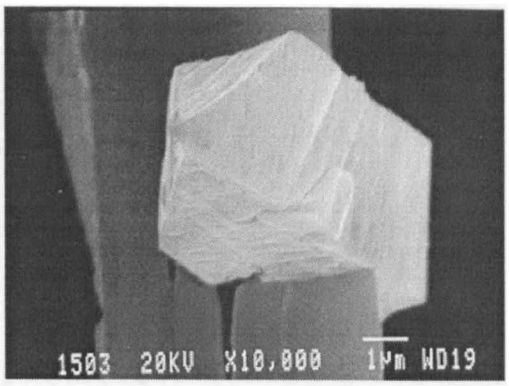

Figure 4.8 Intergrowth of particles (SEM)

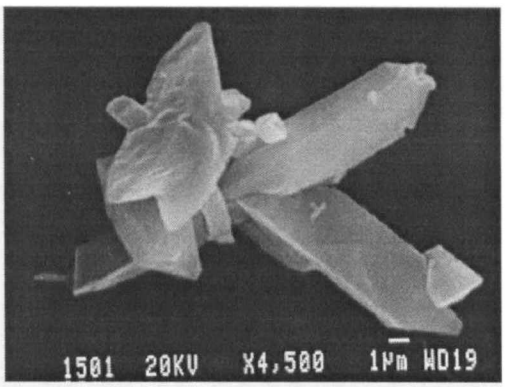

Figure 4.9 Agglomeration and disruption effects (SEM)

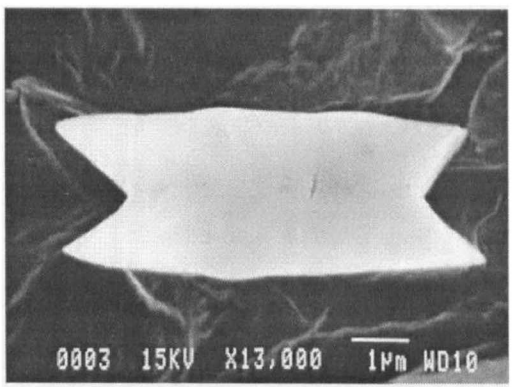

Figure 4.10 Twinned particle (SEM)

A twinned crystal, typical of calcium oxalate monohydrate (COM), under 13,000-fold magnification is shown in Figure 4.10. The uneven surface of the particle could be caused by disintegration of the particle due to the high temperature and vacuum during the sample preparation for the Scanning Electron Microscopy. The conditions referred to above may lead to dehydration of the hydrated particles.

From the visual observations, the hydrate formed is very likely to be calcium oxalate monohydrate, which crystallises in monoclinic form and is the stable hydrate at the temperature at which the experiments were run (37°C). No mixture of different hydrates has been observed, either during or after the experiments.

Calcium carbonate

As mentioned above, calcium carbonate exists in three different polymorphs: calcite, vaterite and aragonite. At 25°C, calcite is the most stable form as it exhibits the lowest solubility product at this temperature (Table 4.3).

From the continuous precipitation experiments, however, it was found that predominantly spherical vaterite was formed, with a very low percentage of calcite (< 1%). One explanation for the formation of this metastable polymorph could be that it is not always the most thermodynamically stable polymorph which is obtained, but rather one that is kinetically favoured (Ostwald's rule of stages).

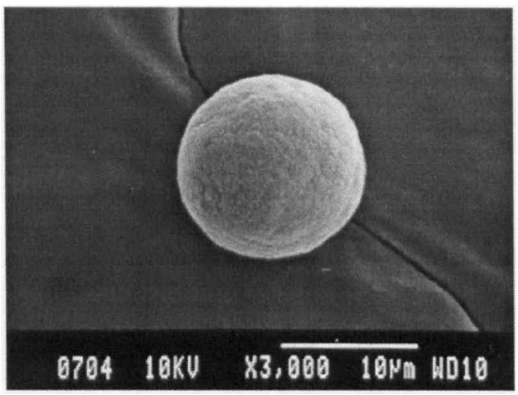

Figure 4.11 Single particle of calcium carbonate (SEM)

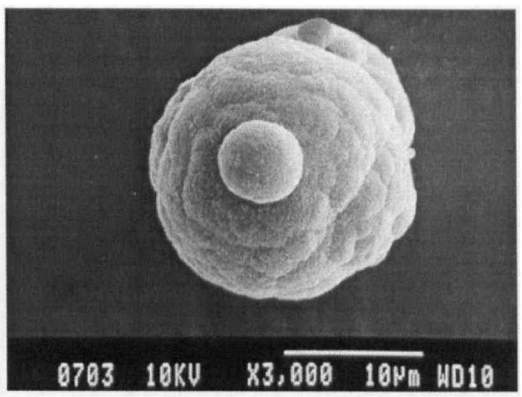

Figure 4.12 Agglomeration of particles (SEM)

Figure 4.11 shows a single vaterite particle (magnification 3000) as it was obtained from continuous precipitation. The SEM sample was prepared immediately after the experiment. The agglomerate in Figure 4.12 consists of primary vaterite particles of very different sizes and underlines the need for an agglomeration model which accounts for agglomeration events between particles of different size classes.

As already seen for calcium oxalate (Figures 4.7 to 4.9), agglomeration plays an important role during the formation of particles. For calcium carbonate, both loose (Figure 4.13) and compact (Figure 4.14) agglomerates consisting of two to about 100 primary particles were obtained. The loose form of agglomerates was predominant in experiments with low energy input, *i.e.* low stirrer speeds (250 rpm). At higher stirrer speeds (>1000 rpm), mainly compact agglomerates were formed. This is possibly because at higher stirrer speeds, higher levels of shear rates in the reactor lead to the breakage of very "exposed" parts of the agglomerate, and only the main body of the agglomerate survives. At low power input, primary particles have sufficient time to stick to each other and form strong bonds by growth. Moreover, it is less likely that parts of the agglomerates will be chipped off by the stirrer or by gradients in the shear field as the energy input is far lower.

At 25°C, the most stable polymorph of calcium carbonate is calcite. In the experiments, however, it was mainly metastable vaterite that formed. Subsequently, the

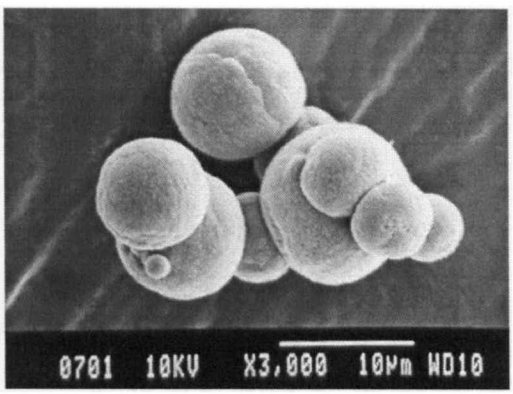

Figure 4.13 Loose agglomerate of calcium carbonate (SEM)

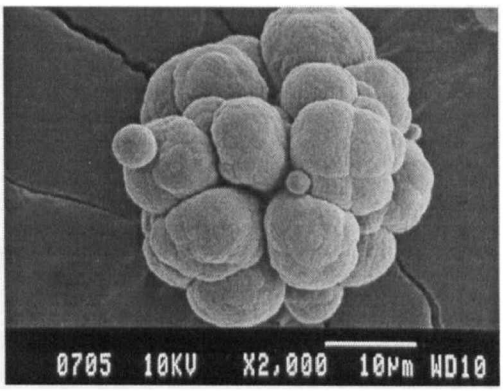

Figure 4.14 Compact agglomerate of calcium carbonate (SEM)

metastable vaterite transformed into calcite when it was left in its saturated solution.

Figure 4.15 shows the onset of this transformation into calcite. Spherical vaterite crystals "dissolve" and rearrange their lattice to form cubic calcite crystals (Spanos and Koutsoukos, 1998). After about 24 hours, a mixture of calcite and vaterite was observed (Figure 4.16). It is believed that if the solution had been stirred continuously throughout this period, the solution-mediated transformation would have taken place to an even greater extent.

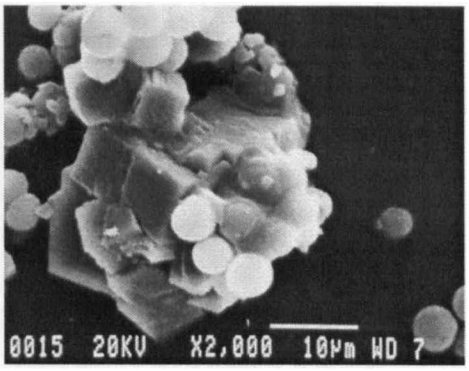

Figure 4.15 Transformation of vaterite into calcite

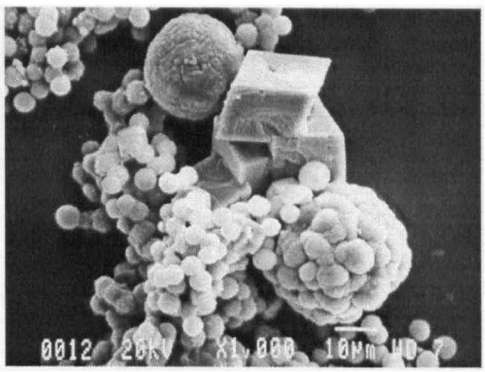

Figure 4.16 Vaterite and calcite after 24 hours

4.9.2 MEAN SIZE AND COEFFICIENT OF VARIATION

In crystallization and precipitation, the sum parameters mean size and coefficient of variation are often used to characterise the crystal size distribution. In general, the mean size is defined as

$$L_{ij} = \left(\frac{\int L^i n dL}{\int L^j n dL} \right)^{\frac{1}{i-j}} = \left(\frac{m_i}{m_j} \right)^{\frac{1}{i-j}} \qquad (4.7)$$

and the coefficient of variation (Allen, 1981) as

$$c.v._{ij} = \frac{\sigma_j}{L_{i,j}} = \left(\frac{L_{ij+1}}{L_{ij}} - 1 \right)^{\frac{1}{2}} \qquad (4.8).$$

The volume mean diameter L_{43} and the number mean coefficient of variation $c.v._{10}$ will be investigated further below.

For calcium oxalate, the results for the volume mean diameter L_{43} show a linear dependence of the mean diameter on the residence time, and therefore the same tendency as that predicted by population balance modelling with MSMPR assumptions (Figure 4.17). As it is the volume mean diameter which is measured with the particle sizing equipment (Coulter Counter), this mean diameter can be assumed to be the most accurate.

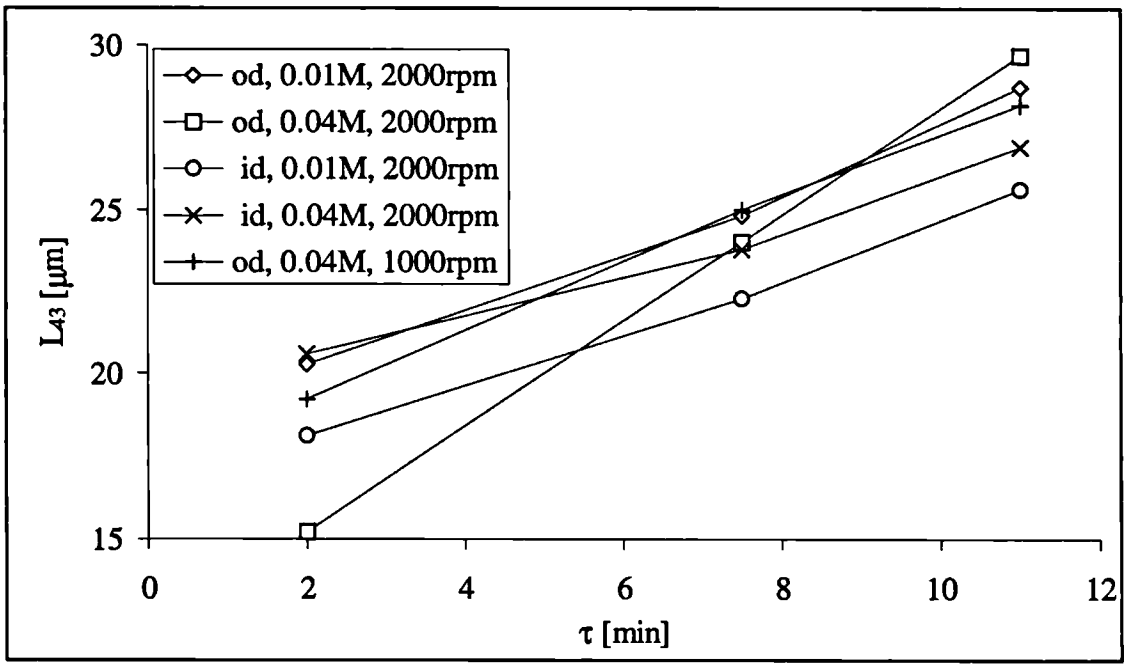

Figure 4.17 Volume mean diameter vs. residence time for calcium oxalate

The curves of the volume mean size versus the specific power input show a maximum at power inputs between 0.15 and 0.7 W/kg (Figure 4.18). Franke and Mersmann (1995) explain this phenomenon by a change from a mesomixing-controlled to a micromixing-controlled system. For low power inputs, mesomixing is limiting. Because of the advantageous geometry of the DTB reactor, however, mesomixing is increased considerably by even a small increase in power input, and high supersaturation levels and therefore excessive nucleation are avoided. Consequently, the

particle size increases. A further increase of the power input causes micromixing limitation of the now homogeneous macrofluid and therefore a decrease in particle size.

Åslund and Rasmuson (1992) observed the same behaviour in their precipitation experiments on benzoic acid. Leeuwen *et al.* (1996a), too, found a maximum of the average crystal size with a mixing parameter for a rectangular flat reactor. The same authors (Leeuwen *et al.*, 1996b) found a similar mixing dependence for barium sulphate. Pohorecki and Baldyga (1988) attempted to model the effect of mixing for their data, which were also obtained for barium sulphate and showed an increase of crystal size with stirrer speed at small stirrer speeds.

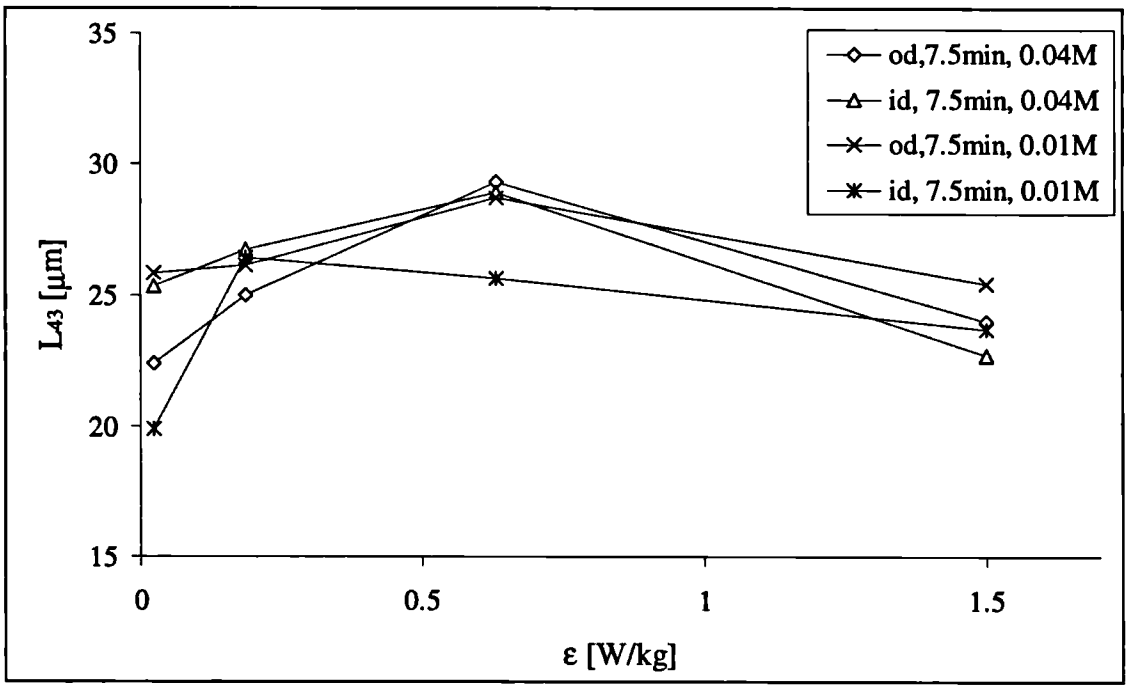

Figure 4.18 Volume mean diameter vs. specific power input for calcium oxalate

It was also found that the mean size depends on the location of the feed point in the reactor. To find out more about this effect, however, knowledge of the individual kinetic parameters is crucial and therefore further investigations will be carried out.

As far as the coefficient of variation is concerned, an increase of the variance with residence time was observed (Figure 4.19). This is reasonable, as with longer residence times the occurrence of large particles is more likely to be due to growth and agglomeration, and a widening of the distribution takes place.

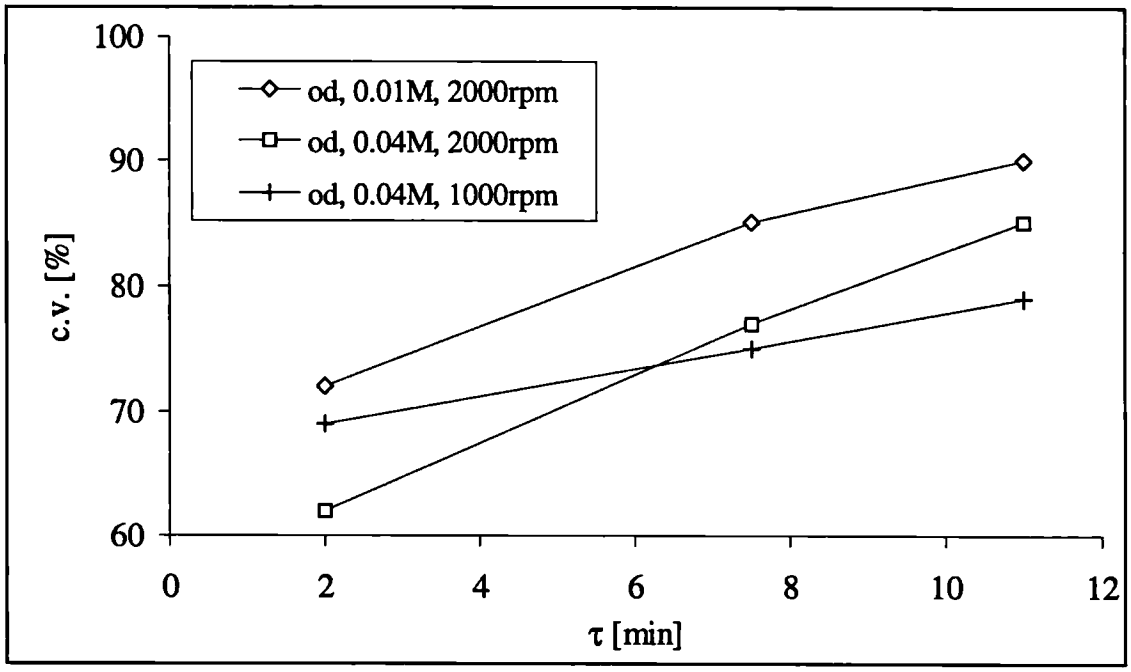

Figure 4.19 Coefficient of variation vs. residence time for calcium oxalate

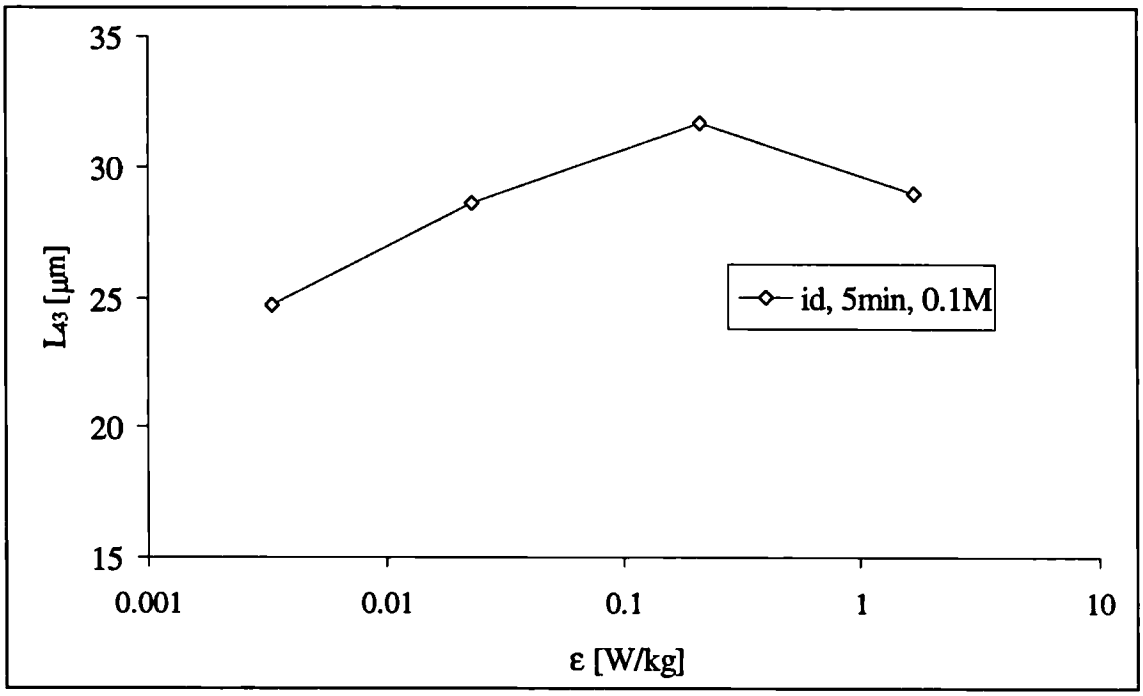

Figure 4.20 Volume mean diameter vs. specific power input for calcium carbonate

A similar dependence of the volume mean size L_{43} on the energy dissipation was observed for calcium carbonate (Figure 4.20). The particle size increases to a maximum and then decreases with increasing power input. The different shape of the curves in Figure 4.18 (calcium oxalate) and Figure 4.20 (calcium carbonate) is due to the different scales used for plotting the specific energy input. For calcium oxalate, a linear scale was plotted and for calcium carbonate a logarithmic scale.

4.9.3 PRECIPITATION KINETICS OF CALCIUM OXALATE

Particle size distribution

Using the Coulter Counter data and the mass of crystals precipitated, it is possible to calculate the number-density distribution and the moments of the distribution.

Mass balance

The mass of calcium oxalate precipitated m_{prec} can be determined from the following mass balance

$$m_{prec} = m_{feed} - m_{liquid} \tag{4.9}$$

as the difference between the mass of CaC_2O_4 in the feed m_{feed} and the mass of calcium oxalate in the liquid phase m_{liquid}. This equation can also be written in terms of concentrations, *e.g.* for calcium

$$c_{Ca,prec} = c_{Ca,feed} - c_{Ca,liquid} \tag{4.10}.$$

The feed concentration is known and the concentration of calcium can be calculated from the measurements with the ion-selective electrode. The concentration of calcium precipitated, and subsequently the mass of calcium oxalate precipitated, can therefore be determined.

Measurements with the calcium ion-selective electrode and determination of the activity coefficients

The activity of the calcium ions in solution is obtained from the measurements carried out with the calcium ion-selective electrode. The activity a_i and the concentration of ions in solution c_i are connected by the activity coefficient γ_i

$$a_i = \gamma_i c_i \tag{4.11}.$$

Davies (1962) related the activity coefficient γ_i to the ionic strength in a modified Debye-Hückel theory according to

$$-\log\gamma_i = Az_i^2\left(\frac{I^{0.5}}{I^{0.5}+1} - 0.3I\right) \tag{4.12}$$

with the ionic strength I defined as

$$I = \frac{1}{2}\sum_i z_i^2 c_i \tag{4.13}$$

and the temperature-dependent constant A (A = 0.5230 for 37^{0}C).

When calculating the ionic strength of calcium oxalate, association processes are accounted for with the following association constants (Garside *et al.* ,1982):

$$K_1 = \frac{a_{H_2C_2O_4}}{a_{H^+}a_{HC_2O_4^-}} = 21010\frac{\text{l}}{\text{mol}}$$

$$K_2 = \frac{a_{HC_2O_4^-}}{a_{H^+}a_{C_2O_4^{2-}}} = 19.40\frac{\text{l}}{\text{mol}}$$

$$K_3 = \frac{a_{Ca_2C_2O_4}}{a_{Ca^{2+}}a_{C_2O_4^{2-}}} = 1869\frac{\text{l}}{\text{mol}}$$

Using the mass balances for calcium and oxalate ions and the equation for electroneutrality, the ionic strength and the activity coefficients can be calculated iteratively (Nancollas, 1966). A FORTRAN90 program was written to perform this task. Typical values obtained for the activity coefficients are in the range of γ_{Ca}= 0.89 to 0.96. Figure 4.21 compares the two cases of calculating the number density distribution with and without the influence of activity coefficients being considered. For small particles (< 10 μm) in particular, differences of up to 10% occur between the two curves, whereas for larger particle sizes the two curves coincide.

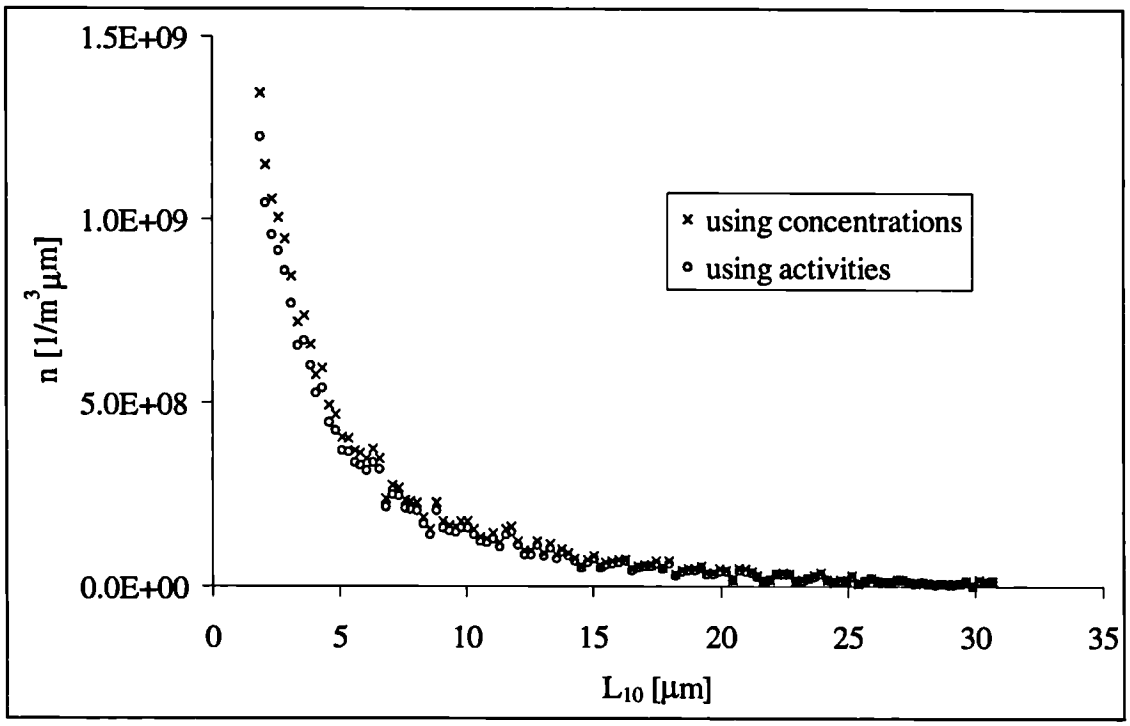

Figure 4.21 Number density distribution calculated using concentrations and activities

The activities and concentrations of all the ions involved in the association and dissociation processes can be calculated from the activity coefficients, and the concentration of ions precipitated c_{prec} can be determined. With the molar weight MW the mass of precipitated crystals is given by

$$m_{prec} = MWc_{prec} \qquad (4.14).$$

When the number-size distribution from the particle size measurement, the mean diameter of each size class and the mass of precipitate m_{prec} are known, it is possible to calculate the number-density distribution and the moments.

Supersaturation

The supersaturation σ is calculated from the activity product AP which is defined as $AP = a_A a_B$ (4.15)

and from the solubility product K_{sp}

to $$\sigma = \left(\frac{AP - K_{sp}}{K_{sp}} \right)^{1/2} \qquad (4.16).$$

Growth rate

The growth rates can be determined directly from the second and third moments as described above. The rates calculated for calcium oxalate range from 27 to 160 µm/h (7.5 to 47 nm/s). Literature values for the growth rate of calcium oxalate monohydrate vary considerably:

39 µm/h (Kavanagh, 1992)

12 to 180 µm/h (Garside *et al.*, 1982)

1 to 40 µm/h (Nielsen and Toft, 1984).

The values obtained from the experiments are therefore within the range of the literature data. It should be borne in mind, however, that direct comparison of kinetic data is not always possible since there is no other kinetic study of calcium oxalate available which includes nucleation, growth, agglomeration *and* disruption.

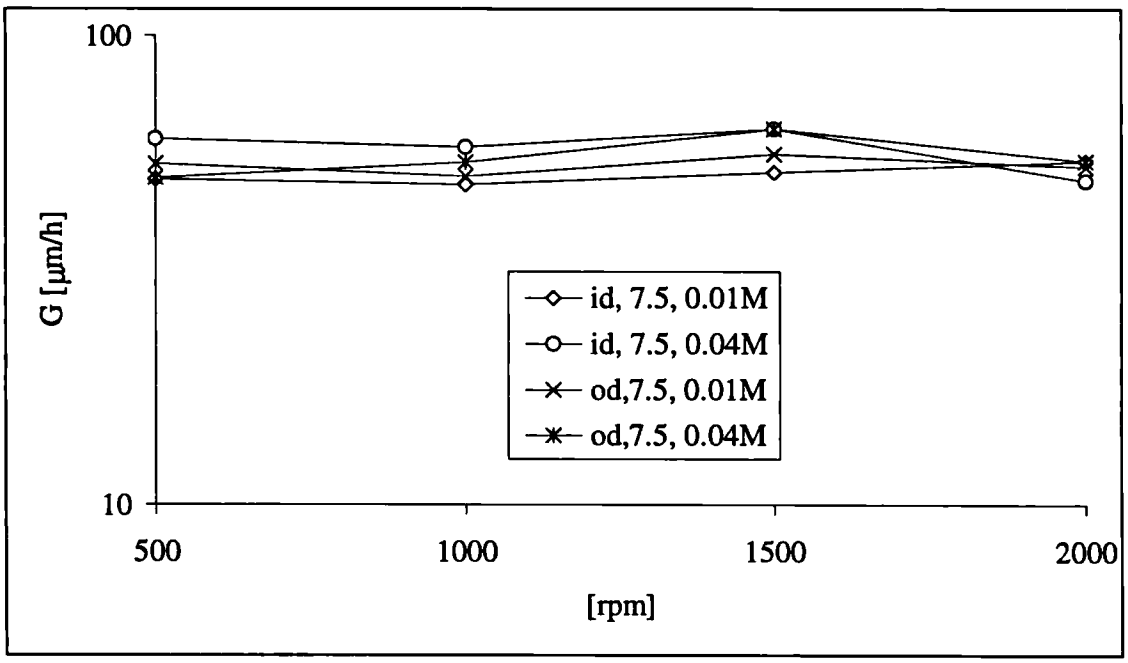

Figure 4.22 Growth rate vs. stirrer speed

Figure 4.22 shows the dependence of the growth rate on the stirrer speed, plotted for different feed point positions and concentrations. The abbreviations for the feed point positions are "id" for inside the draft tube and "od" for outside the draft tube. As the growth rate is virtually independent of the stirrer speed, this leads to the assumption that the growth process is surface-integration controlled rather than mass transfer-controlled. This result is in accordance with the observations by Nielsen and Toft (1984) who also found no transport limitation for the growth of calcium oxalate monohydrate COM.

In Figure 4.23, the growth rate is plotted versus the residence time for different concentrations and stirrer speeds. Under all conditions, an increase in the growth rate is observed as the residence time decreases, as can be expected from higher supersaturation levels. All curves show the same behaviour, regardless of stirrer speed, feed point position and feed concentration.

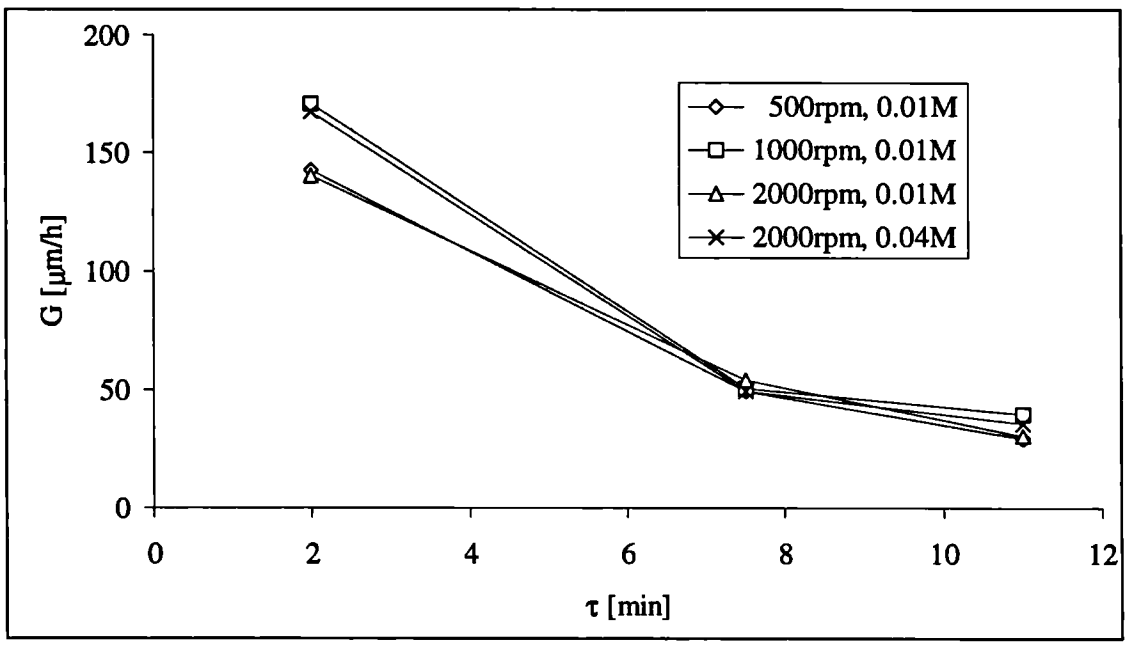

Figure 4.23 Growth rate vs. residence time

With the definition of supersaturation stated above, the growth rate is correlated with σ in Figure 4.24. The linear dependence of $\sqrt{G}$ from σ suggests a power law relationship of the form

$$G = k_g \sigma^2 \tag{4.17}$$

with k_g = 2.1164 µm/h = 5.879×10^{-10} m/s from a least square fit. A kinetic order of two was also observed by Nielsen and Toft (1984) and by Nancollas and Gardner (1974).

The correlation published by Garside *et al.* (1982) gives lower values at low supersaturations, but is close to the data shown here for higher supersaturations.

The second-order dependence of the growth rate on the supersaturation can be explained by a number of growth theories. The most convincing, however, is that of Burton, Cabrera and Frank (1951). In their BCF theory concerning the screw dislocation centred surface spiral step, it is assumed that growth units enter at kinks with a rate proportional to $c - c^*$ and that the kink density is also proportional to $c - c^*$ which gives the factor $(c - c^*)^2 = \sigma^2$ in the rate expression.

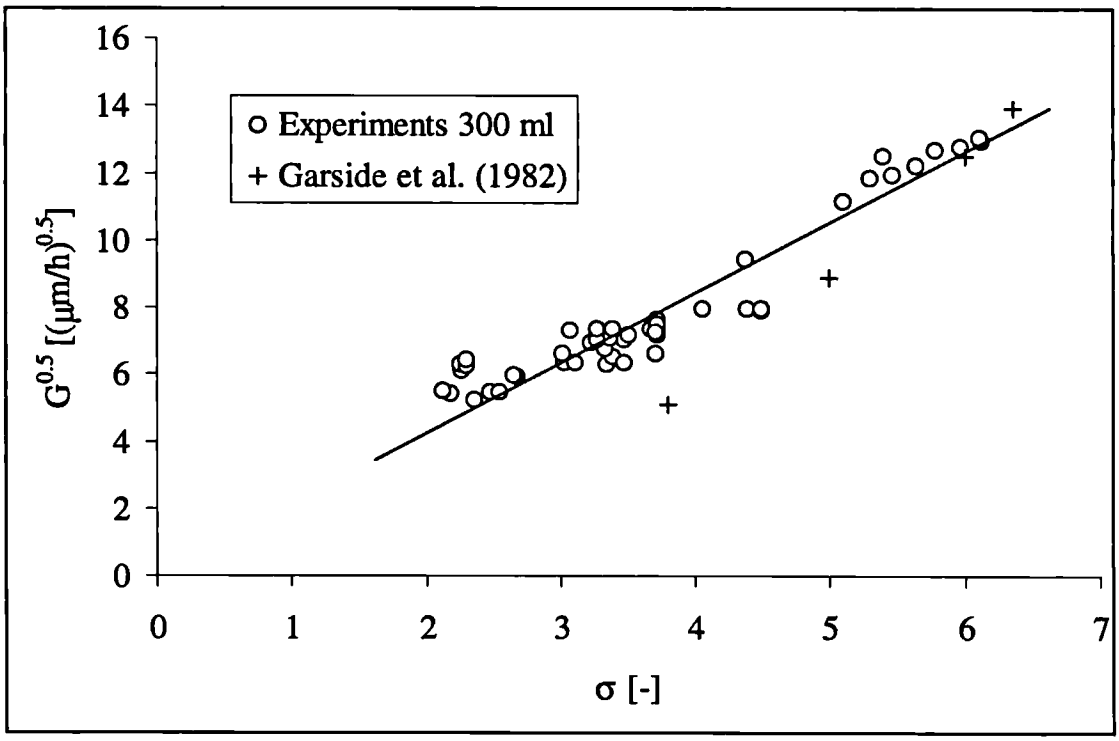

Figure 4.24 Growth rate vs. supersaturation

Nucleation rate

Nucleation rates, which are calculated from the growth rates and the population densities at L = 0.5 μm, cover a range from 10^{12} to 8×10^{14} 1/m^{3}h. Literature values for nucleation rates of calcium oxalate monohydrate are rare; Garside *et al.* (1982) found nucleation rates from 10^{11} to 3×10^{11} 1/m^{3}h for 37°C and 0.001M feed concentration; those calculated from the data of Brown *et al.* (1991) are between 10^8 and 10^{15} 1/m^{3}h for 37°C.

Figure 4.25 shows that the shorter the residence time, the higher the nucleation rate, which is in accordance with high supersaturation levels at short residence times which therefore lead to high nucleation rates. In addition to the stirrer speed and feed point position, the concentration was also varied. The runs with 0.01M feed solutions give lower nucleation rates over the whole range of residence times than those for 0.04M solutions.

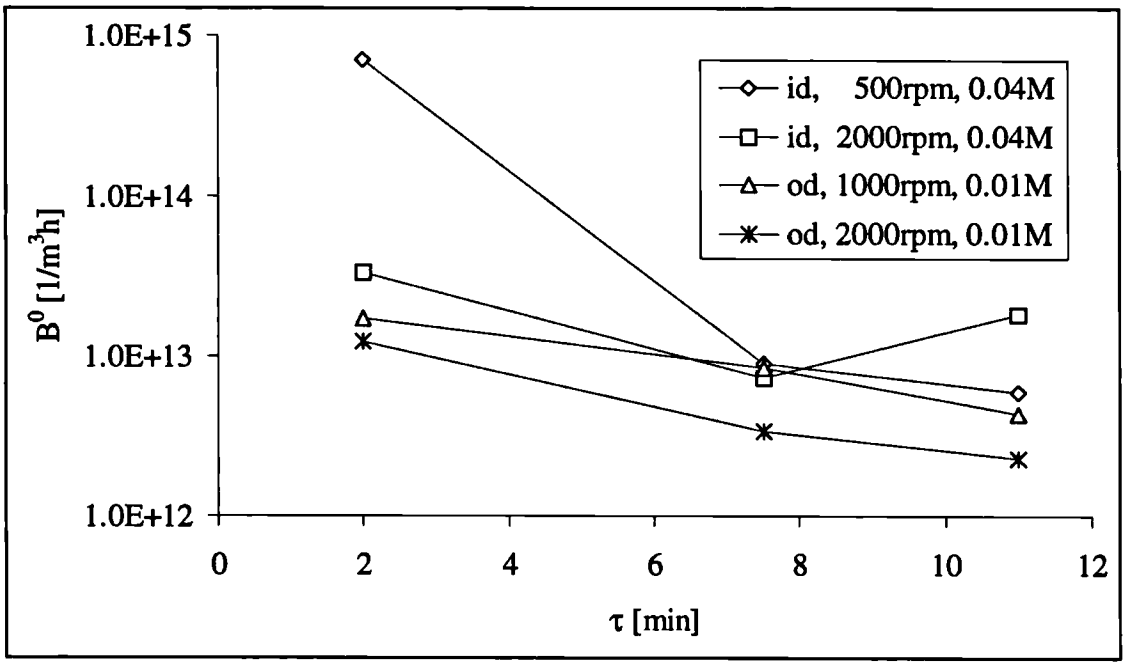

Figure 4.25 Nucleation rate vs. residence time

The dependence of the inferred nucleation rate on stirrer speed is greatly influenced by the feed point position (Figure 4.26). For the feed point inside the draft

tube and a residence time of 11 min, B^0 reaches a maximum at 1500 rpm and decreases at 2000 rpm. This effect could be caused either by the interaction of diffusion and attrition processes as described by Mullin and Raven (1961a and b), or, alternatively, by micromixing (diffusion) and mesomixing (convection) which influence the supersaturation field considerably. High stirrer speeds reduce the size of the turbulent eddies in the feed plumes and therefore lead to a more uniform supersaturation distribution. This effect is more pronounced at high speeds, as at lower power inputs micromixing and mesomixing effects compete with one other. The limiting effect of mesomixing at low stirrer speeds becomes a micromixing-limited effect at higher power inputs (Franke and Mersmann, 1995).

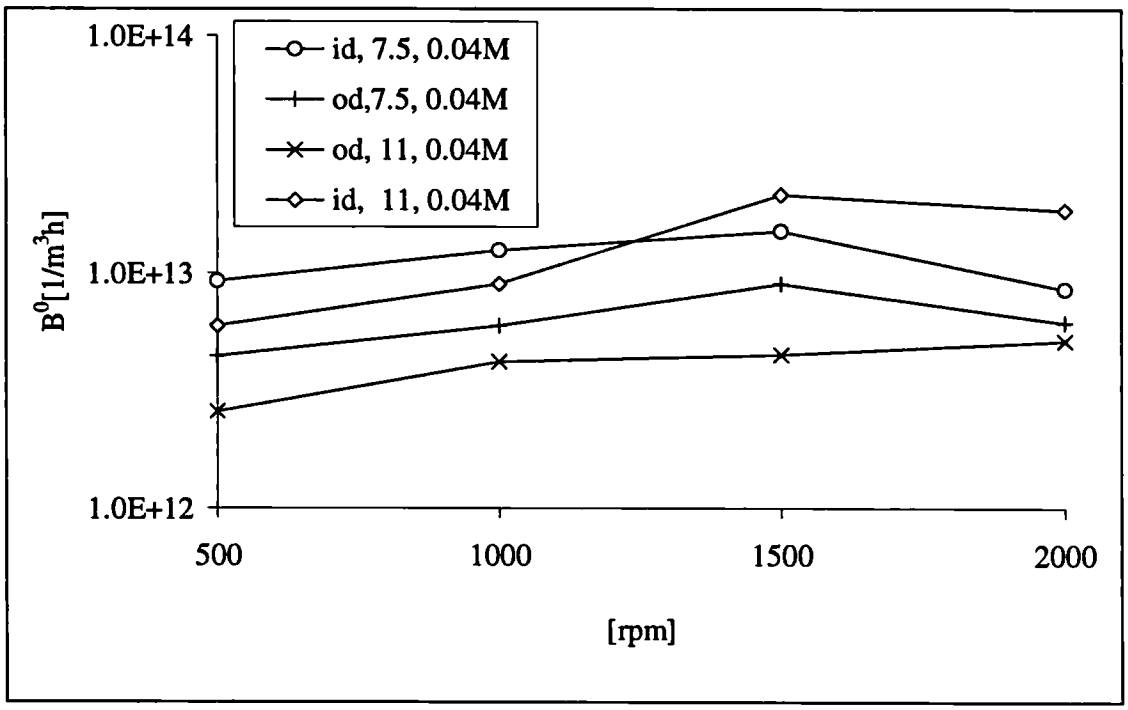

Figure 4.26 Nucleation rate vs. stirrer speed

The effects and influencing factors merit closer examination, however. A micro-mixing/mesomixing model applied to the precipitation kinetics should help to explain the observed behaviour in more detail (see Chapter 5).

In a double logarithmic diagram, the nucleation rate is plotted against the supersaturation for different stirrer speeds (Figure 4.27).

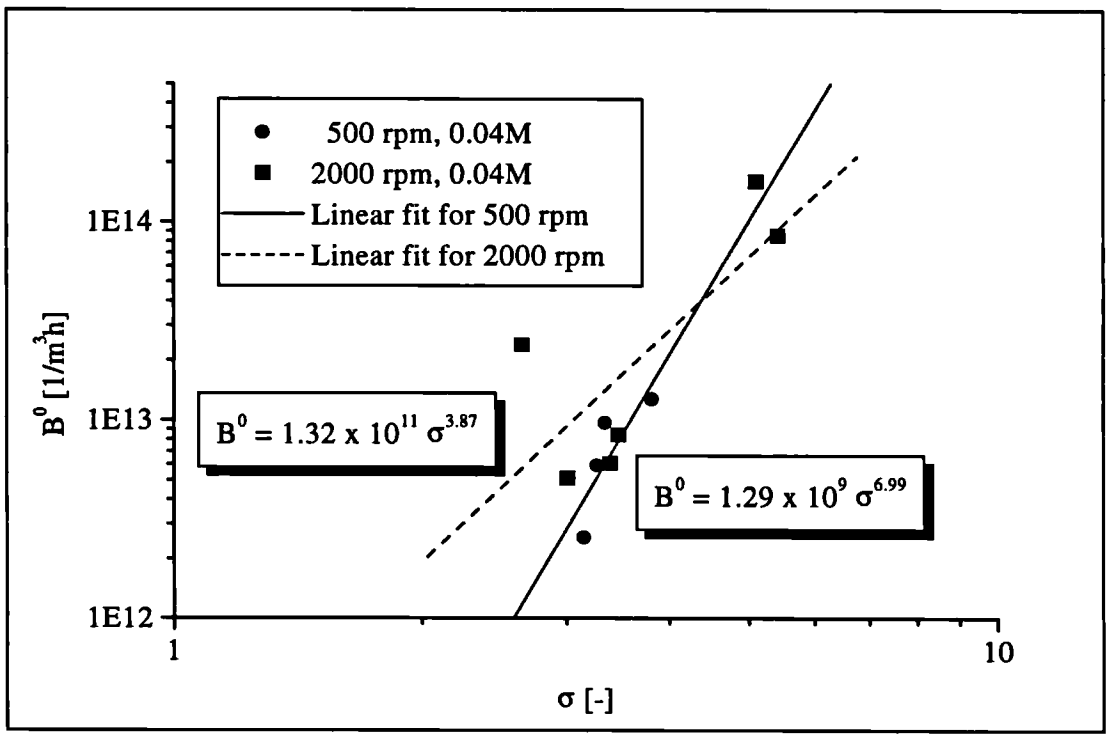

Figure 4.27 Nucleation rate vs. supersaturation

The kinetic order n in

$$B^0 = k_n \sigma^n \tag{4.18}$$

varies between 3.87 and 6.99 depending on the stirrer speed. As the experimental data scatter substantially, the correlation (4.18) seems rather arbitrary than satisfactory.

Disruption kernel

As mentioned above, the disruption kernel was determined from specially designed experiments at different stirrer speeds. Literature data on the disruption of precipitates are very scarce. Wójcik and Jones (1997) found in their study disruption kernels in the range from 0.004 min^{-1} to 0.2 min^{-1} using an attrition model to account for disruption. Hartel *et al.* (1986) observed disruption rates for calcium oxalate in a Couette-flow aggregator from 3.6×10^{-4} to 6.0×10^{-3} $1/\mu m^3 h$ in a narrow stirrer speed

range using a size-dependent disruption kernel and a particle splitting model to account for breakage.

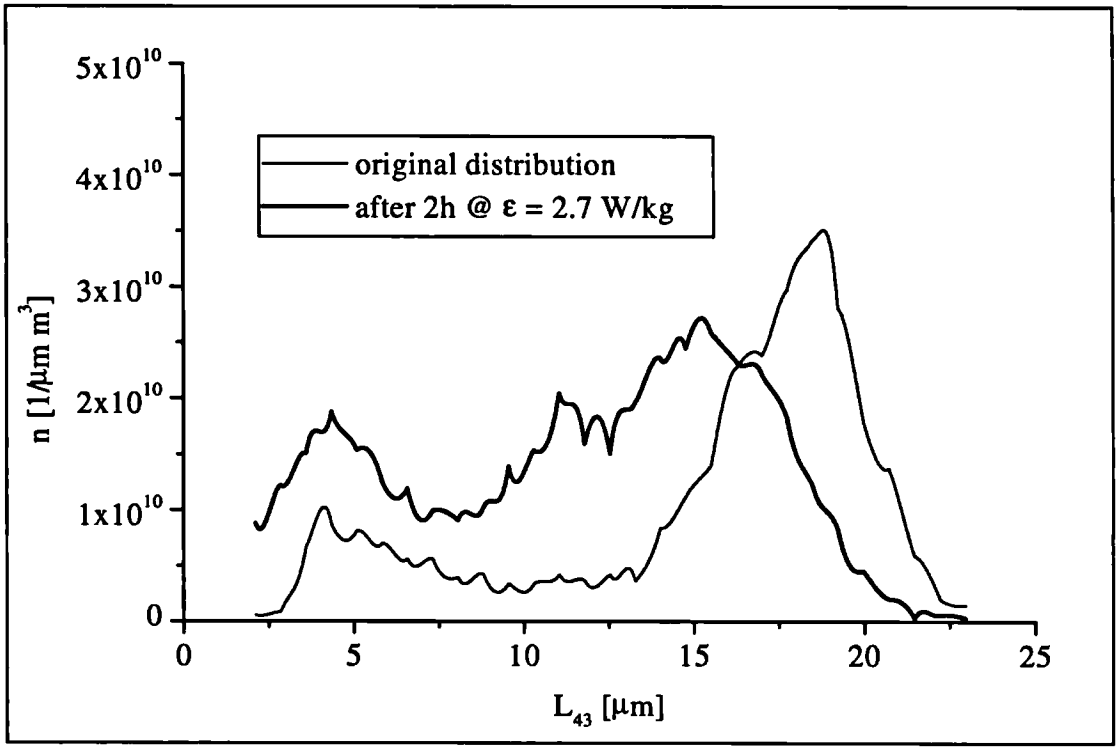

Figure 4.28 Particle size distribution for disruption experiment (ε = 2.7 W/kg)

Figure 4.28 shows the initial particle size distribution and the distribution after two hours of stirring. As a result of attrition and breakage of particles, the distribution gradually shifts to smaller sizes as large particles are reduced in size by breakage or attrition. Furthermore, the total number of particles measured increases as each breakage event leads to a number of daughter particles.

The expected increase in the disruption rate with the stirrer speed was confirmed for all the experiments (Figure 4.29). An almost linear dependence of the disruption kernel on the power input was observed leading to

$$\beta_{disr} \propto \varepsilon \qquad (4.19).$$

The disruption experiments were carried out at $\sigma = 0$ ($S = 1$) and therefore did not account for any effects of the supersaturation on the disruption process. Wójcik and

Jones (1997), who studied the agglomeration and disruption kinetics of calcium carbonate, report a decrease in the disruption rate as growth rate increases.

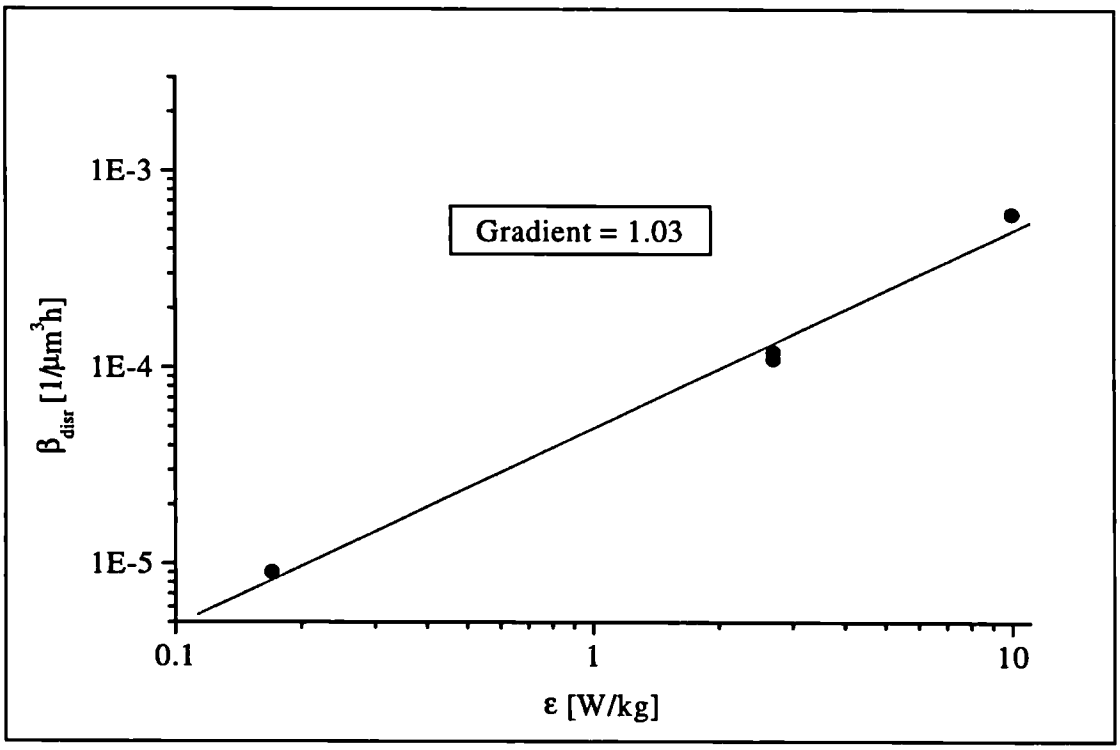

Figure 4.29 Disruption kernel vs. power input

Hartel and Randolph (1986) found the same tendency with calcium oxalate. Based on these findings, a linear decrease of the disruption kernel with the growth rate was assumed, giving

$$\beta_{disr} \propto G^{-1} \text{ or } \beta_{disr} \propto \sigma^{-2} \text{ or } \beta_{disr} \propto S^{-2.15} \qquad (4.20).$$

The final relationship for the disruption kernel is therefore

$$\beta_{disr} = 6.25 \times 10^{-5} \varepsilon S^{-2.15} \qquad (4.21).$$

Agglomeration kernel

To extract the agglomeration kernel from PSD data, the "inverse problem" referred to above must be solved. The population balance equation is thus simulated for different values of the agglomeration kernel, the results are compared with the approximated experimental distributions and the sums of least squares are calculated. The calculated distribution with the minimum sum of least squares fits the experimental distribution best.

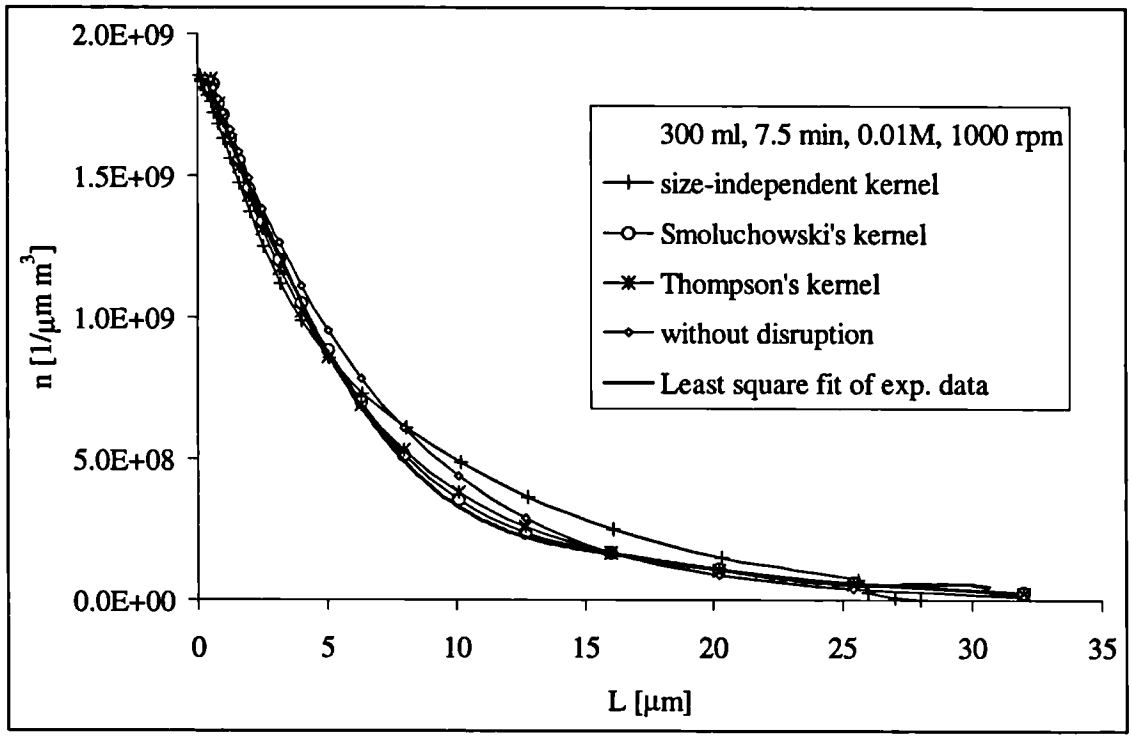

Figure 4.30 Prediction quality of various agglomeration kernels

The parameter estimation was performed for the agglomeration kernels mentioned in 2.3.3. The results for one run are compared in Figure 4.30. It is found that the size-dependent agglomeration kernels suggested by Smoluchowski and Thompson correspond to the experimental data very well, and that Smoluchowski's kernel fits best. For a size-independent agglomeration kernel and estimation without disruption (only nucleation, growth and agglomeration), the least square fits deviate substantially from the experimental data. For this reason, further investigations are carried out with the theoretically-based size-dependent kernel suggested by Smoluchowski, which fitted the data best:

$$K_{aggl}(L_u, L_v) = \frac{4}{3} Sh[L_u + L_v]^3 = \beta_{aggl}[L_u + L_v]^3 \qquad (4.22).$$

Agglomeration kernels obtained vary from 7.1×10^{-19} to 1.1×10^{-14} $m^3/\mu m^3 h$. No literature data were found for agglomeration of calcium oxalate modelled using Smoluchowski's kernel. The values published by Wójcik and Jones (1997) for calcium carbonate cover a range from 10^{-15} to 10^{-13} $m^3/\mu m^3 h$.

Similarly to the disruption rate, the rate of agglomeration also depends on the level of supersaturation in the reactor and on the power input. Wójcik and Jones (1997) found a linear increase of the agglomeration kernel with the growth rate. Therefore, the level of supersaturation was accounted for using

$$\beta_{aggl} \propto G \text{ or } \beta_{aggl} \propto \sigma^2 \text{ or } \beta_{aggl} \propto S^{2.15} \qquad (4.23).$$

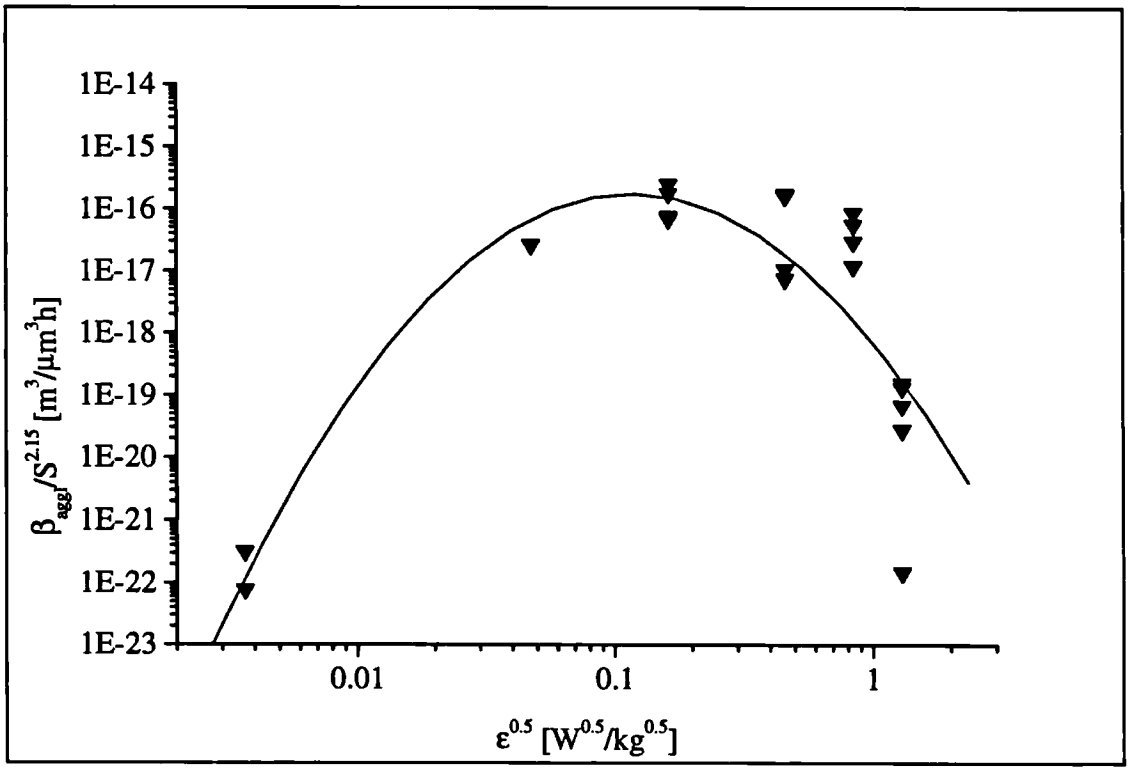

Figure 4.31 Agglomeration rate vs. shear rate

According to Smoluchowski's theory, the agglomeration rate increases in proportion to the shear rate *Sh*

$$\beta_{aggl} \propto Sh \qquad (4.24)$$

and therefore

$$\beta_{aggl} \propto \varepsilon^{\frac{1}{2}} \qquad (4.25).$$

Based on these considerations, Figure 4.31 shows the dependency of the agglomeration rate on the shear rate as obtained from the experiments. At medium power inputs a maximum in the agglomeration rate occurs. This can be explained by the fact that due to very high power inputs, the particles do not have sufficient time to "stick" together and form agglomerates. Mumtaz *et al.* (1997) found similar behaviour in their agglomeration experiments with calcium oxalate monohydrate and theoretically attributed the decrease in the agglomeration rate after a maximum at a certain shear rate to decreased agglomeration efficiency.

The final modelling equation found for the agglomeration kernel is

$$\beta_{aggl} = 5.431\times10^{-17}(1+2.296\varepsilon^{\frac{1}{2}} - 2.429\varepsilon)S^{2.15} \qquad (4.26).$$

In this equation, the first term relates to agglomeration effects independent of power input and the second term in brackets to agglomeration due to shear as described in Smoluchowski's theory. The third term describes the reduced agglomeration efficiency found experimentally at higher shear rates and is consistent with the findings of Mumtaz *et al.* (1997).

Significance of magnitudes

Molecular growth G versus agglomerative growth G_{aggl}

Molecular growth rates G, which were found from Equation (4.4), were compared with agglomerative growth rates G_{aggl} calculated from (Myerson, 1993)

$$G_{aggl} = \frac{L_{43}}{4\tau} \qquad (4.27).$$

The agglomerative growth rate is an apparent growth rate and accounts for both molecular and agglomerative growth. Under the conditions investigated, the agglomerative growth rate G_{aggl} was between 27% (for a residence time of τ = 2 min) and 43% (for a residence time of τ = 11 min) larger than the molecular growth rate G.

Agglomeration inefficiency versus particle disruption

As both mechanisms, agglomeration inefficiency and particle disruption, lead to a decrease in the number of agglomerates, it is advantageous to find out to what extent they influence the particle size distribution. At a specific power input of $\varepsilon = 1$ W/kg and with particles in the range between 35 and 45 µm, agglomeration inefficiency decreases the number of particles in this size class by 1%, whereas the decrease due to disruption is 3%. At the higher power input of $\varepsilon = 20$ W/kg, the size reduction by disruption becomes even more dominant with a decrease in the number of particles by 15% compared to a reduction of 1% due to agglomeration inefficiency. Disruption is the main cause of size reduction at all levels of supersaturation in the reactor.

4.9.4 PRECIPITATION KINETICS OF CALCIUM CARBONATE

The growth, nucleation, agglomeration and disruption kinetics for calcium carbonate $CaCO_3$ were determined in the same way as described for calcium oxalate. The results are listed in Appendix A4.4.

4.10 DETERMINATION OF THE SHAPE FACTOR

The shape of a particle can be defined by shape factors whose calculation is based on one characteristic dimension of the particle, usually on its equivalent diameter d. For example, the following shape factors can be defined (Allen, 1981):

volume: $$k_v = \frac{v}{d^3} \qquad (4.28)$$

surface area: $$k_a = \frac{a}{d^2} \qquad (4.29)$$

sphericity: $$\Psi = \left(\frac{d_v}{d_s}\right)^2 \quad \text{(Wadell, 1932)} \qquad (4.30).$$

For a sphere with diameter d, $k_v = \pi/6$, $k_a = \pi$ and $\Psi = 1$ are obtained, and for a cube with length of a side d, $k_v = 1$, $k_a = 6$ and $\Psi = 0.81$. For needle-like particles (COM)

with the dimensional ratio 5×1×1, the shape factors become k_v = 0.04, k_a = 0.88 and Ψ = 0.64 (Mersmann, 1995).

Using the definition of the sphericity in Equation (4.30), it is possible to determine Ψ experimentally by measuring the mean size using different techniques. The surface-based mean size d_s can be analysed with a laser diffraction analyser, while analysis with a Coulter Counter will yield the volume-based mean size d_v. Figure 4.32 shows mean sizes over a wide range measured using two techniques. The diffraction pattern was obtained using a Sympatec Helos laser diffraction analyser (Heuer and Leschonski, 1985) with suspension cell, giving d_s. A Coulter Counter was used to determine the volume mean size of the particles.

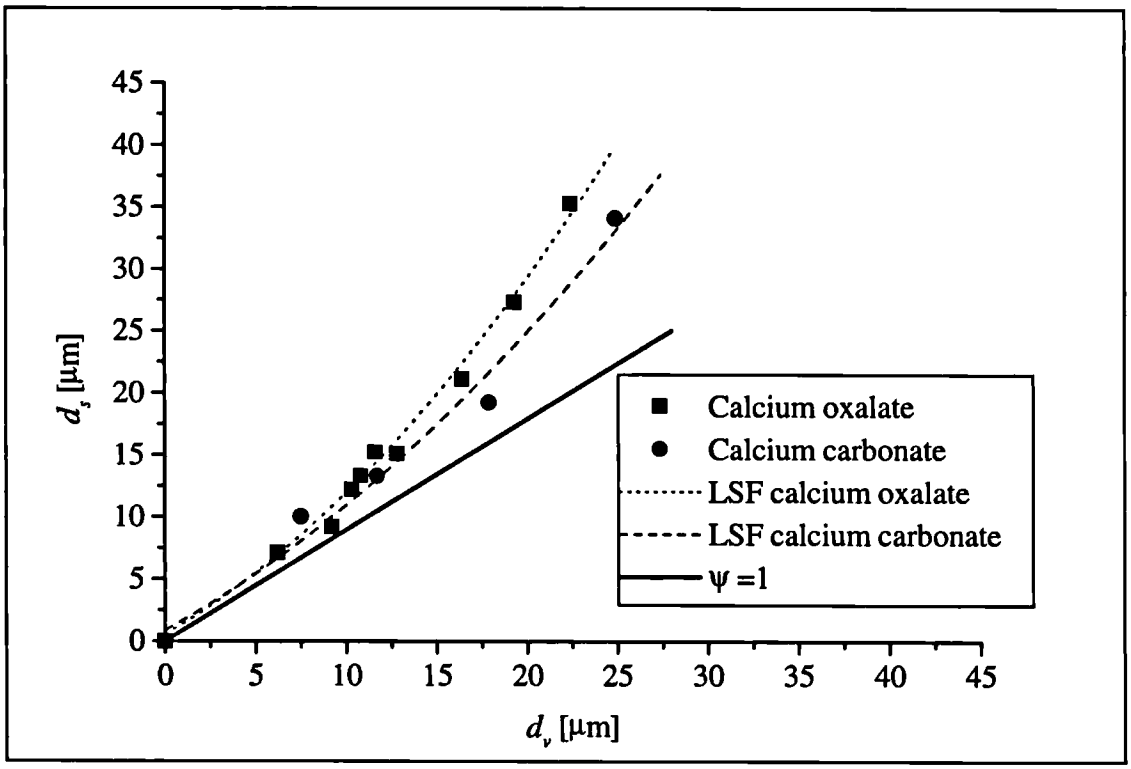

Figure 4.32 Measured surface and volume based mean sizes

As expected, the surface mean particle size d_s is larger than that obtained with the Coulter Counter (d_v), therefore leading to a sphericity $\Psi < 1$. The sphericity changes with the mean particle size (Figure 4.33) from about 0.78 to 0.41, with higher sphericities for small mean sizes. One explanation for this trend could be that particles

for the experiments with small mean sizes were prepared from solutions with high levels of supersaturation and very high nucleation rates. Therefore, the needles did not have enough time to grow in their length direction and remained shorter than the needles obtained at lower supersaturation. In addition, the formation of agglomerates might lead to a further reduction of the sphericity at large mean sizes. The theoretical sphericity of 0.64 (Mersmann, 1995) lies within the range of the experimental values.

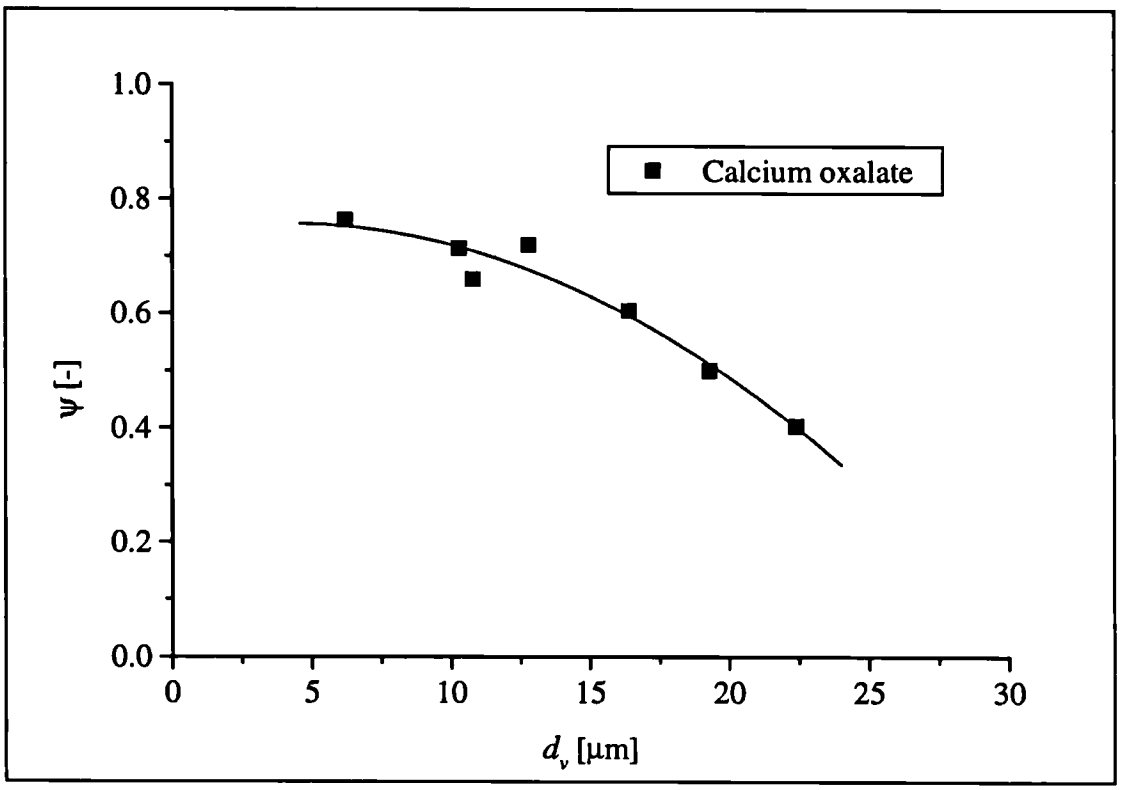

Figure 4.33 Experimental sphericity for calcium oxalate

4.11 DESIGN OF EXPERIMENTS (DOE)

In order to decrease the number of large-scale experiments necessary to scale up a process and to design an efficient experimental plan, the factors with the greatest influence on the process or the final product must be identified. For precipitation, a variety of factors such as concentration, residence time, stirrer speed and feed point position influence the precipitation rates and the final properties of a precipitate. It is thus useful to design the experiments in such a way that the influence of the individual

factors and the effect of their interactions can be evaluated. Such a systematic method is provided by "design of experiments" (DOE).

The small-scale continuous experiments carried out to determine the precipitation kinetics of calcium oxalate were analysed using the DOE technique. The experiments were performed in such a way that changes in the input variables enable the reasons for changes in the output response to be observed and identified. Consequently, it is possible both to determine the variables which have the greatest influence on the response and the set-up of the parameters so that a desired response can be achieved, and to improve the robustness of a process using the information gained from the experiments. Most importantly, key parameters for scale-up can be identified.

Factorial design

Factorial design is one way of carrying out an experiment systematically (Davies, 1979). Each input variable (= factor) is tested at two or more different levels by not only modifying one factor at a time, but also examining all possible combinations of factor levels in order to investigate the effect of each factor (= main effects) and the ways in which each factor may be influenced by the variation of the others (= interactions). Thus, for an n level factorial experiment with k influencing factors, n^k tests have to be carried out. For a two-level factorial experiment with four factors ($n = 2$, $k = 4$), $2^4 = 16$ tests (= treatments) are necessary.

Notation for two-level factorial experiments

A factor is denoted by a capital letter A, B, C,... and the two levels by (1) and the corresponding lower-case letter a, b, c,... By convention, (1) refers to the lower level, the normal condition or the absence of a condition, while "a" refers to a higher level or the presence of a condition, and so on. Details of the notation can be found in Davies (1979). For an experiment with four factors, the following treatment combinations occur (Table 4.4; "+" denotes that the factor is at its higher level, "-" denotes that the factor is at a lower level):

Symbol for treatment combination	Level of factor			
	A	B	C	D
(1)	-	-	-	-
a	+	-	-	-
b	-	+	-	-
ab	+	+	-	-
c	-	-	+	-
ac	+	-	+	-
bc	-	+	+	-
abc	+	+	+	-
d	-	-	-	+
ad	+	-	-	+
bd	-	+	-	+
abd	+	+	-	+
cd	-	-	+	+
acd	+	-	+	+
bcd	-	+	+	+
abcd	+	+	+	+

Table 4.4 Treatment combinations in DOE

Procedure

Using one of the algorithms provided in the literature (Fisher, 1990), it is possible to calculate the main effects A, B, C and D and the interactions AB, AC, AD, BC, BD, CD (second order), ABC, ABD, ACD, BCD (third order) and ABCD (fourth order).

Yates' algorithm (Yates, 1937), which is very convenient for computation, has been used for this purpose. The effects are calculated by systematically adding and subtracting responses. From the effects, the mean squares are calculated, which are essential for the analysis of the variance (ANOVA).

The sum of the mean squares of interactions is an estimate of the error variance of the experiment. When the degree of freedom is known, it is possible to calculate a significant level and subsequently determine whether an effect is significant or not according to its mean square level in relation to the significant level (Davies, 1979). Usually a level of 5% significance is chosen above which an effect is considered important for further investigation.

Having determined the most influencing factors, a design equation can be deduced from the response effects and responses at the intermediate levels calculated. The design equation and the choice of the level of significance are verified by comparing the measured and calculated responses.

Levels of factors

The following levels were chosen for the experimental design (Table 4.5):

Factor	low	high
A concentration	0.01M	0.04M
B residence time	7.5 min	11 min
C specific power input	0.211 W/kg	1.686 W/kg
D feed point position	outside DT (od)	inside DT (id)

Table 4.5 Levels of factors (input parameters)

Example 1: number mean size L_{10}

A "designed experiment" was carried out in order to find the factors which have the greatest influence on the number mean size L_{10} in the 300 ml calcium oxalate precipitation experiments. The possibility of making predictions on a scale-up of this parameter was also investigated.

Treatment combination	$L_{10,exp}$ [μm]	Yates 1	Yates 2	Yates 3	Yates 4	Effect	Factor
(1)	6.4	15.7	32.7	68.7	128.2		
a	9.3	17	36	59.5	17.6	2.2	A
b	6.9	17.4	28.3	9.7	1.4	0.175	B
ab	10.1	18.6	31.2	7.9	-1.2	-0.15	AB
c	7.8	14.4	6.1	2.5	6.2	0.775	C
ac	9.6	13.9	3.6	-1.1	-4.4	-0.55	AC
bc	8.4	15.9	4.9	0.3	-0.2	-0.025	BC
abc	10.2	15.3	3	-1.5	0.4	0.05	ABC
d	5.7	2.9	1.3	3.3	-9.2	-1.15	D
ad	8.7	3.2	1.2	2.9	-1.8	-0.225	AD
bd	6	1.8	-0.5	-2.5	-3.6	-0.45	BD
abd	7.9	1.8	-0.6	-1.9	-1.8	-0.225	ABD
cd	7.1	3	0.3	-0.1	-0.4	-0.05	CD
acd	8.8	1.9	-8.9E-16	-0.1	0.6	0.075	ACD
bcd	7	1.7	-1.1	-0.3	-5.3E-15	-6.7E-16	BCD
abcd	8.3	1.3	-0.4	0.7	1	0.125	ABCD

Table 4.6 Yates' algorithm (Part 1)

The first column of Table 4.6 describes the experimental conditions in terms of the design of experiment nomenclature. Starting with a test with all factors at their lower levels (1), the other runs are arranged in a systematic order. The second column provides the measured response values, in this case the number mean diameters. In the following four columns the main effects and interactions are calculated using Yates' algorithm (Yates, 1937). The results of this procedure are listed in the next column. The last column in Part 1 of Table 4.6 and the first column in Part 2 give the experimental design notation of the factors. The mean squares are calculated from the effects and listed in the next column. The significance test carried out (Davies, 1979) for a

significance of 5% and one degree of freedom (main effects and second order interactions) and five degrees (higher order interactions) results in an error estimate of 0.3933. Therefore, all effects significantly larger than 0.4 have a significant influence on the number mean size L_{10} of the final product.

Factor	Mean square	Signif.	X_1	X_2	X_3	X_4	$L_{10,calc}$ [µm]
			-1	-1	-1	-1	6.825
A	19.36	+++	1	-1	-1	-1	9.575
B	0.1225		-1	1	-1	-1	6.825
AB	0.09		1	1	-1	-1	9.575
C	2.4025	+	-1	-1	1	-1	8.15
AC	1.21	-	1	-1	1	-1	9.8
BC	0.0025		-1	1	1	-1	8.15
ABC	0.01		1	1	1	-1	9.8
D	5.29	--	-1	-1	-1	1	5.675
AD	0.2025		1	-1	-1	1	8.425
BD	0.81		-1	1	-1	1	5.675
ABD	0.2025		1	1	-1	1	8.425
CD	0.01		-1	-1	1	1	7
ACD	0.0225		1	-1	1	1	8.65
BCD	1.77E-30		-1	1	1	1	7
ABCD	0.0625		1	1	1	1	8.65

Table 4.7 Yates' algorithm (Part 2)

It was found not only that the feed concentration is the most important factor, but also that at a feed point position with higher local specific power dissipation (id), smaller number mean sizes are achieved. The power input and the interaction between power input and concentration also influence the final crystal size. This last interaction

can be interpreted as a result of micromixing effects, where local gradients of supersaturation (*i.e.* concentration) and power input (*i.e.* stirrer speed) are decisive for the properties of the final product. In the next four columns, the coded factors are stated. The coding procedure is necessary in order to obtain orthogonality for the design equation. The coded factors

$$X_i = \frac{X - \frac{X_{high} + X_{low}}{2}}{\frac{X_{high} - X_{low}}{2}} \tag{4.31}$$

are calculated to

$$X_1 = \frac{c[M] - 0.025}{0.015} \tag{4.32}$$

$$X_2 = \frac{\tau[\text{min}] - 9.25}{-1.75} \tag{4.33}$$

$$X_3 = \frac{\varepsilon[W/kg] - 0.9485}{0.7375} \tag{4.34}$$

$$X_4 = \begin{cases} +1 \text{ for id} \\ -1 \text{ for od} \end{cases} \tag{4.35}.$$

Using these coded factors, the design equation is obtained (Davies, 1978) from the effects and the overall mean size to

$$L_{10,DOE}\,[\mu m] = 8.01 + 1.1\,X_1 + 0.3875\,X_3 - 0.275\,X_1X_3 - 0.575\,X_4 \tag{4.36}.$$

From this design equation, the number mean sizes are calculated and listed in the penultimate column in the table. The sizes correspond well to the experimental values and confirm the accuracy of the design procedure. The following figure shows a comparison of the measured and calculated number mean sizes (Figure 4.34).

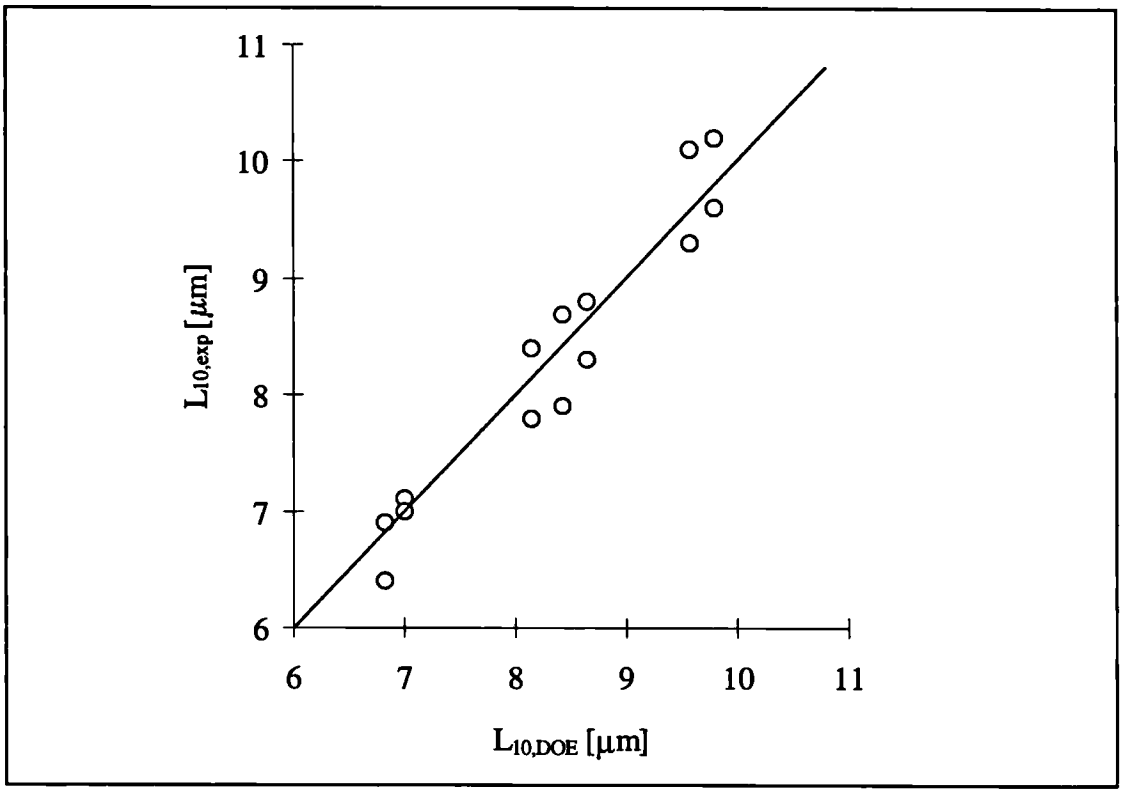

Figure 4.34 Number mean size L_{10} – experimental results vs. designed experiments

The design equation can be used not only to describe the effects of factors on the outcome of an experiment but also to calculate responses for one or more factors at intermediate levels.

The responses for 0.711 W/kg are calculated below using the design equation, and are compared with the measured sizes. For 0.711 W/kg, $X_3 = 0$ and X_1, X_2, $X_4 = \pm 1$ is obtained. The data are plotted in Figure 4.35.

As the calculated and measured number mean sizes show satisfactory agreement, the design equation can be used to predict intermediate responses (*e.g.* mean sizes) from the two-level experiments. It must be mentioned, however, that an extrapolation of data over the range covered by the designed experiments ($-1 < X_1, X_2, X_3, X_4 < 1$) is not recommended, especially if highly non-linear processes are investigated.

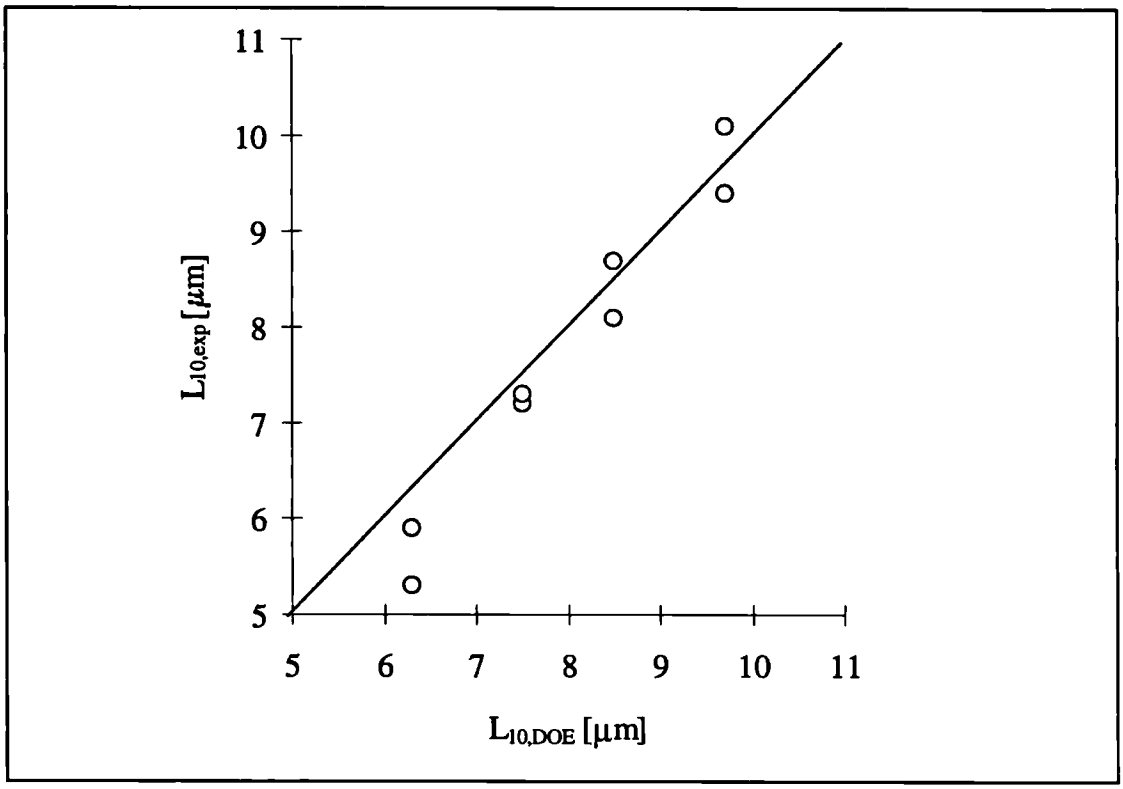

Figure 4.35 Number mean size L_{10} – experimental results and DOE predictions for intermediate conditions

Example 2: volume mean size L_{43}

The same procedure as applied to the number mean size was used to investigate the suitability of design of experiments for the volume mean size L_{43}, leading to the design equation

$$L_{43,DOE}\,[\mu m] = 25.875 + 0.625\,X_2 - 0.825\,X_3 + 1.112\,X_4 + 0.488\,X_1X_2 - 0.988\,X_2X_4 - 0.991\,X_3X_4 \qquad (4.37).$$

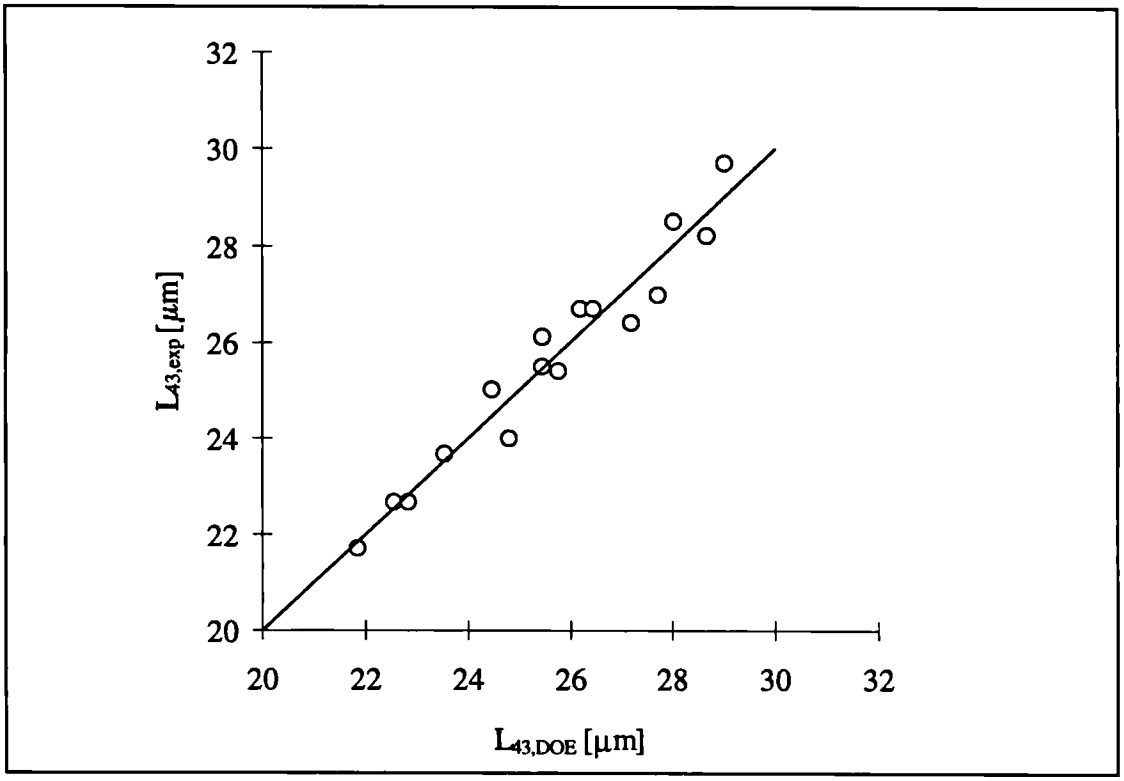

Figure 4.36 Volume mean size L_{43} – experimental results vs. designed experiments

The experimental and DOE data for the higher and lower levels of the factors are shown in Figure 4.36. Using the design equation for the volume mean size (Equation (4.37)), L_{43} was calculated for an intermediate specific power input of 0.711 W/kg and compared with the experimental results. The calculated value for L_{43} of 25.5 µm and the experimental finding of 34.8 µm show unacceptably high differences, however. DOE is not capable of accounting for all the effects influencing the volume mean size and it can therefore be concluded that it is not suitable as a predictive tool for scale-up.

Results of factorial experiments for other parameters

In a similar way to the experimental design applied to the number mean size, this procedure was repeated for the coefficient of variation c.v., supersaturation σ, nucleation rate B^0, growth rate G, agglomeration kernel β_{aggl} and disruption kernel β_{disr}. The results are listed in Table 4.8. A positive sign means that the higher the level, the

more positive the response. The number of signs indicates the strength of the influence, three signs representing a very strong influence.

With regard to supersaturation and growth rate, the residence time can be identified as the single most important factor for these responses. This can be explained by the fact that crystal growth is a comparatively slow kinetic process which is not greatly influenced by high local gradients of energy dissipation and hydrodynamic forces.

As far as the nucleation rate is concerned, the interaction between specific power input and feed point position has a strong impact on the result, which also suggests micromixing limitation of the precipitation process.

Factor	c.v.	σ	B^0	G	β_{aggl}	β_{disr}
A	--				+	-
B		--		---		
C						
D						+
AB	+				+	-
BD						
CD			+			
ABD					+	+

Table 4.8 Influence of the input parameters and interactions on the response variables (properties)

4.12 CONCLUSIONS

A new technique has been introduced to determine the kinetics from the particle size distribution of continuous experiments. This method, where the kinetic rates are extracted separately from the particle size distribution, is a reliable alternative to the simultaneous estimation of all kinetic parameters from the distribution, which is prone to inaccuracies and often incapable of distinguishing between different kinetic mechanisms. Although the nucleation, growth, agglomeration and disruption kinetics of

calcium oxalate precipitation have been extracted successfully, the application of the method is not limited to particle size distributions obtained by precipitation and can also be used to analyse experimental data from other particulate processes, *e.g.* crystallization and grinding. As all modelling and simulation techniques rely on accurate kinetic input data, the importance of fundamental analysis and accurate determination of the kinetics involved is obvious.

For growth, disruption and agglomeration it was possible to relate the kinetics to the specific energy dissipation and/or the level of supersaturation in the reactor. For nucleation, a mixing-limitation of the nucleation rate was found due to the instantaneous reaction of the feed solutions, resulting in high local variations in the nucleation rate. Consequently, it was not possible to correlate the nucleation rates to the mean level of supersaturation and specific power input. Figure 4.37 shows experimentally determined particle size distributions for different stirrer speeds (7.5 min, 0.04M, od). The influence of the fluid dynamics on the kinetic rates of precipitation results in different shapes of the distributions at different stirrer speeds. Nucleation, the first and fastest kinetic step occurring during precipitation, strongly depends on the level of supersaturation, the mixing conditions in the reactor and the feed point position. The approach described above is not therefore suitable for determining fundamental nucleation kinetic data. Söhnel and Garside (1992) and Nielsen (1969) describe other methods based, for example, on turbidity and induction time measurements.

For this research, data published by Brown *et al.* (1991) were used to model the nucleation kinetics. The authors measured the change in turbidity and related the nucleation rates to supersaturation leading to the kinetic expression

$$B^0 = 3.37536 \times 10^{15} \exp^{\frac{52.09}{\ln^2 S}} \qquad (4.38).$$

The size-dependent agglomeration kernel showed a maximum with increasing power input, suggesting a decreasing agglomeration efficiency at higher power inputs and therefore a deviation from Smoluchowski's theory consistent with the findings of Mumtaz *et al.* (1997). In addition, however, breakage occurs as a size-reducing kinetic process, increasing linearly with power input. Thus both mechanisms, *viz.* agglomeration inefficiency and disruption, reduce the number of agglomerates at higher stirrer speeds. By comparing the orders of magnitude of the influence of agglomeration

inefficiency and disruption on the particle size distribution, disruption was identified as the dominant size-reducing mechanism.

By measuring the particle size using different methods based on different measurement principles, it was possible to determine experimentally the sphericity of calcium oxalate crystals.

Design of experiments (DOE) can be a valuable tool for determining the most important parameters influencing different properties and kinetic processes. For the number mean size, growth rate and supersaturation it was possible to identify these parameters. For other important properties, however, such as the volume mean size, the method failed. It was not possible to draw clear conclusions about how this property was influenced by the input variables. The nucleation rate was found to depend on the hydrodynamic conditions, which is a further indication that the nucleation rates are mixing-limited. If specific parameters are to be scaled up, DOE can provide important information on how to conduct the large-scale experiments and how to vary the parameters to achieve the desired result. In general, however, DOE can lead to contradictory or ambiguous results and is thus only suitable to a limited extent for predicting the behaviour on a different scale.

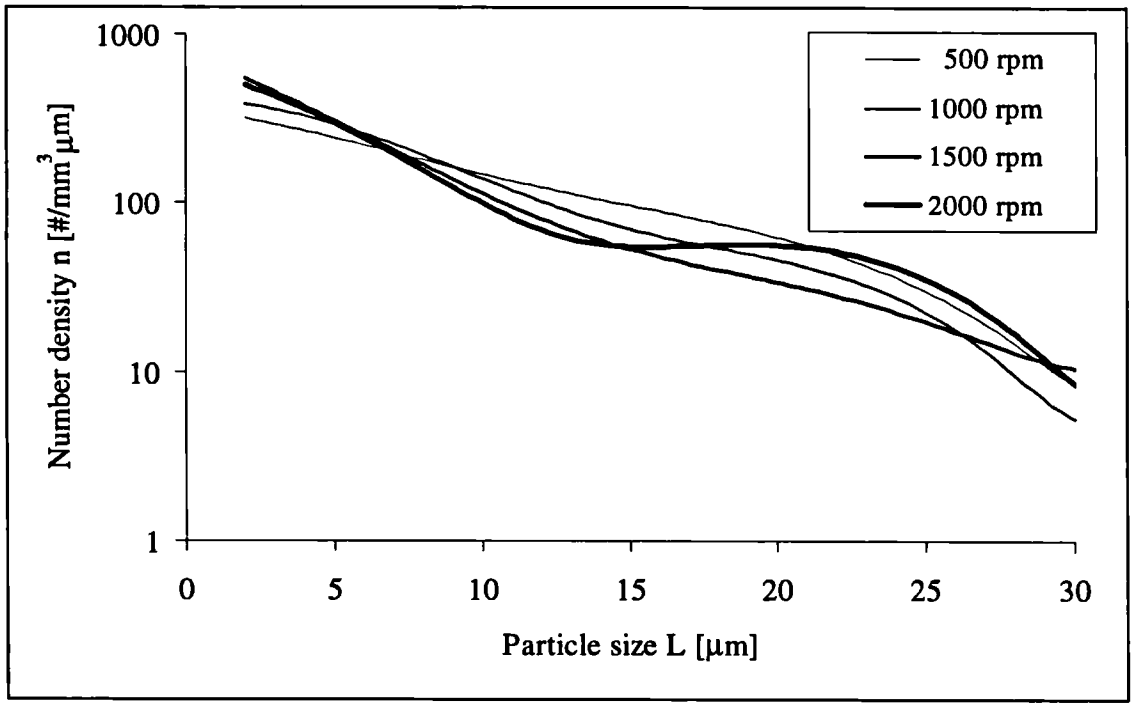

Figure 4.37 Particle size distribution at different stirrer speeds (300 ml reactor, 500 to 2000 rpm, 0.04M, 7.5 min, od)

CHAPTER 5

MIXING, MIXING MODELS AND COMPUTATIONAL FLUID DYNAMICS (CFD)

5.1 INTRODUCTION

As the flow of a reacting fluid through a reactor is a very complex process, idealised models are necessary in order to describe the interaction of the flow pattern with the chemical reaction. These interactions take place on different scales, ranging from the macroscopic scale (macromixing) to the microscopic scale (micromixing).

In this chapter, both macromixing and micromixing models will be introduced. A compartmental mixing model, the Segregated Feed Model (SFM), will be discussed in detail as it will be used to model the influence of the hydrodynamics on a meso- and microscale on continuous and semibatch precipitation. Using Computational Fluid Dynamics (CFD) diffusive and convective mixing parameters in the reactor will be determined.

5.2 MACROMIXING AND MACROMIXING MODELS

The term macromixing refers to the overall mixing performance in a reactor and is usually described by the residence time distribution (RTD). This concept was originally introduced by Danckwerts (1958) and is based on a macroscopic lumped population balance. A fluid element is followed from the time at which it enters the reactor (Lagrangian viewpoint). The probability that the fluid element will leave the reactor after a residence time τ is expressed as the residence time distribution (RTD) function. This function characterises the scale of mixedness in a reactor.

An ideal plug flow reactor, for example, has no spread in residence time because the fluid flows like a "plug" through the reactor (Westerterp *et al.*, 1995). For an ideal continuously stirred reactor, however, the RTD function becomes a decaying exponential function with a wide spread of possible residence times for the fluid elements.

Non-ideal reactors are described by RTD functions between these two extremes and can be approximated by a network of ideal plug flow and continuously stirred reactors. In order to determine the RTD of a non-ideal reactor experimentally, a tracer is introduced into the feed stream. The tracer signal at the output then gives information about the RTD of the reactor. It is thus possible to develop a mathematical model of the system that gives information about flow patterns and mixing.

In this research, the residence time distribution of the DTB reactor was determined for different stirrer speeds and residence times by injecting 5 ml of 1M $CaCl_2$ solution into the feed stream of the reactor. The response function of the ionic concentration was measured using a calcium-ion selective electrode and recorded with PCLab. The electrode was placed next to the withdrawal tube to ensure that the concentration in the outlet stream was measured. Figure 5.1 shows the response of the calcium-ion selective electrode versus the dimensionless residence time. Irrespective of stirrer speed and residence time, all distributions exhibit the same behaviour: a sharp increase in concentration shortly after the $CaCl_2$ trace has been injected and a steady decline afterwards. Comparison with distributions in the literature (Westerterp *et al.*, 1995) shows that under all the conditions investigated, the reactor is well-mixed as far as overall macromixing is concerned.

Tavare (1986) presents a concise overview and comparison of macromixing models available in the literature.

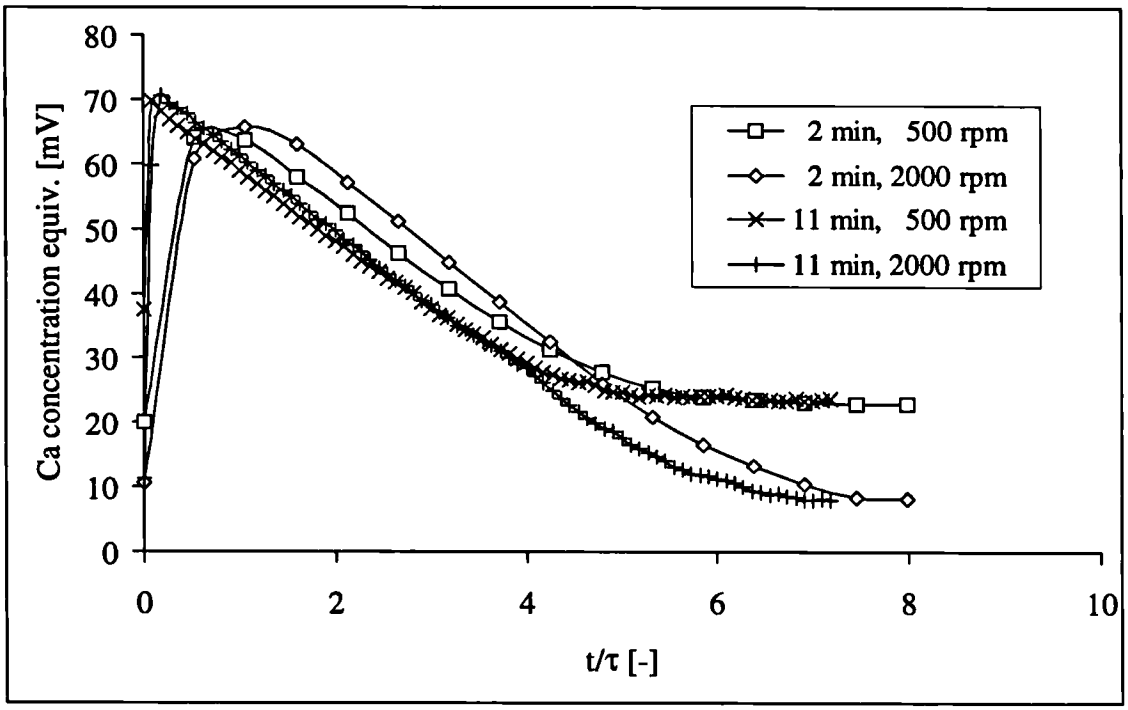

Figure 5.1 Residence time distribution in the 300 ml reactor

5.3 MESOMIXING AND MICROMIXING

The term mesomixing as introduced by Baldyga and Bourne (1992) describes the interaction by mixing between the feed plumes and the bulk. The reactant entering the reactor is eroded from the plumes and its scale reduced to that of large eddies. In the literature, the terms macromixing and mesomixing are not always considered separately, which has led to confusion when reactions were stated to be macromixing-controlled. In terms of the notation above, these processes are mesomixing-limited, as real macromixing limitation is very rare in precipitation reactors because of the well-mixedness on the macroscale and the relatively long residence times of the process. Mesomixing describes the very first moments of a fluid element entering the vessel, whereas macromixing considers the whole lifetime, *i.e.* the age, of an element in the reactor. In terms of space, mesomixing occurs only in the reaction zone.

Based on the time constant proposed by Baldyga *et al.* (1995),

$$t_{meso} = A\frac{\varepsilon_{avg}}{\varepsilon_{loc}}\frac{Q^{\frac{1}{3}}}{N^{\frac{4}{3}}d_s} \qquad (5.1)$$

was used to model mesomixing in a stirred tank, including the term $\varepsilon_{avg}/\varepsilon_{loc}$ to take different feed point positions into account. The inverse of the time constant t_{meso} (mesomixing) can be interpreted as a transfer coefficient for mass transfer by convection.

Micromixing is regarded as turbulent mixing on the molecular level. It comprises the viscous-convective deformation of fluid elements, followed by molecular diffusion (Baldyga and Poherecki, 1995). A characteristic timescale for micromixing is usually based on Kolmogoroff's microscale of eddy lifetime (Baldyga *et al.*, 1995 and Baldyga *et al.*, 1997) and was used in this research

$$t_{micro} = 17.3\times\left(\frac{\nu}{\varepsilon_{loc}}\right)^{1/2} \qquad (5.2).$$

The inverse of the time constant t_{micro} (micromixing) can be interpreted as a transfer coefficient for mass transfer by diffusion.

5.4 MESOMIXING AND MICROMIXING MODELS

Over the last fifty years, many mesomixing and micromixing models have been proposed to describe the influence of mixing on chemical reactions on the meso- and molecular scale. Most of them fall into one of the three categories discussed below (Villermaux and Falk, 1994).

Phenomenological or mechanistic models

This type of model derives from the RTD concept of macromixing as described above, which is applied on a microscopic level using idealised zones and exchange flows. The mixing parameters do not usually have any physical relevance and are determined experimentally.

The coalescence-redispersion (CRD) model was originally proposed by Curl (1963) and is based on imagining a chemical reactor as a number population of droplets that behave as individual batch reactors. These droplets coalesce (mix) in pairs at random, homogenise their concentration and redisperse. The mixing parameter in this model is the average number of collisions that a droplet undergoes.

Another popular phenomenological mixing model is the Interaction by Exchange with the Mean (IEM) model, which was originally suggested by Harada *et al.* (1962). Micromixing takes place by exchange between feed regions (well-mixed batch zones) and a mean environment (bulk) according to a mixing time constant. Garside and Tavare (1985) used the IEM model to model extreme cases of micromixing during precipitation.

In the three and four environment (3E and 4E) models (Ritchie and Togby, 1979 and Mehta and Tarbell, 1983), the reactor is divided into two segregated entering environments and one or two fully mixed leaving environments. The mixing parameter is the transfer coefficient between the environments.

Franck *et al.* (1988) developed a two-compartment mixing model with the exchange flow rate (recycle number) between the two compartments as the only adjustable parameter. They applied their model successfully to the precipitation of salicylic acid.

Chang *et al.* (1986) compare different phenomenological mixing models and demonstrate their analogies and similarities to the theory of turbulence.

Physical models

As their name suggests, these models are based on the physical principles of diffusion and convection, which govern the mixing process. According to the flow pattern, the reactor is divided into different zones with different flow characteristics.

Baldyga and Bourne (1984a to c and 1989a and b) developed models based on the engulfment-deformation-diffusion (EDD) theory. Entering material is engulfed by bulk material forming vortices, subsequently deformed and stretched to form slabs and finally exchanges mass by molecular diffusion. Bourne (1985) applies a one-dimensional diffusion equation to slabs and shows how vorticity is responsible for mixing by engulfment of fluid. Baldyga and Bourne (1989a and b) show that under some conditions engulfment becomes the rate-determining step in micromixing. They describe the molecular mixing based on the spectral interpretation of mixing in an isotropic turbulent field. The concentration spectrum indicates that molecular diffusion starts between the viscous-convective and the viscous-diffusive subrange and becomes dominant as the scale becomes smaller. Fluid elements in this subrange are laminar deformed by stretching and form slabs.

Leeuwen (1998) developed a compartmental mixing model for precipitation based on the engulfment theory mentioned above. The author obtains the mixing parameters between the feed and the bulk zone from the flow characteristics in the reactor and subsequently calculates moments and mean sizes of the precipitate.

Analytical models

Local information on the flow field in a reactor is important and can be obtained using Computational Fluid Dynamics (CFD). By coupling the flow problem with a mixing model, it should become possible to solve the micro- and mesomixing problem analytically. Wei and Garside (1997) studied the precipitation of barium sulphate using CFD. In order to account for the small-scale effects of mixing, however, a very fine grid resolution has to be chosen, and therefore the computational demand often increases

enormously even for very simple reactor geometries. Closure models for micromixing, similar to closure models used in turbulence theory, can be introduced to overcome this problem. In this case, a lack of local micromixing information severely reduces the predictive quality of these models.

From the considerations above, it can be concluded that phenomenological models show a lack of predictive quality as the mixing parameters cannot be determined *a priori*. Furthermore, an analytical solution to the mixing problem in complicated reactor geometries is not yet feasible. Consequently, to date only physical models are suitable for modelling scale-up. Having said this, the model chosen to model the influence of mixing on the precipitation kinetic rates in this research is the Segregated Feed Model (SFM), which originally belonged to the group of phenomenological mixing models. The model has, however, been modified and its mixing parameters, the mesomixing and the micromixing time, have subsequently become "meaningful" physical parameters for diffusion and convection in a physical model and can therefore be related to the flow field in the reactor. The model was first used to investigate micromixing effects of consecutive-competitive semibatch reactions (Villermaux, 1989). It was subsequently applied to predict the effects of mixing on semibatch polymerisation (Tosun, 1992) and to model the semibatch precipitation of barium sulphate without accounting for agglomeration and disruption (Marcant, 1996). The SFM was found to be particularly suitable for modelling mixing effects, as it combines the advantages of both the compartmental IEM model and the physical models.

5.5 SEGREGATED FEED MODEL (SFM)

5.5.1 INTRODUCTION

In the SFM the reactor is divided into three well-mixed zones: two feed zones f_1 and f_2 and the bulk b (Figure 5.2). The feed zones exchange mass with each other and with the bulk as depicted with the flow rates $u_{1,2}$, $u_{1,3}$ and $u_{2,3}$ respectively, according to the time constants of micromixing and mesomixing. As imperfect mixing leads to gradients of the concentrations in the reactor, different supersaturation levels in different compartments govern the precipitation rates, especially the rapid nucleation process.

Using the SFM, the influence of micromixing and mesomixing on the precipitation process and properties of the precipitate can be investigated. Mass and

population balances can be applied to the individual compartments and to the overall reactor accounting for different levels of supersaturation in different zones of the reactor.

The individual volumes of the compartments feed plume 1 (f_1), feed plume 2 (f_2) and bulk (b) and the total volume of the precipitation reactor in steady-state operation can be written as

$$\frac{dV_{f1}}{dt} = Q_{f1} - \frac{V_{f1}}{t_{meso1}} = 0 \tag{5.3}$$

$$\frac{dV_{f2}}{dt} = Q_{f2} - \frac{V_{f2}}{t_{meso2}} = 0 \tag{5.4}$$

$$\frac{dV_b}{dt} = Q_{f1} + Q_{f2} - Q_b = 0 \tag{5.5}$$

$$\frac{dV_{tot}}{dt} = 0 \tag{5.6}$$

with $$V_{tot} = V_{f1} + V_{f2} + V_b \tag{5.7}.$$

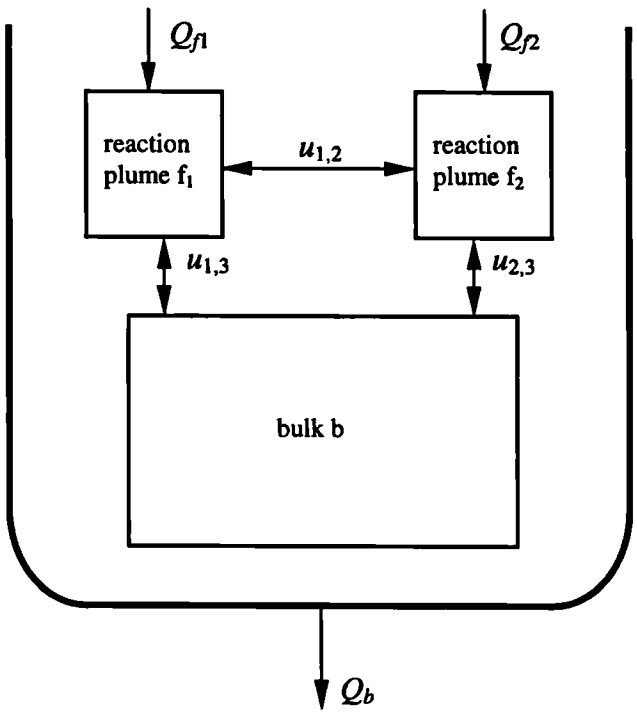

Figure 5.2 Segregated Feed Model (SFM)

The mass balances for a species j in the three zones give

$$\frac{d(V_{f_1}c_{j,f1})}{dt} = r_{j,f1}V_{f1} + Q_{f1}c^0_{j,f1} - u_{j,f1b} - u_{j,f1f2} \tag{5.8}$$

$$\frac{d(V_{f_2}c_{j,f2})}{dt} = r_{j,f2}V_{f2} + Q_{f2}c^0_{j,f2} - u_{j,f2b} + u_{j,f1f2} \tag{5.9}$$

$$\frac{d(V_b c_{j,b})}{dt} = r_{j,b}V_b - Q_b c_{j,b} + u_{j,f1b} + u_{j,f2b} \tag{5.10}$$

with the exchange flows between the compartments

$$u_{j,f1b} = \frac{V_{f_1}c_{j,f1}}{t_{meso1}} + \frac{V_{f1}(c_{j,f1} - c_{j,b})}{t_{micro1}} \tag{5.11}$$

$$u_{j,f2b} = \frac{V_{f_2}c_{j,f2}}{t_{meso2}} + \frac{V_{f2}(c_{j,f2} - c_{j,b})}{t_{micro2}} \tag{5.12}$$

$$u_{j,f1f2} = \frac{(V_{f_1} + V_{f_2})(c_{j,f1} - c_{j,f2})}{t_{12}} \tag{5.13}.$$

5.5.2 EXTREME CASES OF MIXING

Fully micromixed (ideal CSTR or MSMPR)

For an ideal mixed reactor, the mixing times converge to zero, *i.e.*

$$t_{meso1}, t_{meso2}, t_{micro1}, t_{micro2}, t_{12} \rightarrow 0.$$

Therefore, the volumes V_{f1} and V_{f2} also become zero, and furthermore $V_b = V_{tot}$. Under these conditions the set of equations of the general case can be simplified to give

$$\frac{d(V_{tot}c_{j,tot})}{dt} = r_{j,tot}V_{tot} + u_{j,f1b} + u_{j,f2b} - \frac{V_{tot}c_{j,tot}}{\tau} = 0 \tag{5.14}$$

$$r_{j,f1}0 + Q_{f1}c^0_{j,f1} - u_{j,f1b} = 0 \rightarrow \qquad u_{j,f1b} = Q_{f1}c^0_{j,f1b} \tag{5.15}$$

$$r_{j,f2}0 + Q_{f2}c^0_{j,f2} - u_{j,f2b} = 0 \rightarrow \qquad u_{j,21b} = Q_{f2}c^0_{j,f2b} \tag{5.16}$$

and subsequently reduces to

$$r_j V_{tot} + Q_{f1} c^0_{j,f1} + Q_{f2} c^0_{j,f2} - \frac{V_{tot} c_{j,tot}}{\tau} = 0 \qquad (5.17),$$

the general mass balances for species j in a CSTR.

Total segregation (no micromixing takes place)

For a totally segregated reactor, the mixing times converge to infinity, *i.e.*

$$t_{meso1}, t_{meso2}, t_{micro1}, t_{micro2}, t_{12} \rightarrow \infty .$$

Therefore the exchange flow rates $u_{j,f1f2}$, $u_{j,f1b}$ and $u_{j,f2b}$ become zero. From this, it follows that the reaction rates $r_{j,f1}$, $r_{j,f2}$ and $r_{j,b}$ have to be zero and thus that no reaction takes place.

5.5.3 SFM APPLIED TO CONTINUOUS PRECIPITATION

Using the following assumptions, the SFM will be applied to continuous precipitation:

- Instantaneous reaction: $A + B \xrightarrow{k_r} P$. The reaction between the two feed solutions occurs instantaneously as soon as they are mixed.
- Homogeneous conditions within the feed zones and the bulk. Within each compartment, there are no gradients in the field of supersaturation.
- Nucleation is the only kinetic process occurring in the feed plumes. Nucleation, growth, agglomeration and disruption take place in the bulk zone.
- Direct diffusional mass exchange between the feed plumes is negligible as the feed points are too far apart and diffusion is too slow to play a significant role in the diffusional mass exchange between the feed streams, leading to $t_{12} \rightarrow \infty$.

Consequently, the following model equations are obtained.

Volumes of compartments

$$V_{f1} = Q_{f1} t_{meso1} \tag{5.18}$$

$$V_{f2} = Q_{f2} t_{meso2} \tag{5.19}$$

$$V_b = V_{tot} - (V_{f1} + V_{f2}) \tag{5.20}$$

Mass balances

Species A (e.g. $CaCl_2$)

$$\frac{d(V_{f1} c_{A,f1})}{dt} = Q_{f1} c^0_{A,f1} - \frac{V_{f1} c_{A,f1}}{t_{meso1}} - \frac{V_{f1}(c_{A,f1} - c_{A,b})}{t_{micro1}} - B^0_{f1} k_v L^3_0 \frac{\rho_c}{MW_c} V_{f1} = 0 \tag{5.21}$$

$$\frac{d(V_{f2} c_{A,f2})}{dt} = -\frac{V_{f2} c_{A,f2}}{t_{meso2}} - \frac{V_{f2}(c_{A,f2} - c_{A,b})}{t_{micro2}} - B^0_{f2} k_v L^3_0 \frac{\rho_c}{MW_c} V_{f2} = 0 \tag{5.22}$$

$$\frac{d(V_b c_{A,b})}{dt} = -Q_b c_{A,b} + \frac{V_{f1} c_{A,f1}}{t_{meso1}} + \frac{V_{f1}(c_{A,f1} - c_{A,b})}{t_{micro1}} + \frac{V_{f2} c_{A,f2}}{t_{meso2}} + \frac{V_{f2}(c_{A,f2} - c_{A,b})}{t_{micro2}} - B^0_b k_v L^3_0 \frac{\rho_c}{MW_c} V_b - \frac{1}{2} G_b k_a m_2 \frac{\rho_c}{MW_c} V_b = 0 \tag{5.23}$$

Species B (e.g. $Na_2C_2O_4$)

$$\frac{d(V_{f1} c_{B,f1})}{dt} = -\frac{V_{f1} c_{B,f1}}{t_{meso1}} - \frac{V_{f1}(c_{B,f1} - c_{B,b})}{t_{micro1}} - B^0_{f1} k_v L^3_0 \frac{\rho_c}{MW_c} V_{f1} = 0 \tag{5.24}$$

$$\frac{d(V_{f2} c_{B,f2})}{dt} = Q_{f2} c^0_{B,f2} - \frac{V_{f2} c_{B,f2}}{t_{meso2}} - \frac{V_{f2}(c_{B,f2} - c_{B,b})}{t_{micro2}} - B^0_{f2} k_v L^3_0 \frac{\rho_c}{MW_c} V_{f2} = 0 \tag{5.25}$$

$$\frac{d(V_b c_{B,b})}{dt} = -Q_b c_{B,b} + \frac{V_{f1} c_{B,f1}}{t_{meso1}} + \frac{V_{f1}(c_{B,f1} - c_{B,b})}{t_{micro1}} + \frac{V_{f2} c_{B,f2}}{t_{meso2}} + \frac{V_{f2}(c_{B,f2} - c_{B,b})}{t_{micro2}} - B_b^0 k_v L_0^3 \frac{\rho_c}{MW_c} V_b - \frac{1}{2} G_b k_a m_2 \frac{\rho_c}{MW_c} V_b = 0 \quad (5.26)$$

Mixing times

As mentioned above, the inverse of the time constants t_{micro1}, t_{micro2} (micromixing), t_{meso1} and t_{meso2} (mesomixing) can be interpreted as transfer coefficients for mass transfer by diffusion and convection, respectively, and are given by Equations (5.1) and (5.2).

Population balance (Randolph and Larson, 1988)

One of the advantages of using a compartmental model is that the "full" population balance, including terms for size-dependent agglomeration and disruption, can be implemented in the model. Therefore, the population balance for the bulk becomes

$$\frac{\partial n_{P,b}}{\partial t} = -G_b \frac{\partial n_{P,b}}{\partial L} + B_{aggl} + B_{disr} - D_{aggl} - D_{disr} - \frac{n_{P,b} Q_b}{V_{tot}} = 0 \quad (5.27)$$

with the birth terms for agglomeration and disruption

$$B_{aggl} + B_{disr} = \frac{L^2}{2} \int_0^L \frac{K_{aggl} n(L_u) n(L_v) dL_u}{L_v^2} + \int_{L_v}^{\infty} K_{disr} S'(L_u, L_v) n(L_u) n(L_v) dL_u \quad (5.28)$$

and the death terms for agglomeration and disruption

$$D_{aggl} + D_{disr} = n(L) \int_0^{\infty} K_{aggl} n(L_u) dL_u + K_{disr} n(L) \quad (5.29).$$

The expression for the nucleation rate B_j^0 in the compartment j is derived from the theory of primary nucleation and found to be

$$B_j^0 = A \exp\left[-\frac{16\pi\gamma^3 v^2}{3k^3 T^3 \ln^2 S_j} \right] \quad (5.30),$$

with the supersaturation defined as

$$S_j = \left(\frac{c_{A,j}^{\nu_A} c_{B,j}^{\nu_B}}{K_{sp}} \right)^{\frac{1}{\nu_A+\nu_B}} = \sigma_j + 1 \qquad (5.31).$$

The overall nucleation rate in the reactor becomes

$$B_{tot}^0 = \frac{B_b^0 V_b + B_{f1}^0 V_{f1} + B_{f2}^0 V_{f2}}{V_{tot}} \qquad (5.32).$$

The dependence of the growth rate on supersaturation is modelled using the power law expression

$$G_b = k_g \sigma_b^2 \qquad (5.33).$$

Furthermore, the agglomeration and disruption kernels are also assumed to depend on the supersaturation in power law form:

$$K_{aggl} = \beta_{aggl} f(\varepsilon) \sigma_b^2 \qquad (5.34)$$

$$K_{disr} = \beta_{disr} g(\varepsilon) \sigma_b^{-2} \qquad (5.35).$$

The second moment of the particle size distribution used in the mass balances is obtained from

$$m_2 = \int_0^\infty n_{P,b}(L) L^2 dL \qquad (5.36).$$

5.5.4 SFM APPLIED TO SEMIBATCH PRECIPITATION

Using similar assumptions as for the continuous mode, the SFM can be applied to semibatch precipitation:

- Instantaneous reaction: $A + B \xrightarrow{k_r} P$. The reaction between the two feed solutions occurs instantaneously as soon as they are mixed.
- Homogeneous conditions within the feed zone and the bulk.
- Nucleation is the only kinetic process occurring in the feed plume. Nucleation, growth, agglomeration and disruption take place in the bulk zone.

The model equations for the semibatch case are analogous to those of the continuous model.

Volumes of compartments

$$\frac{dV_f}{dt} = Q_f - \frac{V_f}{t_{meso}} \tag{5.37}$$

$$\frac{dV_{tot}}{dt} = Q_f \tag{5.38}$$

$$V_{tot} = V_f + V_b \tag{5.39}$$

Mass balances

Species A (e.g. $CaCl_2$)

$$\frac{d(V_f c_{A,f})}{dt} = Q_f c_{A,f}^0 - \frac{V_f c_{A,f}}{t_{meso}} - \frac{V_f (c_{A,f} - c_{A,b})}{t_{micro}} - B_f^0 k_v L_0^3 \frac{\rho_c}{MW_c} V_f \neq 0 \tag{5.40}$$

$$\frac{d(V_b c_{A,b})}{dt} = \frac{V_f c_{A,f}}{t_{meso}} + \frac{V_f (c_{A,f} - c_{A,b})}{t_{micro}} - B_b^0 k_v L_0^3 \frac{\rho_c}{MW_c} V_b - \frac{1}{2} G_b k_a m_2 \frac{\rho_c}{MW_c} V_b \neq 0 \tag{5.41}$$

Species B (e.g. Na_2Ox)

$$\frac{d(V_f c_{B,f})}{dt} = -\frac{V_f c_{B,f}}{t_{meso}} - \frac{V_f (c_{B,f} - c_{B,b})}{t_{micro}} - B_f^0 k_v L_0^3 \frac{\rho_c}{MW_c} V_f \neq 0 \tag{5.42}$$

$$\frac{d(V_b c_{B,b})}{dt} = \frac{V_f c_{B,f}}{t_{meso}} + \frac{V_f (c_{B,f} - c_{B,b})}{t_{micro}} - B_b^0 k_v L_0^3 \frac{\rho_c}{MW_c} V_b - \frac{1}{2} G_b k_a m_2 \frac{\rho_c}{MW_c} V_b \neq 0 \tag{5.43}$$

Population balance (Randolph and Larson, 1988)

Product P

$$\frac{\partial n_{P,b}}{\partial t} = -G_b \frac{\partial n_{P,b}}{\partial L} + B_{aggl} + B_{disr} - D_{aggl} - D_{disr} \neq 0 \tag{5.44}$$

With the birth terms for agglomeration and disruption

$$B_{aggl} + B_{disr} = \frac{L^2}{2}\int_0^L \frac{K_{aggl} n(L_u) n(L_v) dL_u}{L_v^2} + \int_{L_v}^{\infty} K_{disr} S'(L_u, L_v) n(L_u) n(L_v) dL_u \quad (5.45)$$

and the death terms for agglomeration and disruption

$$D_{aggl} + D_{disr} = n(L)\int_0^{\infty} K_{aggl} n(L_u) dL_u + K_{disr} n(L) \quad (5.46)$$

the population balance becomes an integro-partial differential equation.

The expression for the nucleation rate B_j^0 in the compartment j is analogous to that for the continuous case. The overall nucleation rate becomes

$$B_{tot}^0 = \frac{B_b^0 V_b + B_f^0 V_f}{V_{tot}} \quad (5.47).$$

5.5.5 GENERAL MODEL RESULTS

In order to illustrate the model, the following figures reflect a qualitative analysis of the precipitation process. A quantitative analysis using experimental data can be found in Chapter 6 and 7. The kinetic parameters used for the simulations are listed in Chapter 4.

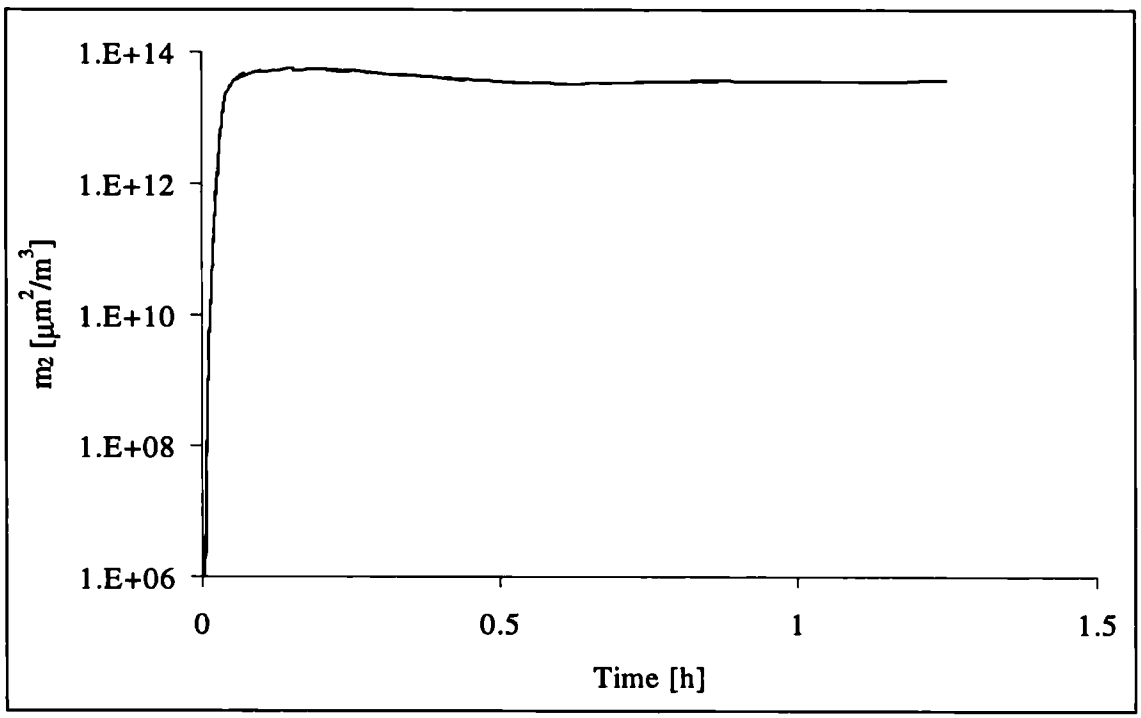

Figure 5.3 Time-dependence of the second moment m_2

In order to model the time-dependent behaviour of the continuous system, the mass balances were solved together with the population balance over an interval of ten residence times. After that time, it is assumed that the continuous system has achieved steady state. Being a measure of the crystal surface area available for growth, the second moment m_2 is an important factor for crystal growth (Figure 5.3). It increases sharply at the beginning and maintains a constant level after about four residence times. In contrast, the number mean size (Figure 5.4) exhibits almost oscillating behaviour. It approaches a maximum after about two residence times (1.4 times larger than the steady state mean size) and then decreases before increasing again, eventually approaching

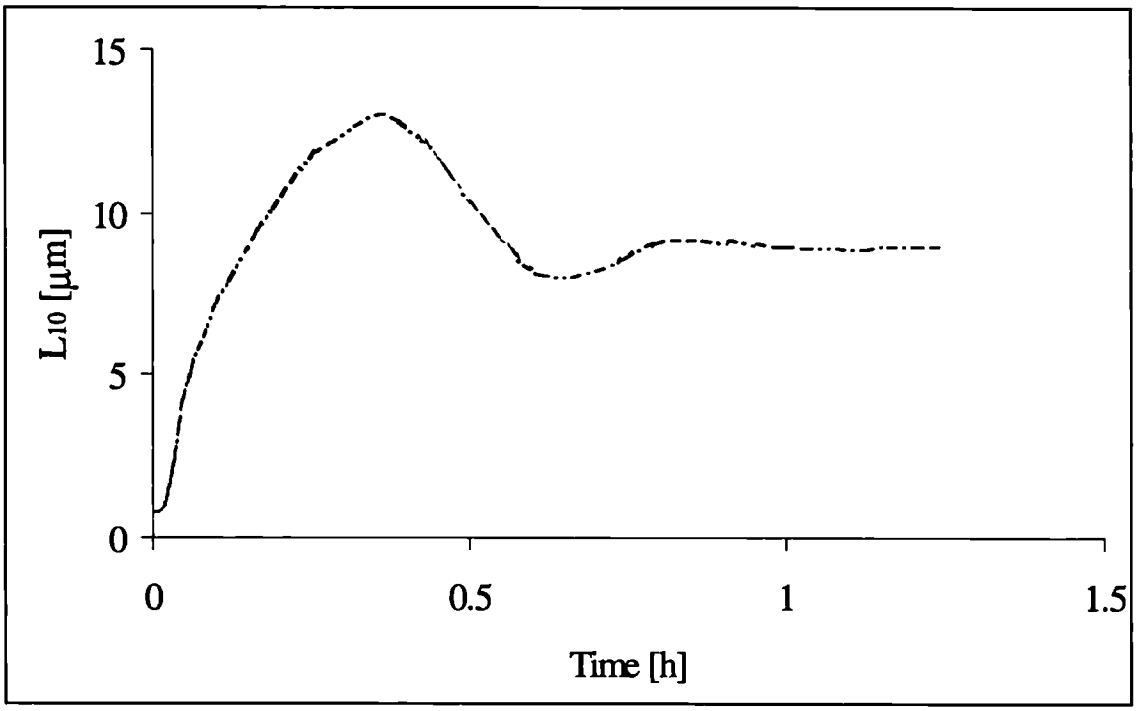

Figure 5.4 Time-dependence of number mean size

steady state after nine residence times. Another interesting result of the SFM is shown in Figure 5.5. The population density distribution in the reactor changes from the early moments dominated by high (primary) nucleation to a bimodal distribution after about 4.5 residence times and to the final steady-state particle size distribution after ten residence times.

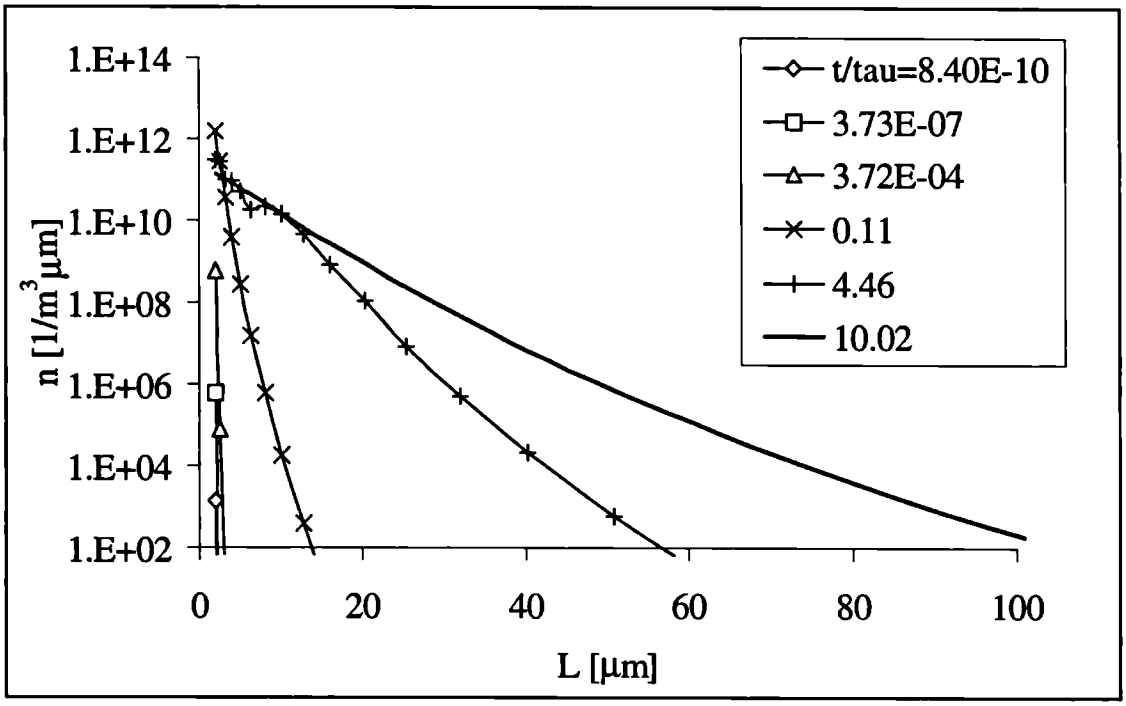

Figure 5.5 Time-dependence of the particle size distribution

Figure 5.6 shows predictions for the overall nucleation rate in the continuous reactor. The micromixing time and mesomixing time vary between 0.004 and 2.05 s and between 0.002 and 1.02 s respectively. Therefore, the volume of the feed zones V_{f1} and V_{f2} covers a range from 0.0002 to 0.1% of the total volume, and the reaction and fast nucleation process take place in a very limited volume around the feed zones, while the slower kinetic processes occur in the bulk zone. This result clearly shows the importance of mixing in systems with very fast or instantaneous reactions.

The nucleation rate shows a maximum under poor micro- and mesomixing conditions. Under very good micromixing conditions (diffusion is not limiting), the nucleation rates show a maximum at medium mesomixing times. One explanation for this observation could be that, on the one hand, the level of supersaturation becomes uniform very quickly at very low mesomixing times and therefore does not cause excessive nucleation, and on the other, that the reaction zone remains very small at very high mesomixing times and therefore restricts nucleation to a very limited zone and retards nucleation. Under conditions in between, however, the nucleation rate can

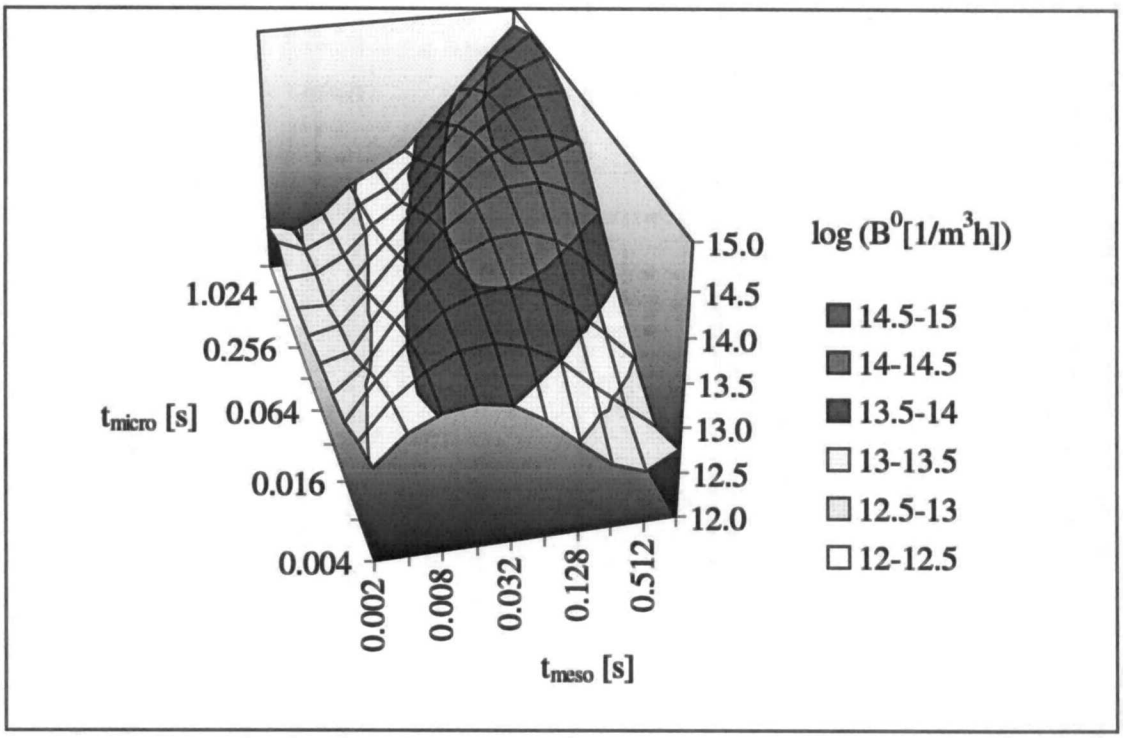

Figure 5.6 Dependence of the nucleation rate on the mixing conditions

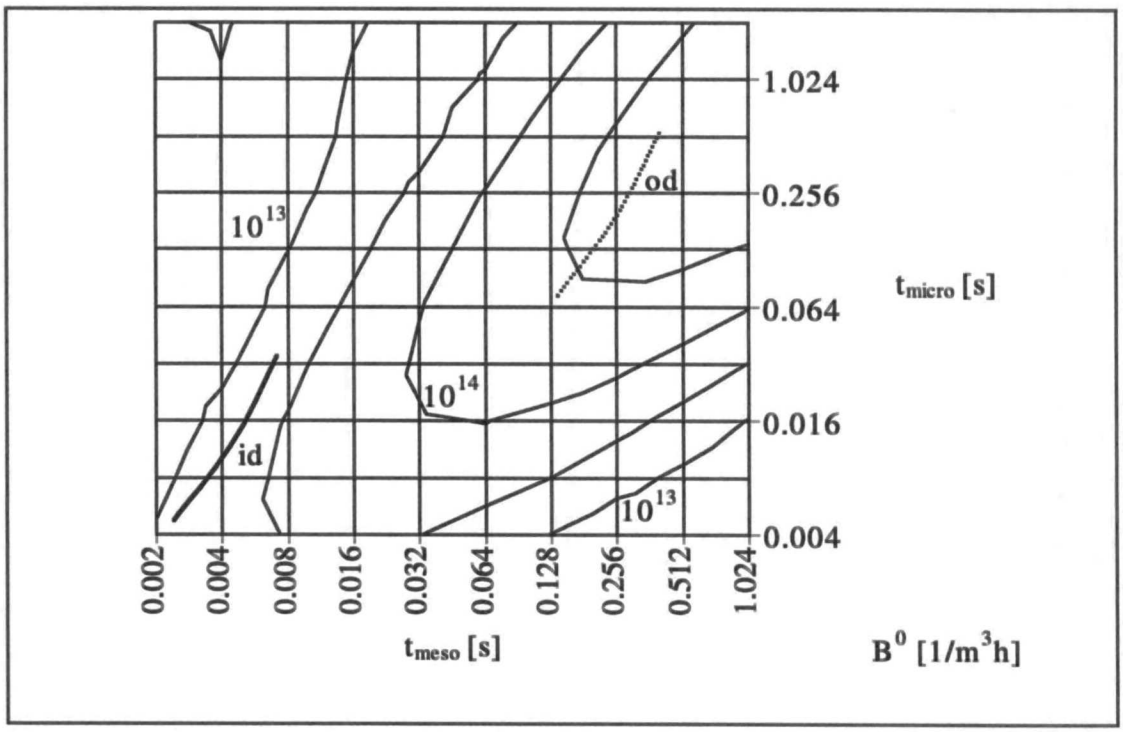

Figure 5.7 Two-dimensional projection of Figure 5.6

increase to a maximum. The same applies to mean mesomixing times. In this case, the nucleation rate exhibits a maximum for mean micromixing times. David and Marcant (1994) observed the same behaviour in their model for double-jet semibatch precipitation.

A two-dimensional plot of Figure 5.6 gives Figure 5.7 with iso-nucleation curves. Additionally, two different feed point positions (id and od) show the influence of the feed point on the nucleation rate in a qualitative way.

5.6 COMBINED MACROMIXING AND MICROMIXING MODELS

If the residence time distribution deviates from that of an ideally mixed reactor, both micro- and mesomixing and also macromixing have to be accounted for. This can be achieved by combining a micromixing model, for example the Segregated Feed Model SFM, and a macromixing model, for example a network of ideal reactors. In Figure 5.8, such a combination of mixing models is illustrated. In this example of a combined model, the two feed solutions enter the first reactor, which is not fully micro- and mesomixed. Thus, this reactor is divided into feed zones and a bulk compartment according to the Segregated Feed Model SFM. The series of four reactors represents a typical reaction-engineering model accounting for the deviation from the residence time distribution of an ideal continuously stirred tank reactor (CSTR).

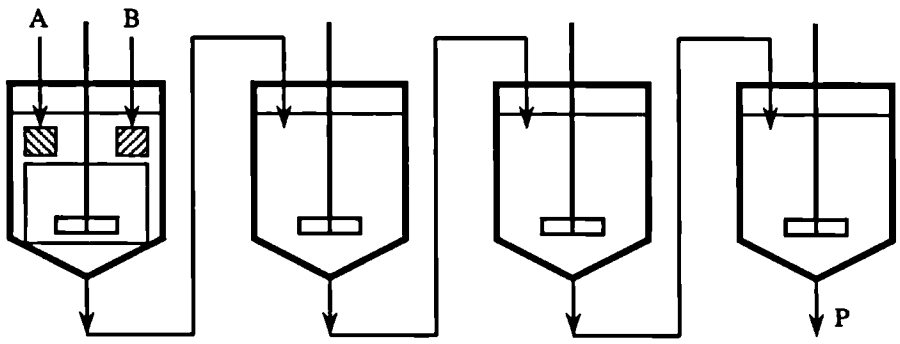

Figure 5.8 Example of a combined macro-meso-micromixing model

A listing of the FORTRAN program for the Segregated Feed Model can be found in Appendix A5.4.

5.7 DETERMINATION OF MIXING TIMES USING COMPUTATIONAL FLUID DYNAMICS (CFD)

5.7.1 INTRODUCTION

Computational Fluid Dynamics (CFD) is the numerical analysis of systems involving transport processes by computer simulation. Elementary equations which describe the conservation of mass, momentum and energy for fluid flow or heat transfer are solved for a number of subregions of the flow field (Versteeg and Malalasekera, 1995). Various companies provide ready-to-use CFD codes to perform this task and usually offer a choice of solution methods, model equations (for example turbulence models for turbulent flow or combustion models for combustion processes) and visualisation tools. One of these codes is CFX 4.1 from AEA Harwell, which was used for the CFD calculations in this chapter.

5.7.2 ELEMENTS OF A CFD CODE

All commercially available CFD codes have three main elements in common.

Firstly, the **pre-processor** enables the user to define the geometry, which is often referred to as the computational domain or flow domain of the problem, for example, of a stirred vessel. The geometry can be created either by using the mesh generation facilities of the code or by converting an external file (*e.g.* a Computer Aided Design (CAD) file), and consists of a number of blocks which form the actual geometric layout of the problem. By subdividing the blocks into smaller regions, a grid of computational cells is obtained. The number of grid cells determines the complexity of the problem. A very fine grid resolves the local gradients of the flow variables very accurately, gives a very large number of cells and therefore slows down the simulation. On the other hand, a coarse grid consists of less grid cells, but often causes convergence problems of the numerical solution. There are no hard and fast rules as to how fine the grid has to be made, but it must be ensured that the solution is "grid-independent", *i.e.* that a further refinement of the grid has no influence on the results of the simulation.

Secondly, the **solver** performs the actual calculation of the numerical solution. Three different solution methods can be distinguished:

- finite difference (Smith, 1985)
- finite element (Zienkiewitz and Taylor, 1991)

- spectral techniques (Gottlieb and Orszag, 1977).

CFX 4.1 uses the finite volume method, which is nowadays by far the most common method for solving fluid flow problems (Versteeg and Malalasekera, 1995). The balance equations are solved for each grid cell using an iterative solution approach, as the underlying physical phenomena are complex.

Finally, the **post-processor** helps to visualise the huge amount of data produced by the flow solver. Vector, contour and shaded contour plots of the velocity field, the energy dissipation distribution or other variable fields can be plotted for lines, cross sections or surfaces of the geometry. Some packages even offer particle tracing facilities and animation for transient problems.

5.7.3 SIMULATIONS OF THE FLUID DYNAMICS IN A STIRRED TANK

Stirred tanks are the most common form of chemical reactors. Nevertheless, due to high local gradients of the energy dissipation, the fluid dynamics are not well understood and depend to a large extent on the geometry of the reactor. Different forms of impellers, baffles and draft tubes can produce very different flow fields.

As a stirred tank contains a moving impeller, the fluid cells surrounding the impeller are modelled as rotating blocks in CFD (Bakker *et al.*, 1997). A sliding mesh technique was chosen to account for the movement of the rotating impeller grid relative to the surrounding motionless tank cells. Xu and McGrath (1996) compared the sliding mesh simulation results for a stirred tank with experimental Laser Doppler Anemometry (LDA) data and found that the data corresponded very well. An alternative to the sliding mesh technique is the momentum source model, where the impeller region is modelled as a black-box source of momentum. In this case, however, experimental data concerning the forces acting on the impeller are necessary. Furthermore, no local data in the impeller region can be obtained (black box) when using the momentum source model. For a sliding mesh simulation, on the other hand, no experimental data are necessary and the flow field in the vicinity of the impeller is readily obtained.

Guichardon *et al.* (1994) studied the energy dissipation in liquid-solid suspensions and did not observe any effect of the particles on micromixing for solids concentrations up to 5%. The precipitation experiments in this research were carried out

for solids concentrations in the range from 0.1 to 5 %. Therefore, the stirred tank is modelled as a single-phase isothermal system, *i.e.* only the hydrodynamics of the reactor are simulated. The conservation equations for mass (continuity equation)

$$\frac{D\rho}{Dt} + \rho \nabla v = 0 \tag{5.48}$$

and momentum (Navier-Stokes equations for incompressible flow with constant viscosity)

$$\rho \frac{Dv}{Dt} = \rho g - \nabla p + \mu \Delta v \tag{5.49}$$

are valid for both laminar and turbulent flow. Theoretically, it is possible to solve this set of equations for the latter by Direct Numerical Solution (DNS). However, as a very high resolution in both time and space is necessary to account for the turbulent fluctuations, the computational problem usually becomes very complex and can only be solved for low Reynolds numbers and simple geometries of the flow domain. Thus, in an alternative approach the variables will be represented by their time average $\bar{v}$ and their fluctuation component v'(Reynolds decomposition)

$$v = \bar{v} + v' \tag{5.50}.$$

Consequently, six additional unknowns, the Reynolds stresses $-\rho\overline{v_i' v_j'}$, are obtained and the equations for turbulent flow become

$$\frac{D\rho}{Dt} + \rho \nabla \bar{v} = 0 \tag{5.51}$$

$$\rho \frac{D\bar{v}}{Dt} = \rho g - \nabla p + \nabla \tau \tag{5.52}$$

with $$\tau_{ij} = \mu \frac{d\bar{v}_i}{dx_j} - \rho\overline{v_i' v_j'} \tag{5.53}.$$

Using turbulence models, this new system of equations can be closed. The most widely used turbulence model is the k-ε-model, which is based on an analogy of viscous and Reynolds stresses. Two additional transport equations for the turbulent kinetic energy k and the turbulent energy dissipation ε describe the influence of turbulence:

$$\mu_t = \rho C_\mu \frac{k^2}{\varepsilon} \qquad \text{(eddy viscosity)} \tag{5.54}$$

and $$-\rho\overline{v_i'v_j'} = 2\mu_t E_{ij} - \frac{2}{3}\rho k\delta_{ij} \qquad (5.55)$$

(extended Boussinesq relationship)

with $$E_{ij} = \frac{1}{2}\left[\frac{\partial\overline{v}_i}{\partial x_j} + \frac{\partial\overline{v}_j}{\partial x_i}\right] \qquad (5.56).$$

In these model equations it is assumed that turbulence is isotropic, *i.e.* it has no favoured direction. The k-ε model frequently offers a good compromise between computational economy and accuracy of the solution. It has been used successfully to model stirred tanks under turbulent conditions (Ranade, 1997). Manninen and Syrjänen (1998) modelled turbulent flow in stirred tanks and tested and compared different turbulence models. They found that the standard k-ε model predicted the experimentally measured flow pattern best.

More advanced models, for example the Algebraic Stress Model (ASM) and the Reynolds stress model (RSM), are not based on the eddy-viscosity concept and can thus account for anisotropic turbulence. In addition to the transport equations, however, the algebraic equations for the Reynolds stress tensor also have to be solved. These models are therefore computationally far more complex than simple closure models (Kuipers and Swaaij, 1997).

When using large eddy simulation (LES), the computational mesh is chosen in such a way that it resolves large scale turbulent eddies. As a direct consequence, only the small-scale turbulence, which is isotropic and can be specified quite easily, has to be modelled with a closure model. LES is therefore a stage between simulations using the closure models mentioned above and the Direct Numerical Solution (DNS) which resolves even small-scale fluctuations of the turbulent motion. Due to the high resolution of the grid, LES is still computationally very demanding.

5.7.4 CALCULATION OF LOCAL MICROMIXING TIMES

One of the great advantages of CFD is that local data for the fluid velocity v and energy dissipation ε can be obtained. As the local energy dissipation is a measure of the degree of local micromixing in the reactor, the micromixing time can be calculated directly from this parameter using Equation (5.2).

5.7.5 GRID GENERATION

When using CFD, generating the geometry and subsequently the grid of the flow domain is the first and often most time-consuming step of the procedure. As mentioned earlier, the geometry and grid can be generated using mesh-generating software provided by the CFD code supplier. In this research, MESHBUILD from CFX was used.

The set-up of the continuous experiments consisted of a draft tube baffled (DTB) reactor and a marine-type propeller. In order to account for the rotation of the impeller, the zone surrounding the propeller was modelled using a sliding mesh approach. After generating the geometry of the reactor, the flow domain was further divided into grid cells. The density of the grid must be chosen such that the final solution of the CFD problem becomes grid-independent, *i.e.* no longer depends on the size and number of grid cells for which the equations were solved. Grid-independence was established for all the problems solved in this research by stepwise and/or local refining of the grid until the solution for the energy dissipation of a grid cell close to the impeller no longer changed by more than 1%.

The grid for the semibatch reactor was generated in the same way. Three different types of impeller, a Rushton turbine, a 45°-pitched blade turbine and a propeller were defined as groups and implemented in the geometry.

As the reactors on different scales are geometrically similar, the geometry of the small-scale flow domain was used for the larger scales and the number of grid cells was increased according to the criterion of grid-independence. As the large-scale DTB vessels have a slightly different geometry from the small-scale 300 ml vessel, their geometry was created independently of the small-scale flow domain. The number of grid cells varied between 8640 (small-scale reactor) and 256,128 (large-scale DTB reactor).

5.7.6 SOLVER OPTIONS

The command file includes the actual options of solution method, turbulence model, physical data and other information relevant to solving the problem. The hydrodynamics were solved as a transient problem using a k-ε turbulence model. By monitoring the residuals of mass, energy dissipation and velocities, convergence of the solution was checked. After a number of time steps and iterations, equivalent to about

ten rotations of the impeller, steady state was achieved. A sample command file of the CFD simulations is listed in Appendix A5.2.

5.7.7 RESULTS

Geometry and flow pattern

Figure 5.9 shows the geometry and flow pattern obtained from simulations of a DTB reactor (4.3 l, 100 rpm). The four baffles and the draft tube are represented as solid walls of infinitely small thickness, while the three-dimensional structure of the propeller blades is accounted for by dividing each blade into a number of plane segments. The flow map in a plane through the shaft of the impeller shows that the highest velocities occur in the impeller zone in both the axial and the tangential direction, while in the upper part of the vessel the flow becomes predominately axial, due to the guiding effect of the baffles and the draft tube.

For the semibatch experiments a baffled reactor with different impellers was used. Figure 5.10 depicts the geometric set-up with a six-bladed Rushton turbine. The reactor contains four baffles, but no draft tube. At the level of the impeller, the velocity components in the radial and the tangential direction dominate, leading to large eddies above and below the impeller zone. The flow pattern obtained by the CFD simulations corresponds very well to experimental flow patterns (Myerson, 1993 and Mersmann *et al.*, 1994).

The flow field produced by a 45°-pitched blade turbine appears uniform and has less steep gradients in the velocity field (Figure 5.11). Between the impeller and the baffles, recirculation zones form which lead to an increased axial flow in the reactor. Below the impeller, however, a "dead" zone with low velocities might cause unwanted deposition of particles during precipitation.

The propeller (marine-type axial impeller) produces a very even flow pattern throughout the reactor (Figure 5.12). No secondary recirculations or dead zones occur, and even in the upper part of the reactor remote from the impeller a smooth flow pattern is generated. Being an axial-type impeller, the propeller has the highest pumping capacity, producing the most efficient fluid circulation of the three impellers investigated. The *Re* number for the stirred tanks simulated varied between 8400 and 1.3×10^6, leading to turbulent conditions in every case.

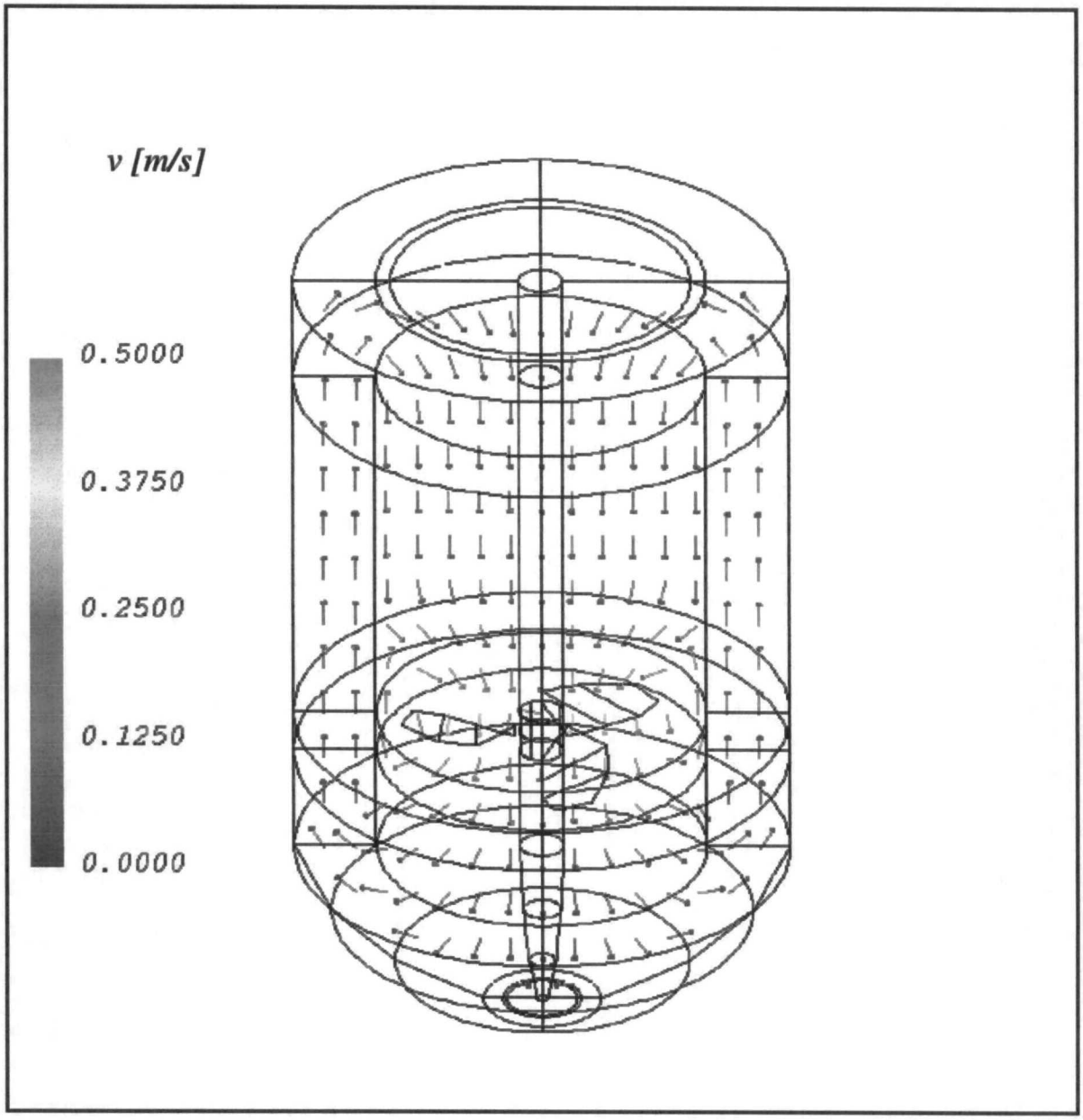

Figure 5.9 Geometry and velocity field in a draft tube baffled (DTB) reactor equipped with a propeller (4.3 l, 100 rpm)

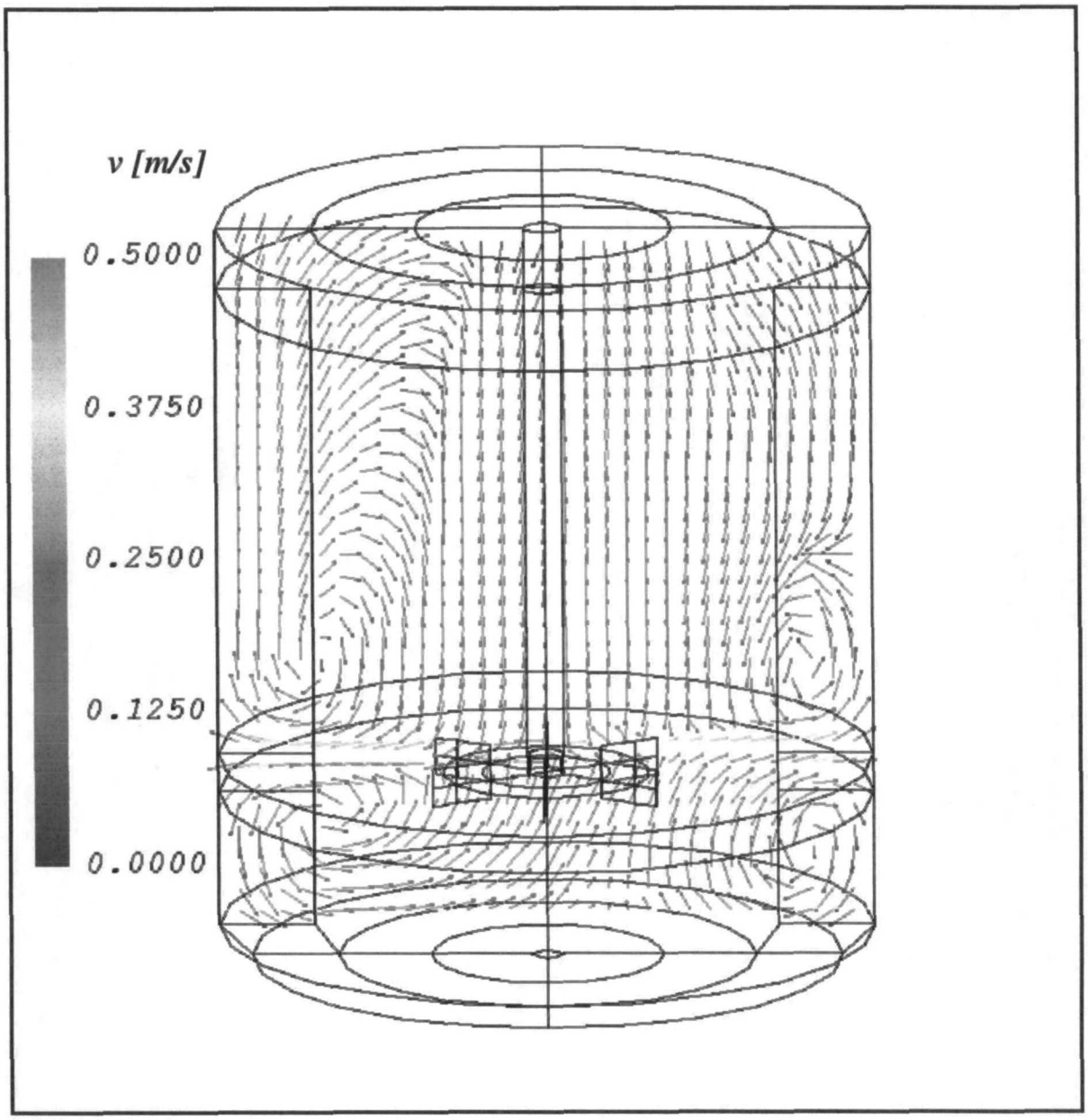

Figure 5.10 Geometry and velocity field in baffled reactor equipped with a Rushton turbine (1 l, 500 rpm)

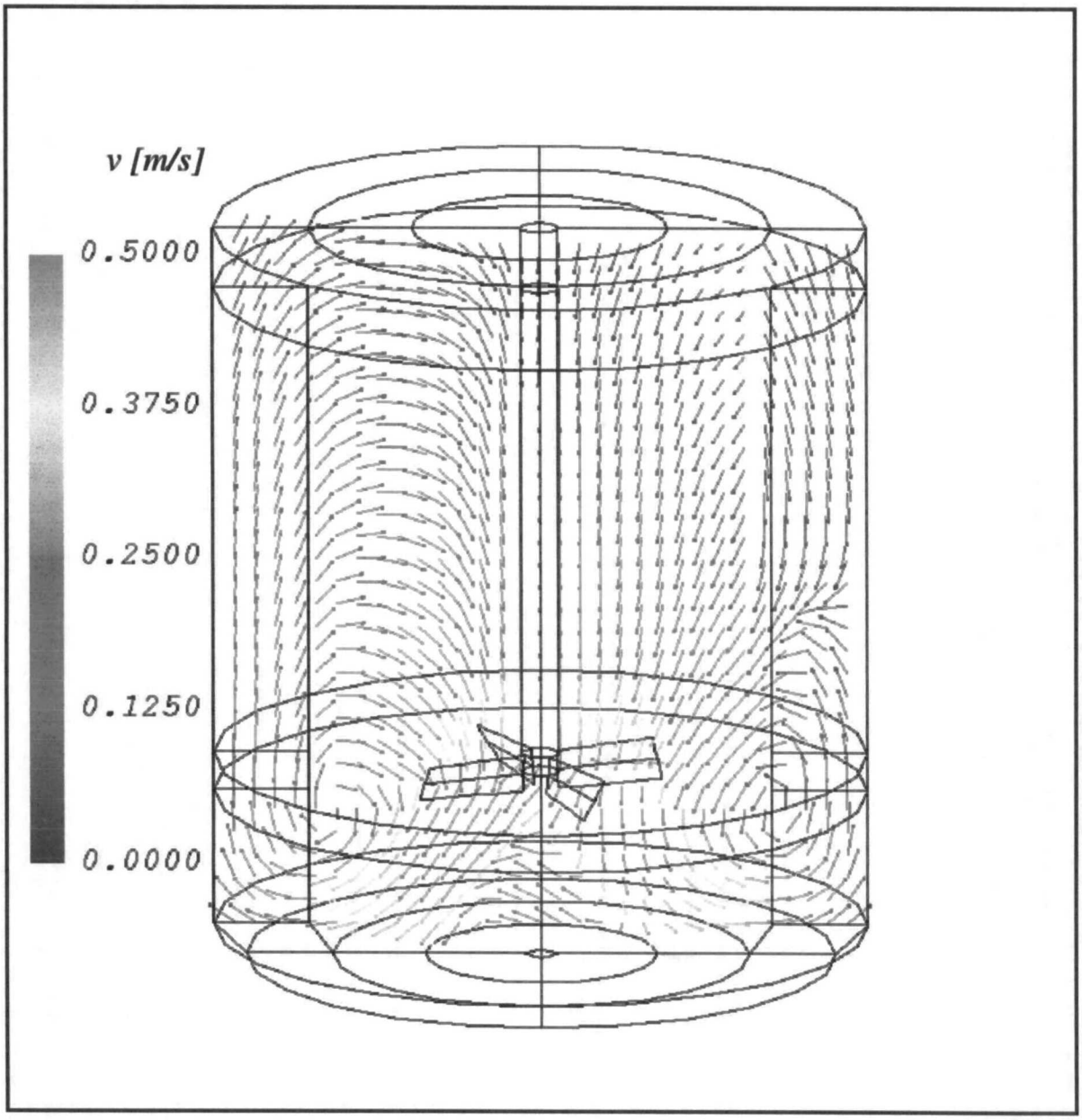

Figure 5.11 Geometry and velocity field in baffled reactor equipped with a 45°-pitched blade turbine (1 l, 500 rpm)

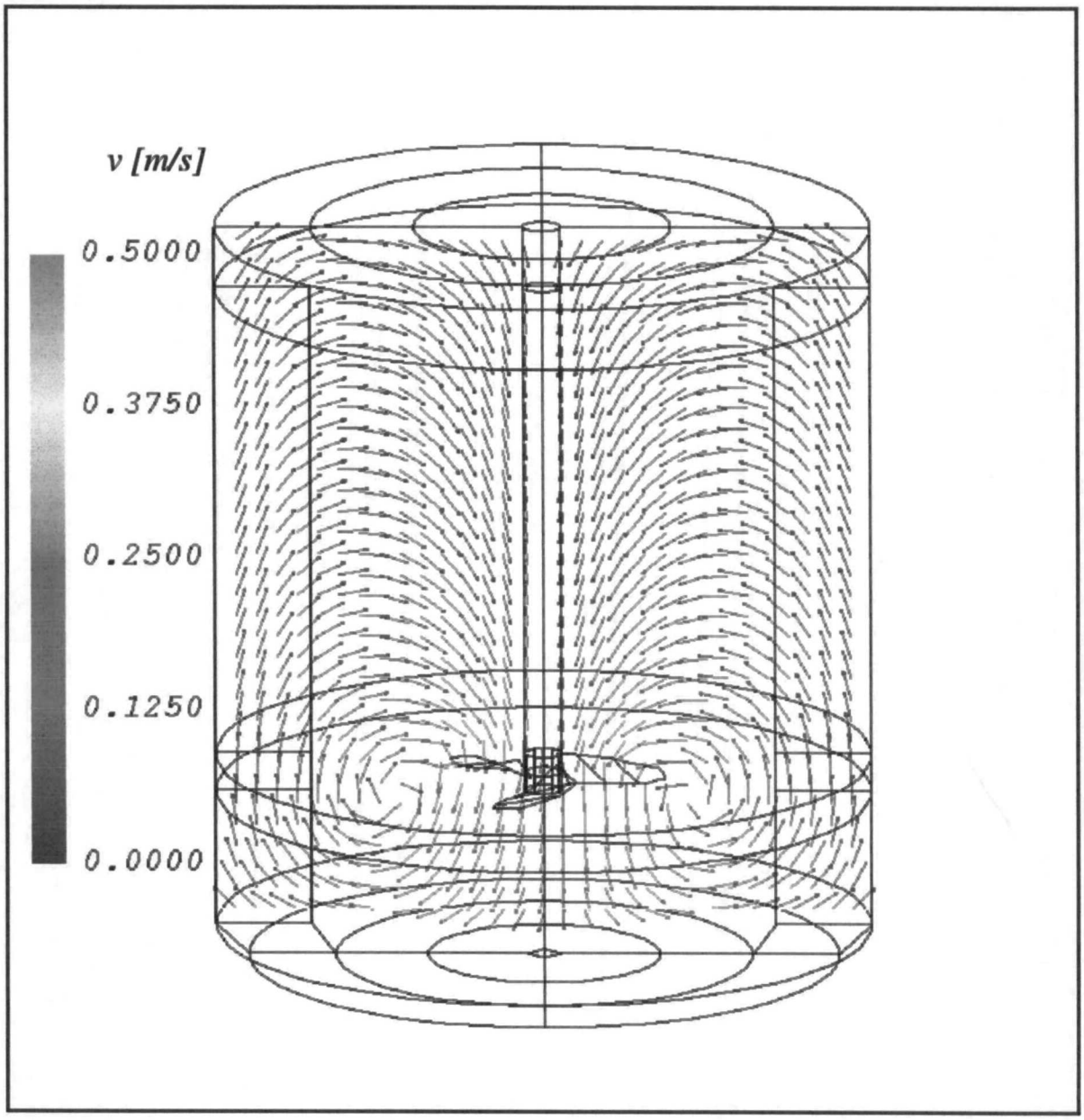

Figure 5.12 Geometry and velocity field in baffled reactor equipped with a marine-type impeller (propeller) (1 l, 500 rpm)

Energy dissipation

The importance of energy dissipation in micromixing has already been referred to earlier in this chapter. In order to find the micromixing times in the feed zones and the mesomixing time characteristic of blending of the feed solutions with the bulk in the Segregated Feed Model, it is essential to determine the local distribution of the specific energy dissipation in the reactor. Using CFD, it is possible to obtain this local distribution and find the diffusive and convective exchange parameters.

When scaling up mixing operations, it has been observed that the shear rate distribution, and therefore the local energy distribution, changes with scale-up (Oldshue, 1985). With larger scales, the maximum shear rate in the impeller zone increases while the average shear rate in this zone decreases. Therefore, even when scaling up with constant power input per unit volume, the flow field looks different for different scales of operation. This effect was observed in the CFD simulations of this research. Figure 5.13 to 5.15 show the field of energy dissipation in a horizontal plane through the impeller for a 1 l, 5 l and 25 l vessel each equipped with a Rushton turbine with all three vessels having the same mean specific power input. For the larger vessels, higher local maxima of the shear rate of up to 8.6 W/kg occur compared to maxima of 5.2 W/kg at the 1 l scale. This difference in the energy distribution leads to different micromixing times on different scales for the *same* mean specific power input.

Figure 5.16 shows the local variations in the energy dissipation in a vertical plane through the axis of the impeller shaft. The energy very quickly dissipates further away from the Rushton turbine leading to zones with significantly lower local energy dissipation. These results are in accordance with the experimental findings of Geisler *et al.* (1991) and Mersmann *et al.* (1994), who determined flow maps for different geometrical set-ups using Laser Doppler Anemometry (LDA). In their LDA experiments, the authors observed a similar shape of the zone with high energy dissipation around the impeller and levels of low energy dissipation in the upper part of the vessel. For example, the zone of $\varepsilon_{loc}/\varepsilon_{avg} = 3.0$ in this study and in that of Mersmann *et al.* (1994) are similar in both size and shape.

Appendix A5.1 summarises the results for the local energy dissipation and mixing times for different geometries, stirrer speeds and feed point positions.

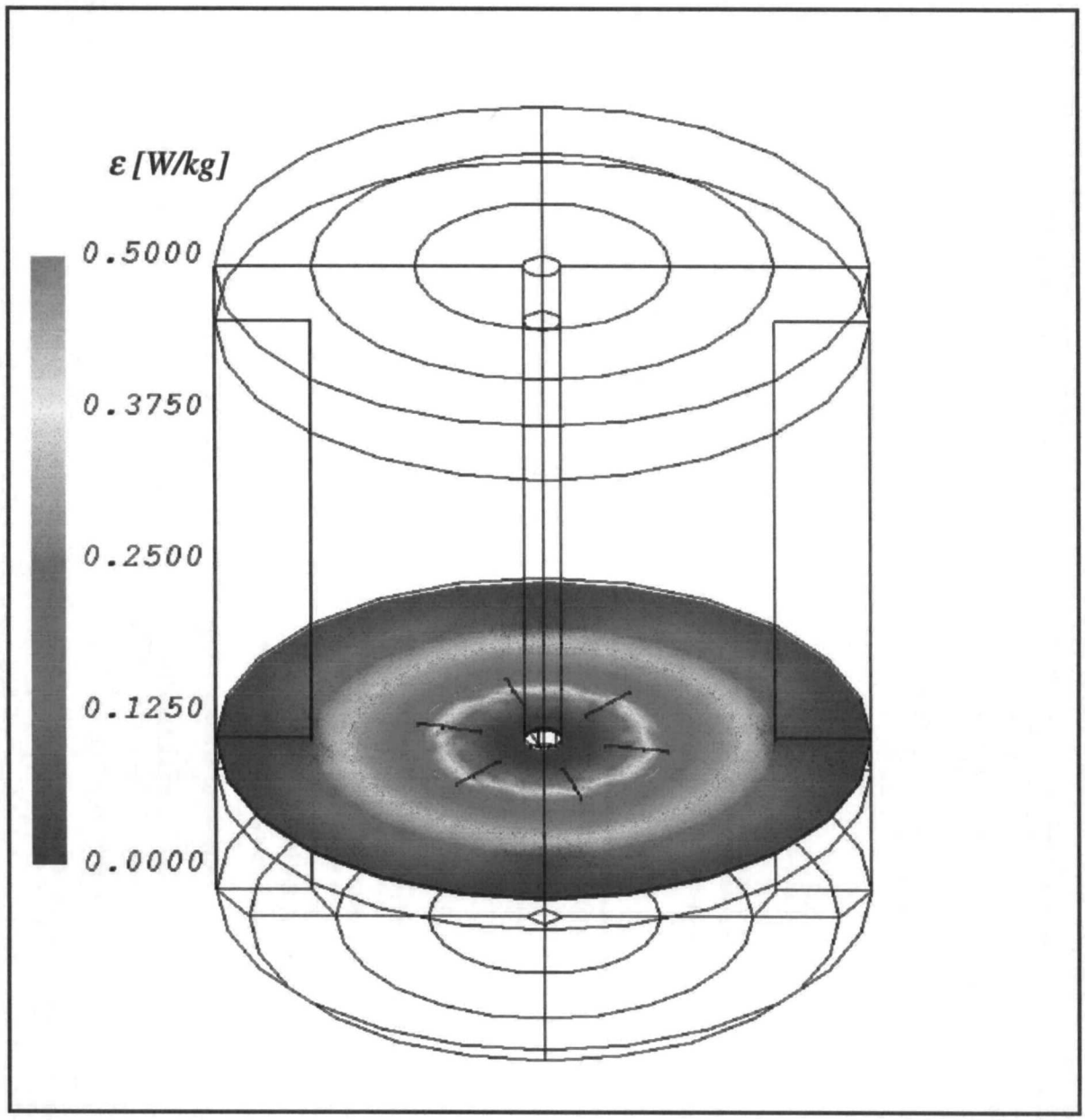

Figure 5.13 Local energy dissipation in baffled reactor equipped with a Rushton turbine (1 l, 461 rpm)

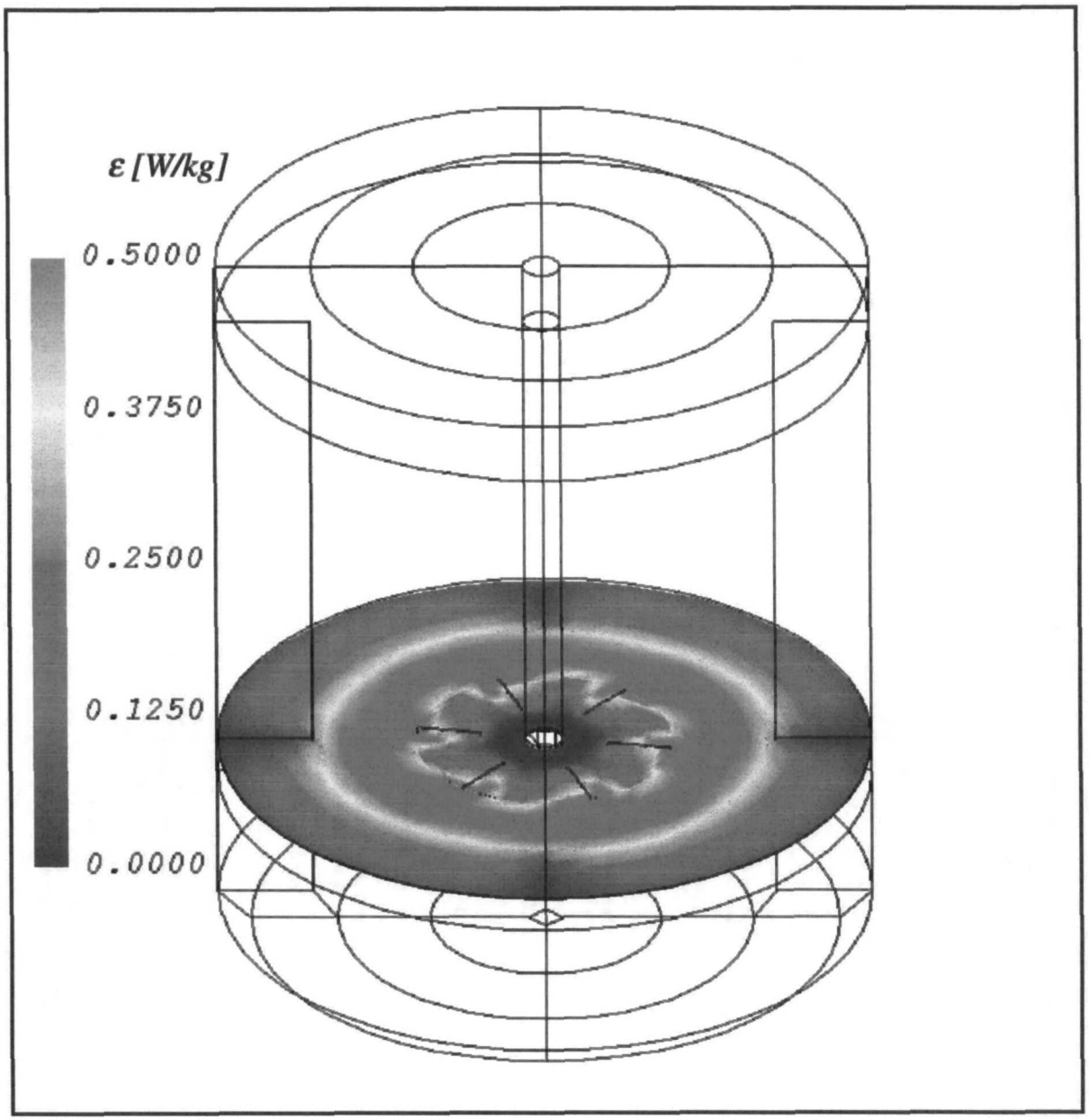

Figure 5.14 Local energy dissipation in baffled reactor equipped with a Rushton turbine (5 l, 351 rpm)

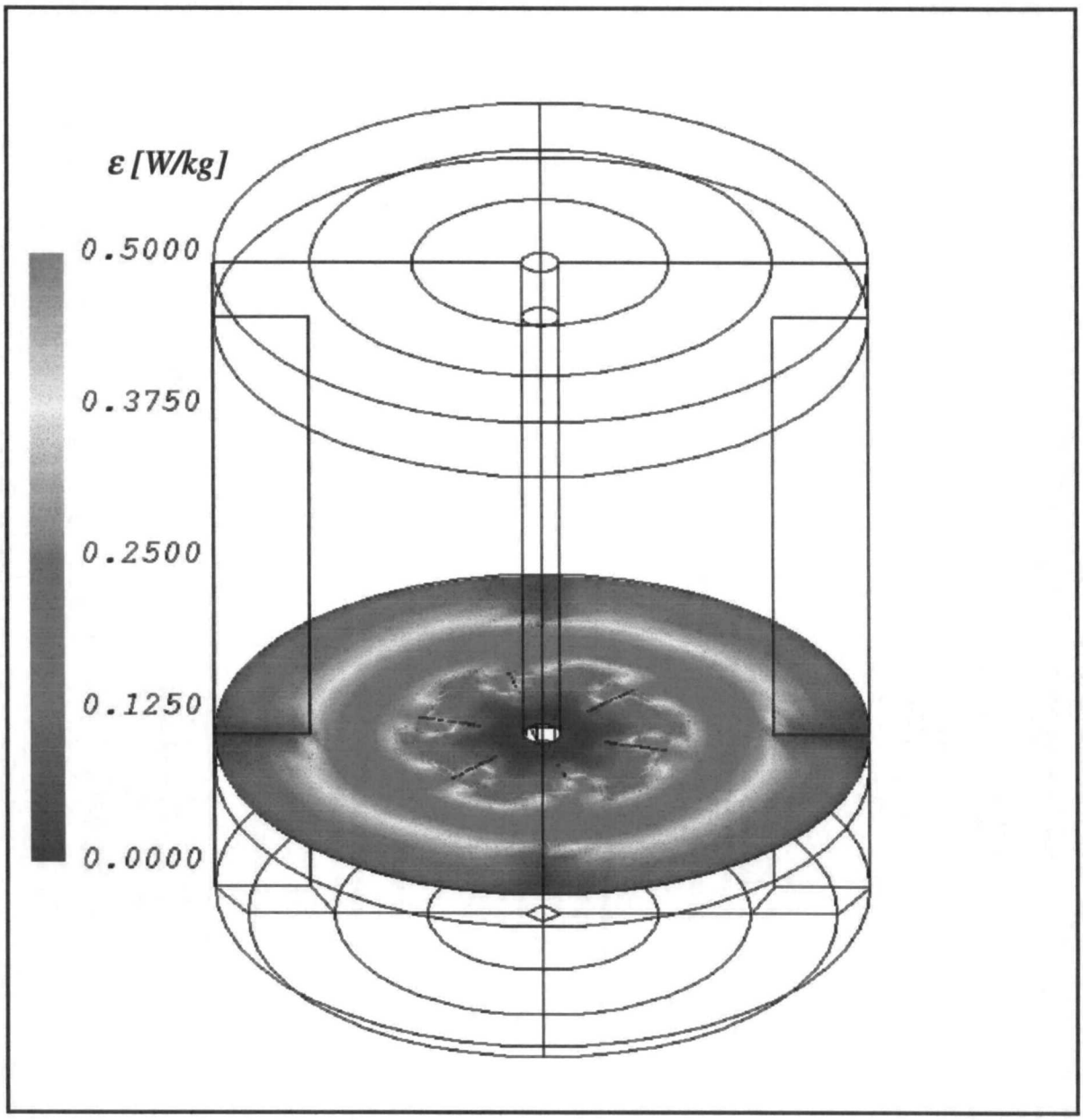

Figure 5.15 Local energy dissipation in baffled reactor equipped with a Rushton turbine (25 l, 250 rpm)

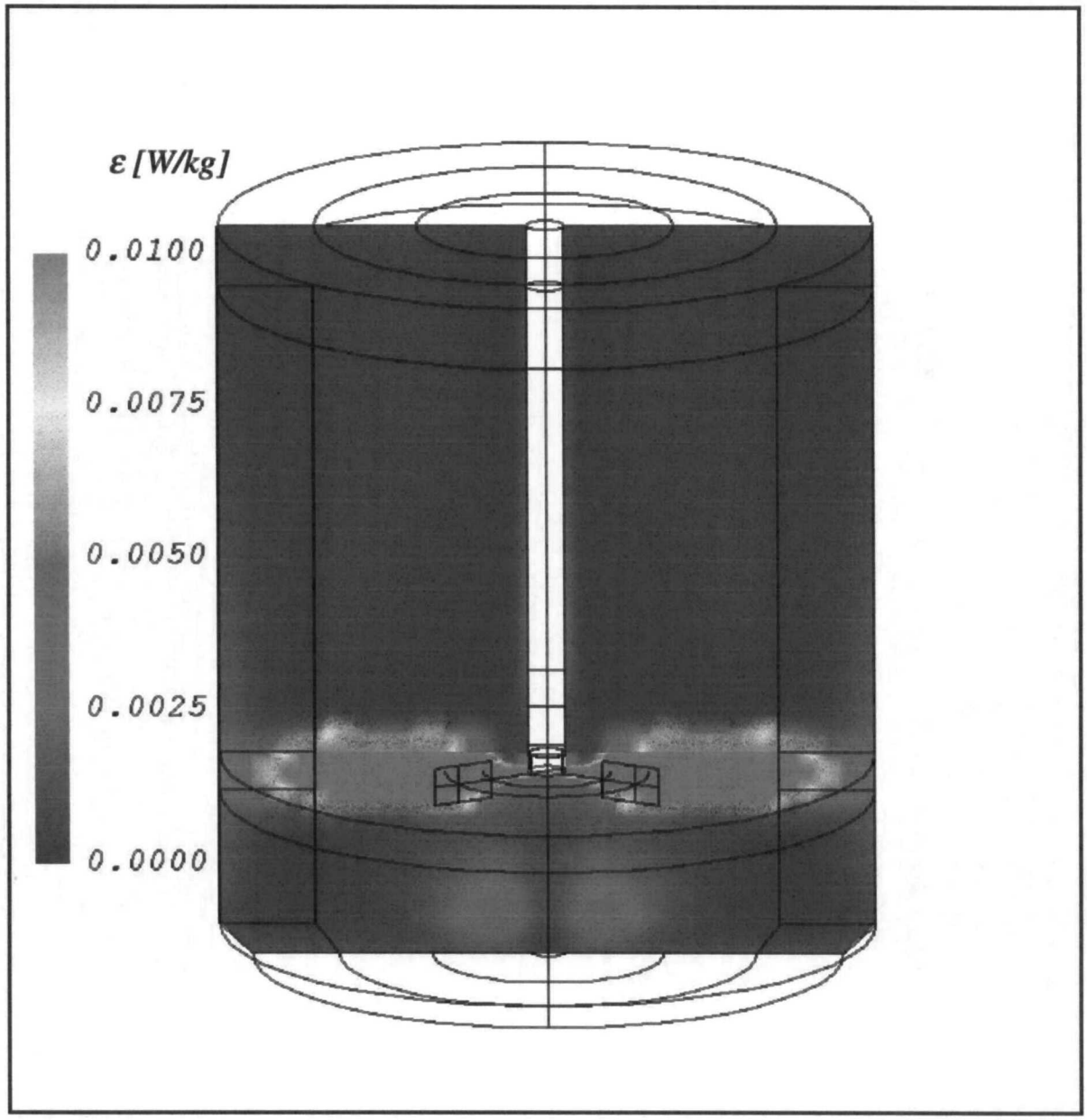

Figure 5.16 Local energy dissipation in baffled reactor equipped with a Rushton turbine (1 l, 100 rpm)

Micromixing and mesomixing times

The micromixing and mesomixing times were determined from the local energy dissipation at the feed points. The micromixing times calculated vary between 0.0014 s and 1.73 s and the mesomixing times between 0.0063 s and 19.6 s depending on the geometry, scale, stirrer speed and feed point position. Because the local energy dissipation is different on different scales of operation with the same mean specific power input, the micromixing (diffusion) and mesomixing (convection) times on different scales differ. Consequently, different diffusive and convective mass transfer between the feed zones and the bulk zone leads to different levels of supersaturation on different scales and therefore to different precipitation kinetic rates and mean crystal sizes with scale-up.

With the high accuracy and local resolution of flow variables obtained using CFD, the mixing times can be determined and used in the Segregated Feed Model (SFM). Furthermore, dead zones in the reactor can be located and avoided by simple geometric modifications.

CHAPTER 6

SCALE-UP OF CONTINUOUS PRECIPITATION – EXPERIMENTAL AND MODELLING RESULTS

6.1 INTRODUCTION

After a discussion of the apparatus, the experimental conditions will be chosen and the experimental results of the 4.3 l and 12 l reactors will be compared with the simulation data obtained using the Segregated Feed Model (SFM) and Computational Fluid Dynamics (CFD). The suitability of "design of experiments" (DOE) as already discussed in Chapter 4 for reducing the number of scale-up experiments as an alternative to the mixing model will be investigated, thus representing a more empirical scale-up approach.

6.2 EXPERIMENTAL SET-UP AND PROCEDURE

The experimental set-up (Figure 6.1) used for the large-scale experiments is similar to that used for the determination of the precipitation kinetics on the 300 ml scale as described in Chapter 4.6. The only differences between the two set-ups are the reactor itself and the size of the tubing. In order to achieve the same residence times on different scales, the diameter of the tubing and flow rate through the pumps must be increased with scale-up.

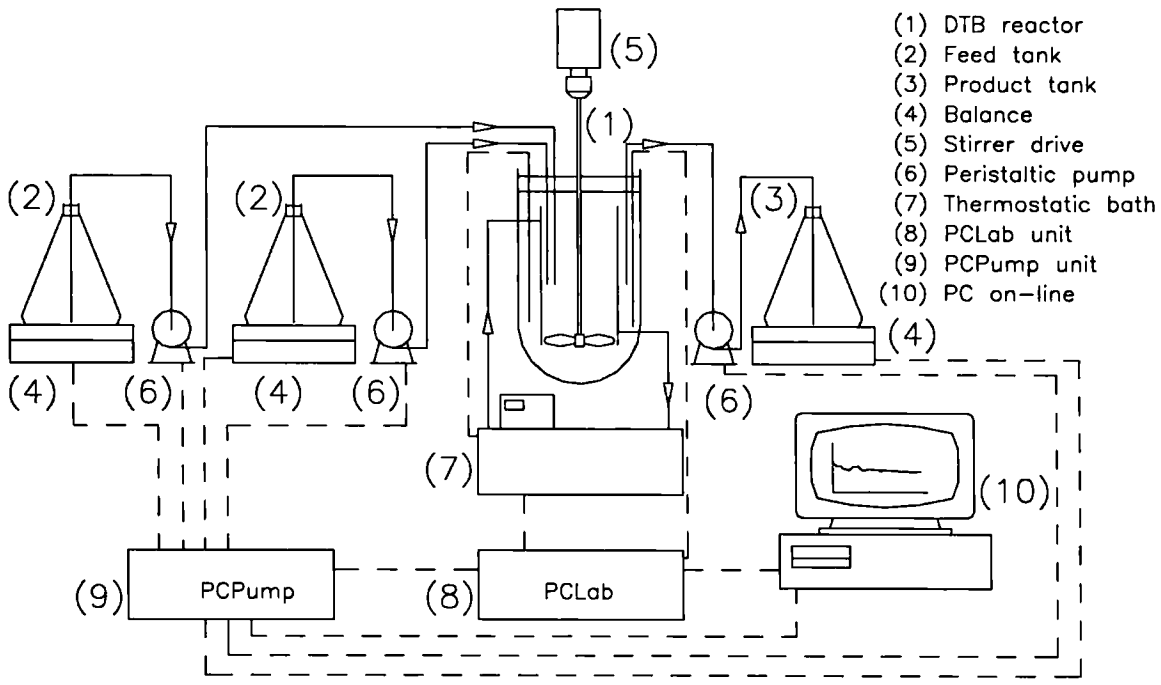

Figure 6.1 Experimental set-up for continuous scale-up experiments

The geometries of the 4.3 l and 12 l precipitation reactors are shown in Figure 6.2. The dimensions in brackets refer to the 4.3 l vessel. The draft tubes of the reactor are hollow in order to allow cooling or heating fluid to circulate. The draft tube, baffles, feed tubes, shaft and impeller are made of stainless steel, while the vessel itself is made of glass. A marine-type impeller (propeller) provides a smooth and even flow field throughout the reactor.

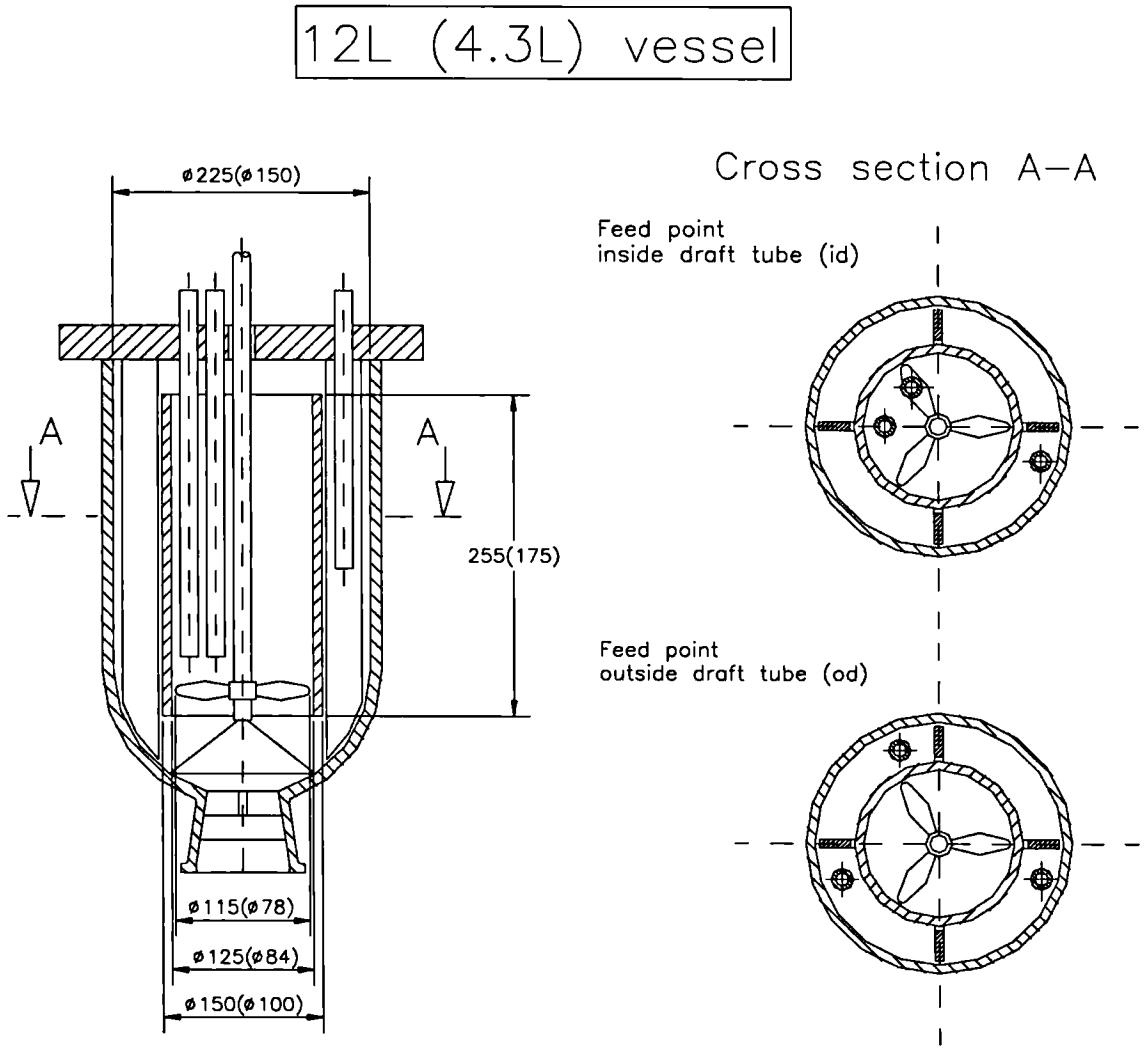

Figure 6.2 Dimensions of the 4.3 l and 12 l large-scale DTB reactors

The experimental procedure for the large-scale continuous experiments is identical to that described in Chapter 4.7 for the small-scale experiments.

The macromixedness of the reactors was determined by measuring the residence time distribution (RTD) in the reactor. As already observed for the 300 ml reactor, the RTD for the large-scale reactors also showed ideal macromixing. Figure 6.3 depicts the RTD for the 12 l reactor at 100 rpm. Even at this low stirrer speed, the response function of the Ca-ion concentration at the outlet follows an exponential decay function. If a non-ideal RTD had been observed, the SFM could have been combined with a compartmental macromixing model as mentioned in Chapter 5.6.

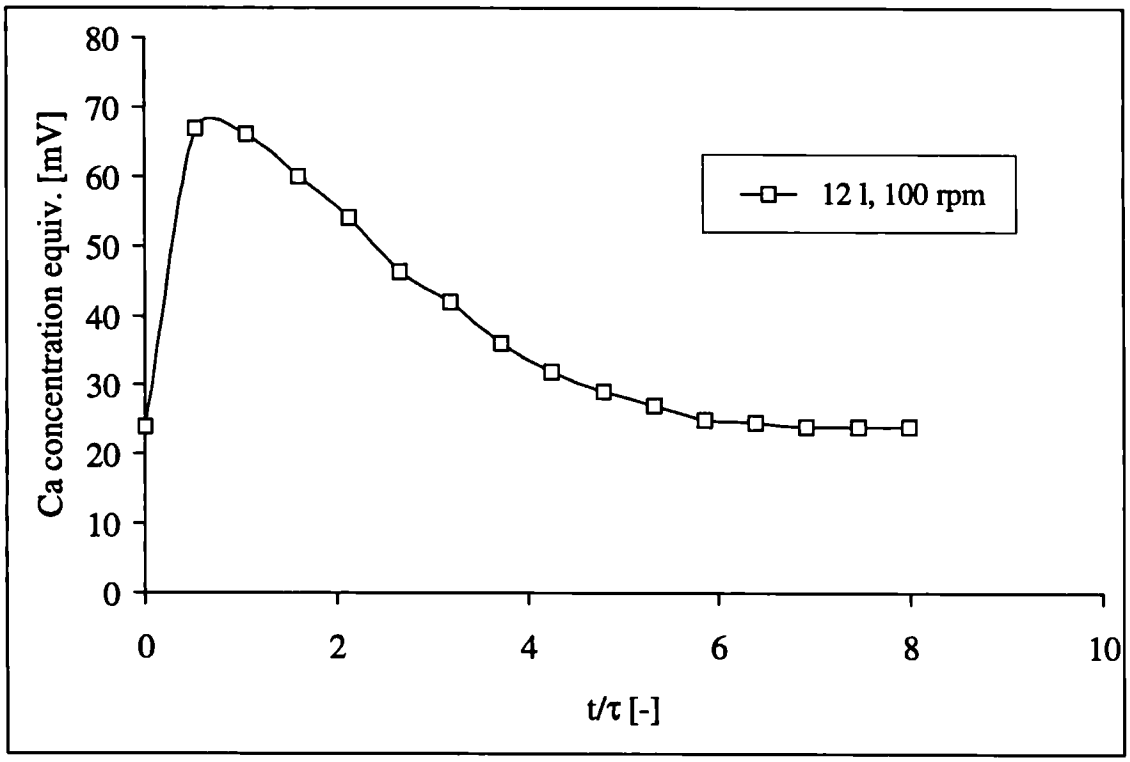

Figure 6.3 Residence time distribution of the 12 l reactor, 100 rpm

6.3 EXPERIMENTAL CONDITIONS

The following sets of conditions were chosen for the large-scale experiments (Table 6.1):

Condition	Set 1	Set 2
Concentration	0.04M	0.01M
Residence time	7.5 min	11 min
Feed point position	inside DT (id)	outside DT (od)

Table 6.1 Experimental conditions for large-scale continuous experiments

The specific power input was varied between 0.0024 and 8.09 W/kg in order to investigate the influence of mixing on scale-up. These parameters cover a wide range and should give a concise picture of the precipitation process under different conditions and on different scales.

6.4 EXPERIMENTAL AND MODELLING RESULTS

6.4.1 MORPHOLOGY

Using the SEM, the morphology of the calcium oxalate precipitate obtained from the large-scale experiments was investigated and compared to that of the small-scale experiments. As in the 300 ml continuous experiments, agglomerated particles of calcium oxalate monohydrate (COM) were observed in the scale-up experiments (Figure 6.4). Unfortunately, the high temperature and vacuum during the SEM sample preparation severely damaged the hydrated needle-like crystals (top right-hand corner of Figure 6.4). An interesting detail is that with this type of agglomerate, where two needles grow into one another, the angle between the two primary crystals is always roughly the same – the two crystals align according to their crystallographic axis.

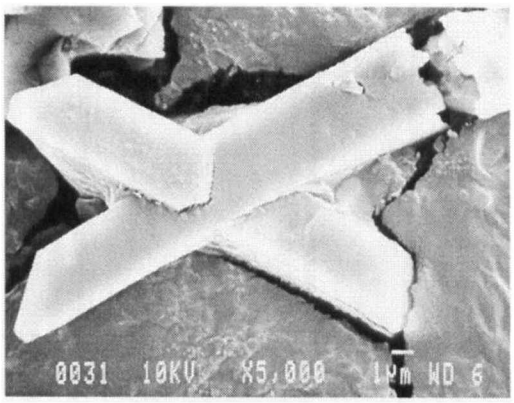

Figure 6.4 Calcium oxalate precipitate from large-scale experiment (12 l, 250 rpm, 0.01M, 11 min, od)

6.4.2 DETERMINATION OF THE MESOMIXING TIME CONSTANT

The mesomixing time, which is the convective exchange parameter in the Segregated Feed Model (SFM), has the form (see Equation (5.1))

$$t_{meso} = A\frac{\varepsilon_{avg}}{\varepsilon_{loc}}\frac{Q^{\frac{1}{3}}}{N^{\frac{4}{3}}d_s}$$

and has already been discussed in Chapter 5. In order to determine the factor A, which is still unknown, a least square fit of the 300 ml continuous calcium oxalate precipitation results for the number mean size and nucleation rate was performed. From these calculations, the factor A was obtained as 17.7, giving the mesomixing time

$$t_{meso} = 17.7\frac{\varepsilon_{avg}}{\varepsilon_{loc}}\frac{Q^{\frac{1}{3}}}{N^{\frac{4}{3}}d_s} \qquad (6.1).$$

6.4.3 SMALL-SCALE RESULTS

Using this result for the mesomixing time, the mean size L_{10} and the nucleation rate B^0 are plotted in Figures 6.5 and 6.6. It should again be mentioned that A was obtained only from small-scale data, *i.e.* without any large-scale information.

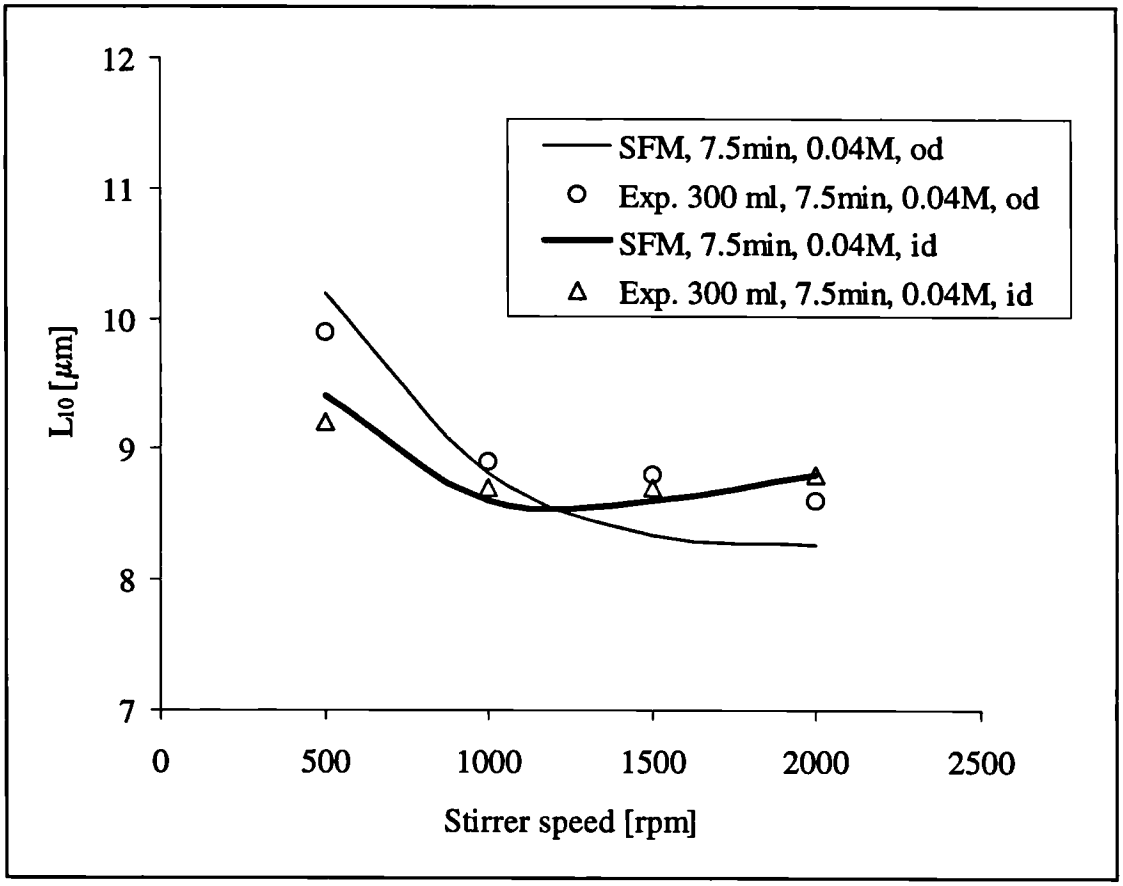

Figure 6.5 Experimental and SFM results for the number mean size (300 ml, 500 to 2000 rpm, 0.04M, 7.5 min, id and od)

Under one set of conditions (300 ml, 0.04M, 7.5 min, id), the number mean size shows a minimum with stirrer speed (Figure 6.5). Under the other set of conditions (300 ml, 0.04M, 7.5 min, od), L_{10} decreases continually with stirrer speed. In both cases, the Segregated Feed Model (SFM) predicts the trend correctly.

The maximum of the nucleation rate, which was experimentally observed under both sets of conditions, was also predicted correctly by the model (Figure 6.6). The maximum occurs due to the interaction of micro- and mesomixing and has already been observed in the qualitative simulations in Chapter 5.

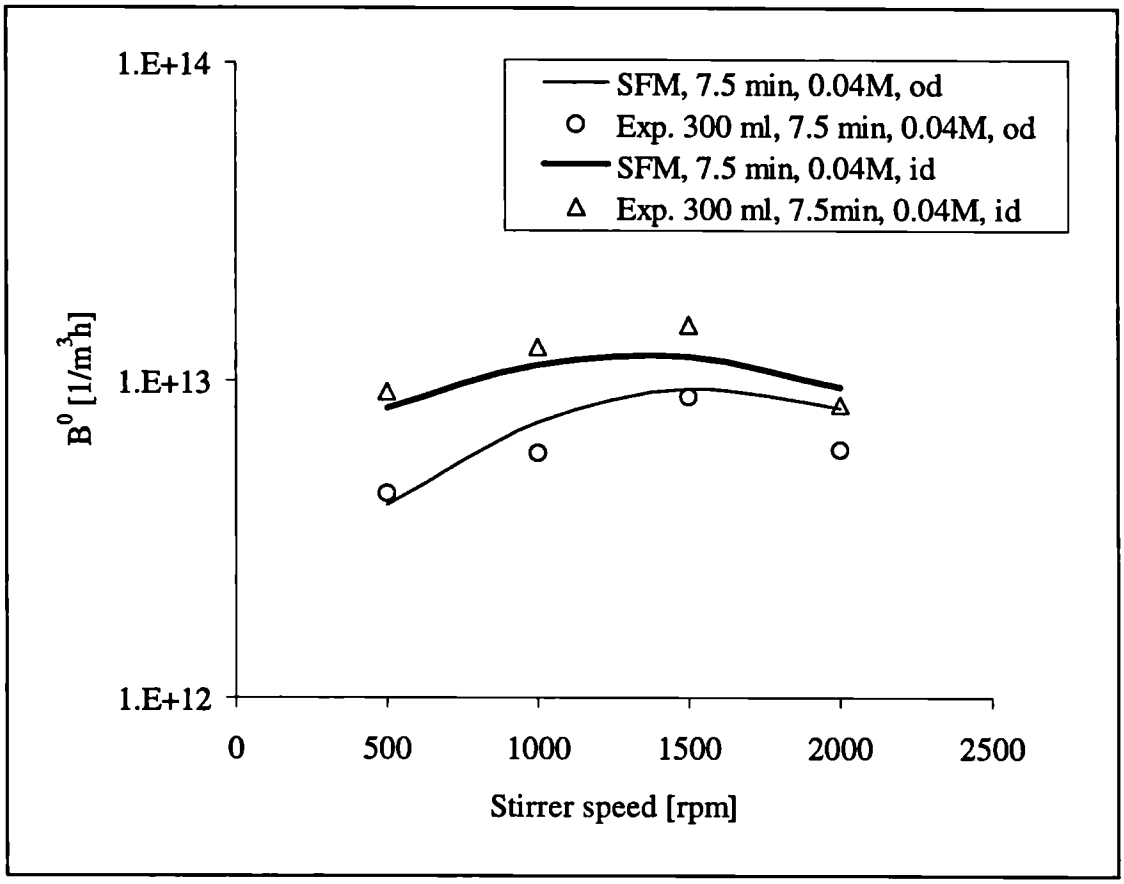

Figure 6.6 Experimental and SFM results for the nucleation rate (300 ml, 500 to 2000 rpm, 0.04M, 7.5 min, id and od)

Figure 6.7 depicts the particle size distribution under one set of conditions (Set 1, 500 rpm). The Segregated Feed Model predicts the experimental size distribution very accurately, especially in the small particle range. Due to agglomeration, particle disruption and inhomogeneous mixing conditions, the number-density distribution deviates from the straight relationship obtained under MSMPR conditions. With larger particles, the experimental data determined using the Coulter Counter tend to scatter significantly and therefore comparison with the model is probably not feasible for large particles.

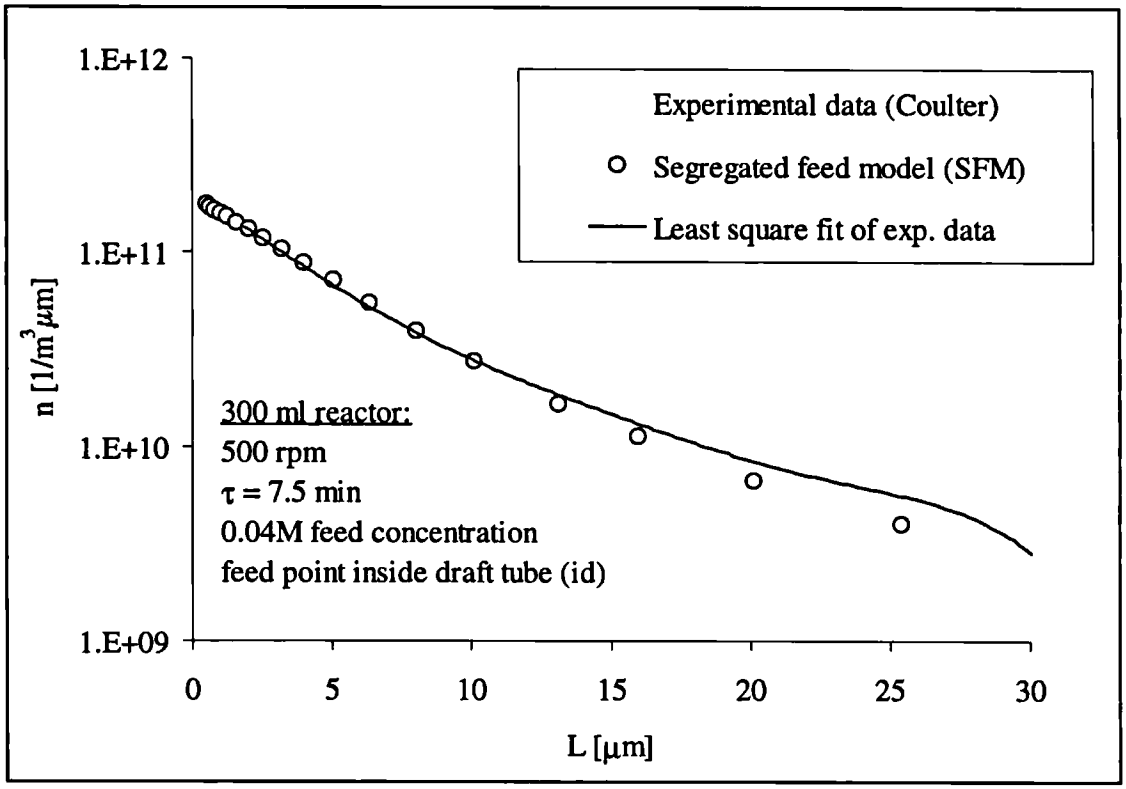

Figure 6.7 Particle size distribution (300 ml, 500 rpm, 0.04M, 7.5 min, id)

6.4.4 RESULTS ON DIFFERENT SCALES

The large-scale experiments were carried out in the same way as the small-scale experiments discussed in Chapter 4 and the parameters were estimated according to the procedure described in the same chapter. In Chapter 4.11, the suitability of design of experiments (DOE) as a design tool for precipitation reactors was investigated and the conclusion reached that it can be useful for individual parameters. One of those parameters, where a direct dependence of the response on the input variables was observed, was the number mean size (Chapter 4.11, Example 1). Using the design equation (4.36), number mean sizes for the large-scale precipitation processes were therefore calculated *a priori* and compared with experimental scale-up data. Under the two sets of conditions (0.04M, 7.5 min, id and 0.01M, 11 min, od) and a mean specific power input of ε = 0.71 W/kg assuming the scale-up criterion ε = constant, the following results were obtained (Table 6.2 and 6.3):

Scale	$L_{10,exp}$ [µm]	$L_{10,DOE}$ [µm]
300 ml	9.0	8.5
4.3 l	8.7	8.5
12 l	8.4	8.5

Table 6.2 Experimental and DOE results for the number mean size (0.7 W/kg, 0.04M, 7.5 min, id)

Scale	$L_{10,exp}$ [µm]	$L_{10,DOE}$ [µm]
300 ml	7.2	7.7
4.3 l	5.3	7.7
12 l	5.1	7.7

Table 6.3 Experimental and DOE results for the number mean size (0.7 W/kg, 0.01M, 11 min, od)

Under the first set of conditions (Table 6.2), the predictions are close to the experimental results and DOE can therefore be considered as a potential scale-up tool. Under the second set (Table 6.3), however, DOE significantly over-predicts the number mean size. As the conditions under which DOE delivers accurate predictions cannot be determined *a priori*, it is only of limited use for scaling up precipitation processes.

Using the kinetic parameters determined in Chapter 4 and the mixing times from Chapters 5 and 6, the large-scale experiments were simulated with the Segregated Feed Model (SFM) and compared with the experimental findings.

Volume mean size L_{43}

In Figure 6.8, the volume mean size is plotted versus the specific power input for the 300 ml, 4.3 l and 12 l reactors and under the conditions according to Set 1 in Table 6.1. Both the experimental and modelling results show a maximum of L_{43} for a power input between 0.4 and 0.5 W/kg. Such a maximum was observed earlier for the precipitation of barium sulphate (Kim and Tarbell, 1996). The steep decrease in the volume mean size for specific power inputs greater than 1 W/kg is probably due to very high disruption rates under these vigorously agitated conditions. The model predicts the experimental data satisfactorily, but no clear trend with scale-up can be determined. Under this particular set of conditions, scale-up with constant mean specific power input could be a reasonably good scale-up criterion. In this case, the curves on different scales would thus merge into one curve. The ideal MSMPR model, in which it has been

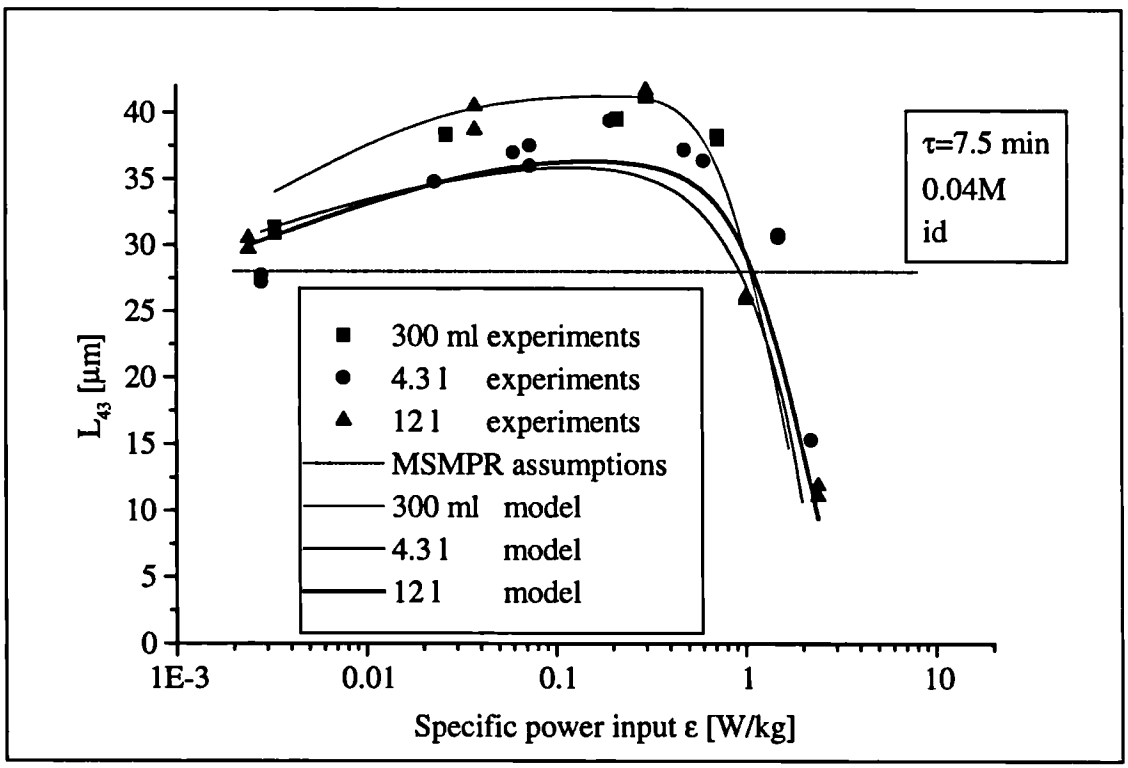

Figure 6.8 Scale-up of continuous calcium oxalate precipitation: Volume mean size L_{43} (300 ml, 4.3 l and 12 l; 0.04M, 7.5 min, id)

assumed that the nucleation rate and the growth rate are constant and that secondary nucleation does not occur, is not capable of predicting any of the experimentally observed effects of power input on mean size, as one of the assumptions for an MSMPR crystallizer is well-mixedness.

The results of the second set of conditions (0.01M, 11 min, od) are depicted in Figure 6.9. Surprisingly, the volume mean size obtained from the 300 ml small-scale experiments is substantially larger than that from the 4.3 l and 12 l scales. This might also be the reason why the DOE procedure could not be applied successfully to predict large-scale parameters. Without adjusting any parameters and only using small-scale kinetic data, the Segregated Feed Model (SFM) correctly predicts both the larger mean sizes observed on the 300 ml scale and the smaller mean sizes on the 4.3 l and 12 l scales. As already observed above, the ideal MSMPR model cannot account for any of the mixing effects and under- or over-predicts the volume mean size.

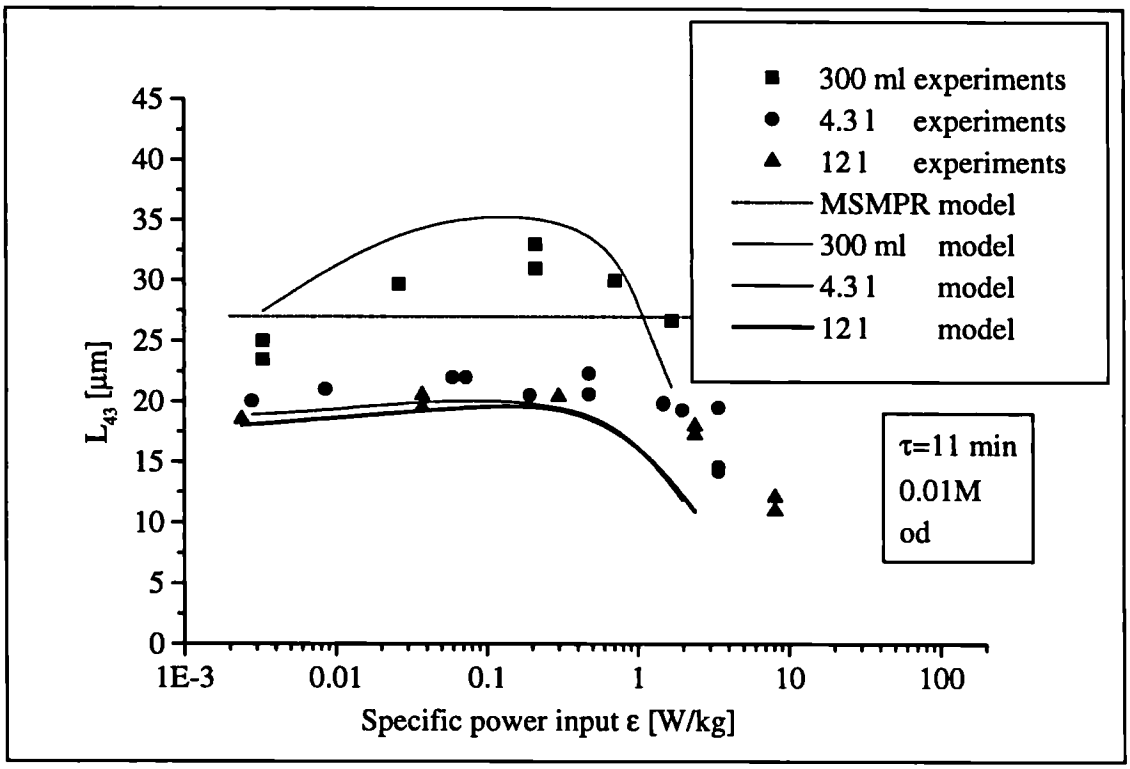

Figure 6.9 Scale-up of continuous calcium oxalate precipitation:
Volume mean size L_{43}
(300 ml, 4.3 l and 12 l; 0.01M, 11 min, od)

One explanation for the smaller values of L_{43} on the larger scales could be that even in geometrically similar locations in the reactors, different mixing conditions prevail due to the different shear rate gradients in reactors of different sizes. In the 300 ml reactor, the energy dissipation at the feed point is higher than in the same region of the larger reactors, even though the feed point is remote from the impeller zone (feed point position od outside the draft tube), as steeper gradients in the shear rate distribution lead to lower levels of specific energy dissipation in regions remote from the impeller zone on the larger scales. The different fields of energy dissipation, obtained on different scales of vessels, have already been discussed in the Computational Fluid Dynamics (CFD) simulations section in Chapter 5. As the precipitation rates and consequently the mean size of the product are different, different mixing times on different scales account for this effect.

The conventional scale-up criteria based on constant specific power input, constant tip speed and constant stirrer speed fail. A detailed analysis of these criteria can be found in Chapter 8.

Coefficient of variation c.v.

The coefficient of variation c.v., which is defined according to Equation (4.8) and a measure of the width or spread of a particle size distribution, is plotted versus the specific power input in Figure 6.10. For an ideal MSMPR, a c.v. of 0.5 independent of the mixing conditions (assumption of perfect mixedness) is obtained. In the experiments and simulations, a c.v. larger than 0.5 was found under almost the whole range of conditions, indicating a wider spread than in the ideal scenario. This increase in spread could be caused by the occurrence of agglomeration on the one hand and on the other by the inhomogeneity of the field of supersaturation resulting in locally different rates. For a very high specific power input, a coefficient of variation smaller than 0.5 was found; this could provide further proof of the importance of particle disruption, which narrows the distribution, thereby leading to a smaller c.v. The model predictions and experimental data correspond well.

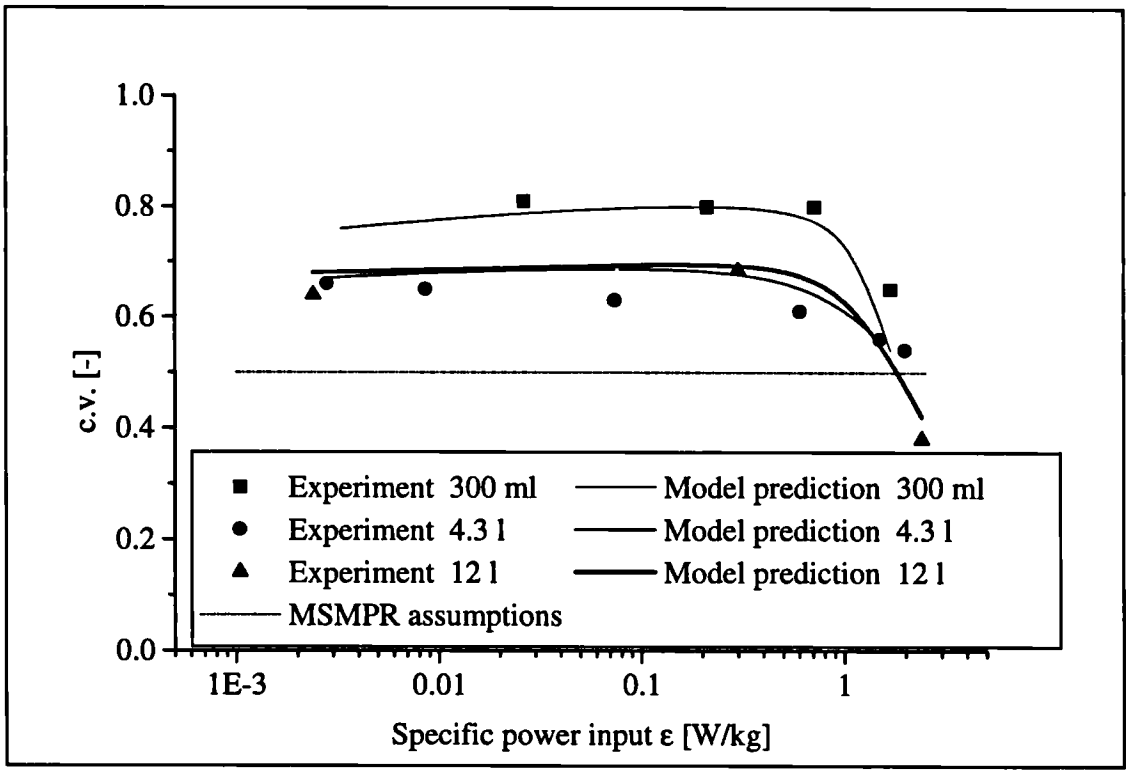

Figure 6.10 Scale-up of continuous calcium oxalate precipitation: Coefficient of variation c.v. (300 ml, 4.3 l and 12 l; 0.01M, 11 min, od)

Nucleation rate B^0

As mentioned above, nucleation is the first kinetic process occurring during precipitation and depends to a large extent on the level of supersaturation. In Figure 6.11, the overall mean nucleation rate in the reactor is shown, plotted versus the specific power input. Depending on the scale of operation, a maximum occurred between 0.03 and 0.1 W/kg. The experimental and modelling results exhibit the same trend and cover the same order of magnitude; however, no pronounced effect of scale-up on the nucleation rate was found. The decrease in B^0 at high power inputs was attributed to shorter mixing times and therefore a more uniform level of supersaturation throughout the reactor. The decrease of B^0 at low power inputs might be due to insufficient mesomixing (blending) leading to very small zones where nucleation can

occur. These effects have already been predicted qualitatively by the Segregated Feed Model in Chapter 5. At mean mixing times a maximum in the nucleation rate was predicted according to the SFM, which has now been validated experimentally. In addition, Figure 6.11 shows that the model predicts larger nucleation rates on the 4.3 l scale than on the 300 ml and 12 l scales. This could be an indication that both micromixing (diffusion) and mesomixing (convection) can become limiting, depending on the scale.

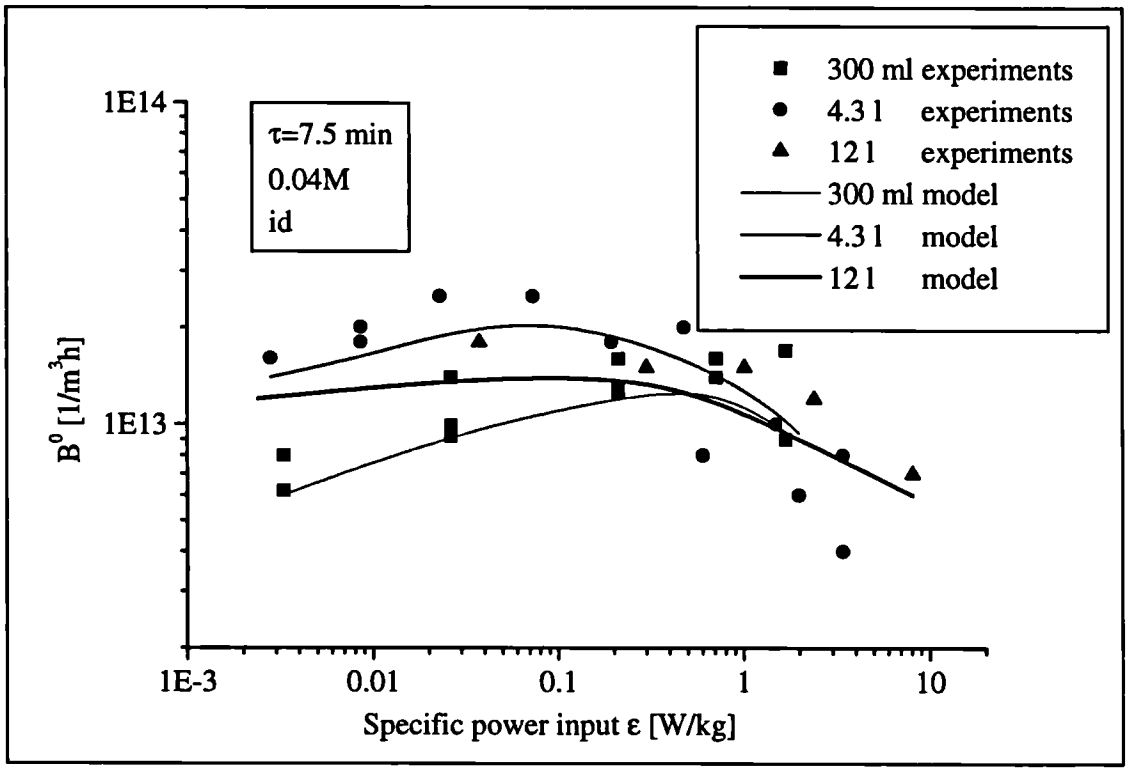

Figure 6.11 Scale-up of continuous calcium oxalate precipitation:
Nucleation rate B^0
(300 ml, 4.3 l and 12 l; 0.04M, 7.5 min, id)

Growth rate G

In contrast to nucleation, crystal growth is a relatively slow kinetic process mainly occurring in the large bulk zone of the precipitation reactor. Figure 6.12 depicts the experimental results for the growth rate; it was found that the latter does not depend

to any significant extent on the mixing conditions. The growth rates of the three scales are very similar, indicating that the level of supersaturation in the bulk zone of the reactor does not change significantly with scale-up.

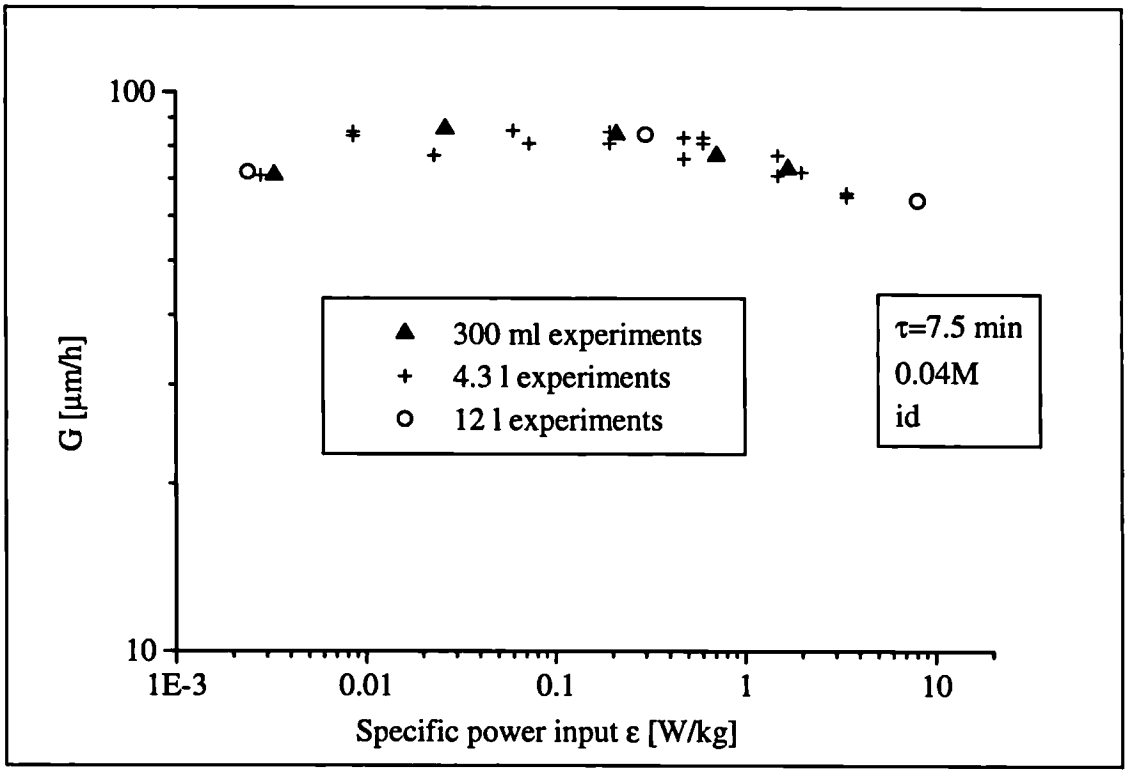

Figure 6.12 Scale-up of continuous calcium oxalate precipitation:
Growth rate G
(300 ml, 4.3 l and 12 l; 0.04M, 7.5 min, id)

CHAPTER 7

SCALE-UP OF SEMIBATCH PRECIPITATION – EXPERIMENTAL AND MODELLING RESULTS

7.1 INTRODUCTION

In this chapter the influence of different process and mixing parameters on particle properties obtained by semibatch precipitation will be discussed. Furthermore, the experimental results for calcium oxalate and calcium carbonate precipitation in the 1 l, 5 l and 25 l reactors will be compared with the simulation data obtained using the Segregated Feed Model (SFM) and Computational Fluid Dynamics (CFD) simulations.

7.2 EXPERIMENTAL SET-UP AND PROCEDURE

The experimental set-up (Figure 7.1) used for the semibatch experiments is similar to that used for the continuous experiments described in detail in Chapters 4 and 6. The semibatch reactor (1), which is stirred using a stirrer drive (5), already contains one reactant at the start of an experiment, while the other reactant is fed from a feed tank (2) into the reactor using a peristaltic pump (4) (semibatch mode of operation). In order to control the addition rate, the flow through the peristaltic pump has been calibrated and the amount fed is checked on the feed tank balance (3). The process conditions are monitored with a pH meter (6) and a calcium-ion meter (7) for determining the level of supersaturation during precipitation.

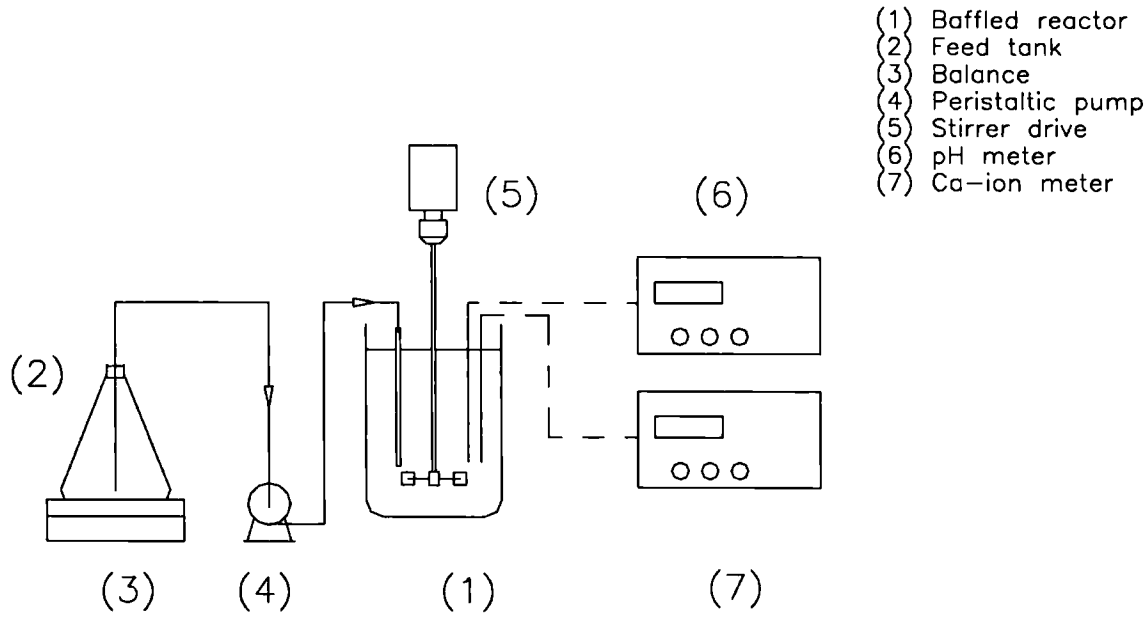

Figure 7.1 Experimental set-up for semibatch precipitation experiments

The particle size distribution was determined using a Coulter Counter Multisizer II and/or a Sympatec Helos laser scattering analyser.

The detailed geometry of the precipitation reactor with a Rushton turbine as stirrer is shown in Figure 7.2. The vessel is equipped with four baffles, but in contrast to the reactor used for the continuous experiments does not contain a draft tube. For reproducible conditions, accurate positioning of the feed tube is very important. The dimensions for the 1 l, 5 l and 25 l reactors with different impellers (Rushton turbine, 45^0-pitched blade turbine and marine-type propeller) and design drawings are given in Appendix A7.1. The baffles, feed tubes and shaft are made of stainless steel, while the actual vessel is made of glass.

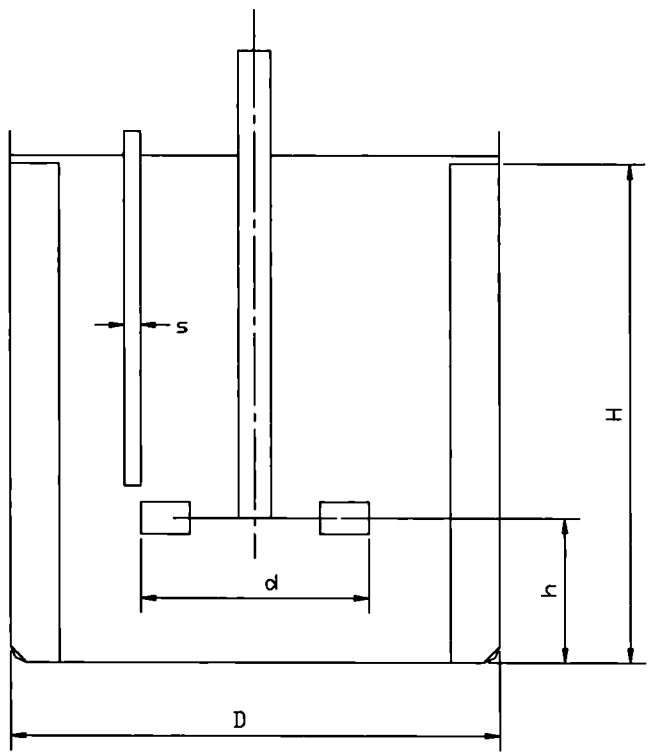

Figure 7.2 Semibatch reactor with Rushton turbine
(dimensions in Appendix A7.1)

7.3 EXPERIMENTAL CONDITIONS

The following conditions were chosen for the 1 l, 5 l and 25 l experiments (Table 7.1 and 7.2):

Calcium oxalate

Condition	from	to	reference
End concentration	0.008M	0.04M	0.008M
Feed time	10 min	60 min	40 min
$V_{feed}/V_{reactor}$	0.2	0.5	0.2
Specific energy input	2.5×10^{-4} W/kg	21.6 W/kg	-
Feed point position	Impeller region	Surface region	Impeller region

Table 7.1 Experimental conditions for semibatch experiments (CaOx)

Calcium carbonate

Condition	from	to	reference
End concentration	0.04M	0.16M	0.04M
Feed time	10 min	40 min	40 min
Specific energy input	2.5×10^{-4} W/kg	21.6 W/kg	-
Feed point position	Impeller region	Surface region	Impeller region

Table 7.2 Experimental conditions for semibatch experiments ($CaCO_3$)

7.4 EXPERIMENTAL AND MODELLING RESULTS

7.4.1 MORPHOLOGY

Using the SEM, the morphology of the calcium oxalate and calcium carbonate precipitate obtained from the semibatch experiments was investigated and compared to that of the continuous experiments.

Calcium oxalate precipitates – as already observed in Chapter 4 – in single crystals and agglomerates. Figure 7.3 depicts a twinned crystal as obtained by semibatch precipitation. The rough surface may be due to the SEM sample preparation, which caused partial dehydration of the crystal. The samples, which were coated with chromium and supported by a polycarbonate membrane, were analysed using a Zeiss Gemini DSM 982 Digital Scanning Microscope with a maximum magnification of

200,000. Figure 7.4 shows the highly agglomerated structure of a calcium oxalate particle, which has probably been damaged by the high temperature and vacuum occurring during the sample preparation.

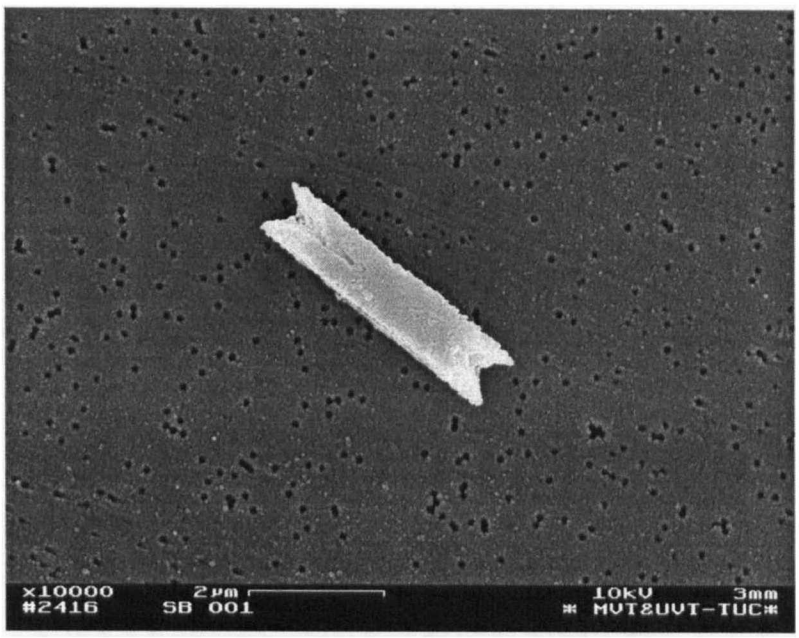

Figure 7.3 Twinned calcium oxalate crystal

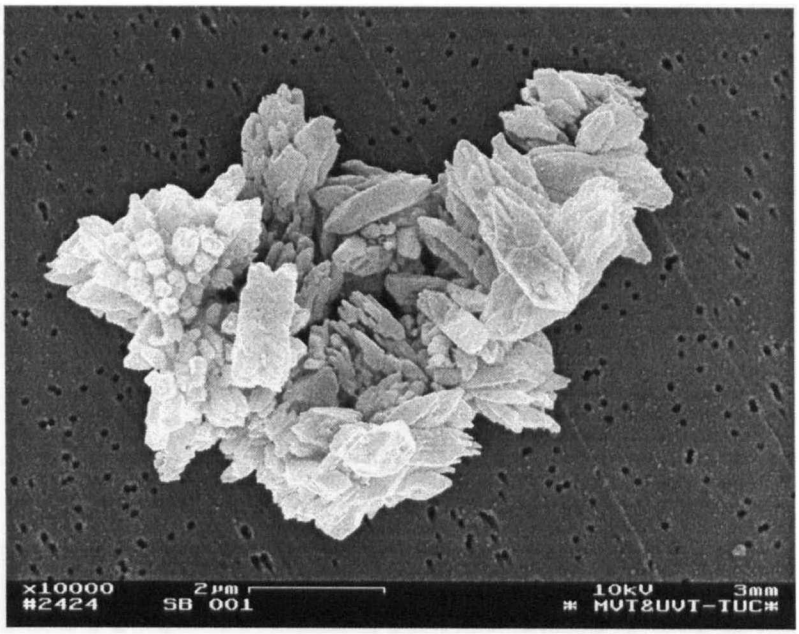

Figure 7.4 Calcium oxalate agglomerate

In the continuous precipitation of calcium carbonate, only spherical vaterite was observed (Figure 4.11 to Figure 4.14). In the semibatch experiments, however, a mixture of both calcite and vaterite was obtained (Figure 7.27). Both polymorphs tend to form agglomerates consisting of a mixture of calcite and vaterite. Left in solution (*e.g.* overnight), the metastable vaterite crystals change to stable calcite to form agglomerates consisting only of calcite (Figure 7.5).

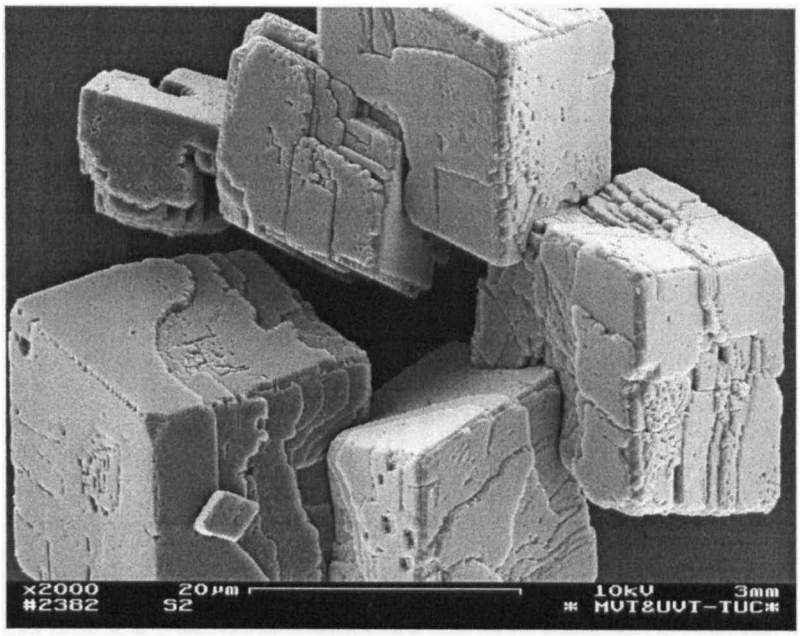

Figure 7.5 Calcium carbonate (calcite) agglomerate

The surface structure of the calcite crystals consists of kinks where crystal growth is likely to take place. The high magnification of 10,000 in Figure 7.6 also shows the edge structure of the crystals in great detail. The edge forms a channel which is roughly 500 nm wide and is divided by "bridges" of crystalline material. The calcite crystals which were originally formed exhibit a very smooth surface (Figure 7.7), whereas calcite formed by solution-mediated transformation from vaterite generally has a rougher surface structure with layers and steps. In Figure 7.8, which shows vaterite particles that have been partly transformed to calcite, the dissolution of the vaterite structure is clearly visible. Figure 7.9 depicts a fully transformed calcite agglomerate, exhibiting the layered structure mentioned above.

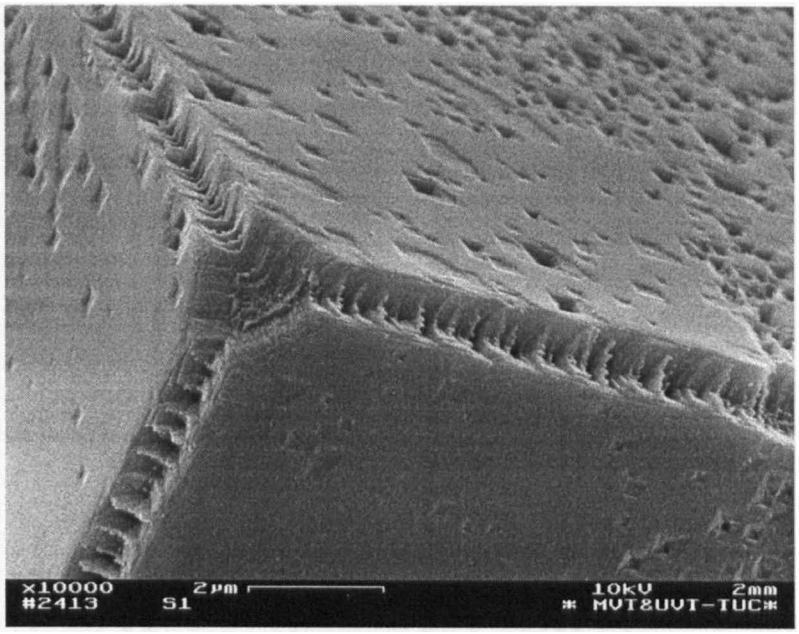

Figure 7.6 Detail of the edges and faces of a calcite crystal

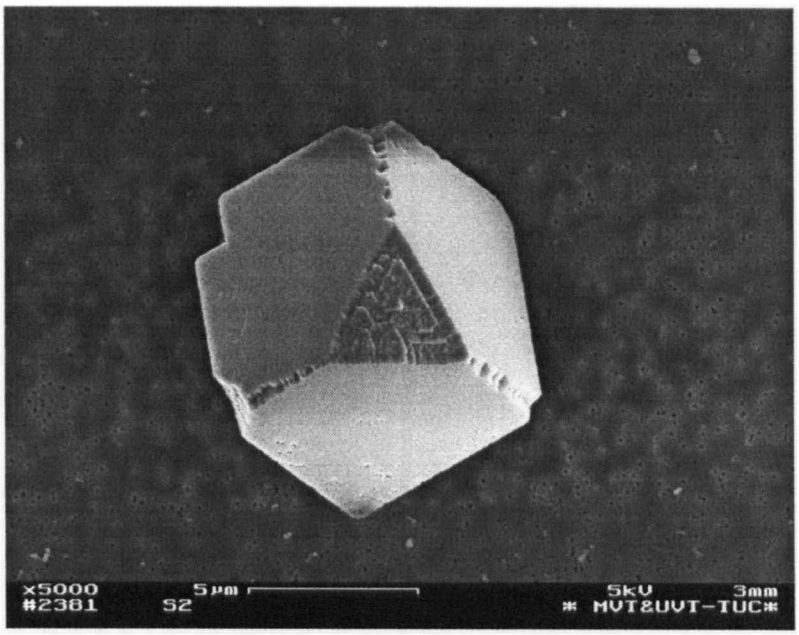

Figure 7.7 Calcite crystal (directly precipitated)

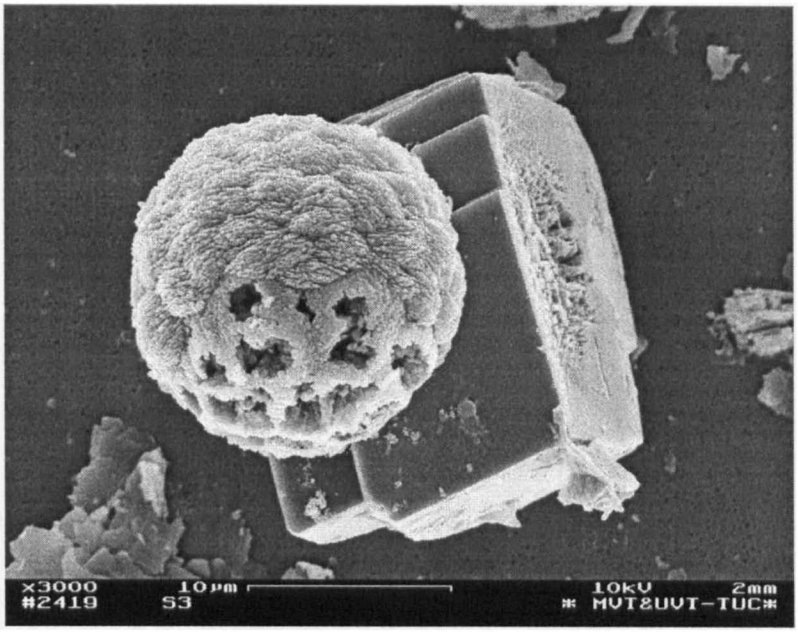

Figure 7.8 Calcite crystal with dissolving vaterite crystal

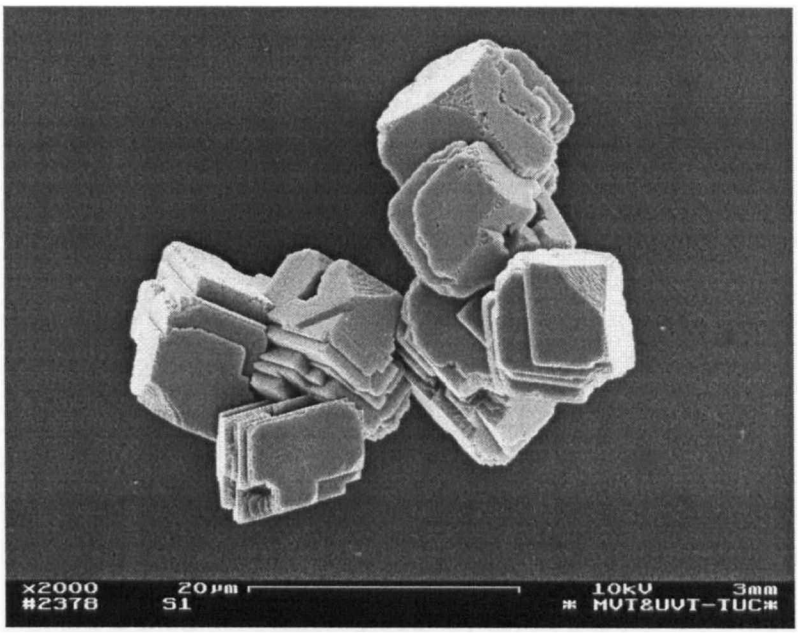

Figure 7.9 Fully transformed calcite agglomerate

7.4.2 SMALL-SCALE RESULTS

In order to investigate process and mixing conditions, the influence of the impeller type, feed tube diameter, feed rate, feed point position, feed concentration and feed volume ratio on the mean particle size were analysed on the 1 l scale. Unless stated otherwise, the system investigated was calcium oxalate.

Impeller type

The flow patterns generated by different impeller types have already been discussed in Chapter 5. These flow patterns lead to different local rates of energy dissipation and therefore to different micro- and mesomixing conditions. Consequently, different product properties are to be expected.

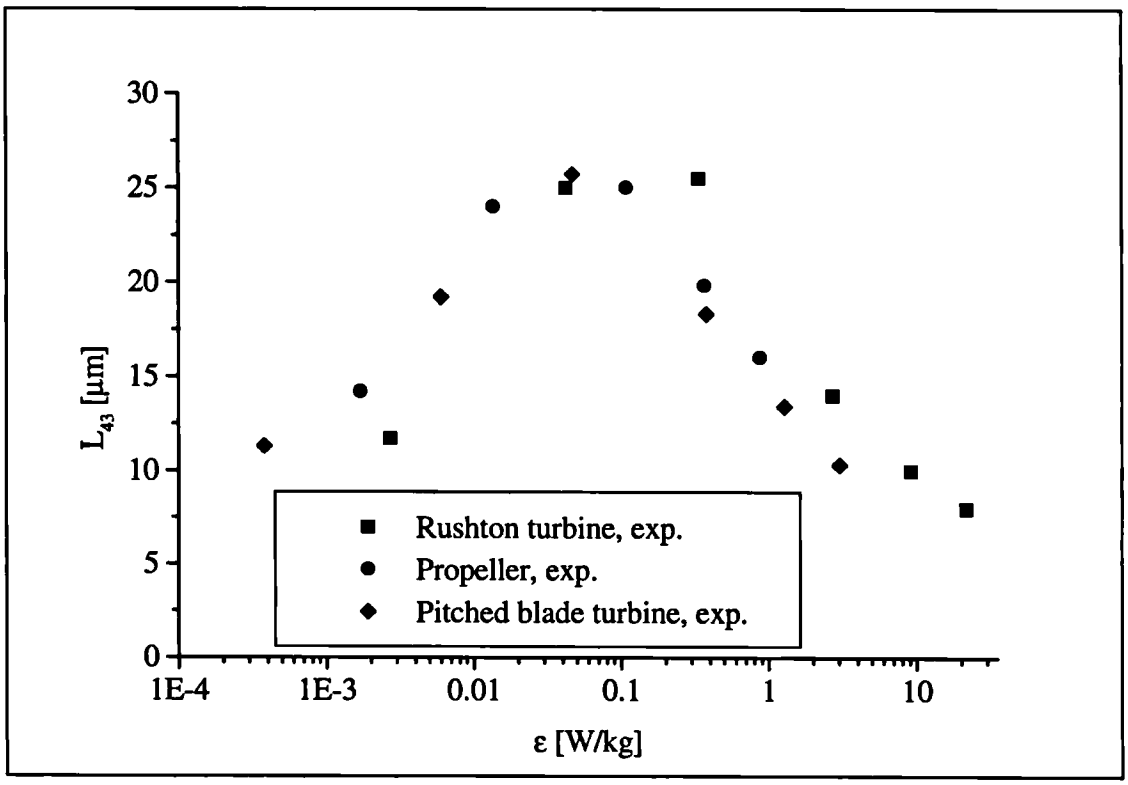

Figure 7.10 Particle size vs. specific energy input for different impeller types (CaOx, 40 min feed time, feed point position close to the impeller, total concentration 0.008M)

Åslund and Rasmuson (1992) observed strong dependence of the weight mean size on the stirrer speed with both a Rushton turbine and a propeller in semibatch experiments with benzoic acid. The authors also found that different stirrer types give the same mean particle size at the same specific power input. In Figure 7.10, the mean particle size of calcium oxalate crystals is plotted versus the specific power input, confirming the results of the authors mentioned above. The three different stirrer types (Rushton turbine, 45°-pitched blade turbine and propeller) give very similar volume mean sizes over a wide range of energy dissipation rates.

Figure 7.11 shows the results of the mean particle size of the experiments and of the Segregated Feed Model (SFM) versus the stirrer speed. The three different impellers give very different curves due to their differences in creating energy dissipation. The experimental results are predicted very accurately by the model considering that only kinetic information from the continuous small-scale experiments was used.

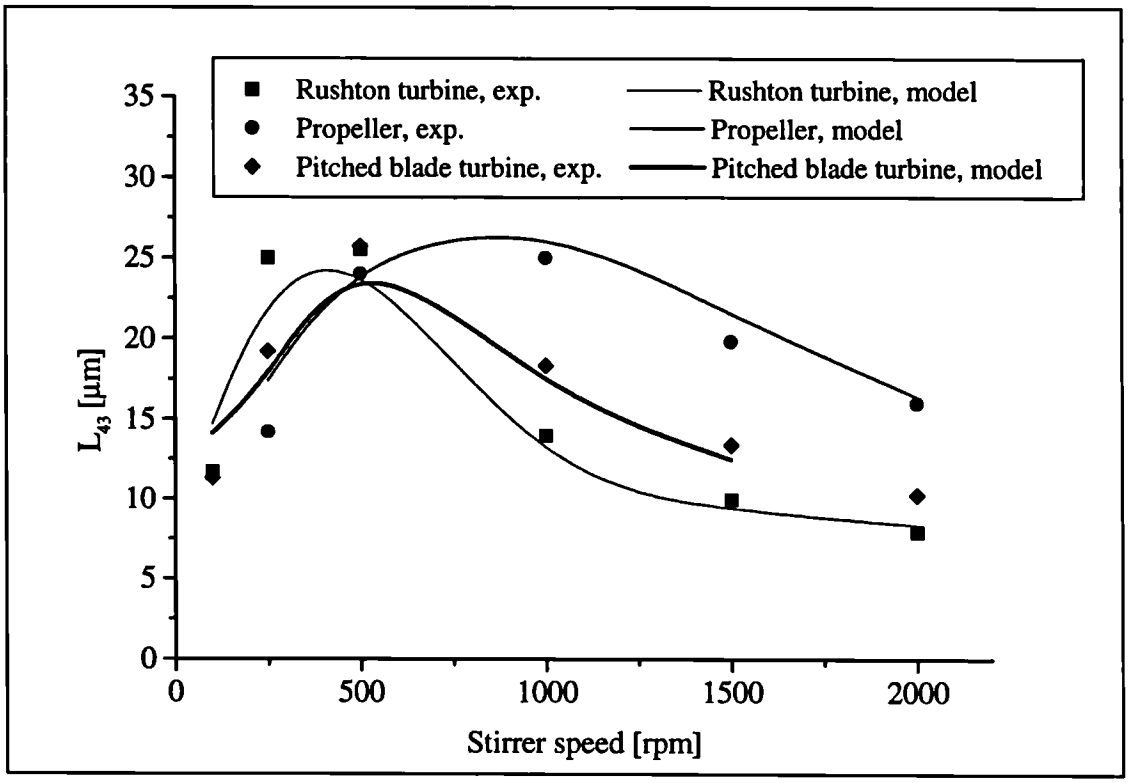

Figure 7.11 Particle size vs. stirrer speed for different impeller types (CaOx, 40 min feed time, feed point position close to the impeller, total concentration 0.008M)

Feed tube diameter

The experiments carried out with different feed tube diameters (2.4 mm, 5.0 mm and 7.1 mm) showed that the feed tube diameter and therefore the velocity of the feed stream entering the reactor could influence particle size (Figure 7.12). At very high and very low power inputs this influence is almost negligible, while for mean power inputs and a small feed tube larger particles are produced, since mixing is increased probably due to the higher feed stream velocity, and the local level of supersaturation thus decreases leading to lower nucleation rates.

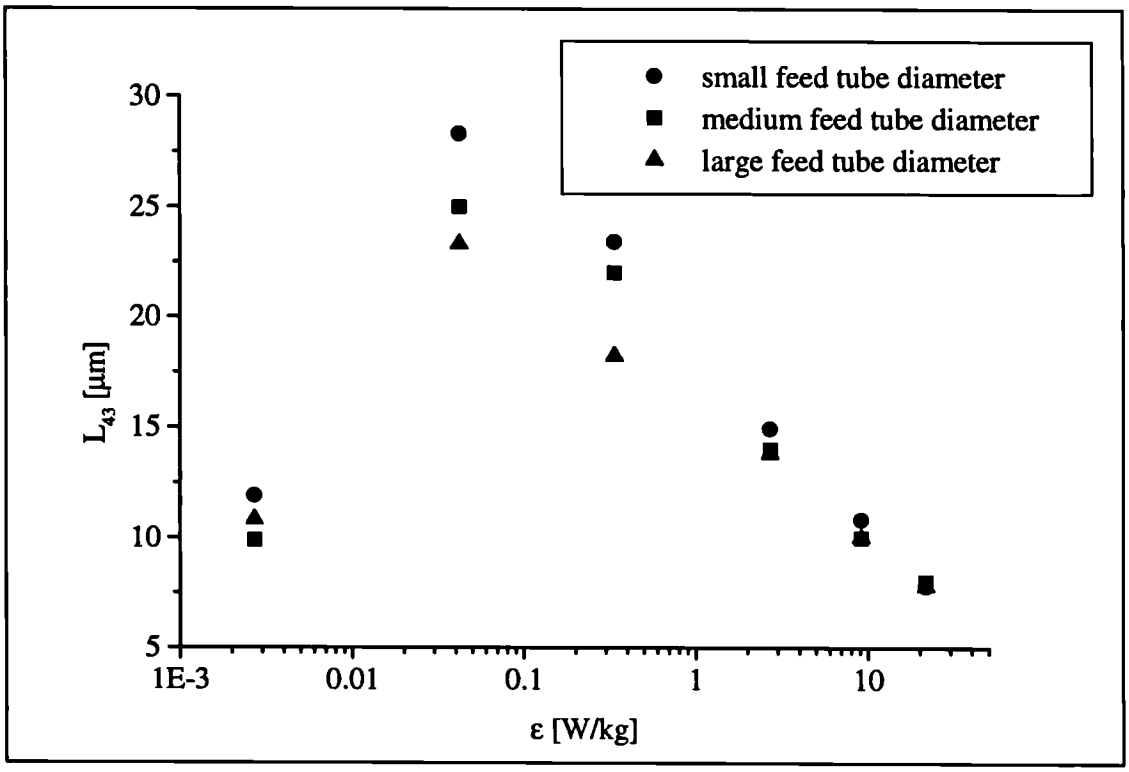

Figure 7.12 Mean particle size vs. specific energy input for different feed tubes (CaOx, Rushton turbine, 40 min feed time, feed point position close to the impeller, total concentration 0.008M)

Feed rate

Similar considerations to those for the feed tube diameter apply to the feed rate of the reactant. At high feed rates (20 ml/min) the level of supersaturation in the reactor is higher, therefore causing higher nucleation rates and smaller particles. This tendency

was experimentally observed not only in this research (Figure 7.13), but also by Marcant (1996) and Baldyga *et al.* (1995) for barium sulphate. Due to the rapidity of the mixing, the influence of the feed rate is not as pronounced at higher power inputs. Analogously, larger particles have been predicted and observed at lower feed rates (3.3 ml/min).

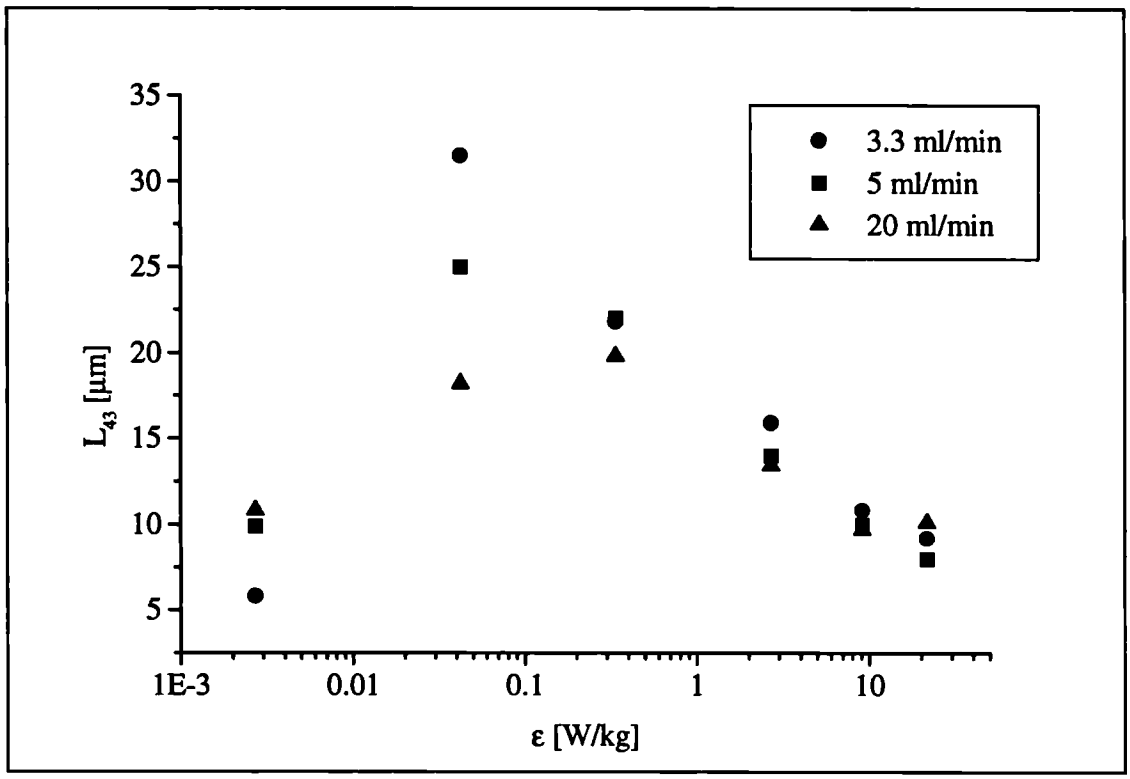

Figure 7.13 Mean particle size vs. specific energy input for different feed rates (CaOx, Rushton turbine, feed point position close to the impeller, total concentration 0.008M)

Feed point position

In order to investigate the dependence of the particle size on the feed point position, one set of experiments was carried out with a feed point close to the impeller and another set with a feed point close to the surface. At low power inputs, the mean particle size obtained for the feed point in a highly turbulent zone near the Rushton turbine resulted in larger particles, giving mean particle sizes up to twice as large as those produced with a feed point close to the surface (Figure 7.14). Åslund and Rasmuson (1992)

investigated feed points near the impeller, in the bulk and close to the surface. The authors observed the same behaviour: at low stirrer speeds substantially larger particles were produced with the feed point close to the impeller, while at high stirrer speeds almost no influence of the feed point position on the weight mean size was found. The predictions of the Segregated Feed Model (SFM) support the experimental observations mentioned above. Calcium carbonate exhibited the same behaviour (Figure 7.15), with the difference that at high power inputs the particles produced at a feed point remote from the impeller were slightly larger than those produced with a feed point in a highly turbulent zone. This shows that both mixing and the interplay of mixing and precipitation have to be taken into account. Åslund and Rasmuson (1992) and Chen *et al.* (1996) obtained similar results with benzoic acid and barium sulphate, respectively.

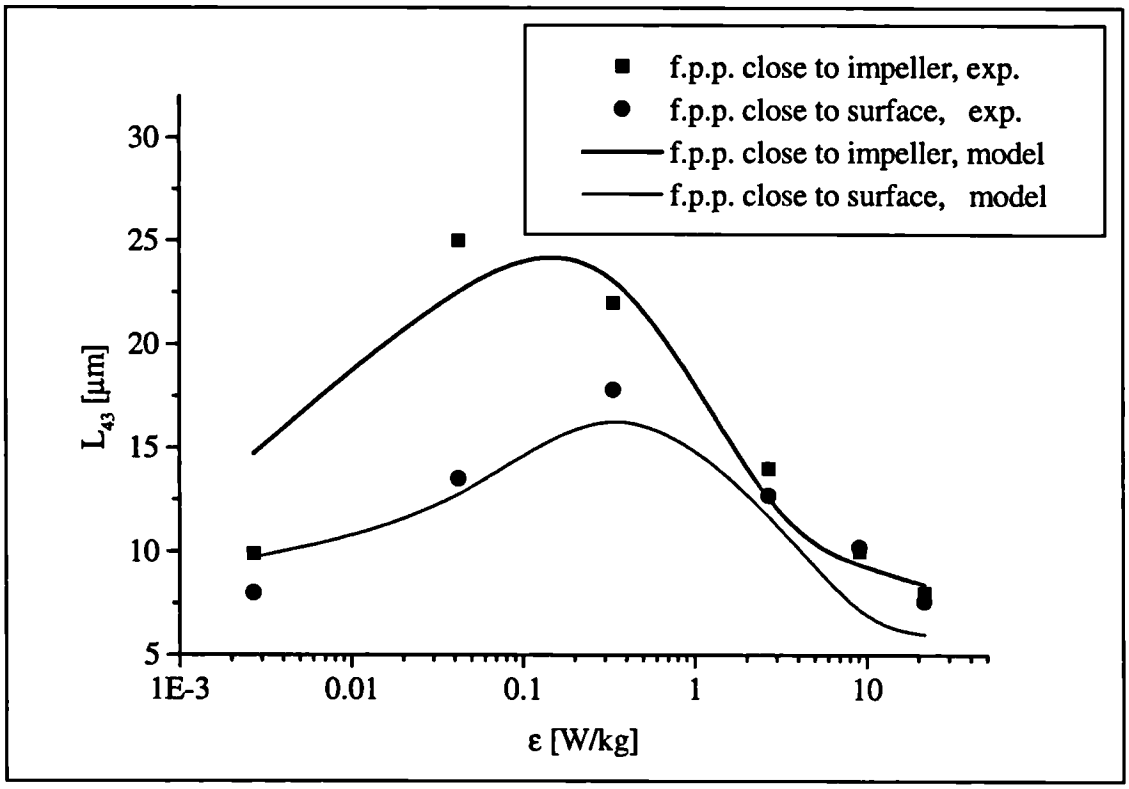

Figure 7.14 Mean particle size vs. specific energy input
for different feed point positions (f.p.p.)
(CaOx, Rushton turbine, 40 min feed time, total concentration 0.008M)

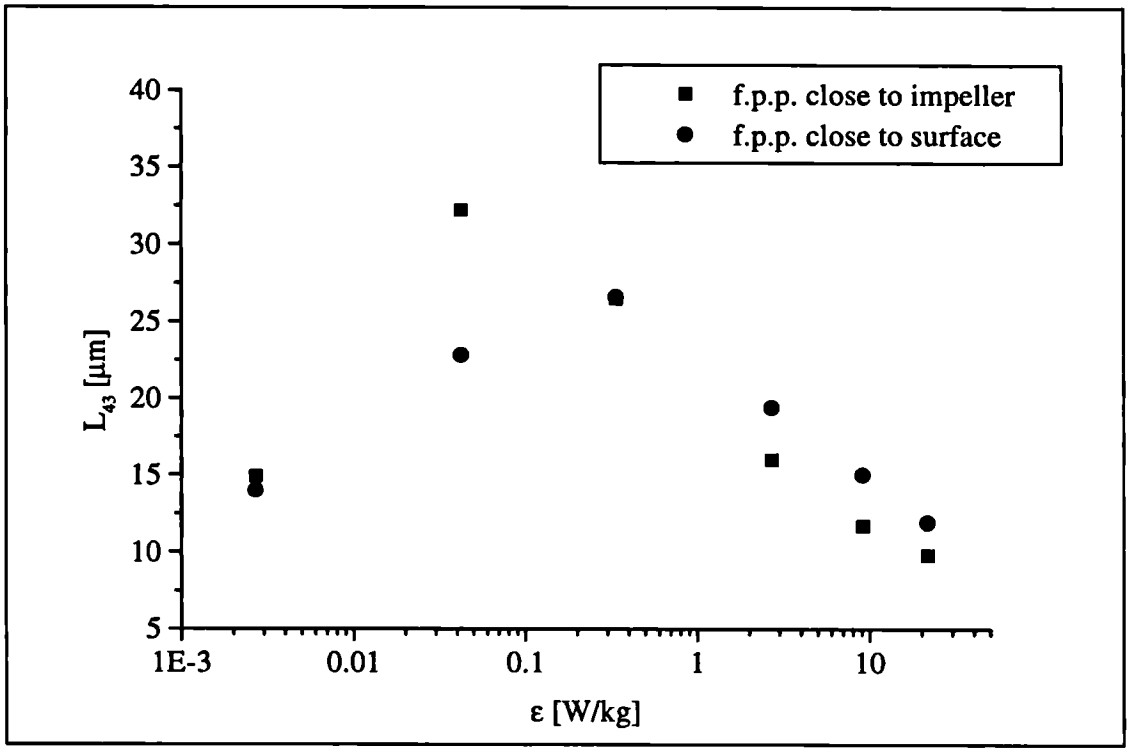

Figure 7.15 Mean particle size vs. specific power input
for different feed point positions
($CaCO_3$, Rushton turbine, 40 min feed time, total concentration 0.04M)

Feed concentration

Figure 7.16 depicts the mean size versus the specific power input at different feed concentrations. Over the whole range of mixing conditions investigated, the particle size obtained from experiments at a high feed concentration lies between 15% and 45% of the size at a lower concentration. The same trend, which can be explained by the higher level of supersaturation at higher feed concentrations, was experimentally observed by Åslund and Rasmuson (1992) and Tosun (1988) with barium sulphate.

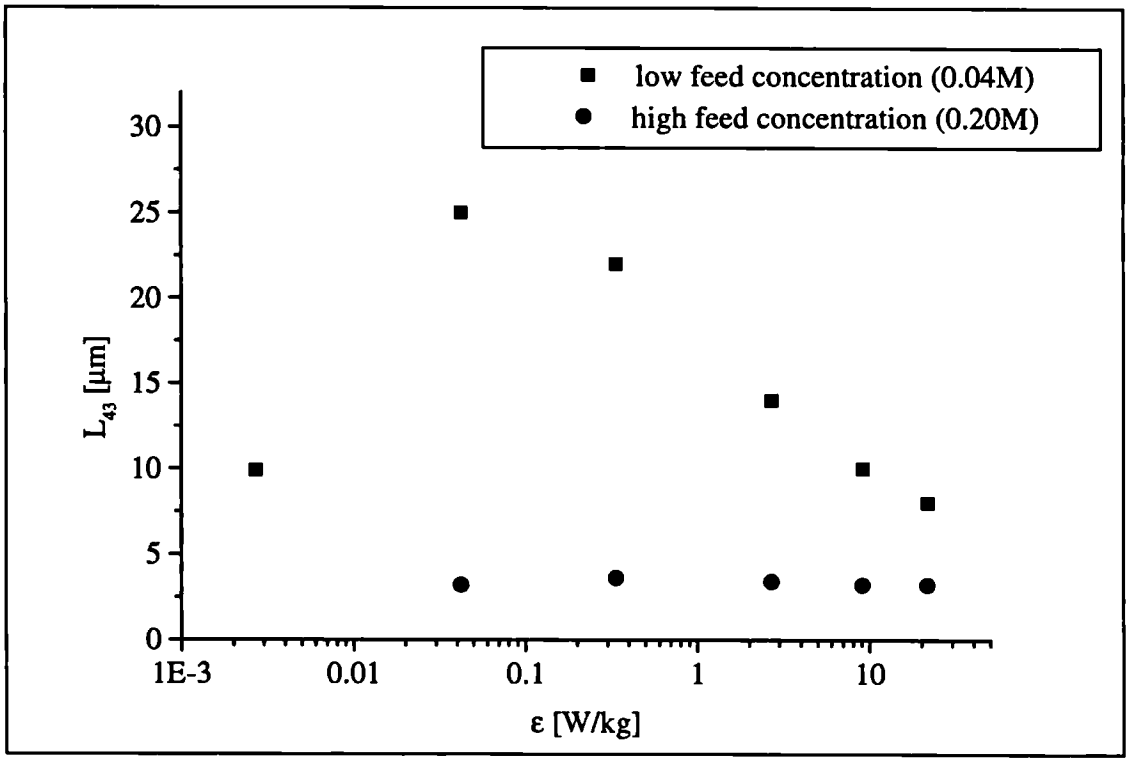

Figure 7.16 Particle size vs. specific power input for different feed concentrations (CaOx, Rushton turbine, 40 min feed time, feed point position close to the impeller)

Feed volume ratio

Equimolarity at the end of a semibatch experiment can be achieved by, for example, either feeding a small amount of highly concentrated feed solution or by feeding a larger amount of diluted feed solution into the precipitation reactor. In the majority of experiments, a ratio of feed volume to reactor volume of 0.2 was chosen (reference conditions). In Figure 7.17, these data are compared with a feed volume ratio of 0.5, *i.e.* 500 ml of the feed reactant are fed to 500 ml of the other reactant already present in the reactor. As one would expect, the mean particle size increases for a volume ratio of 0.5 due to the lower level of local supersaturation around the feed point. It should be mentioned, however, that the feeding time under these conditions is 2.5 times longer than under the original conditions. Clearly, a trade-off between feeding time and particle size will lead to economic operation of the reactor.

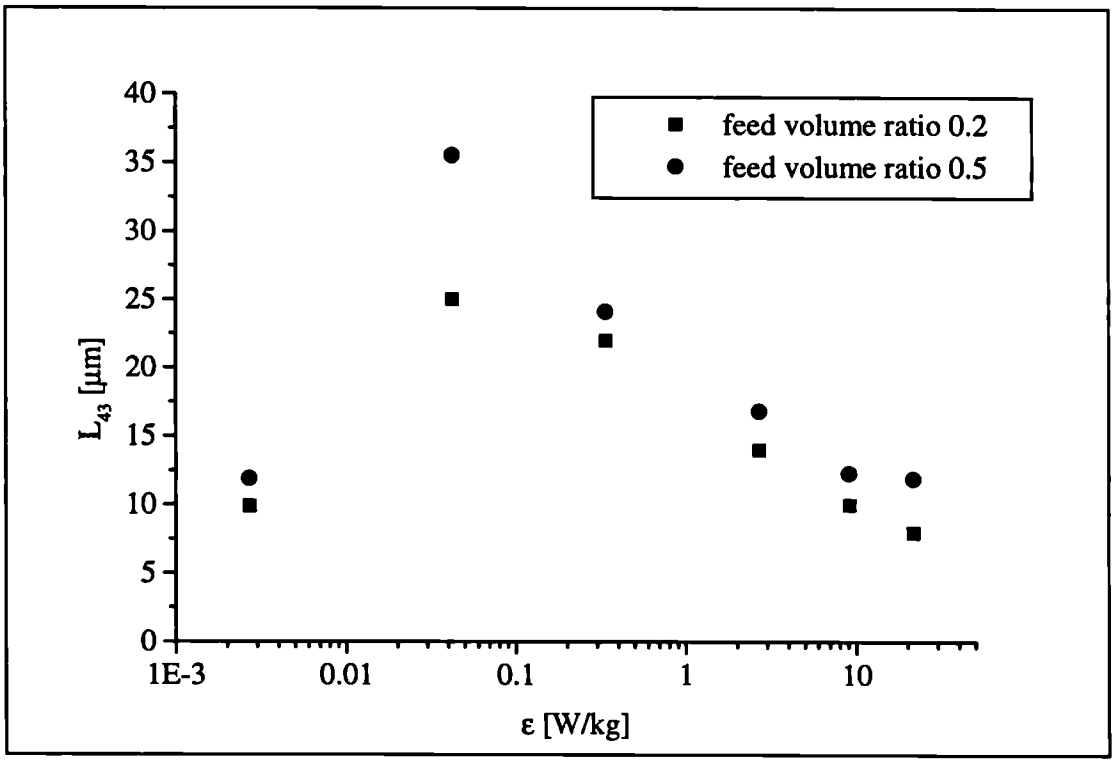

Figure 7.17 Particle size vs. specific power input for different feed volume ratios (CaOx, Rushton turbine, 40 min feed time, feed point position close to the impeller, total concentration 0.008M)

7.4.3 RESULTS FOR CALCIUM OXALATE ON DIFFERENT SCALES

Volume mean size L_{43}

In comparison with the continuous mode of operation, the mean size was found to depend to a greater degree on the mixing conditions on all scales in the semibatch mode. In Figure 7.18, the results for the reference conditions (Rushton turbine, 40 min feed time, feed point position close to the impeller, total concentration 0.008M) for calcium oxalate confirm this observation. By changing the energy input, the volume mean size was varied over a wide range from 7 to 26 µm. For the two reactor scales of 1 l and 5 l, scale-up with constant specific power input seems appropriate, while for the

25 l scale smaller particle sizes are obtained in the industrially important range from 0.1 to 1 W/kg.

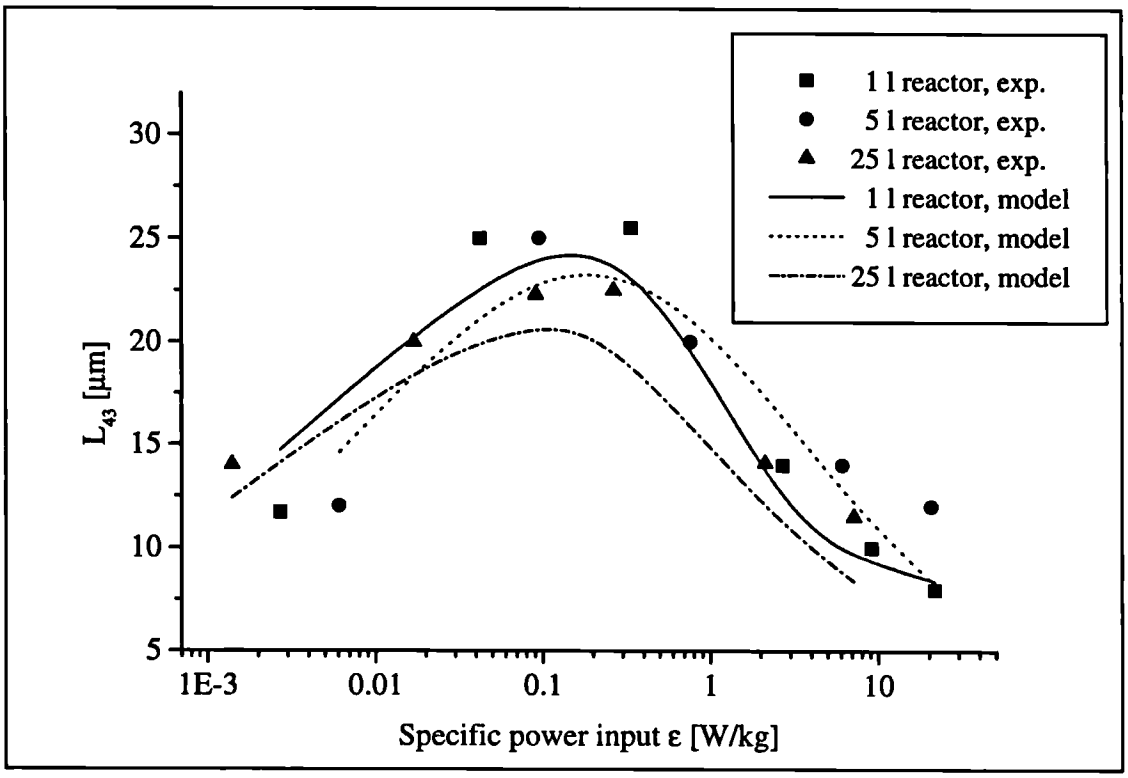

Figure 7.18 Mean particle size for reference conditions
(CaOx, Rushton turbine, 40 min feed time, feed point position close to the impeller, total concentration 0.008M)

The kinetic parameters, which were determined from laboratory-scale continuous experiments as a function of the energy input and/or supersaturation, were applied to the semibatch mode of operation without any adjustments or parameter fitting. The Segregated Feed Model (SFM) slightly underestimates the mean particle size in the range between 0.01 and 1 W/kg, but correctly predicts the smaller particle size obtained experimentally for the 25 l reactor. On the same scale, the model also predicts a lesser degree of dependence of the particle size on the specific power input due to the interactions of mixing and the precipitation kinetics. This behaviour has also been observed experimentally.

For a different stirrer type, *i.e.* the marine-type propeller, a different range of specific energy dissipations is covered with the same range of stirrer speeds (Figure 7.19). The propeller stirrer was operated between 100 rpm (ε = 10^{-3} W/kg, $Re = 6.3\times10^4$) and 1500 rpm ($\varepsilon = 4.67$ W/kg, $Re = 1.3\times10^6$). Analogously to the scale-up experiments with a Rushton turbine, the mean particle size on the 25 l scale is smaller than that on the smaller scales. This could be explained by the lower level of energy dissipation around the feed point, which is caused by an increase in gradient in the shear rate with scale-up. Consequently, the local energy dissipation in the feed region decreases on a larger scale and the mixing times increase. As already pointed out for the Rushton turbine, the model also correctly predicts this trend for the propeller.

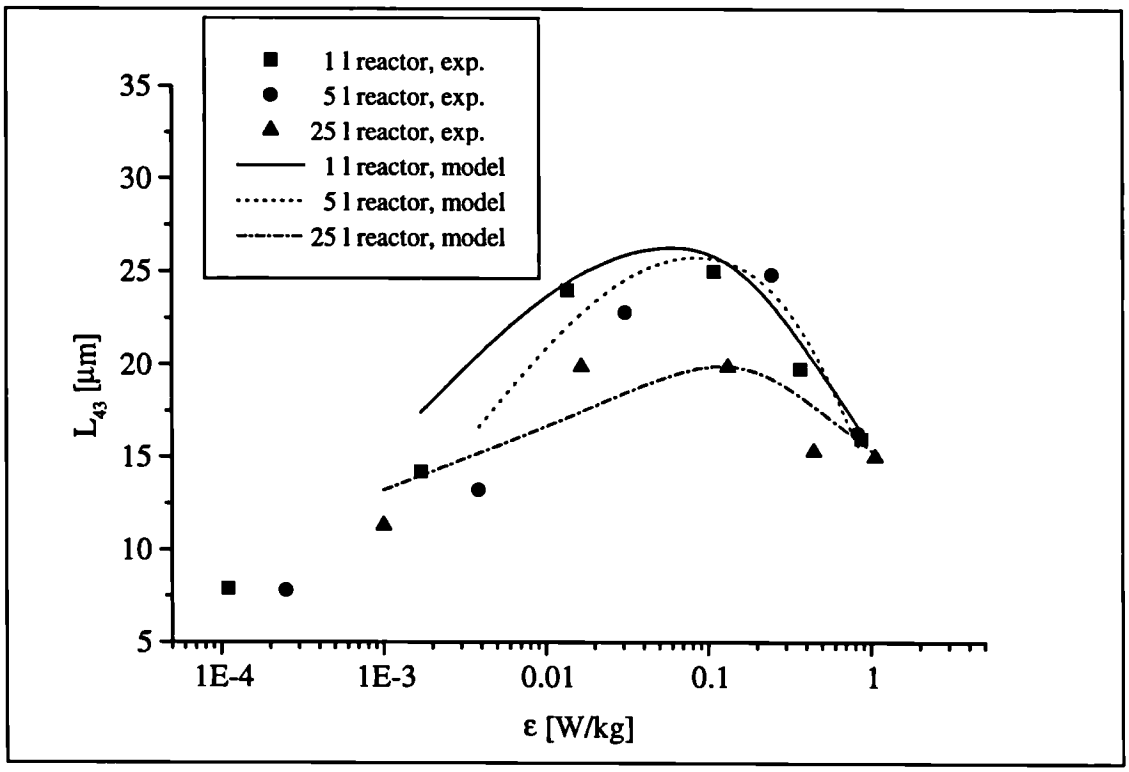

Figure 7.19 Mean particle size for marine-type impeller (CaOx, 40 min feed time, feed point position close to the impeller, total concentration 0.008M)

Small particle sizes obtained at low energy inputs are probably a result of local zones with very high levels of supersaturation and therefore high nucleation rates. At high energy inputs, in contrast, breakage might act as a size-reducing process, leading to smaller particles.

When the feed point position is moved to a position further away from the impeller in a zone with lower local energy dissipation, the particle size drops by about 25% for the whole range of conditions (Figure 7.20). Under such conditions, the effect of producing smaller mean particle sizes on the 25 l scale is even more pronounced. Again, all curves show a maximum; the influence of the power input on particle size is weakest on the largest scale, however, causing a shallower maximum than on the 1 l and 5 l scales.

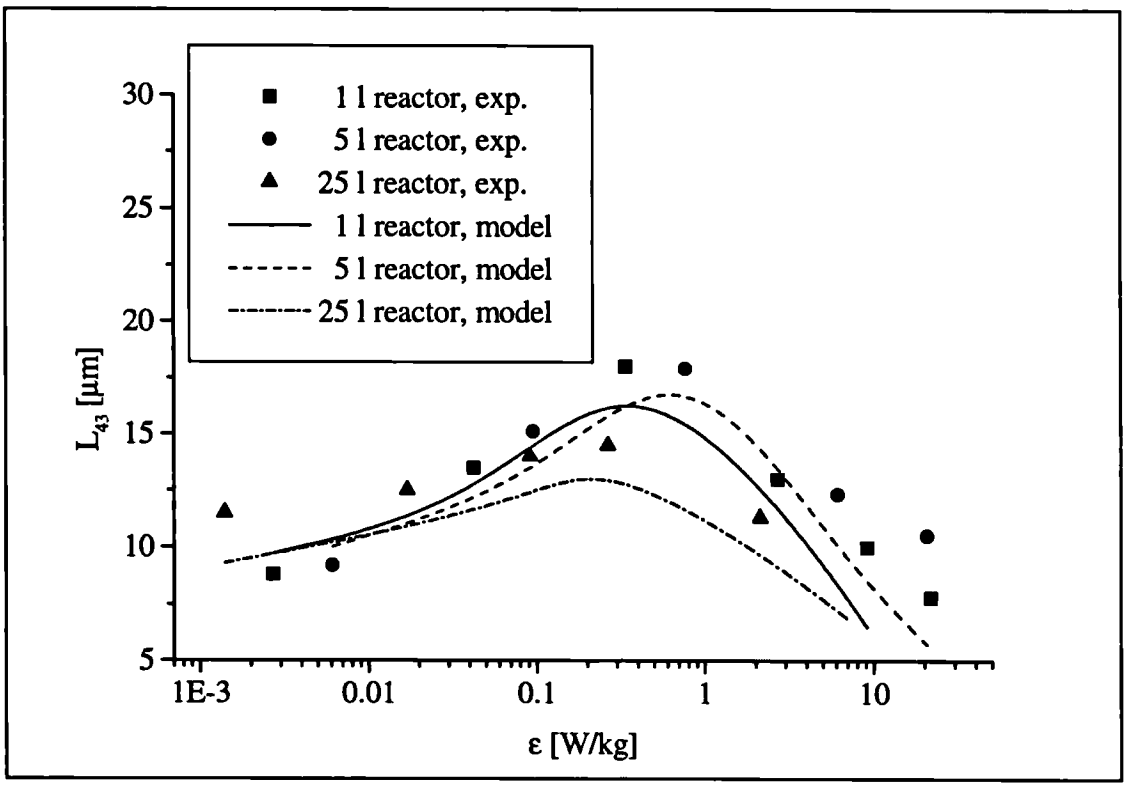

Figure 7.20 Mean particle size for feed point position close to surface (CaOx, Rushton turbine, 40 min feed time, total concentration 0.008M)

At a higher feed rate (10 min feeding time instead of 40 min), the model slightly underestimates the volume mean particle size. The particle size is approximately 30% smaller than that for the reference conditions, as a higher level of supersaturation prevails in the reactor due to the faster feeding (Figure 7.21). Therefore, moving the feed point position to a zone with lower local energy dissipation and increasing the feed rate have the same effect. An increase in feed rate, however, reduces the feed time and therefore the batch time and increases the efficiency of the process.

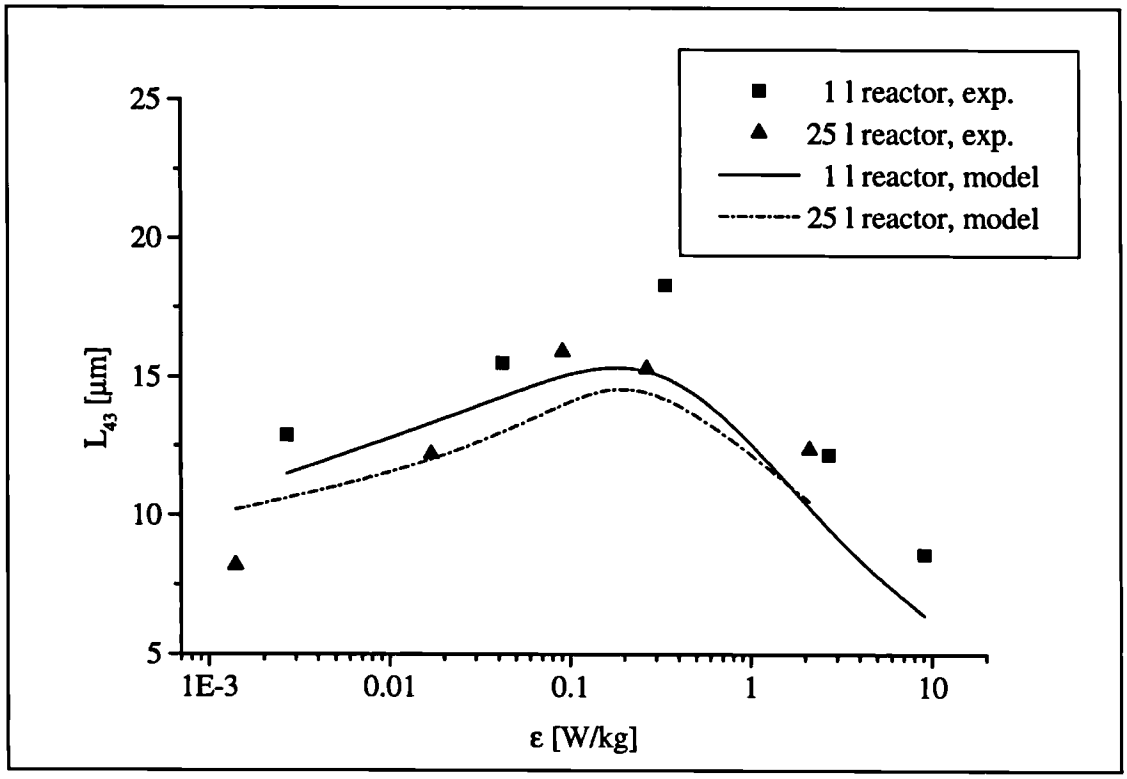

Figure 7.21 Mean particle size for high feed rate
(CaOx, Rushton turbine, feed point position close to the impeller,
total concentration 0.008M)

Total number of particles m_0

In order to fully characterise a particle size distribution, it is not sufficient to know only the mean particle size, as it does not contain any information about the spread of the distribution or number of particles formed. Additional properties are

therefore required to characterise the particle size distribution. One of these properties is the total number of particles, which is nothing other than the zeroth moment of the distribution.

For the reference conditions, Figure 7.22 shows that the zeroth moment m_0 can be scaled up with the specific power input. For very low power inputs, the number of particles obtained is very high. This effect can again be explained by high levels of local supersaturation causing excessive nucleation and thus a large number of particles as a result of insufficient mixing in the feed zone. In the semibatch mode of operation, the two reactants are mixed directly and not via the bulk as is the case in continuous precipitation. The level of local supersaturation is thus even higher. At mean micro- and mesomixing times the number of particles exhibits a minimum due to improved mixing and agglomeration, while at higher power inputs the number of particles increases again, most probably due to particle breakage.

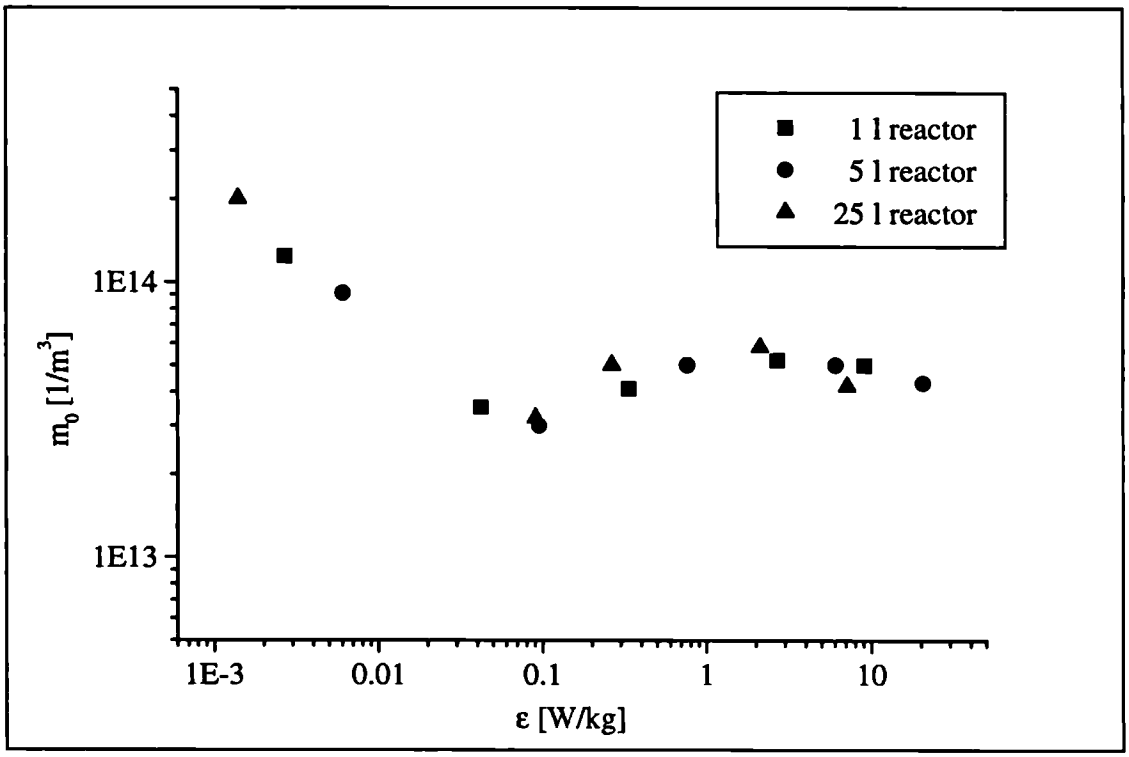

Figure 7.22 Total number of particles for reference conditions
(CaOx, Rushton turbine, 40 min feed time, feed point position close to the impeller, total concentration 0.008M)

At very high power inputs, increased breakage and decreased nucleation rates maintain the balance so that the total number of particles for power inputs $\varepsilon > 0.5$ W/kg stays roughly constant.

In Figure 7.23, the data for the 1 l and 5 l reactor with propeller show a similar trend at low power inputs with a minimum of the total number at about $\varepsilon = 0.1$ W/kg. At higher power inputs, however, the number of particles increases steadily up to a power input of about $\varepsilon = 2.5$ W/kg, probably due to decreased agglomeration efficiency and increased particle disruption at high power inputs.

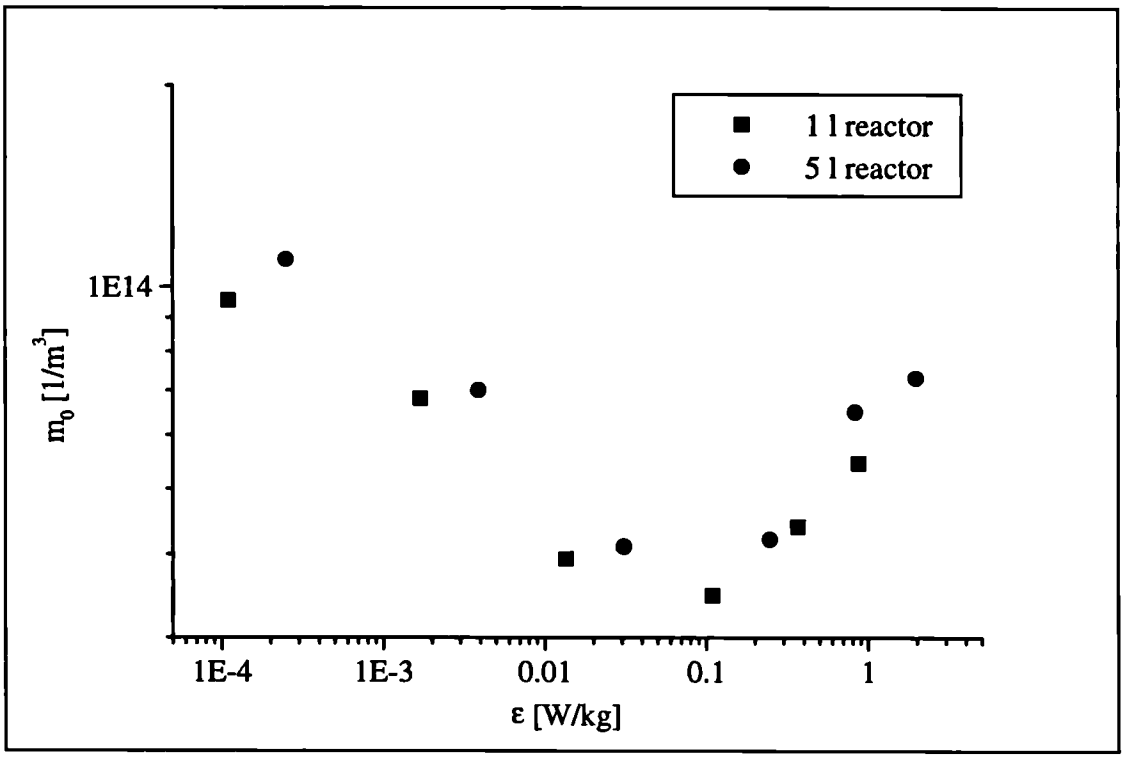

Figure 7.23 Total number of particles for marine-type impeller (CaOx, Rushton turbine, 40 min feed time, feed point position close to the impeller, total concentration 0.008M)

Number density of particles in the first size interval $n(L_0)$

As the nucleation rate in a semibatch precipitation reactor is strongly time-dependent, an alternative quantity - the number density of particles in the first size interval $n(L_0)$ - was chosen to characterise nucleation. The lower limit of the first size

class is determined by the detection limit of the particle analyser and was 0.5 µm for the Sympatec Helos laser scattering analyser.

In Figure 7.24 the results for the reference conditions on the 1 l and 5 l scales confirm the high nucleation rates and therefore large number of particles expected at low power inputs. Up to about ε = 1 W/kg, a decrease of $n(L_0)$ was found experimentally, while at higher power inputs the data scattered substantially. As the number density was calculated from a volume size distribution, even small deviations in the mass distribution result in large errors in the number distribution. Therefore, its sensitivity to experimental errors is very high.

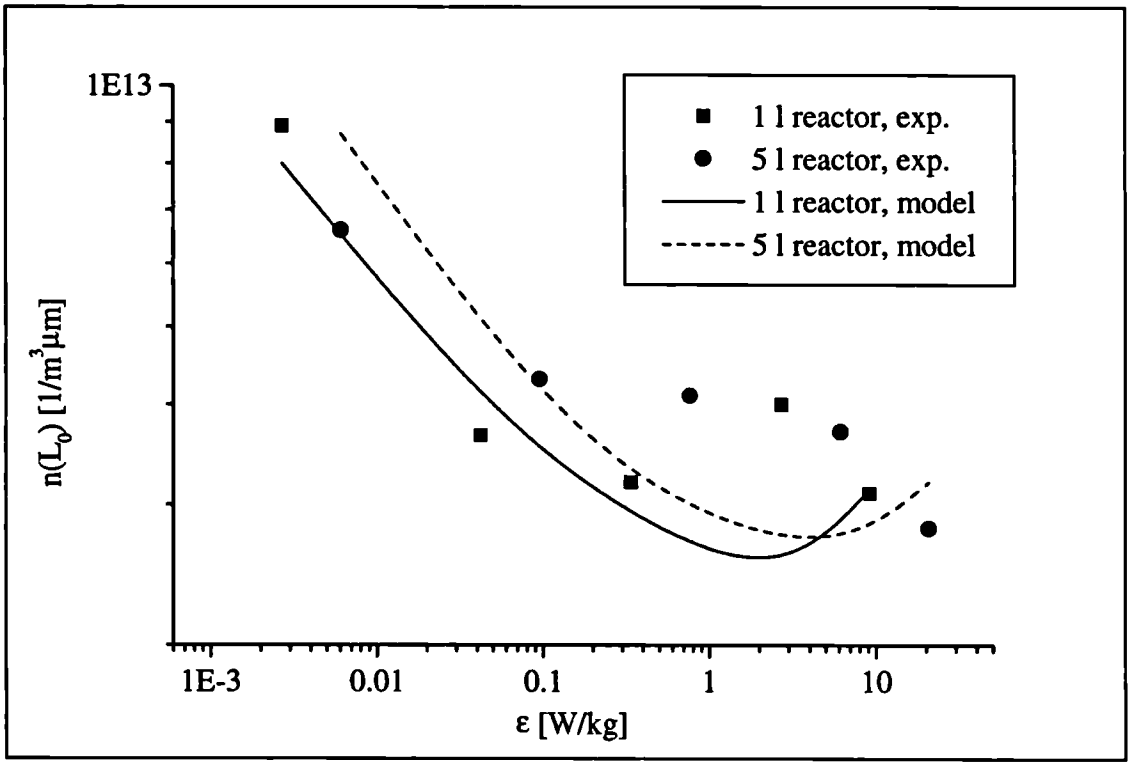

Figure 7.24 Number density of nuclei for reference conditions (CaOx, Rushton turbine, 40 min feed time, feed point position close to the impeller, total concentration 0.008M)

The SFM predicts the trend of the decrease, but deviates where the data start to scatter with increasing power input. At even higher power inputs, the model predicts an increase in $n(L_0)$. This increase has been experimentally verified for experiments carried out with a propeller impeller (Figure 7.25). On both scales (1 l and 5 l) this minimum in the number of particles formed was observed at about $\varepsilon = 0.1$ W/kg, while for higher energy inputs the number density of particles in the first size interval increased again.

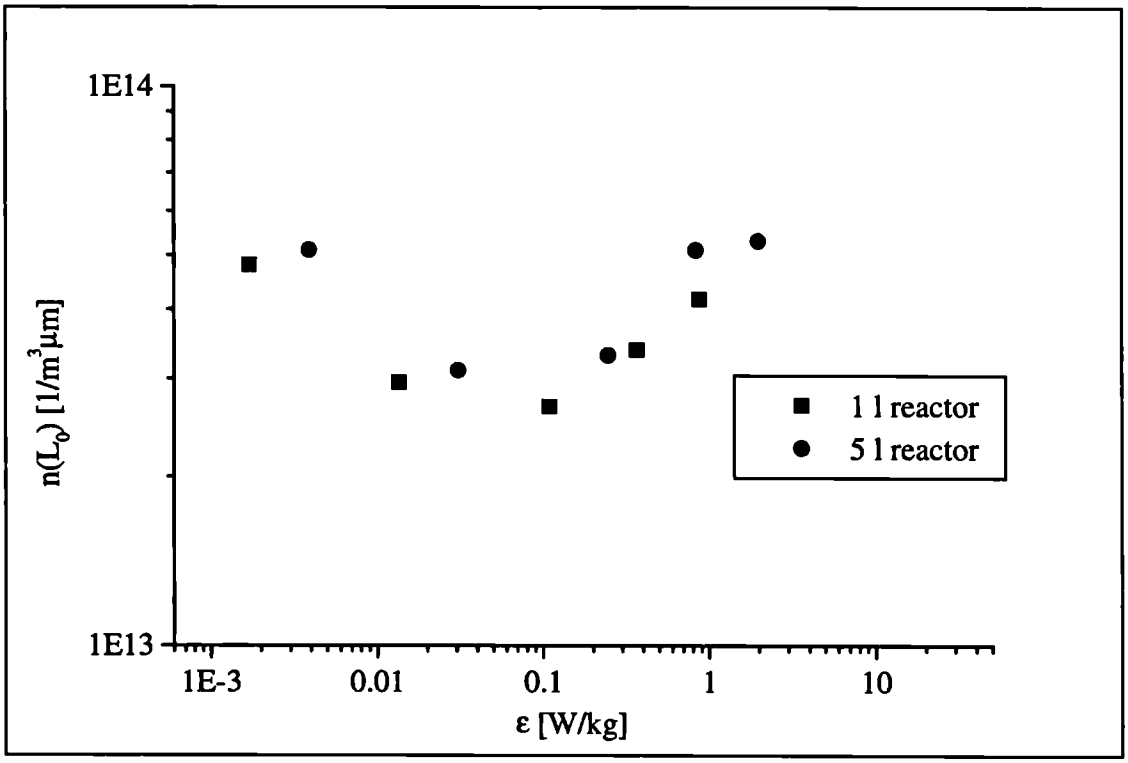

Figure 7.25 Number density of nuclei for marine-type impeller (CaOx, 40 min feed time, feed point position close to the impeller, total concentration 0.008M)

7.4.4 RESULTS FOR CALCIUM CARBONATE ON DIFFERENT SCALES

Volume mean size L_{43}

As already observed for calcium oxalate, the volume mean size depends significantly on the energy input in the reactor. In the semibatch experiments with calcium carbonate, L_{43} exhibited a maximum at approx. $\varepsilon = 0.04$ W/kg for the reference conditions (Rushton turbine, 40 min feed time, feed point position close to the impeller, total concentration 0.04M) on different scales (Figure 7.26). Due to the direct mixing of the incoming reactant with the second reactant already present in the bulk, even higher levels of local supersaturation than in the continuous mode of operation are achieved.

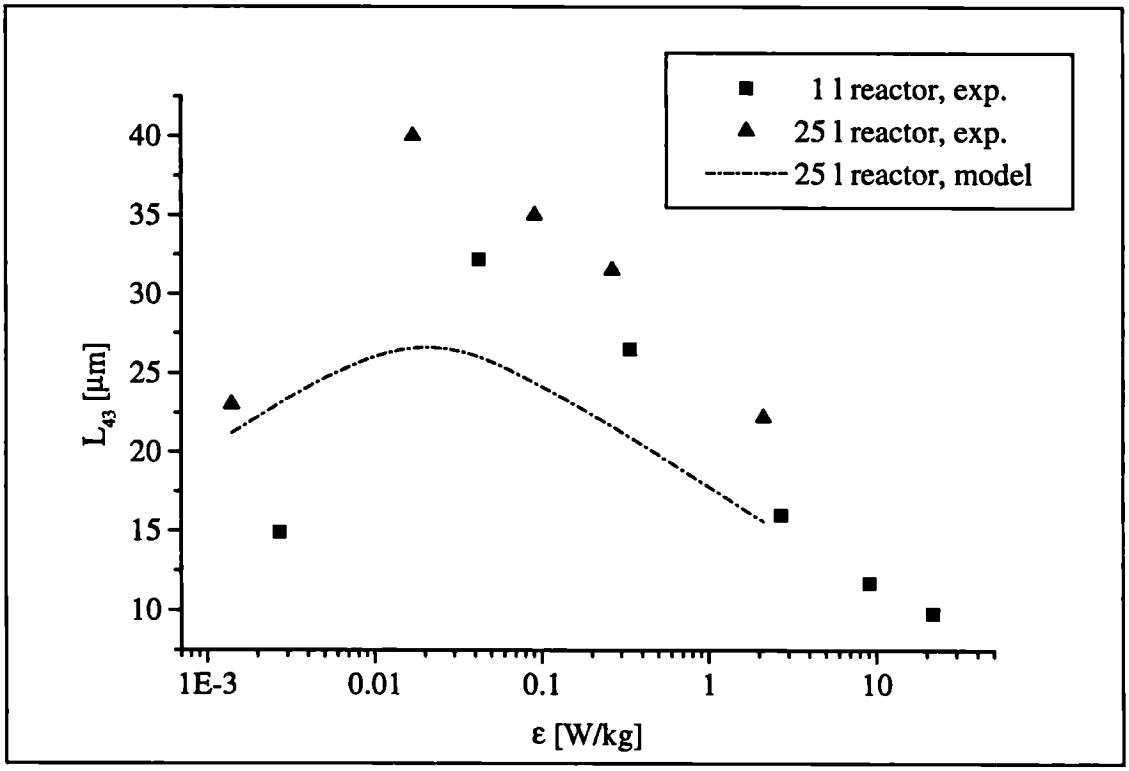

Figure 7.26 Mean particle size for reference conditions ($CaCO_3$, Rushton turbine, 40 min feed time, feed point position close to the impeller, total concentration 0.04M)

On the largest scale (25 l), the particles formed were generally larger than on the 1 l and 5 l scale. The Segregated Feed Model SFM, which predicted the particle properties of calcium oxalate very accurately, clearly underestimates the particle size of calcium carbonate. The reason for this discrepancy between the experimental findings and simulation results is the formation of different polymorphs during calcium carbonate precipitation. While only the metastable form vaterite occurred in the continuous experiments, SEM micrographs clearly show the formation of both vaterite and calcite during semibatch precipitation (Figure 7.27).

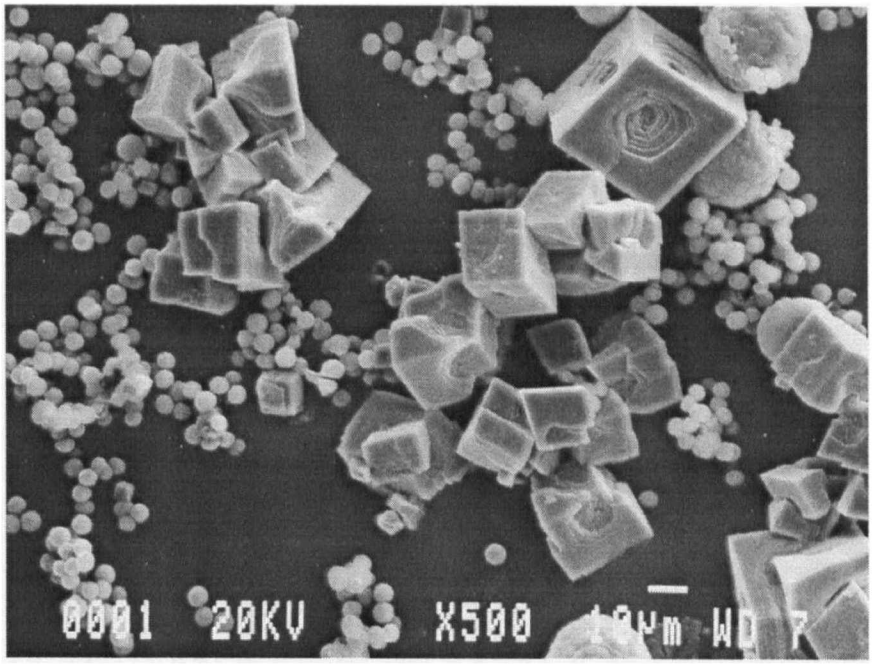

Figure 7.27 SEM micrograph of vaterite and calcite

Reasons for the formation of both polymorphs could include the longer time available for transformation of the vaterite crystals in the precipitation reactor, and therefore the increased amount of time for the metastable polymorph to change into the more stable calcite, and the different pH range in the semibatch experiments favouring the formation of calcite. As the nucleation, growth, agglomeration and disruption kinetics of the two polymorphs are different, the kinetic parameters determined from the continuous experiments, where only vaterite occurred, no longer apply. However, an

extensive study of the precipitation kinetics of calcite and an extension of the SFM to account for different polymorphs, which would improve the results from the simulations, is beyond the scope of this research.

Total number of particles m_0

In Figure 7.28, the number of particles m_0, plotted versus the specific power input, scatters on different scales. On all three scales a minimum was found; however, there was no clear trend with increasing scale. This could result from a different degree of the solution-mediated transformation of vaterite into calcite on different scales, leading to different total numbers of particles.

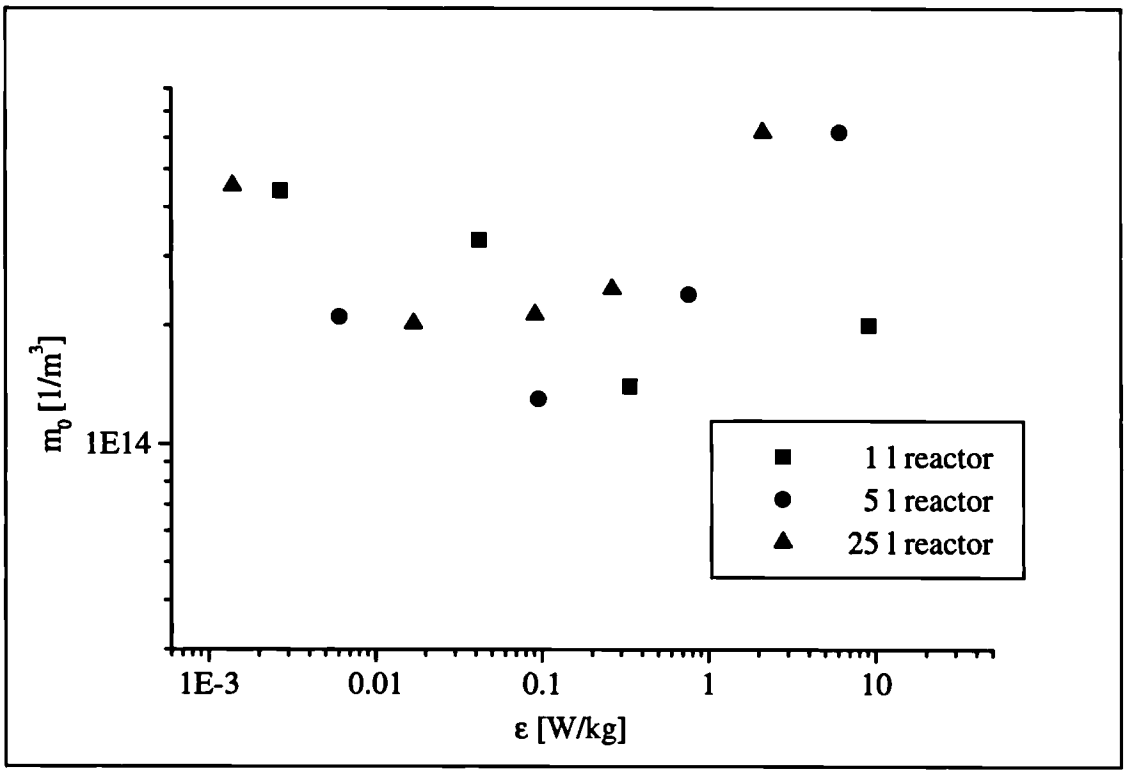

Figure 7.28 Total number of particles for reference conditions ($CaCO_3$, Rushton turbine, 40 min feed time, feed point position close to the impeller, total concentration 0.04M)

Number density of particles in the first size interval $n(L_0)$

In contrast to the total number of particles, the number density of the smallest detectable particles and therefore a property quantifying nucleation, plotted versus the specific power input, corresponds more satisfactorily on different scales (Figure 7.29). As the particles usually nucleate as metastable, but kinetically favoured, vaterite, the kinetics of which were determined from the continuous laboratory-scale experiments, the number of particles can be modelled and scaled up. The subsequent polymorph transformation into calcite, however, cannot be accounted for by the SFM, which is the reason why it cannot predict the total number of particles and mean size.

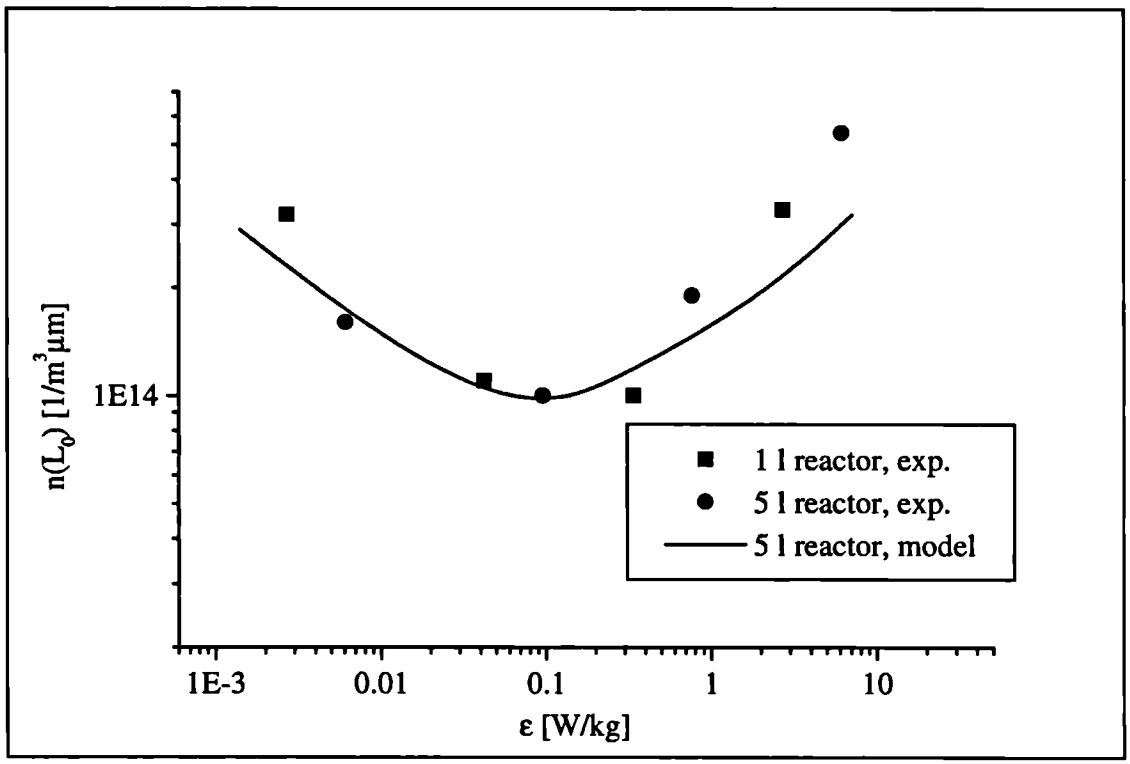

Figure 7.29 Number density of nuclei for reference conditions ($CaCO_3$, Rushton turbine, 40 min feed time, feed point position close to the impeller, total concentration 0.04M)

As already mentioned with regard to calcium oxalate, poor mixing conditions result in high nucleation rates and thus large numbers of nuclei. The level of

supersaturation in the feed zone can become very high, as the feed reactant is directly mixed with the second reactant and not via the bulk as in the continuous mode of operation.

Coefficient of variation c.v.

The coefficient of variation, which is a measure of the width of the particle size distribution, is shown in Figure 7.30. Under insufficient mixing conditions, the distribution is very wide as the two polymorphs, vaterite and calcite, form particles of very different sizes. In Figure 7.31, large calcite crystals amongst numerous small vaterite crystals are formed by transformation from agglomerates of vaterite (Spanos and Koutsoukos, 1998). The coefficient of variation is therefore high.

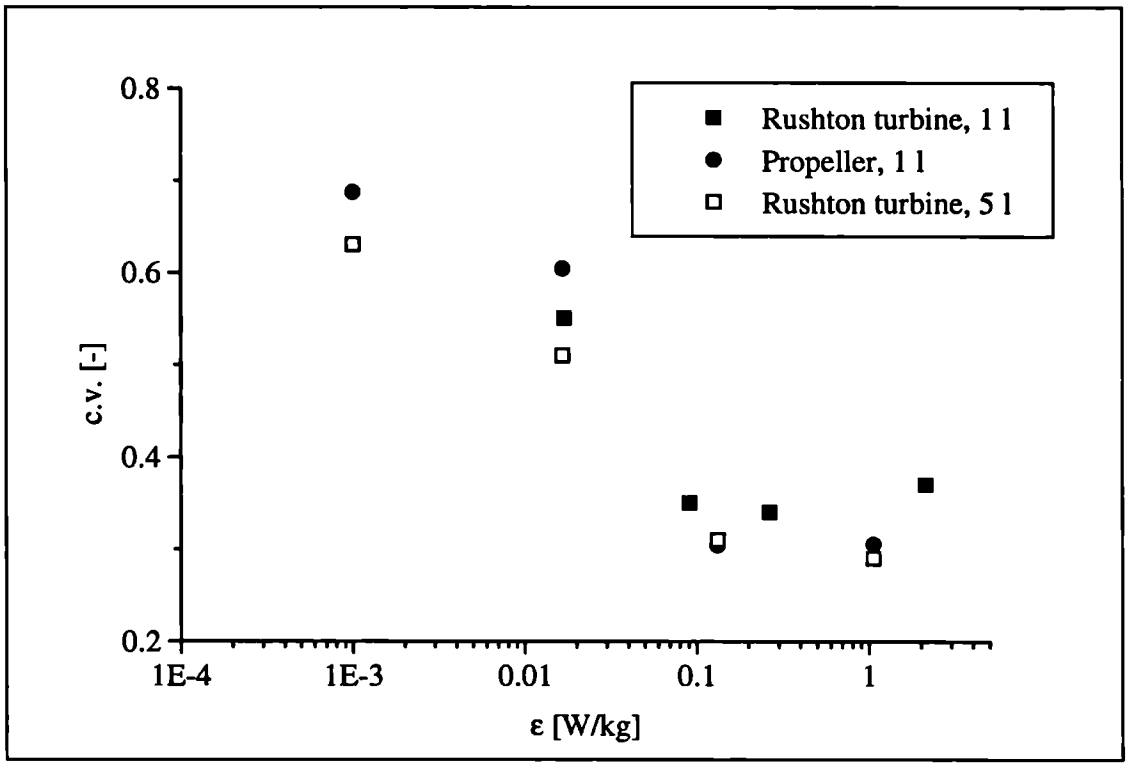

Figure 7.30 Coefficient of variation for reference conditions ($CaCO_3$, Rushton turbine, 40 min feed time, feed point position close to the impeller, total concentration 0.04M)

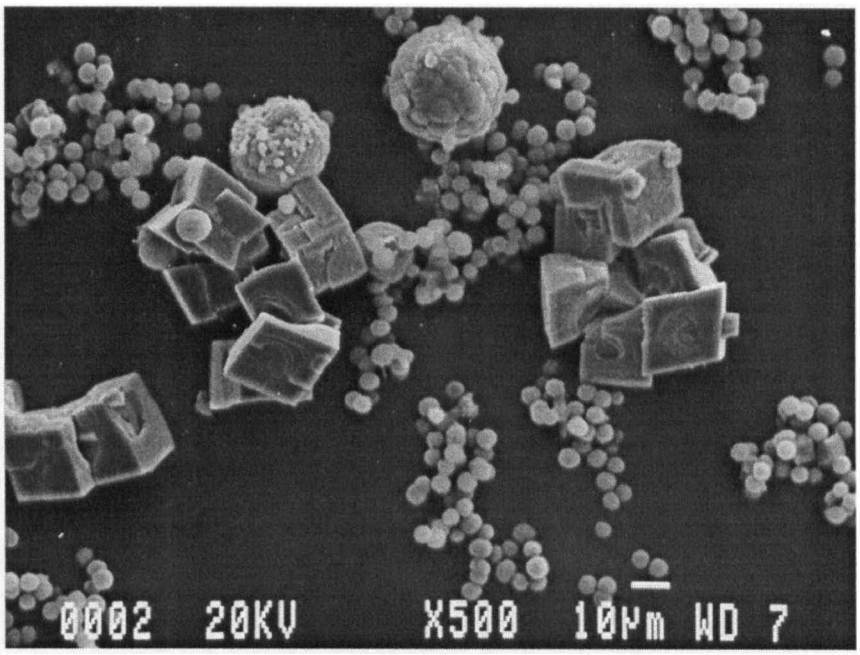

Figure 7.31 SEM micrograph of vaterite and calcite (100 rpm)

With a higher stirrer speed and better mixing, the mean size of the two polymorphs formed is very similar, resulting in a narrower size distribution and a smaller coefficient of variation (Figure 7.32). In addition, increased particle breakage and agglomeration inefficiency lead to a c.v. of about 0.3 and therefore narrower size distributions than are obtained from an MSMPR reactor, where the coefficient of variation independent of power input is 0.5.

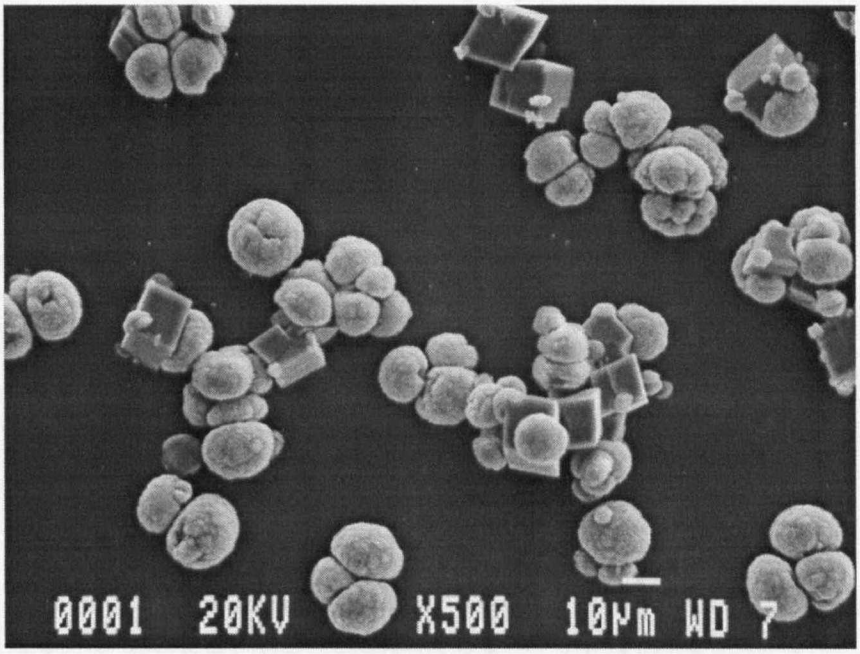

Figure 7.32 SEM micrograph of vaterite and calcite (500 rpm)

CHAPTER 8

SCALE-UP RECOMMENDATIONS, CONCLUSIONS AND FURTHER RESEARCH

8.1 SCALE-UP RECOMMENDATIONS

For many unit operations in chemical engineering, theoretical or empirical scale-up rules have been established. In processes where kinetic rates (*e.g.* reaction or precipitation rates) are controlled by the degree of mixing, however, these simple scale-up criteria often fail. The approach to scale-up developed in this research takes into account these mixing effects on different scales and has thus been successfully applied to continuous and semibatch precipitation processes.

Scale-up with constant stirrer speed

This scale-up criterion is based on achieving a constant pumping rate per unit volume with scale-up and therefore leads to similar macromixing on different scales, as the circulation time in the reactor remains constant.

The pumping rate per unit volume is defined as

$$Q_{pump} = \frac{k_{pump} N d_s^3}{V} = const. \qquad (8.1).$$

With

$$Q_{pump,1} = \frac{k_{pump} N_1 d_{s1}^3}{V_1} = Q_{pump,2} = \frac{k_{pump} N_2 d_{s2}^3}{V_2} \qquad (8.2)$$

and

$$\frac{d_{s2}}{d_{s1}} = \left(\frac{V_2}{V_1}\right)^{1/3} \qquad (8.3)$$

$$N_1 = N_2 \qquad (8.4)$$

is obtained.

In Figures 8.1 and 8.2, the mean particle size is plotted versus the stirrer speed for continuous and semibatch precipitation of calcium oxalate. The data scatter substantially with scale-up; this criterion is therefore not suitable for scaling up precipitation processes. This result is not unexpected since it was proven in Chapter 4 that macromixing was not the controlling process for the geometries under investigation, the residence time distribution (RTD) obtained suggesting ideal macromixing.

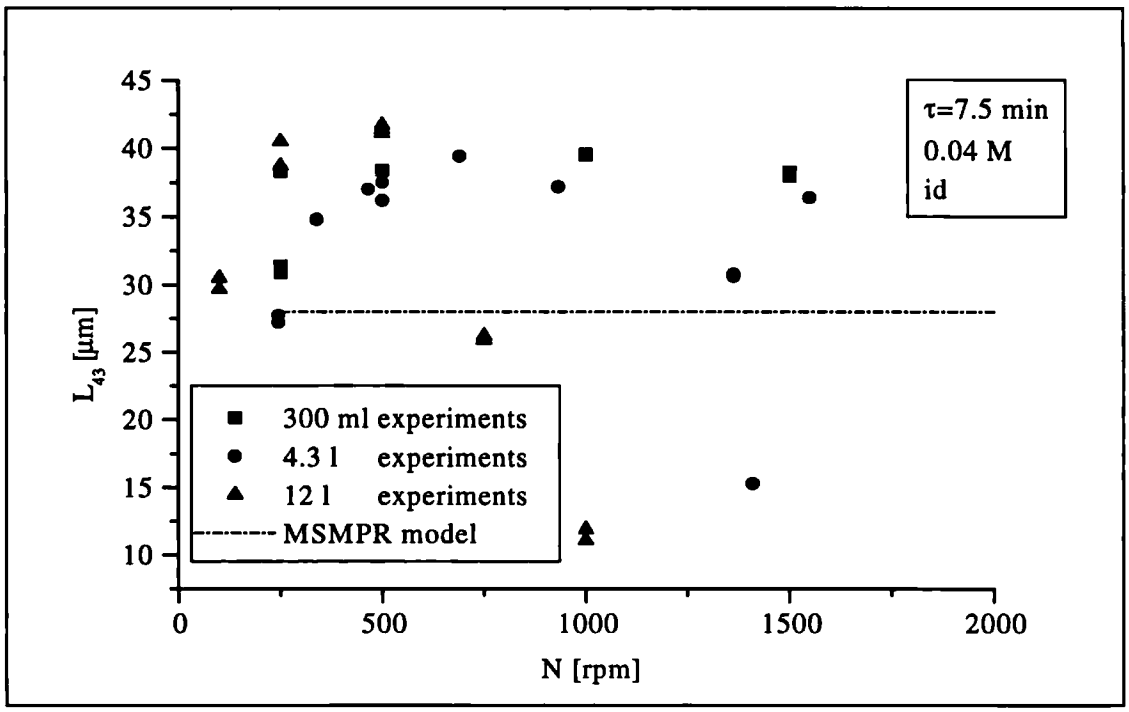

Figure 8.1 Scale-up with constant stirrer speed (continuous precipitation)

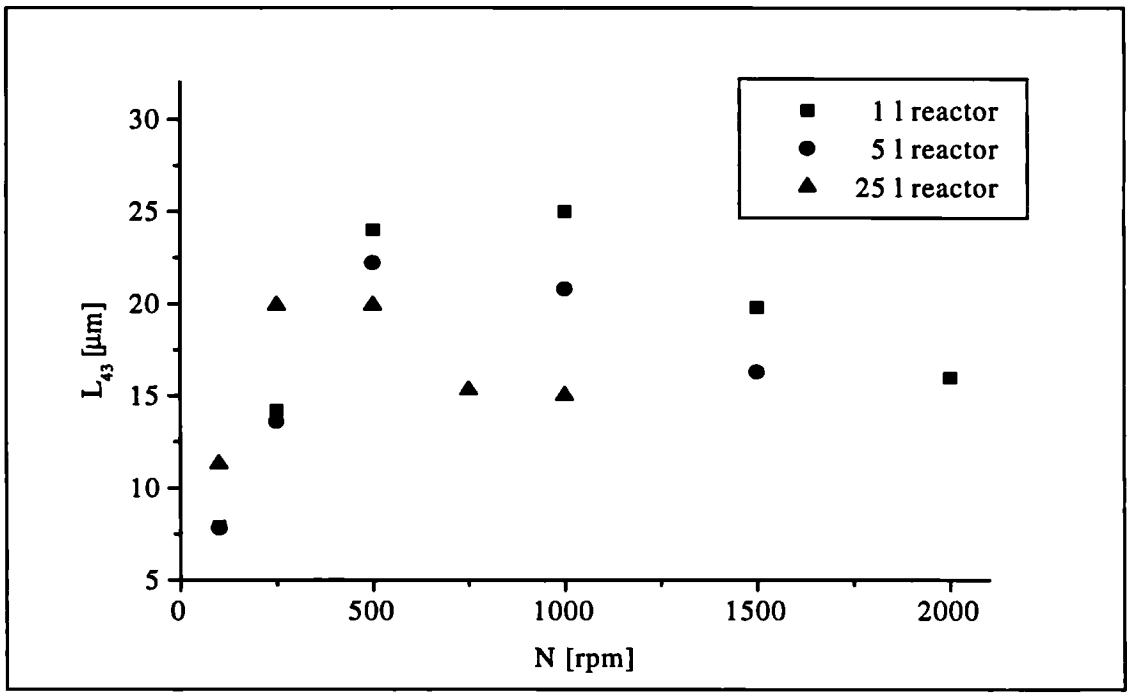

Figure 8.2 Scale-up with constant stirrer speed (semibatch precipitation)

Scale-up with constant tip speed

If the tip speed of the impeller blades is kept constant with scale-up, *i.e.*

$$N_1 \pi d_{s1} = N_2 \pi d_{s2} = const. \qquad (8.5),$$

the criterion for scale-up becomes

$$N_2 = N_1 \left(\frac{V_2}{V_1} \right)^{-1/3} \qquad (8.6).$$

This criterion has been applied to the same set of data as above, with the result that the data on different scales are less scattered than for scale-up with constant stirrer speed (Figures 8.3 and 8.4). Scale-up with constant tip speed, which implies constant shear in the impeller region, can be considered an approximation to scale-up with constant mesomixing, as the blending of the incoming reactant with the bulk or second reactant is closely linked to the shear field in the mixing zone. As Oldshue (1983) pointed out, however, the shear rate distribution changes with scale-up and this criterion is therefore only an approximation, based on mean shear rates in the impeller zone.

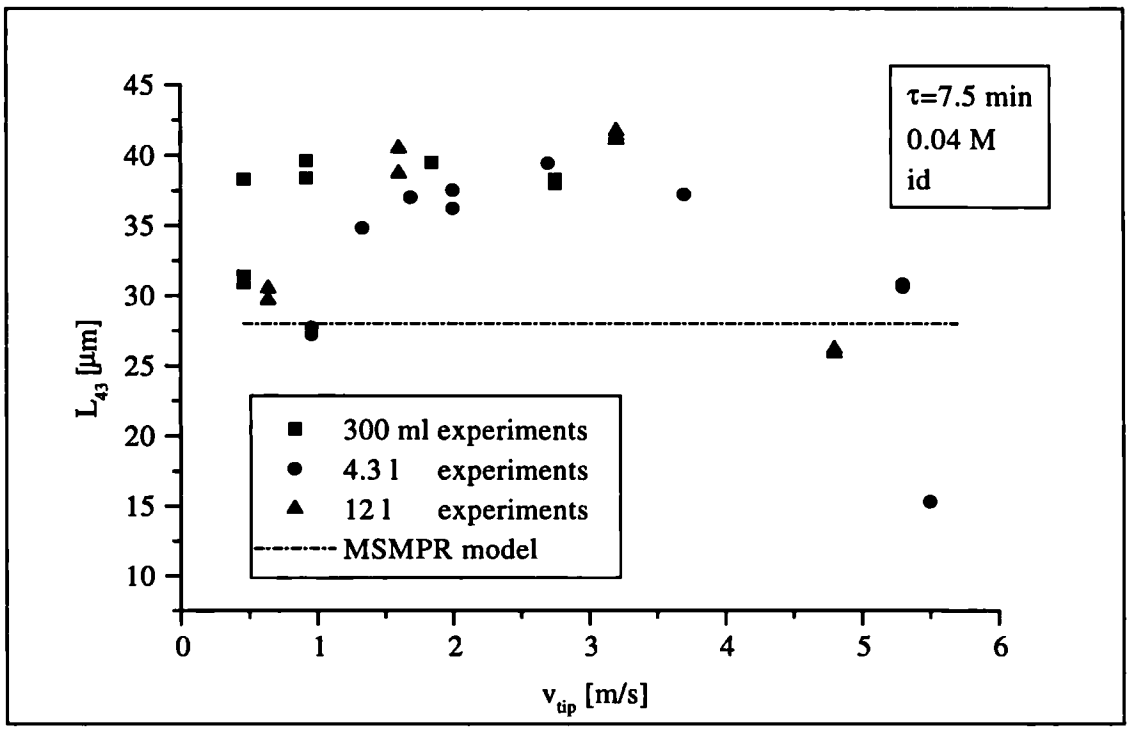

Figure 8.3 Scale-up with constant tip speed (continuous precipitation)

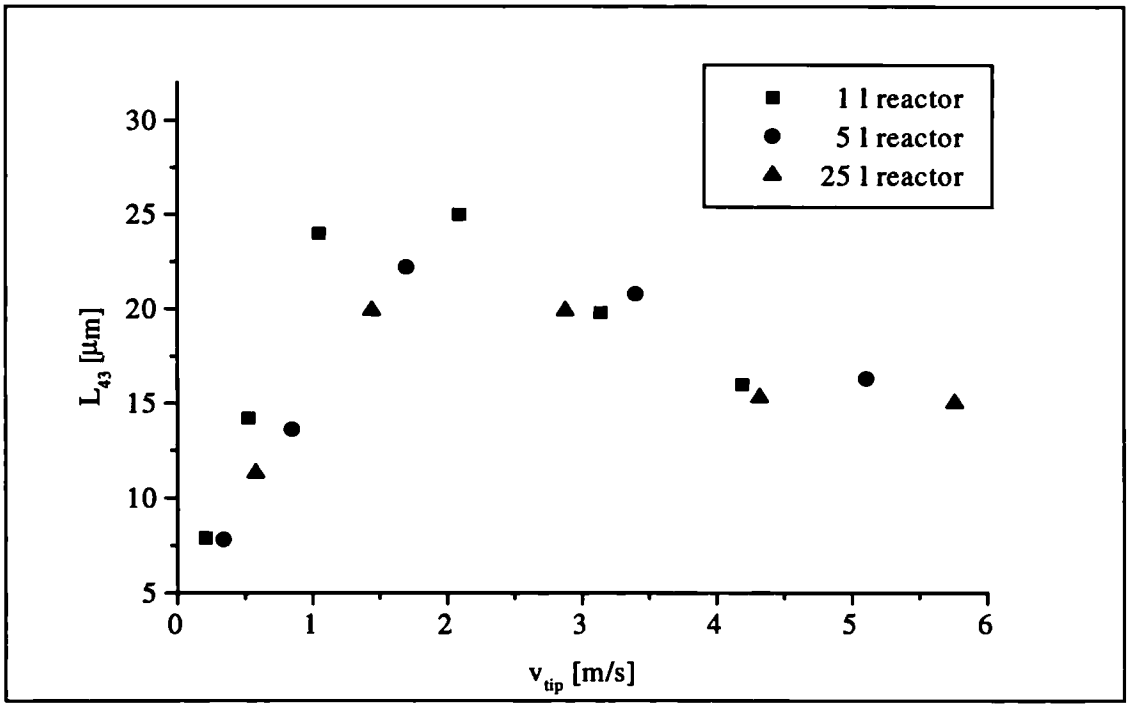

Figure 8.4 Scale-up with constant tip speed (semibatch precipitation)

Scale-up with constant power input per unit volume

The scale-up criterion which is probably most widely used for mixing-limited unit operations is based on constant power input per unit volume according to

$$\varepsilon = \frac{k_{power} d_s^5 N^3}{V} = const. \tag{8.7}$$

and

$$\frac{k_{power1} d_{s1}^5 N_1^3}{V_1} = \frac{k_{power2} d_{s2}^5 N_2^3}{V_2} \tag{8.8}.$$

This leads to

$$N_2 = N_1 \left(\frac{V_2}{V_1} \right)^{-2/9} \tag{8.9}.$$

The importance of the local energy dissipation and thus the specific power input for micromixing has already been referred to in Chapter 5, where the micromixing time

was related to the Kolmogoroff length scale of mixing. Even though it was possible to predict properties on different scales using this criterion, it failed with respect to other conditions. Figure 6.9 shows the experimental results of scale-up of continuous precipitation, where the application of ε = constant was not successful. In Figure 7.19, widely scattering results were also obtained with this criterion.

The failure of "conventional" criteria may be due to the fact that it is not only one mixing process which can be limiting, but for example an interplay of micromixing and mesomixing that can influence the kinetic rates. Thus, by scaling up with constant micromixing times on different scales, the mesomixing times cannot be kept constant but will differ, and consequently the precipitation rates (*e.g.* nucleation rates) will tend to deviate with scale-up.

Scale-up with the Segregated Feed Model (SFM)

In order to account for both micromixing and mesomixing effects, a mixing model for precipitation based on the Segregated Feed Model (SFM) has been developed (Chapter 5) and applied to continuous and semibatch precipitation (Chapters 6 and 7). As suggested in Chapter 5.6, the model can be extended by establishing a network of ideally macromixed reactors if macromixing plays a dominant role.

The model is able to predict the influence of mixing on particle properties and kinetic rates on different scales for a continuously operated reactor and a semibatch reactor with different types of impellers and under a wide range of operational conditions. From laboratory-scale experiments, the precipitation kinetics for nucleation, growth, agglomeration and disruption have to be determined as described in Chapter 4. The fluid dynamic parameters, *i.e.* the local specific energy dissipation around the feed point, can be obtained either from Computational Fluid Dynamics (CFD) or from Laser Doppler Anemometry (LDA) measurements. In the compartmental Segregated Feed Model (SFM), the population balance is solved and the particle properties of the final product are predicted. As the model contains physical rather than phenomenological parameters, it can be used for scale-up.

8.2 CONCLUSIONS

In this research it has been proven that scale-up of continuous and semibatch precipitation processes from laboratory scale to pilot scale is possible but that conventional rules are inadequate. For successful scale-up the methodology introduced in this research should be followed carefully.

Precipitation kinetics

Reliable kinetic data are of paramount importance for scale-up. Apart from nucleation and growth, secondary processes such as agglomeration and particle disruption occur and cannot be neglected as they have a strong influence on the particle size distribution and product properties. If necessary, even ageing and ripening processes, as described in Chapter 2, have to be investigated experimentally and implemented in the population balance. In the case of calcium carbonate, the formation of different stable and metastable polymorphs leads to a further complication of the precipitation kinetics.

The method for determining the kinetic rates for nucleation, growth, agglomeration and disruption, as presented in this research with regard to calcium oxalate and calcium carbonate, proved to be both reliable and accurate. As not all the kinetic parameters have to be estimated at once from the population density distribution, they may be obtained individually and sequentially, and therefore sources of error can be reduced.

Design of experiments (DOE), a method of minimising the number of experiments necessary to describe the influence of parameters on a process, was applied to the laboratory-scale continuous precipitation experiments with calcium oxalate. In an analysis of the reliability of this method for scale-up predictions, it was found that only part of the kinetic parameters and properties was predicted correctly on the larger scales; it can therefore be concluded that the suitability of DOE for scale-up of precipitation processes is limited.

Computational Fluid Dynamics (CFD)

From a single-phase sliding mesh Computational Fluid Dynamics (CFD) simulation of the reactor geometry, the local rates of the specific energy dissipation around the feed points were obtained. These local values are crucial for the nucleation rates in the reactor, as the degree of micromixing and mesomixing determines the field of supersaturation around the feed zones. Due to high levels of supersaturation, very rapid primary nucleation is likely to occur in these zones, while in the other zones of the reactor the "slower" kinetic processes, *e.g.* growth, take place. Therefore, the mixed-suspension mixed-product-removal (MSMPR) concept, which is often applied in conventional crystallisation, fails as the reactor is no longer ideally mixed – one of the assumptions for an MSMPR crystallizer.

Scale-up using the Segregated Feed Model (SFM)

The Segregated Feed Model (SFM) can account for these local differences in the level of supersaturation mentioned above. As this is a compartmental model, the feed and bulk zones exchange mass by diffusion (micromixing) and convection (mesomixing). Since the exchange parameters in the model, the micromixing and mesomixing time are physical parameters and can thus be calculated directly from the fluid dynamics in the reactor, the model can be used for scale-up.

Qualitative analysis of the influence of mixing on the precipitation rates and the particle properties showed the important role that mixing plays in precipitation processes. A detailed quantitative analysis of continuous and semibatch precipitation further proved that the model is also capable of quantitatively predicting the mean particle size on different scales for a variety of process conditions. While conventional scale-up criteria failed, the experimental results on three different scales corresponded very well with the results obtained from the SFM.

Why do conventional scale-up criteria fail?

The conventional scale-up criteria "scale-up with constant stirrer speed", "scale-up with constant tip speed" and "scale-up with constant specific energy input" are all based on the assumption that only one mixing process is limiting. If, for example, the specific energy input is kept constant with scale-up, the same micromixing behaviour could be expected on different scales. The mesomixing time, however, will change with scale-up; as a result, the kinetic rates and particle properties will be different and scale-up will fail. In Figure 5.6, the qualitative dependence of the nucleation rate on micromixing and mesomixing is shown for continuous precipitation; it can be seen that even if the micromixing time is kept constant with scale-up, a different mesomixing time leads to a difference in the nucleation rate and therefore to different particle properties.

Process conditions

The SFM successfully accounts for the influence of mixing, feed point position, stirrer type and residence time/feed time on the particle properties. By varying the parameters mentioned above, the properties can be influenced to a great extent, leading to products with very different properties, for example mean size, surface area and filtrability. Using the model, it is possible to predict *a priori* the change in properties due to a change in the operational conditions. Generally, it was found that in the semibatch mode of operation a change in the parameters has a greater effect on the precipitation rates and the particle properties than in the continuous mode.

Scale-up methodology

The methodology of how to scale up a precipitation process is depicted in Figure 8.5. For large-scale predictions, kinetic information can be obtained from laboratory-scale experiments. On the large scale, only CFD simulations (or LDA measurements) need to be carried out in order to obtain the local energy dissipation in the feed zone(s). Using this information, the Segregated Feed Model predicts the

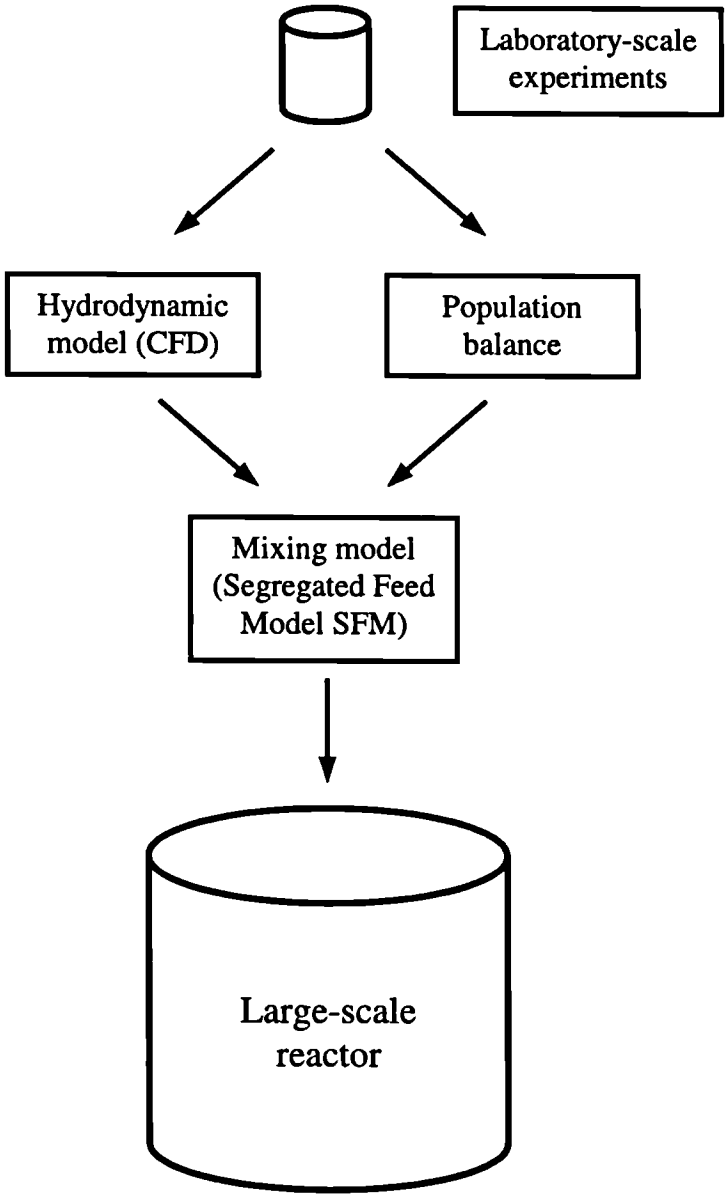

Figure 8.5 Scale-up methodology

particle properties on the large scale. Scale-up thus becomes possible without time-consuming and costly large-scale precipitation experiments. This methodology is very efficient as it combines the advantages of both a CFD and a population balance approach without having to solve the equations together, which is currently still impracticable due to the computational demand and simulation time required. The results of the model have been successfully validated with experiments under a wide range of conditions for the precipitation of calcium oxalate and calcium carbonate for both continuous and semibatch precipitation (Chapters 6 and 7).

8.3 FURTHER RESEARCH

Even though a concise method of precipitation scale-up has been developed in this research, the work also opens up new questions and suggests areas for further research. Recommendations for further research may be given in the following areas.

Scale-up of precipitation processes to industrial scale

This research was concerned with scale-up from laboratory scale to pilot scale, covering a volumetric scale-up ratio of about 100. For scale-up to industrial scale, a further increase in the reactor volume by a factor of about 100 is necessary. Experimental results obtained on the industrial scale could be modelled using the Segregated Feed Model. As the model developed is scale-independent, it could be applied directly to the industrial scale.

Scale-up without geometrical similarity on different scales

Scale-up was performed on geometrically similar precipitation reactors on different scales; it was found, however, that the SFM predicts the correct particle properties for different geometries of stirred tanks, for example, for different stirrer types in the semibatch experiments. Thus, it has been indirectly proven that the approach can also be applied to geometrically non-similar scale-up. An extended

application of the method to other types of mixing equipment, for example Tee-mixers and jet mixers, as described in Chapter 2, has yet to be made.

Macromixing limitation

If, in addition to micromixing and mesomixing, macromixing controls the precipitation rates, the model can be extended as suggested in Chapter 5. Using a tank-in-series model, as is well established in chemical reaction engineering, non-ideal macromixing of the reactor contents can be accounted for. Where necessary, the model can be further refined and recycle loops and plug flow zones can be included in order to model different flow characteristics in different zones of the reactor.

High suspension density

At high suspension densities in the precipitation reactor, a single-phase Computational Fluid Dynamics (CFD) simulation of the flow field may no longer be sufficient, as the influence of the particles on the fluid dynamics can no longer be ignored. Furthermore, in the semibatch mode of operation, the specific energy input and suspension properties, for example the viscosity and density, become time-dependent. Due to the modular concept of the scale-up method presented in this research, these extensions can be implemented in the Segregated Feed Model without having to fundamentally change the approach.

Extension of the population balance

The population balance as used in this work accounts for nucleation, growth, agglomeration and particle disruption. For some applications, it might be necessary to include the kinetics for Ostwald ripening, recrystallization or other ageing processes. With respect to calcium carbonate, in the semibatch mode of operation the formation of different polymorphs has to be included in the population balance concept in order to improve the model predictions. For example, Chakraborty and Bhatia (1996a) solved the

population balance for the precipitation of calcium carbonate as a mixture of polymorphs and verified their method experimentally (Chakraborty and Bhatia, 1996b).

Application of the SFM to consecutive-competitive reaction systems

By using consecutive-competitive reaction systems, a segregation index can be defined and therefore the degree of micromixing can be analysed (Villermaux and Falk, 1994 and Fournier *et al.*, 1996). Experimental results on different scales (Bourne and Yu, 1994) can be compared with the predictions of the Segregated Feed Model as the authors could not model the experimental results with their model.

Application of the scale-up method for precipitation to other unit operations

The scale-up method proposed for precipitation can also be applied to other unit operations where the reaction rates are mixing-limited. In polymerisation processes, for example, the molecular weight distribution of the polymer depends to a significant extent on the degree of mixing in the polymerisation reactor (Lee and Lee, 1987 and Tosun, 1992). This dependence is similar to that of the crystal size distribution on micromixing and mesomixing in precipitation processes. Therefore, scale-up of polymerisation processes can be tackled in a similar way to the method suggested in this research.

NOMENCLATURE

a [-]	aggregation parameter
a_g [-]	growth parameter
a_i [mol m^{-3}]	activity
A [m^2]	area, cross section
A [$m^{1.5}$ $mol^{-0.5}$]	constant in Debye-Hückel equation
A_{het} [m^{-3} s^{-1}]	heterogeneous nucleation rate constant
$A_{1,het}$ [m^{-3} s^{-1}]	heterogeneous nucleation rate constant in power law
A_{hom} [m^{-3} s^{-1}]	homogeneous nucleation rate constant
$A_{1,hom}$ [m^{-3} s^{-1}]	homogeneous nucleation rate constant in power law
A_{sec} [m^{-3} s^{-1}]	secondary nucleation rate constant
A_T [m^2 m^{-3}]	surface area per unit volume
b(v,x_k) [-]	breakage function
b_g [-]	growth parameter
B [m^{-4} s^{-1}]	birth rate
B^0 [m^{-3} s^{-1}]	nucleation rate (general)
B^0_i [m^{-3} s^{-1}]	nucleation rate in compartment i
B^0_{hom} [m^{-3} s^{-1}]	homogeneous nucleation rate
B^0_{het} [m^{-3} s^{-1}]	heterogeneous nucleation rate
B^0_{sec} [m^{-3} s^{-1}]	secondary nucleation rate
c [mol m^{-3}]	concentration
c^* [mol m^{-3}]	equilibrium concentration
c_g [-]	growth parameter
c_I [mol m^{-3}]	concentration at interface
c_j [mol m^{-3}]	concentration of reactant j
c_0 [mol m^{-3}]	initial concentration
c_j^0 [mol m^{-3}]	feed concentration of reactant j
Δc [mol m^{-3}]	concentration difference
c.v. [-]	coefficient of variation
C_A [-]	aggregation parameter in Thompson kernel
d [m]	characteristic length
d_S [m]	diameter of stirrer

D [m]	reactor diameter
D [m^{-4} s^{-1}]	death rate
E_i [-]	collection efficiency
E_{ij} [s^{-1}]	velocity gradient in Boussinesq equation
$f(\varphi)$ [-]	nucleation enhancement function
g [-]	growth rate order
g [m s^{-2}]	acceleration of free fall
G [m s^{-1}]	growth rate
I [-]	ionic strength
k [J K^{-1}]	Boltzmann constant
k [m^2 s^{-2}]	kinetic energy
k_a [-]	surface area shape factor
k_d [mol m^{-2} s^{-1}]	diffusion mass transfer coefficient
k_g [m s^{-1}]	growth rate coefficient
k_m [mol m^{-2} s^{-1}]	mass transfer coefficient
k_n [m^{-4} s^{-1}]	nucleation rate coefficient
k_{power} [-]	power coefficient
k_{pump} [-]	pumping rate coefficient
k_r [mol m^{-2} s^{-1}]	reaction mass transfer coefficient
k_v [-]	volumetric shape factor
K_1, K_2, K_3 [m^3 mol^{-1}]	association constants
K_{aggl} [m^3 s^{-1}]	agglomeration rate
K_{ap} [mol^2 m^{-6}]	activity product
K_{disr} [s^{-1}]	disruption rate
K_{sp} [mol^2 m^{-6}]	solubility product
L [m]	particle size
L_0 [m]	particle size of lower bound of first size class
L_{10} [m]	number mean size
L_{43} [m]	volume mean size
L_d [m]	dominant size
L_T [m]	cumulative length

L_u [m]	particle size of class u
L_v [m]	particle size of class v
ΔL_j [m]	width of particle size class j
m (L) [kg m^{-1}]	mass density function
m_{feed} [kg m^{-3}]	specific mass of a component in the feed solution
m_j [m^{j-3}]	jth moment of distribution
m_{liquid} [kg m^{-3}]	specific mass of a component in solution
m_{prec} [kg m^{-3}]	specific mass of a precipitated component
m_{susp} [kg]	mass of suspension
ΔM_j [kg]	mass fraction
M_T [kg m^{-3}]	solids concentration, suspension density
MW_j [kg mol^{-1}]	molecular weight of component j
n [-]	nucleation rate order
n [# m^{-4}]	population density (general)
$n_{i,k}$ [-]	weighting term (i,k) in weighting matrix
n_k [# m^{-4}]	population density of stream k
n_P [# m^{-4}]	population density of product P
n_0 [# m^{-3}]	population density of nuclei
$n(x)$ [# m^{-4}]	population density at point with location x (x,y,z)
N_1, N_2 [s^{-1}]	stirrer speed on scales 1 and 2 respectively
N_i [# m^{-3}]	number of particles in size class i
N_T [#]	total number of particles
P [W]	power input
Po [-]	power number
Q_k [m^3 s^{-1}]	flow rate of stream k
Q_{pump} [m^3 s^{-1}]	pumping capacity of impeller
r [-]	volumetric discretization ratio
r [m]	particle radius
$r_{j,k}$ [-]	reaction rate of component j in compartment k
S [-]	supersaturation (general)
S' [-]	disruption function

S_{ap} [-]	supersaturation based on activity product
S_{init} [-]	initial supersaturation
S_{sp} [-]	supersaturation based on solubility product
Sh [s^{-1}]	shear rate
t [s]	time
t_{12} [s]	time constant for direct mixing of feed streams
t_c [s]	circulation time
t_{ind} [s]	induction time
t_{macro} [s]	time constant for macromixing
$t_{meso,j}$ [s]	time constant for mesomixing in compartment j
$t_{micro,j}$ [s]	time constant for micromixing in compartment j
T [K]	temperature
T [Nm]	torque
$u_{j,ik}$ [mol m^{-3}]	exchange flow of component j between compartments i,k
U [s^{-1}]	velocity gradient
v [m s^{-1}]	velocity (general)
v_e [m s^{-1}]	external velocity
v_i [m s^{-1}]	internal velocity
$\bar{v}$ [m s^{-1}]	mean velocity
v' [m s^{-1}]	fluctuating velocity
v_{tip} [m s^{-1}]	tip speed
$v\,(L)$ [m^3 m^{-1}]	volumetric density function
V [m^3]	volume
V_j [m^3]	subvolume of compartment j
V_{tot} [m^3]	reactor volume
x_k [m^3]	discretized particle volume
X_i [-]	coded factor for design of experiments (DOE)

Greek

β_{aggl}	agglomeration kernel
β_{disr}	disruption kernel
γ [J m^{-2}]	surface energy
γ_i [-]	activity coefficient
$\delta_{j,k}$ [-]	Kronecker delta function
ε [W kg^{-1}]	specific power input
φ [-]	wetting angle
η [-]	volume correction function
μ [kg m^{-1}s^{-1}]	dynamic viscosity
μ_t [kg m^{-1}s^{-1}]	turbulent viscosity
ν [m^3 mol^{-1}]	molecular volume
ν [m^2 s^{-1}]	kinematic viscosity
ν_i [-]	stoichiometric coefficient of component *i*
Ψ [-]	sphericity
ρ [kg m^{-3}]	solution density
ρ_c [kg m^{-3}]	crystal density
ρ_s [kg m^{-3}]	solids density
σ [-]	supersaturation (general)
σ_j [-]	supersaturation in compartment *j*
σ^2 [-]	variance of distribution
τ [s]	residence time
τ_{ij} [N m^{-2}]	shear stress in plane $x_i x_j$
ω [s^{-1}]	angular velocity

REFERENCES

Allen, T. *Particle Size Measurement.* 3rd edn., Chapham and Hall (1981).

Åslund, B. L. and Rasmuson, Å. C. Semibatch reaction crystallization of benzoic acid. *AIChE J.*, **38**, 328-342 (1992).

Austin, L., Shoji, V., Jindal, V., Savage, K. and Kimpel, R. Some results on the description of size reduction as a rate process in various mills. *Ind. Eng. Chem. Process Des. Dev.*, **15**, 187-196 (1976).

Bakker, A., Laroche, R. D., Wang, M. H. and Calabrese, R. V. Sliding mesh simulation of laminar flow in stirred reactors. *Trans. IChemE*, **75**, 42-44 (1997).

Baldyga, J. and Bourne, J. R. A fluid mechanical approach to turbulent mixing and chemical reaction. Part I: Inadequacies of available methods. *Chem. Eng. Commun.*, **28**, 231-241 (1984a).

Baldyga, J. and Bourne, J. R. A fluid mechanical approach to turbulent mixing and chemical reaction. Part II: Micromixing in the light of turbulence theory. *Chem. Eng. Commun.*, **28**, 243-258 (1984b).

Baldyga, J. and Bourne, J. R. A fluid mechanical approach to turbulent mixing and chemical reaction. Part III: Computational and experimental results for the new micromixing model. *Chem. Eng. Commun.*, **28**, 259-281 (1984c).

Baldyga, J. and Bourne, J. R. Simplification of micromixing calculations. I. Derivation and application of new model. *Chem. Eng. J.*, **42**, 83-92 (1989a).

Baldyga, J. and Bourne, J. R. Simplification of micromixing calculations. II. New applications. *Chem. Eng. J.*, **42**, 93-101 (1989b).

Baldyga, J. and Bourne, J. R. Interactions between mixing on various scales in stirred tank reactors. *Chem. Eng. Sci.*, **47**, 1839-1848 (1992).

Baldyga, J., Podgorska, W. and Pohorecki, R. Mixing-precipitation model with application to double feed semibatch precipitation. *Chem. Eng. Sci.*, **50**, 1281-1300 (1995).

Baldyga, J. and Poherecki, R. Turbulent micromixing in chemical reactors - a review. *Chem. Eng. J.*, **58**, 183-195 (1995).

Baldyga, J., Bourne, J. R. and Hearn, S. J. Interaction between chemical reactions and mixing on different scales. *Chem. Eng. Sci.*, **52**, 457-466 (1997).

Berthoud, A. Théorie de la formation des faces d'un crystal. *Journal de Chimie Physique*, **10**, 624-653 (1912).

Bisio, A. and Kabel, R. L. *Scale-up of Chemical Processes: Conversion from Laboratory Scale Tests to Successful Commercial Size Design.* Wiley, New York (1985).

Bourne, J. R. Micromixing revisited. *IChemE Symp. Ser.* **87** (ISCRE 8), 797-813 (1985).

Bourne, J. R. and Dell'Ava, P. Micro- and macromixing in stirred tank reactors of different sizes. *Chem. Eng. Res. Des.*, **65**, 180-186 (1987).

Bourne, J. R. and Yu, S. Investigation of micromixing in stirred tank reactors using parallel reactions. *Ind. Eng. Chem. Res.*, **33**, 41-55 (1994).

Bramley, A. S. Hounslow, M. J. and Ryall, R. L. Aggregation during precipitation from solution: A method for extracting rates from experimental data. *J. Coll. Int. Sci.*, **183**, 155-165 (1996a).

Bramley, A. S. Hounslow, M. J. and Ryall, R. L. Aggregation during precipitation from solution. Kinetics for calcium oxalate monohydrate. *Chem. Eng. Sci.*, **52**, 747-757 (1996b).

Brecevic, Lj., Skrtic, D. and Garside, J. Transformation of calcium oxalate hydrates. *J. of Crystal Growth*, **74**, 399-408 (1986).

Brecevic, Lj. and Kralj, D. Factors influencing the distribution of hydrates in calcium oxalate precipitation. *J. of Crystal Growth*, **97**, 460-468 (1989).

Brown, C. M., Ackermann, D. K., Purich, D. L. and Finlayson, B. Nucleation of calcium oxalate monohydrate: use of turbidity measurements and computer-assisted simulations in characterising early events in crystal formation. *J. of Crystal Growth*, **108**, 455-464 (1991).

Buckingham, E. On physically similar systems; illustrations of the use of dimensional equations. *Phys. Review*, **4**, 335-376 (1914).

Burton, W. K., Cabrera, N. and Frank, F. C. The growth of crystals and the equilibrium structure of their surfaces. *Philosophical Transactions*, **A243**, 299-358 (1951).

Chakraborty, D. and Bhatia, S. K. Formation and aggregation of polymorphs in continuous precipitation. 1. Mathematical modelling. *Ind. Eng. Chem. Res.*, **35**, 1985-1994 (1996a).

Chakraborty, D. and Bhatia, S. K. Formation and aggregation of polymorphs in continuous precipitation. 2. Kinetics of $CaCO_3$ precipitation. *Ind. Eng. Chem. Res.*, **35**, 1995-2006 (1996b).

Chang, L.-J., Mehta, R. V. and Tarbell, J. M. An evaluation of models of mixing and chemical reaction with a turbulence analogy. *Chem. Eng. Commun.*, **42**, 139-155 (1986).

Chen, J., Zheng, C. and Chen, G. Interaction of macro- and micromixing on particle size distribution in reactive precipitation. *Chem. Eng. Sci.*, **51**, 1957-1966 (1996).

Choplin, L. and Villermaux, J. Viscous mixing in polymer reactors. *AIChE Symp. Ser.*, **299**, 123-129 (1994).

Curl, R. L. Dispersed phase mixing-theory and effects in simple reactors. *AIChE J.*, **9**, 175 (1963).

Da Vinci, Leonardo *Notebooks.* (c. A.D. 1500).

Danckwerts, P. V. The effect of incomplete mixing on homogeneous reactions. *Chem. Eng. Sci.*, **8**, 93-99 (1958).

David, R. and Marcant, B. Prediction of micromixing effects in precipitation: Case of double-jet precipitators. *AIChE J.*, **40**, 424-432 (1994).

Davies, C. W. *Ion Association.* Butterworths, London (1962).

Davies, O. L. *The Design and Analysis of Industrial Experiments.* 2nd edn., Longman Group Limited (1979).

Dickey, D. S. Dimensional analysis, similarity and scale-up. *AIChE Symp. Ser.*, **293**, 143-150 (1993).

Fisher, R. A. *Statistical Methods, Experimental Design and Scientific Inference.* Oxford University Press (1990).

Fournier, M.-C. Falk, L. and Villermaux, J. A new parallel competing reaction system for assessing micromixing efficiency - experimental approach. *Chem. Eng. Sci.*, **51**, 5053-5064 (1996).

Franck, R., David, R., Villermaux, J. and Klein, J. P. Crystallization and precipitation engineering - II. A chemical reaction engineering approach to salicylic acid precipitation: Modelling of batch kinetics and application to continuous operation. *Chem. Eng. Sci.*, **43**, 69-77 (1988).

Franke, J. and Mersmann, A. The influence of the operational conditions on the precipitation process. *Chem. Eng. Sci.*, **50**, 1737-1753 (1995).

Galilei, Galileo *Discorsi.* German in Ostwalds Klassiker, **11**, 106-109 (1638).

Gardner, G. L. and Nancollas, G. H. Kinetics of dissolution of calcium oxalate monohydrate. *J. Phys. Chem.*, **79**, 2597-2600 (1975).

Garside, J. and Jancic, S. Measurement and scale-up of secondary nucleation kinetics for the potash alum-water system. *AIChE J.*, **25**, 948-958 (1979).

Garside, J., Brecevic, Lj. and Mullin, J. W. The effect of temperature on the precipitation of calcium oxalate. *J. of Crystal Growth*, **57**, 233-240 (1982).

Garside, J. and Tavare, N. S. Mixing, reaction and precipitation: limits of micromixing in an MSMPR crystallizer. *Chem. Eng. Sci.*, **40**, 1485-1493 (1985).

Geisler, R., Mersmann, A. and Voit, H. Macro- and micromixing in stirred tanks. *Int. Chem. Eng.*, **31**, 642-653 (1991).

Gelbard, F. and Seinfeld, J. H. Numerical solution of the dynamic equation for particulate systems. *J. Comp. Physics*, **28**, 357 (1978).

Gelbard, F., Tambour, Y. and Seinfeld, J. H. Sectional representations for simulating aerosol dynamics. *J. Coll. Int. Sci.*, **76**, 541 (1980).

Gottlieb, D. and Orszag, S. A. *Numerical Analysis of Spectral Methods: Theory and Applications.* SIAM, Philadelphia (1977).

Green, D. A., Kontomaris, K., Grenville, R. K., Etchells, A. W., Kendall, R. E. and Jacobs, G. Suspension dynamics and mixing in industrial crystallizers. *Industrial Crystallization 1996*, Toulouse, 525-530 (1996).

Guichardon, P., Falk, L., Fournier, M. C. and Villermaux, J. Study of micromixing in a liquid-solid suspension in a stirred reactor. *AIChE Symp. Ser.*, **299**, 123-130 (1994).

Harada, M., Arima, K., Eguchi, W. and Nagata, S. Micromixing in a continuous flow reactor. *Mem. Fac. Eng., Kyoto Univ., Japan*, **24**, 431 (1962).

Harnby, N., Edwards, M. F. and Nienow, A. W. *Mixing in Process Industries.* Butterworth & Co (1985).

Hartel, R. W., Gottung, B. E., Randolph, A. D. and Drach, G. W. Mechanisms and kinetic modelling of calcium oxalate crystal aggregation in a urinelike liquor. Part I: Mechanisms. *AIChE J.*, **32**, 1176-1185 (1986).

Hartel, R. W. and Randolph, A. D. Mechanisms and kinetic modelling of calcium oxalate crystal aggregation in a urinelike liquor. Part II: Kinetic modelling. *AIChE J.*, **32**, 1186-1195 (1986).

Heuer, M. and Leschonski, K. Results obtained with a new instrument for the measurement of particle size distributions from diffraction patterns. *Part. Charact.*, **2**, 7-15 (1985).

Hill, P. J. and Ng, K. M. New discretization procedure for the breakage equation. *AIChE J.*, **41**, 1204-1217 (1995).

Hill, P. J. and Ng, K. M. Statistics of multiple particle breakage. *AIChE J.*, **42**, 1600-1608 (1996).

Hostomský, J. Particle size distribution of agglomerated crystal product from a continuous crystallizer. *Coll. Czech. Chem. Commun.*, **52**, 1186-1197 (1987).

Hostomský, J. and Jones, A. G. Calcium carbonate crystallization, agglomeration and form during continuous precipitation from solution. *J. Phys. D: Appl. Phys.*, **24**, 165-170 (1991).

Houcine, I., Plasari, E., David, R. and Villermaux, J. Influence of mixing characteristics on the quality and size of precipitated calcium oxalate in a pilot scale reactor. *Trans. IChemE*, **75**, 252-256 (1997).

Hounslow, M. J., Ryall, R. L. and Marshall, V. R. A discretized population balance for nucleation, growth and aggregation. *AIChE J.*, **34**, 1821-1832 (1988).

Hounslow, M. J. A discretized population balance for continuous systems at steady state. *AIChE J.*, **36**, 106-116 (1990a).

Hounslow, M. J. Nucleation, growth and aggregation rates from steady-state experimental data. *AIChE J.*, **36**, 1748-1753 (1990b).

Hulburt, H. M. and Katz, S. Some problems in particle technology - a statistical mechanical formulation. *Chem. Eng. Sci.*, **19**, 555-574 (1964).

Johnstone, R. E. and Thring, M. W. *Pilot Plants, Models and Scale-up Methods in Chemical Engineering.* McGraw Hill (1957).

Jones, A. G., Hostomský, J. and Wachi, S. Modelling and analysis of particle formation during agglomerative crystal precipitation processes. *Chem. Eng. Comm.*, **146**, 105-130 (1996).

Kavanagh, J. P. Methods for the study of calcium oxalate crystallization and their application to urolithiasis research. *Scanning Microscopy*, **6**, 685-705 (1992).

Kim, W.-S. and Tarbell, J. M. Micromixing effects on barium sulfate precipitation in an MSMPR reactor. *Chem. Eng. Comm.*, **146**, 33-56 (1996).

Klimpel, R. R. and Austin, L. G. The back-calculation of specific rates of breakage from continuous mill data. *Powder Technology*, **38**, 77-91 (1984).

Kramer, H. J. M., O'Meadhra, R. S., Neumann, A. M. and Rosmalen, G. M. van Scale-up of ammonium sulphate crystallization in a DTB crystallizer. *Industrial Crystallization 1996*, Toulouse, 619-625 (1996).

Krei, G. A. and Buschmann, E. Von der Laborsynthese zum Produktionsverfahren. *Spektrum der Wissenschaft, Spezial 6: Pharmaforschung,* 38-47 (1998).

Kuipers, J. A. M. and Swaaij, W. P. M. van Application of computational fluid dynamics to chemical reaction engineering. *Reviews in Chem. Eng.*, **13**, 1-110 (1997).

Kumar, S. and Ramkrishna, D. On the solution of population balance by discretization I. A fixed pivot technique. *Chem. Eng. Sci.*, **51**, 1311-1332 (1996a).

Kumar, S. and Ramkrishna, D. On the solution of population balance by discretization II. A moving pivot technique. *Chem. Eng. Sci.*, **51**, 1333-1342 (1996b).

Lee, Y.-M. and Lee, L. J. Effect of mixing and reaction on a fast step growth polymerization. *Int. Polymer Processing*, **1**, 144-152 (1987).

Leeuwen, M. L. J. van, Bruinsma, O. S. L. and Rosmalen, G. M. van Influence of mixing on the product quality in precipitation. *Chem. Eng. Sci.*, **51**, 2595-2600 (1996a).

Leeuwen, M. L. J. van, Bruinsma, O. S. L. and Rosmalen, G. M. van Three-zone approach for precipitation of barium sulphate. *J. of Crystal Growth*, **166**, 1004-1008 (1996b).

Leeuwen, M. L. J. van Precipitation and mixing. *Ph.D. thesis*, Univ. of Delft, The Netherlands (1998).

Litster, J. D., Smit, D. J. and Hounslow, M. J. Adjustable discretized population balance for growth and agglomeration. *AIChE J.*, **41**, 591-603 (1995).

Low, G. C. Agglomeration effects in aluminium trihydroxide precipitation. *Ph.D. Diss.*, Univ. Queensland, Australia (1975).

Mahajan, A. J. and Kirwan, D. J. Micromixing effects in a two-impinging-jets precipitator. *AIChE J.*, **42**, 1801-1814 (1996).

Manninen, M. and Syrjänen, J. Modelling turbulent flow in stirred tanks. *CFX Update*, **16**, 10-11 (1998).

Marcant, B. Prediction of mixing effects in precipitation from laser sheet visualisation. *Industrial Crystallization 1996*, Toulouse, 531-538 (1996).

Marmo, L., Manna, L., Chiampo, F., Sicardi, S. and Bersano, G. Influence of mixing on the particle size distribution of an organic precipitate. *J. of Crystal Growth*, **166**, 1027-1034 (1996).

Mehta, R. V. and Tarbell, J. M. A four environment model of mixing and chemical reaction. Part I – model development. *AIChE J.*, **29**, 320 (1983).

Mersmann, A. and Laufhütte, H. D. Scale-up of agitated vessels for different mixing processes. *5th European Conference on Mixing 1985*, Würzburg, 273-284 (1985).

Mersmann, A., Angerhöfer, M. and Franke, J. Controlled precipitation. *Chem. Eng. Technol.*, **17**, 1-9 (1994).

Mersmann, A., *Crystallization Technology Handbook*. Dekker (1995).

Momonaga, M., Yazawa, H. and Kagara, K. Reactive crystallization of methyl α-methoxyimino acetoacetate. *J. Chem. Eng. of Japan*, **25**, 237-242 (1992).

Mullin, J. W. *Crystallization*. 3rd edn., Butterworth-Heinemann, Oxford (1993).

Mullin, J. W. and Raven, K. D. Nucleation in agitated solutions. *Nature*, **190**, 251 (1961a).

Mullin, J. W. and Raven, K. D. Influence of mechanical agitation on the nucleation of some aqueous salt solutions. *Nature*, **195**, 35-38 (1961b).

Mumtaz, H. S., Hounslow, M. J., Seaton, N. A. and Paterson, W. R. Orthokinetic aggregation during precipitation: A computational model for calcium oxalate monohydrate. *Trans. IChemE*, **75**, 152-159 (1997).

Muralidar, R. and Ramkrishna, D. An inverse problem in agglomeration kinetics. *J. Coll. Int. Sci.*, **112**, 348-361 (1986).

Myerson, A. S. *Handbook of Industrial Crystallization.* Butterworth-Heinemann (1993).

Nancollas, G. H. *Interactions in Electrolyte Solutions.* Elsevier Publishing Company (1966).

Nancollas, G. H. and Gardner, G. L. Kinetics of crystal growth of calcium oxalate monohydrate. *J. of Crystal Growth*, **21**, 267-276 (1974).

Newton, I. *Principia.* (1687).

Nielsen, A. E. Nucleation and growth of crystals at high supersaturation. *Kristall und Technik*, **4**, 17-38 (1969).

Nielsen, A. E. and Toft, J. M. Electrolyte crystal growth kinetics. *J. of Crystal Growth*, **67**, 278-288 (1984).

O'Hara, M. and Reid, R. C. *Modelling Crystal Growth Rates from Solution.* Prentice-Hall, Englewood Cliffs (1973).

Ohsol, E. O. What does it cost to pilot a process? *Chem. Eng. Prog.*, **69**, 17-20 (1973).

Ohtaki, H. *Crystallization Processes.* Wiley Series in Solution Chemistry, Volume 3, John Wiley & Sons, West Sussex (1998).

Oldshue, J. Y. *Fluid Mixing Technology.* McGraw-Hill (1983).

Oldshue, J. Y. Scale-up of unique industrial fluid mixing processes. *5th European Conference on Mixing*, Würzburg, 35-51 (1985).

Ploß, R., Tengler, T. and Mersmann, A. Scale-up of MSMPR-Crystallizers. *Ger. Chem. Eng.*, **1**, 42-48 (1986).

Pohorecki, R. and Baldyga, J. The effects of micromixing and the manner of reactor feeding on precipitation in stirred tank reactors. *Chem. Eng. Sci.*, **43**, 1949-1954 (1988).

Qian, R., Chen, Z., Ni, H., Fan, Z. and Cai, F. Crystallization kinetics of potassium chloride from brine and scale-up criterion. *AIChE J.*, **33**, 1690-1697 (1987).

Ramkrishna, D. The status of population balances. *Reviews in Chem. Eng.*, **3**, 49-95 (1985).

Ranade, V. V. An efficient computational model for simulating flow in stirred vessels: a case of Rushton turbine. *Chem. Eng. Sci.*, **52**, 4473-4484 (1997).

Randolph, A. D. and Larson, M. A. *Theory of Particulate Processes.* 2nd edn., Academic Press, New York (1988).

Rayleigh, Lord The principle of similitude. *Nature*, **95**, 66-68 (1915).

Rice, R. W. and Baud, R. E. The role of micromixing in the scale-up of geometrically similar batch reactors. *AIChE J.*, **36**, 293-298 (1990).

Ritchie, B. W. and Togby, A. H. A three-environment micromixing model for chemical reactors with arbitrary separate feedstreams. *Chem. Eng. J.*, **17**, 173 (1979).

Schuler, H. *Prozeßsimulation.* VCH-Verlag, Weinheim (1996).

Sie, S. T. and Krishna, R. Process development and scale-up: 1. Process development strategy and methodology. *Reviews in Chem. Eng.*, **14**, 46-87 (1998).

Smith, G. D. *Numerical Solution of Partial Differential Equations: Finite Difference Methods*. 3rd edn., Clarendon Press (1985).

Smoluchowski, M. V. Drei Vorträge über Diffusion, Brownsche Molekularbewegung und Koagulation von Kolloidteilchen. *Physik. Zeitung*, **XVII**, 557-599 (1916).

Söhnel, O. and Garside, J. *Precipitation*. Butterworth-Heinemann, Oxford (1992).

Spanos, N. and Koutsoukos, P. G. The transformation of vaterite to calcite: effect of the conditions of the solutions in contact with the mineral phase. *J. of Crystal Growth*, **191**, 783-790 (1998).

Synowiec, P., Jones, A. G. and Shamlou, P. A. Crystal break-up in dilute turbulently agitated suspensions. *Chem. Eng. Sci.*, **48**, 3485-3495 (1993).

Tai, C. Y. and Chen, F.-B. Polymorphism of $CaCO_3$ precipitated in a constant-composition environment. *AIChE J.*, **44**, 1790-1798 (1998).

Tavare, N. S. Mixing in continuous crystallizers. *AIChE J.*, **32**, 705-732 (1986).

Thompson, P. D. A transformation of the stochastic equation for droplet coalescence. *Proc. Int. Conf. Cloud Physics*, Toronto, 115-126 (1968).

Tipnis, S. K., Penney, W. R. and Fasano, J. B. An experimental investigation to determine a scale-up method for fast competitive parallel reactions in agitated vessels. *AIChE Symp. Ser.*, **299**, 78-91 (1994).

Tomazic, B. and Nancollas, G. H. The kinetics of dissolution of calcium oxalate hydrates. *J. of Crystal Growth*, **46**, 355-361 (1979).

Tosun, G. An experimental study of the effect of mixing on the particle size distribution in $BaSO_4$ precipitation reaction. *6th European Conference on Mixing*, Pavia, 161-170 (1988).

Tosun, G. A mathematical model of mixing and polymerization in a semibatch stirred tank reactor. *AIChE J.*, **38**, 425-437 (1992).

Versteeg, H. K. and Malalasekera W. *An introduction to Computational Fluid Dynamics.* Longman (1995).

Villermaux, J. A simple model for partial segregation in a semibatch reactor. *AIChE Annual Meeting,* San Francisco, Paper 114a (1989).

Villermaux, J. and Falk, L. A generalised mixing model for initial contacting of reactive fluids. *Chem. Eng. Sci.*, **49**, 5127-5140 (1994).

Wachi, S. and Jones, A. G. Dynamic modelling of particle size distribution and degree of agglomeration during precipitation. *Chem. Eng. Sci.*, **47**, 3145-3148 (1992).

Wadell, H. Volume, shape and roundness of rock particles. *J. Geology*, **40**, 443-451 (1932).

Walton, A. G. *The Formation and Properties of Precipitates.* R. E. Krieger Publishing Company, New York (1979).

Wang, Y.-D. and Mann, R. Partial segregation in stirred batch reactors: effect of scale-up on the yield of a pair of competing reactions. *Trans. IChemE*, **70**, 282-290 (1992).

Wei, H. Y. and Garside, J. Application of CFD modelling to precipitation systems. *Trans. IChemE*, **75**, 219-227 (1997).

Westerterp, K. R., Swaaij, W. P. M. van and Beenackers, A. A. C. M. *Chemical Reactor Design and Operation.* John Wiley & Sons (1995).

Wójcik, J. and Jones, A. G. Experimental investigation into dynamics and stability of continuous MSMPR agglomerative precipitation of $CaCO_3$ crystals. *Trans. IChemE*, **75**, 113-118 (1997).

Wójcik, J. and Jones, A. G. Dynamics and stability of continuous MSMPR agglomerative precipitation: numerical analysis of the dual particle coordinate model. *Comp. Chem. Eng.*, **22**, 535-545 (1998a).

Wójcik, J. and Jones, A. G. Particle disruption of precipitated $CaCO_3$ crystal agglomerates in turbulently agitated suspensions. *Chem. Eng. Sci.*, **53**, 1097-1101 (1998b).

Xu, Y. and McGrath, G. CFD predictions of stirred tank flows. *Trans. IChemE*, **74**, 471-475 (1996).

Yates, F. *Design and Analysis of Factorial Experiments.* Imperial Bureau of Soil Science, London (1937).

Zienkiewicz O. C. and Taylor, R. L. *The Finite Element Method – Solid and Fluid Mechanics.* McGraw-Hill (1991).

Zlokarnik, M. Modellübertragung bei partieller Ähnlichkeit. *Chemie-Ingenieur-Technik*, **57**, 410-416 (1985).

Zlokarnik, M. *Dimensional Analysis and Scale-up in Chemical Engineering.* Springer-Verlag (1991).

APPENDIX

A2.1 Fluid dynamic parameters

0.3 l draft tube baffled vessel

[rpm]	250	500	750	1000	1500	2000
Re	16000	32000	48000	64000	96000	128000
v_{tip} [m/s]	0.458	0.916	1.37	1.83	2.75	3.67
ε_{avg} [W/kg]	0.0033	0.0263	0.089	0.211	0.711	1.686

4.3 l draft tube baffled vessel

[rpm]	100	250	500	1000	1500	1800
Re	29400	73600	147200	295000	442000	530000
v_{tip} [m/s]	0.393	0.982	1.96	3.93	5.89	7.06
ε_{avg} [W/kg]	0.0029	0.0086	0.073	0.605	1.98	3.43

12 l draft tube baffled vessel

[rpm]	100	250	500	750	1000	1500
Re	80000	195000	390000	585000	800000	1.2×10^6
v_{tip} [m/s]	0.639	1.58	3.19	4.79	6.39	9.58
ε_{avg} [W/kg]	0.0024	0.0375	0.300	1.01	2.30	8.09

1 l baffled vessel, Rushton turbine

[rpm]	100	250	500	1000	1500	2000
Re	8400	21000	42000	84000	126000	168000
v_{tip} [m/s]	0.209	0.524	1.05	2.09	3.14	4.19
ε_{avg} [W/kg]	0.0027	0.0422	0.3378	2.70	9.12	21.6

1 l baffled vessel, pitched blade turbine

[rpm]	100	250	500	1000	1500	2000
Re	8400	21000	42000	84000	126000	168000
v_{tip} [m/s]	0.209	0.524	1.05	2.09	3.14	4.19
ε_{avg} [W/kg]	0.0004	0.0060	0.047	0.379	1.28	3.03

1 l baffled vessel, marine-type impeller

[rpm]	100	250	500	1000	1500	2000
Re	8400	21000	42000	84000	126000	168000
v_{tip} [m/s]	0.209	0.524	1.05	2.09	3.14	4.19
ε_{avg} [W/kg]	0.0001	0.0017	0.0136	0.109	0.368	0.872

5 l baffled vessel, Rushton turbine

[rpm]	100	250	500	750	1000	1500
Re	22000	55000	110000	165000	221000	332000
v_{tip} [m/s]	0.341	0.852	1.70	2.55	3.40	5.11
ε_{avg} [W/kg]	0.0061	0.0956	0.765	2.58	6.12	20.7

5 l baffled vessel, marine-type impeller

[rpm]	100	250	500	1000	1500	2000
Re	22000	55000	110000	221000	332000	442000
v_{tip} [m/s]	0.341	0.852	1.70	3.40	5.11	6.80
ε_{avg} [W/kg]	0.0003	0.0039	0.0309	0.247	0.834	1.98

25 l baffled vessel, Rushton turbine

[rpm]	100	250	500	750	1000	1500
Re	63000	158000	317000	475000	630000	1.3×10^6
v_{tip} [m/s]	0.581	1.44	2.88	4.32	5.76	8.64
ε_{avg} [W/kg]	0.0171	0.266	2.13	7.17	17.0	57.4

25 l baffled vessel, marine-type impeller

[rpm]	100	250	500	750	1000	1500
Re	63000	158000	317000	475000	630000	1.3×10^6
v_{tip} [m/s]	0.581	1.44	2.88	4.32	5.76	8.64
ε_{avg} [W/kg]	0.0010	0.0166	0.133	0.477	1.06	3.58

A4.1 Conditions of laboratory-scale precipitation experiments (CaOx) for parameter estimation

Run	τ	St. speed	Feed conc.	Feed point position
	[min]	[rpm]	[mol/l]	[-]
id016	2	500	0.01	inside draft tube
id028	2	2000	0.01	inside draft tube
id018	7.5	500	0.01	inside draft tube
id021	7.5	1000	0.01	inside draft tube
id025	7.5	1500	0.01	inside draft tube
id029	7.5	2000	0.01	inside draft tube
id020	11	250	0.01	inside draft tube
id024	11	500	0.01	inside draft tube
id027	11	1000	0.01	inside draft tube
id031	11	2000	0.01	inside draft tube
id001	2	500	0.04	inside draft tube
id008	2	2000	0.04	inside draft tube
id002	7.5	500	0.04	inside draft tube
id004	7.5	1000	0.04	inside draft tube
id006	7.5	1500	0.04	inside draft tube

continued

Run	τ	St. speed	Feed conc.	Feed point position
	[min]	[rpm]	[mol/l]	[-]
id009	7.5	2000	0.04	inside draft tube
id003	11	500	0.04	inside draft tube
id005	11	1000	0.04	inside draft tube
id007	11	1500	0.04	inside draft tube
id010	11	2000	0.04	inside draft tube
id012	7.5	1000	0.10	inside draft tube
id014	7.5	2000	0.10	inside draft tube
id013	11	1000	0.10	inside draft tube
idm001	7.5	250	0.01	inside draft tube/surface
idm002	7.5	500	0.01	inside draft tube/surface
idm003	7.5	1000	0.01	inside draft tube/surface
idm004	7.5	2000	0.01	inside draft tube/surface
idm005	7.5	1000	0.04	inside draft tube/surface
idm006	7.5	2000	0.04	inside draft tube/surface
od003	2	1000	0.01	outside draft tube
od008	2	2000	0.01	outside draft tube
od001	7.5	500	0.01	outside draft tube
od004	7.5	1000	0.01	outside draft tube
od006	7.5	1500	0.01	outside draft tube
od009	7.5	2000	0.01	outside draft tube
od002	11	500	0.01	outside draft tube
od005	11	1000	0.01	outside draft tube
od007	11	1500	0.01	outside draft tube
od010	11	2000	0.01	outside draft tube
od016	2	1000	0.04	outside draft tube
od021	2	2000	0.04	outside draft tube
od014	7.5	500	0.04	outside draft tube
od017	7.5	1000	0.04	outside draft tube
od019	7.5	1500	0.04	outside draft tube
od022	7.5	2000	0.04	outside draft tube
od015	11	500	0.04	outside draft tube
od018	11	1000	0.04	outside draft tube
od020	11	1500	0.04	outside draft tube
od023	11	2000	0.04	outside draft tube

A4.2 Sample results of parameter estimation for calcium oxalate

Run	σ [–]	G [µm/h]	B^0 [1/m^{3}h]	β_{aggl} [m^3/µm^{3}h]	β_{disr} [1/µm^{3}h]
id002	3.81	60.42	0.92E13	1.31E-15	1.19E-8
id004	3.72	57.90	1.23E13	1.22E-15	1.02E-7
id006	4.06	63.42	1.49E13	1.43E-15	6.31E-7
id009	3.47	49.31	0.84E13	3.51E-17	7.25E-6
od002	2.26	37.38	0.62E13	3.57E-16	3.66E-8
od005	2.25	39.36	0.73E13	4.02E-16	3.19E-7
od007	2.29	38.82	0.55E13	3.68E-16	2.23E-6
od010	2.55	30.01	0.41E13	4.39E-17	1.63E-5

A4.3 Conditions of laboratory-scale precipitation experiments ($CaCO_3$) for parameter estimation

Run	τ	St. speed	Feed conc.	Feed point position
	[min]	[rpm]	[mol/l]	[-]
kalk1	5	250	0.1	inside draft tube
kalk2	5	500	0.1	inside draft tube
kalk3	5	1000	0.1	inside draft tube
kalk4	5	2000	0.1	inside draft tube
kalk5	10	250	0.1	inside draft tube
kalk6	10	500	0.1	inside draft tube
kalk7	10	1000	0.1	inside draft tube
kalk8	10	2000	0.1	inside draft tube

A4.4 Kinetic parameters of calcium carbonate

The growth, disruption and agglomeration kinetics for calcium carbonate ($CaCO_3$) were determined in the same way from laboratory-scale experiments as

described for calcium oxalate. The pre-exponential factor of the nucleation rate was extracted using the simulation results for the micromixing and mesomixing times.

$$G = 2.231 \times \sigma^2$$

$$\beta_{disr} = 4.49 \times 10^{-7} \varepsilon S^{-2.15}$$

$$\beta_{aggl} = 6.181 \times 10^{-17} (1 + 3.089 \varepsilon^{\frac{1}{2}} - 2.578 \varepsilon) S^{2.15}$$

$$B^0 = 3.01 \times 10^{15} \exp^{-\frac{35.55}{\ln^2 S}}$$

A5.1 Local energy dissipation and mixing times for different geometries, stirrer speeds and feed point positions from CFD simulations

0.3 l draft tube baffled vessel, feed point position close to the impeller

[rpm]	100	500	750	1000	1500	2000
ε_{loc} [W/kg]	0.0051	0.041	0.138	0.327	1.10	2.61
t_{micro} [s]	0.24	0.085	0.047	0.030	0.016	0.011
t_{meso} [s]	1.15	0.134	0.079	0.053	0.032	0.021

0.3 l draft tube baffled vessel, feed point position remote from the impeller

[rpm]	100	500	750	1000	1500	2000
ε_{loc} [W/kg]	0.0010	0.0081	0.027	0.063	0.21	0.51
t_{micro} [s]	0.52	0.19	0.10	0.010	0.037	0.024
t_{meso} [s]	5.90	0.68	0.40	0.27	0.16	0.11

4.3 l draft tube baffled vessel, feed point position close to the impeller

[rpm]	100	250	500	1000	1500	1800
ε_{loc} [W/kg]	0.0043	0.013	0.11	0.91	2.96	5.10
t_{micro} [s]	0.26	0.15	0.051	0.018	0.010	0.0076
t_{meso} [s]	1.48	0.41	0.17	0.066	0.039	0.028

4.3 l draft tube baffled vessel, feed point position remote from the impeller

[rpm]	100	250	500	1000	1500	1800
ε_{loc} [W/kg]	0.0009	0.0032	0.022	0.18	0.59	1.03
t_{micro} [s]	0.58	0.32	0.12	0.041	0.023	0.017
t_{meso} [s]	7.00	1.98	0.79	0.31	0.18	0.14

12 l draft tube baffled vessel, feed point position close to the impeller

[rpm]	100	250	500	750	1000	1500
ε_{loc} [W/kg]	0.0030	0.054	0.44	1.46	3.35	11.7
t_{micro} [s]	0.32	0.074	0.026	0.014	0.0095	0.0051
t_{meso} [s]	1.21	0.36	0.14	0.082	0.056	0.033

12 l draft tube baffled vessel, feed point position remote from the impeller

[rpm]	100	250	500	750	1000	1500
ε_{loc} [W/kg]	0.0007	0.011	0.091	0.30	0.69	2.43
t_{micro} [s]	0.66	0.17	0.57	0.032	0.021	0.011
t_{meso} [s]	5.83	1.72	0.68	0.40	0.27	0.16

1 l baffled vessel, Rushton turbine, feed point position close to the impeller

[rpm]	100	250	500	1000	1500	2000
ε_{loc} [W/kg]	0.0081	0.13	1.01	8.12	27.4	65.1
t_{micro} [s]	0.19	0.048	0.017	0.0061	0.0033	0.0021
t_{meso} [s]	0.34	0.10	0.040	0.016	0.0093	0.0063

1 l baffled vessel, Rushton turbine, feed point position remote from the impeller

[rpm]	100	250	500	1000	1500	2000
ε_{loc} [W/kg]	0.0001	0.0025	0.020	0.16	0.54	1.28
t_{micro} [s]	1.73	0.35	0.12	0.043	0.024	0.015
t_{meso} [s]	17.1	5.07	2.01	0.80	0.47	0.32

1 l baffled vessel, pitched blade turbine, feed point position close to the impeller

[rpm]	100	250	500	1000	1500	2000
ε_{loc} [W/kg]	0.0007	0.011	0.085	0.68	2.32	5.47
t_{micro} [s]	0.65	0.17	0.060	0.021	0.011	0.0074
t_{meso} [s]	0.54	0.16	0.064	0.025	0.015	0.010

1 l baffled vessel, marine-type impeller, feed point position close to the impeller

[rpm]	100	250	500	1000	1500	2000
ε_{loc} [W/kg]	0.0002	0.0026	0.021	0.17	0.57	1.35
t_{micro} [s]	1.22	0.34	0.12	0.042	0.023	0.015
t_{meso} [s]	0.63	0.19	0.074	0.029	0.017	0.012

5 l baffled vessel, Rushton turbine, feed point position close to the impeller

[rpm]	100	250	500	750	1000	1500
ε_{loc} [W/kg]	0.018	0.27	2.14	7.24	17.3	58.1
t_{micro} [s]	0.13	0.033	0.012	0.0064	0.0040	0.0026
t_{meso} [s]	0.37	0.11	0.043	0.025	0.017	0.0099

5 l baffled vessel, Rushton turbine, feed point position remote from the impeller

[rpm]	100	250	500	750	1000	1500
ε_{loc} [W/kg]	0.0003	0.0053	0.043	0.15	0.34	1.16
t_{micro} [s]	1.01	0.24	0.083	0.045	0.030	0.016
t_{meso} [s]	18.4	5.42	2.15	1.25	0.85	0.50

5 l baffled vessel, marine-type impeller, feed point position close to the impeller

[rpm]	100	250	500	1000	1500	2000
ε_{loc} [W/kg]	0.0004	0.0056	0.045	0.36	1.20	2.86
t_{micro} [s]	0.87	0.23	0.082	0.029	0.016	0.010
t_{meso} [s]	0.71	0.21	0.083	0.033	0.019	0.013

25 l baffled vessel, Rushton turbine, feed point position close to the impeller

[rpm]	100	250	500	750	1000	1500
ε_{loc} [W/kg]	0.045	0.71	5.66	19.1	45.2	151.3
t_{micro} [s]	0.081	0.021	0.0072	0.0039	0.0026	0.0014
t_{meso} [s]	0.39	0.12	0.046	0.027	0.018	0.011

25 l baffled vessel, Rushton turbine, feed point position remote from the impeller

[rpm]	100	250	500	750	1000	1500
ε_{loc} [W/kg]	0.0011	0.014	0.11	0.38	0.94	2.91
t_{micro} [s]	0.55	0.15	0.051	0.028	0.018	0.009
t_{meso} [s]	19.6	5.79	2.30	1.34	0.91	0.53

25 l baffled vessel, marine-type impeller, feed point position close to the impeller

[rpm]	100	250	500	750	1000	1500
ε_{loc} [W/kg]	0.001	0.022	0.17	0.63	1.40	4.67
t_{micro} [s]	0.55	0.12	0.042	0.022	0.015	0.0081
t_{meso} [s]	0.77	0.23	0.090	0.052	0.036	0.021

A5.2 Sample CFX code of command file for CFD simulations

```
/************************************************************/
 /* TURBULENT FLOW IN A VESSEL                 */
 /************************************************************/
 >>CFXF3D
 >>SET LIMITS
  TOTAL INTEGER WORK SPACE 8000000
  TOTAL REAL WORK SPACE 20000000
  TOTAL CHARACTER WORK SPACE 25000
  >>OPTIONS
   THREE DIMENSIONS
   TURBULENT FLOW
   TRANSIENT GRID
   TRANSIENT FLOW
/*   STEADY STATE */
   UNMATCHED GRIDS
   USE DATABASE
   END

 >>MODEL TOPOLOGY
  >>INPUT TOPOLOGY
```

```
  READ GEOMETRY FILE
 >>GLUE PATCHES FOR UNMATCHED GRIDS
  FIRST PATCH NAMES 'imp'
  SECOND PATCH NAMES 'rushton'

>>MODEL DATA
 >>MATERIALS DATABASE
  >>SOURCE OF DATA
   PCP
   END
  >>FLUID DATA
   FLUID 'WATER'
   MATERIAL TEMPERATURE 310.0
   MATERIAL PHASE 'LIQUID'
   END
 >>TITLE
  PROBLEM TITLE 'FIRST ATTEMPT WITH SLIDING MESH'
  END
 >>PHYSICAL PROPERTIES
  >>GRID MOTION PARAMETERS
    BLOCK NAMES  'BLOCK-NUMBER-46'  +
   'BLOCK-NUMBER-47' 'BLOCK-NUMBER-48' 'BLOCK-NUMBER-49' +
   'BLOCK-NUMBER-50' 'BLOCK-NUMBER-51' 'BLOCK-NUMBER-52' +
   'BLOCK-NUMBER-54' 'BLOCK-NUMBER-55' 'BLOCK-NUMBER-56' +
   'BLOCK-NUMBER-57' 'BLOCK-NUMBER-58' 'BLOCK-NUMBER-59' +
   'BLOCK-NUMBER-60' 'BLOCK-NUMBER-61' 'BLOCK-NUMBER-62' +
   'BLOCK-NUMBER-63' 'BLOCK-NUMBER-64' 'BLOCK-NUMBER-65' +
   'BLOCK-NUMBER-66' 'BLOCK-NUMBER-67' 'BLOCK-NUMBER-68' +
   'BLOCK-NUMBER-69' 'BLOCK-NUMBER-70' 'BLOCK-NUMBER-71' +
   'BLOCK-NUMBER-72' 'BLOCK-NUMBER-73' 'BLOCK-NUMBER-74' +
   'BLOCK-NUMBER-75' 'BLOCK-NUMBER-76' 'BLOCK-NUMBER-77' +
```

```
    'BLOCK-NUMBER-78' 'BLOCK-NUMBER-79' 'BLOCK-NUMBER-80' +
    'BLOCK-NUMBER-81' 'BLOCK-NUMBER-82' 'BLOCK-NUMBER-83' +
    'BLOCK-NUMBER-84' 'BLOCK-NUMBER-85' 'BLOCK-NUMBER-53'
    POSITION VECTOR ON MOTION AXIS 0.0 0.0 0.0
    DIRECTION VECTOR ON MOTION AXIS 0.0 0.0 1.0
    ROTATION SPEED 104.7
  >>TRANSIENT PARAMETERS
 /*   >>FIXED TIME STEPPING
      TIME STEPS 250*0.0025      */
      >>ADAPTIVE TIME STEPPING
        NUMBER OF TIME STEPS  500
        INITIAL TIME STEP 0.001
        MINIMUM TIME STEP 0.001
        MAXIMUM TIME STEP 0.1
        MULTIPLY TIME STEP BY 2.0
        MINIMUM INTERVAL BETWEEN INCREMENTS 5
        MAXIMUM NUMBER OF CONTIGUOUS DECREMENTS 20
      END
>>SOLVER DATA
  >>EQUATION SOLVERS
    U VELOCITY 'AMG'
    V VELOCITY 'AMG'
    W VELOCITY 'AMG'
    PRESSURE 'AMG'
    K 'AMG'
    EPSILON 'AMG'
  >>PROGRAM CONTROL
    MAXIMUM NUMBER OF ITERATIONS 20
    OUTPUT MONITOR POINT 2 2 2
    OUTPUT MONITOR BLOCK 'BLOCK-NUMBER-40'
    MASS SOURCE TOLERANCE 1.0E-4
```

```
   END
/*  >>DEFERRED CORRECTION
   EPSILON START 100
   EPSILON END 100
   END        */
>>MODEL BOUNDARY CONDITIONS

>>STOP
```

A5.3 FORTRAN90 code for conversion of concentration into activity

```
PROGRAM acti
        Version 1.2
        11.06.1997
        Rudolf Zauner
IMPLICIT NONE
DOUBLE PRECISION ::k1,k2,k3,aca,tca,eps,i,ineu,tox,gamca,gamh,gamhox,gamox,s
  DOUBLE PRECISION ::gamh2ox,gamcaox,cca,ch,cox,chox,ccaox,g1,g2,g3,ch2ox
  DOUBLE PRECISION ::b,d,ksp,ph,tcay,deltca,sid
  INTEGER :: k,j
k1=21010.
k2=19.40
k3=1869.
ksp=2.51E-9
tcay=0.00005
deltca=0.000001
ph=6.5
Ineu=4.*tcay
```

```
 OPEN (Unit=6,FILE="supsat1")
DO j=1,100
  DO k=1,20
I=Ineu
gamca=10.0**(-4.*0.5230*(I**0.5/(I**0.5+1.)-0.3*I))
gamh=10.0**(-0.5230*(I**0.5/(I**0.5+1.)-0.3*I))
gamhox=10.0**(-0.5230*(I**0.5/(I**0.5+1.)-0.3*I))
gamox=10.0**(-4.*0.5230*(I**0.5/(I**0.5+1.)-0.3*I))
gamcaox=10.0**(-3.*0.5230*(I**0.5/(I**0.5+1.)-0.3*I))
gamh2ox=10.0**(-3.*0.5230*(I**0.5/(I**0.5+1.)-0.3*I))
g1=k1*gamh*gamhox/gamh2ox
g2=k2*gamh*gamox/gamhox
g3=k3*gamca*gamox/gamcaox
ch=10.**(-ph)
cca=tcay/gamca
ccaox=(2.*cca+ch)/(2./g3/cca+ch/cca)
cox=ccaox/g3/cca
chox=g2/g3*ch*ccaox/cca
ch2ox=g1*ch*chox
Ineu=0.5*(4.*cca+4.*cox+ch+chox)
  END DO
s=(cca*gamca*gamox*cox)/ksp
sid=(tcay**2.)/ksp
tcay=tcay+deltca
Ineu=4.*tcay
WRITE (Unit=6,FMT=101) cca,tcay,gamca,gamox
101 FORMAT (5E16.8)
END DO
END PROGRAM acti
```

A5.4 FORTRAN90 code of Segregated Feed Model with population balance

```
MODULE RAMI
        Version 3.2
        13.11.1998
        Rudolf Zauner
IMPLICIT NONE
SAVE
INTEGER,PARAMETER :: imaxl=26,imax=20,iw=(12+imaxl)*imaxl+50
DOUBLE PRECISION ::lo,bo,growth3,beta0,disker0,m0dis,m1dis,m2dis,m3dis
DOUBLE PRECISION :: kv,ka,kn,kg,ksp,rhoc,mw,tau,tfeed,masssolnew
DOUBLE PRECISION :: beta,disker,l10,l32,l43,mom3bal,corr
DOUBLE PRECISION :: ca0,tm,bavg,massmom,massin,masssol,massprec,massbal,
DOUBLE PRECISION :: Vges,nu,epsloc,epsavg,tnucl,dimp,nimp,cv,t12,cb0,V(3)
DOUBLE PRECISION :: w(iw),l(100),npop(100),tmicro(2),Qf(3),birth(3),growth(3)
DOUBLE PRECISION :: sigmaab(3),mom3alt,bavg2,mom0_L
DOUBLE PRECISION ::mom0(3),mom1(3),mom2(3),mom3(3),mom4(3) 0
DOUBLE PRECISION, DIMENSION (100,100) :: nd
END MODULE RAMI
PROGRAM einsram
        Version 3.2
        13.11.1998
        Rudolf Zauner
USE RAMI
DOUBLE PRECISION :: tol,to,tend
INTEGER :: IFAIL,i,k,p,ms,mm
DOUBLE PRECISION :: n(100)
EXTERNAL D02EAF,FCN
tau=0.125
lo=1.
Vges=0.3
```

```
ka=4.4
kv=0.45
rhoc=2200.
mw=146.1
nu=1.e-6
epsavg=0.0263
epsloc=1.55*epsavg
ca0=0.04
cb0=0.04
ksp=2.51e-9
dimp=0.035
nimp=500.
beta0=5.431e-17*(1.+2.296*epsavg**0.5-2.429*epsavg)
disker0=6.23e-5*epsavg
kg=2.1164
DO i=1,imax
        IF (i==1) THEN
                l(i)=lo
        ELSE
                l(i)=l(i-1)*2**(1.0/3.0)
        END IF
 END DO
DO i=1,imax
  DO k=1,imax
    nd(i,k)=0.0
  END DO
END DO
DO k=2,imax
   DO i=1,k
     IF (i.ne.k) THEN
```

```
      nd(i,k)=(l(i)**3./(l(i+1)**3.-l(i)**3.)+l(i)**3./(l(i)**3.-l(i-
1)**3.))*(6.*l(i)**9./l(k)**9.-8.*l(i)**6./l(k)**6.+3.*l(i)**3./l(k)**3.)&
      -(l(i+1)**3./(l(i+1)**3.-l(i)**3.)+l(i-1)**3./(l(i)**3.-l(i-
1)**3.))*(8.*l(i)**9./l(k)**9.-12.*l(i)**6./l(k)**6.+6.*l(i)**3./l(k)**3.)&
      +l(i+1)**3./(l(i+1)**3.-l(i)**3.)*(2.*l(i+1)**9./l(k)**9.-
4.*l(i+1)**6./l(k)**6.+3.*l(i+1)**3./l(k)**3.)&
      +l(i-1)**3./(l(i)**3.-l(i-1)**3.)*(2.*l(i-1)**9./l(k)**9.-4.*l(i-
1)**6./l(k)**6.+3.*l(i-1)**3./l(k)**3.)
    END IF
    IF (i.eq.1) THEN
      nd(i,k)=(l(i)**3./(l(i+1)**3.-l(i)**3.))*(6.*l(i)**9./l(k)**9.-
8.*l(i)**6./l(k)**6.+3.*l(i)**3./l(k)**3.)&
      -(l(i+1)**3./(l(i+1)**3.-l(i)**3.))*(8.*l(i)**9./l(k)**9.-
12.*l(i)**6./l(k)**6.+6.*l(i)**3./l(k)**3.)&
      +l(i+1)**3./(l(i+1)**3.-l(i)**3.)*(2.*l(i+1)**9./l(k)**9.-
4.*l(i+1)**6./l(k)**6.+3.*l(i+1)**3./l(k)**3.)
    END IF
    IF (i.eq.k) THEN
      nd(i,k)=(l(i)**3./(l(i)**3.-l(i-1)**3.))*(6.*l(i)**9./l(k)**9.-
8.*l(i)**6./l(k)**6.+3.*l(i)**3./l(k)**3.)&
      -(l(i-1)**3./(l(i)**3.-l(i-1)**3.))*(8.*l(i)**9./l(k)**9.-
12.*l(i)**6./l(k)**6.+6.*l(i)**3./l(k)**3.)&
      +l(i-1)**3./(l(i)**3.-l(i-1)**3.)*(2.*l(i-1)**9./l(k)**9.-4.*l(i-
1)**6./l(k)**6.+3.*l(i-1)**3./l(k)**3.)
    END IF
  END DO
END DO
n(1)=1.e1
 DO i=2,imax
   n(i)=0.
 END DO
```

```
n(imax+1)=0.95*ca0
n(imax+2)=2.05*ksp**0.5
n(imax+3)=2.05*ksp**0.5
n(imax+4)=2.05*ksp**0.5
n(imax+5)=0.95*cb0
n(imax+6)=2.05*ksp**0.5
growth(1)=10.
birth(1)=1.e2
growth(2)=10.
birth(2)=1.e2
Qf(1)=Vges/2./tau
Qf(2)=Vges/2./tau
mom2=1.e1
tm=17.7*epsavg/epsloc/3600.*(Qf(1)/3600./1000.)**0.33333/dimp/(nimp/60.)**(4./3.)
tmicro(1)=1./3600.*17.3*(nu/epsloc)**0.5
tmicro(2)=1./3600.*17.3*(nu/epsloc)**0.5
V(1)=Qf(1)*tm
V(2)=Qf(2)*tm
growth(3)=10.
birth(3)=1.e2
Qf(3)=Qf(1)+Qf(2)
V(3)=Vges-(V(1)+V(2))
t12=1.e20*tmicro(1)
tol=1.0E-3
to=0.0
tend=10.0*tau
CALL D02EAF(to,tend,imaxl,n,tol,FCN,w,iw,ifail)
DO i=1,imax
   npop(i)=n(i)/(l(i+1)-l(i))
END DO
m0dis=0.0
```

```
  m1dis=0.0
  m2dis=0.0
  m3dis=0.0
DO i=1,imax
        m0dis=m0dis+n(i)
        m1dis=m1dis+(1.+1.12996)/2.*l(i)*n(i)
        m2dis=m2dis+((1.+1.12996)/2.*l(i))**2.0*n(i)
        m3dis=m3dis+((1.+1.12996)/2.*l(i))**3.0*n(i)
 END DO
OPEN (Unit=6,FILE="id7504_500")
  WRITE (Unit=6,FMT=101)
tmicro(1)*3600.,tm*3600.,bo,growth(3),beta,disker,m0dis,mom0(3),mom3(3)
  WRITE (Unit=6,FMT=101) cv,l10,l32,l43,massbal,sigmaab(1),sigmaab(3)
  WRITE (Unit=6,FMT=101)
n(imax+1),n(imax+2),n(imax+3),n(imax+4),n(imax+5),n(imax+6)
  DO i=1,imax
    WRITE (Unit=6,FMT=102) l(i),npop(i)
  END DO
 101 FORMAT (11E12.5)
 102 FORMAT (2E12.5)
END
SUBROUTINE FCN (t,n,nges)
USE RAMI
IMPLICIT NONE
 DOUBLE PRECISION :: t
INTEGER :: i,e
DOUBLE PRECISION, DIMENSION (100) :: nagg,ngro,n,nges
IF (n(imax+1).LE.n(imax+4)) THEN
  sigmaab(1)=((n(imax+1)*n(imax+1)-ksp)/ksp)**0.5
    IF ((n(imax+1)*n(imax+1)-ksp).LE.0.0001) THEN
      sigmaab(1)=0.00001
```

```
    END IF
  ELSE
  sigmaab(1)=((n(imax+4)*n(imax+4)-ksp)/ksp)**0.5
    IF ((n(imax+4)*n(imax+4)-ksp).LE.0.0001) THEN
      sigmaab(1)=0.00001
    END IF
END IF
IF (n(imax+2).LE.n(imax+5)) THEN
  sigmaab(2)=((n(imax+2)*n(imax+2)-ksp)/ksp)**0.5
    IF ((n(imax+2)*n(imax+2)-ksp).LE.0.0001) THEN
      sigmaab(2)=0.00001
    END IF
  ELSE
  sigmaab(2)=((n(imax+5)*n(imax+5)-ksp)/ksp)**0.5
    IF ((n(imax+5)*n(imax+5)-ksp).LE.0.0001) THEN
      sigmaab(2)=0.00001
    END IF
END IF
IF (n(imax+3).LE.n(imax+6)) THEN
  sigmaab(3)=((n(imax+3)*n(imax+3)-ksp)/ksp)**0.5
    IF ((n(imax+3)*n(imax+3)-ksp).LE.0.0001) THEN
      sigmaab(3)=0.00001
    END IF
  ELSE
  sigmaab(3)=((n(imax+6)*n(imax+6)-ksp)/ksp)**0.5
    IF ((n(imax+6)*n(imax+6)-ksp).LE.0.0001) THEN
      sigmaab(3)=0.00001
    END IF
END IF
sigmaab(1)=((n(imax+1)*n(imax+4)-ksp)/ksp)**0.5
sigmaab(2)=((n(imax+2)*n(imax+5)-ksp)/ksp)**0.5
```

```
sigmaab(3)=((n(imax+3)*n(imax+6)-ksp)/ksp)**0.5
bo=3.37536e15*(V(1)*exp(-52.09/(log(sigmaab(1)+1.))**2.)+V(2)*exp(-
52.09/(log(sigmaab(2)+1.))**2.)&
+V(3)*exp(-52.09/(log(sigmaab(3)+1.))**2.))/Vges
growth(1)=kg*sigmaab(1)**2.
growth(2)=kg*sigmaab(2)**2.
growth(3)=kg*sigmaab(3)**2.
beta=beta0*(1.+sigmaab(3))**2.15
disker=disker0*(1.+sigmaab(3))**(-2.15)
growth3=growth(3)
mom0(3)=0.0
      mom1(3)=0.0
      mom2(3)=0.0
      mom3(3)=0.0
      mom4(3)=0.0
   DO i=4,imax
         mom0(3)=mom0(3)+n(i)
         mom1(3)=mom1(3)+((1.+1.12996)/2.*l(i))*n(i)
         mom2(3)=mom2(3)+((1.+1.12996)/2.*l(i))**2.0*n(i)
         mom3(3)=mom3(3)+((1.+1.12996)/2.*l(i))**3.0*n(i)
         mom4(3)=mom4(3)+((1.+1.12996)/2.*l(i))**4.0*n(i)
   END DO
l10=mom1(3)/mom0(3)
      l32=mom3(3)/mom2(3)
      l43=mom4(3)/mom3(3)
mom0_L0=n(1)
      cv=(mom0(3)*mom2(3)/mom1(3)/mom1(3)-1.)**0.5
nges(imax+1)=Qf(1)*ca0-Qf(1)*n(imax+1)-V(1)/tmicro(1)*(n(imax+1)-n(imax+3))&
      -(V(1)+V(2))/t12*(n(imax+1)-n(imax+2))-birth(1)*lo**3*kv*rhoc*V(1)/mw*1.e-
18
nges(imax+2)=-Qf(2)*n(imax+2)-V(2)/tmicro(2)*(n(imax+2)-n(imax+3))&
```

```
      +(V(1)+V(2))/t12*(n(imax+1)-n(imax+2))-birth(2)*lo**3*kv*rhoc*V(2)/mw*1.e-
18
nges(imax+3)=-Qf(3)*n(imax+3)+Qf(1)*n(imax+1)+V(1)/tmicro(1)*(n(imax+1)-
n(imax+3))&
      +Qf(2)*n(imax+2)+V(2)/tmicro(2)*(n(imax+2)-n(imax+3))-
0.5*growth(3)*ka*mom2(3)&
      *V(3)*rhoc/mw*1.e-18-birth(3)*lo**3*kv*rhoc*V(3)/mw*1.e-18
nges(imax+4)=-Qf(1)*n(imax+4)-V(1)/tmicro(1)*(n(imax+4)-n(imax+6))&
      -(V(1)+V(2))/t12*(n(imax+4)-n(imax+5))-birth(1)*lo**3*kv*rhoc*V(1)/mw*1.e-
18
nges(imax+5)=Qf(2)*cb0-Qf(2)*n(imax+5)-V(2)/tmicro(2)*(n(imax+5)-n(imax+6))&
      +(V(1)+V(2))/t12*(n(imax+4)-n(imax+5))-birth(2)*lo**3*kv*rhoc*V(2)/mw*1.e-
18
nges(imax+6)=-Qf(3)*n(imax+6)+Qf(1)*n(imax+4)+V(1)/tmicro(1)*(n(imax+4)-
n(imax+6))&
      +Qf(2)*n(imax+5)+V(2)/tmicro(2)*(n(imax+5)-n(imax+6))-
0.5*growth(3)*ka*mom2(3)&
      *V(3)*rhoc/mw*1.e-18-birth(3)*lo**3*kv*rhoc*V(3)/mw*1.e-18
massin=0.5*ca0
masssol=n(imax+3)
massprec=mom3(3)*kv*rhoc/mw*Vges*1.e-18
massbal=massin-(masssol+massprec)
massprec=ABS(massin-masssol)
mom3bal=massprec/(kv*rhoc/mw*Vges*1.e-18)
corr=mom3bal/mom3(3)
CALL aggi(n,nagg)
CALL growi(n,ngro)
DO i=1,imax
        nges(i)=nagg(i)+ngro(i)-n(i)/tau
        IF (nges(i).LT.0.0) THEN
          nges(i)=0.0
```

```
        END IF
 END DO
111 FORMAT (5E16.8)
RETURN
END
SUBROUTINE aggi(n,nagg)
USE RAMI
IMPLICIT NONE
DOUBLE PRECISION :: agg1,agg1neu,agg2,agg2neu,agg3,agg3neu,agg4,agg4neu,&
                    ndisdum
  INTEGER :: i,j,k
  DOUBLE PRECISION, DIMENSION (100) :: nagg,n,ndis
DO i=1,imax
          agg1 =0.0
          agg1neu =0.0
          agg2 =0.0
          agg2neu =0.0
          agg3 =0.0
          agg3neu =0.0
          agg4 =0.0
          agg4neu =0.0
               DO j=1,i-2
                    agg1neu = agg1+2.0**(j-i+1)*n(j)*(l(i-1)+l(j))**3
                    agg1=agg1neu
               END DO
                    agg1=agg1*n(i-1)
               agg2=0.5*n(i-1)**2.0*(2.*l(i-1))**3
               DO j=1,i-1
                    agg3neu=agg3+2.0**(j-i)*n(j)*(l(j)+l(i))**3
                    agg3=agg3neu
               END DO
```

```
                agg3=agg3*n(i)
                DO j=i,imax
                        agg4neu=agg4+n(j)*(l(j)+l(i))**3
                        agg4=agg4neu
                END DO
                agg4=agg4*n(i)
                nagg(i)=beta*(agg1+agg2-agg3-agg4)
  END DO
i=1
 ndisdum=0.
    DO k=1,imax
      ndisdum=ndisdum+nd(i,k)*disker*n(k)*l(k)**3
    END DO
  ndis(1)=ndisdum
DO i=2,imax
  ndisdum=0.
    DO k=i,imax
      ndisdum=ndisdum+nd(i,k)*disker*n(k)*l(k)**3
    END DO
  ndis(i)=ndisdum-disker*n(i)*l(i)**3
END DO
DO i=1,imax
        nagg(i)=nagg(i)+ndis(i)
END DO
END SUBROUTINE aggi
SUBROUTINE growi(n,ngro)
USE RAMI
IMPLICIT NONE
DOUBLE PRECISION :: r,r1,r2
  INTEGER :: i
  DOUBLE PRECISION, DIMENSION (imax) :: ngro,n
```

```
        r=2.0**(1.0/3.0)
        r1=r+1.0
        r2=r/(r**2.0-1.0)
        ngro(1)=2.0*growth3/l(1)/r1*((1-r*r2)*n(1)-r2*n(2))+bo
DO i=2,imax
        ngro(i)=2.0*growth3/l(i)/r1*(r2*n(i-1)+n(i)-r2*n(i+1))
  END DO
END SUBROUTINE growi
```

Alternatively, Ramkrishna's discretization procedure can be used (Kumar and Ramkrishna, 1996a and b). In this case, the discretization in the main part of the program and the SUBROUTINE aggi become

```
DO i=1,imax
                IF (i==1) THEN
                xx(i)=xo
                l(i)=xx(i)**(1./3.)
        ELSE
                xx(i)=xx(i-1)*s
              l(i)=xx(i)**(1./3.)
        END IF
 END DO
i=1
DO k=1,imax
    DO j=1,imax
      v(j,k)=xx(j)+xx(k)
                IF ((v(j,k).GE.xx(1)).AND.(v(j,k).LE.xx(2))) THEN
                        eta(j,k,1)=(xx(2)-v(j,k))/(xx(2)-xx(1))
                ELSE IF ((v(j,k).GE.0.0).AND.(v(j,k).LE.xx(i))) THEN
                        eta(j,k,1)=(v(j,k))/(xx(1))
                ELSE
```

```
                eta(j,k,1)=0.0
            END IF
        END DO
    END DO
    DO i=2,imax-1
     DO k=1,imax
        DO j=1,imax
          v(j,k)=xx(j)+xx(k)
            IF ((v(j,k).GE.xx(i)).AND.(v(j,k).LE.xx(i+1))) THEN
                eta(j,k,i)=(xx(i+1)-v(j,k))/(xx(i+1)-xx(i))
            ELSE IF ((v(j,k).GE.xx(i-1)).AND.(v(j,k).LE.xx(i))) THEN
                eta(j,k,i)=(v(j,k)-xx(i-1))/(xx(i)-xx(i-1))
            ELSE
                eta(j,k,i)=0.0
            END IF
        END DO
     END DO
    END DO
    DO k=1,imax
     DO j=1,imax
        IF (j==k) THEN
            delta(j,k)=1.
        ELSE
            delta(j,k)=0.0
        END IF
     END DO
    END DO
    SUBROUTINE aggi(n,nagg)
    USE RAMI
    IMPLICIT NONE
    DOUBLE PRECISION :: agg1,agg1neu,agg2,agg2neu,agg3,agg3neu,agg4,agg4neu,&
```

```
                ndisdum
DOUBLE PRECISION :: dodl1,dodl2
INTEGER :: i,j,k
DOUBLE PRECISION, DIMENSION (100) :: nagg,n,abl1,abl2
i=1
dodl1=0.0
DO k=1,imax
    DO j=1,k
        IF((xx(j)+xx(k)).GE.0.0.AND.(xx(j)+xx(k)).LE.xx(i+1)) THEN
        dodl1=dodl1+(1.-0.5*delta(j,k))*eta(j,k,i)*beta*n(j)*n(k)
        END IF
    END DO
END DO
abl1(1)=dodl1+bo
DO i=2,imax
 dodl1=0.0
  DO k=1,imax
   DO j=1,k
        IF((xx(j)+xx(k)).GE.xx(i-1).AND.(xx(j)+xx(k)).LE.xx(i+1)) THEN
        dodl1=dodl1+(1.-0.5*delta(j,k))*eta(j,k,i)*beta*n(j)*n(k)
        END IF
    END DO
  END DO
 abl1(i)=dodl1
END DO
DO i=1,imax
 dodl2=0.0
 DO k=1,imax
  dodl2=dodl2+beta*n(k)
 END DO
abl2(i)=-dodl2*n(i)
```

```
END DO
DO i=1,imax
 nagg(i)=abl1(i)+abl2(i)
END DO
DO i=1,imax
 DO k=1,imax
  nd(i,k)=0.0
 END DO
END DO
DO k=2,imax
  DO i=1,k
    IF (i==1) THEN
     nd(i,k)=(l(i+1)**3-l(i)**3)/l(k)**3
    ELSE IF (i==k) THEN
     nd(i,k)=(l(i)**3-l(i-1)**3)/l(k)**3
    ELSE
     nd(i,k)=(l(i+1)**3-l(i-1)**3)/l(k)**3
    END IF
  END DO
END DO
i=1
 ndisdum=0.
    DO k=1,imax
      ndisdum=ndisdum+nd(i,k)*disker*n(k)*l(k)**3
    END DO
  ndis(1)=ndisdum
DO i=2,imax
  ndisdum=0.
    DO k=i,imax
      ndisdum=ndisdum+nd(i,k)*disker*n(k)*l(k)**3
    END DO
```

```
  ndis(i)=ndisdum-disker*n(i)*l(i)**3
END DO
DO i=1,imax
                nagg(i)=nagg(i)+ndis(i)
END DO
END SUBROUTINE aggi
```

A6.1 Experimental and modelling results for volume mean size L_{43} (continuous mode of operation)

Continuous experiments (0.04M, 7.5 min, id)

	[rpm]	100	250	500	750	1000	1500	2000
0.3 l	$L_{43,exp}$ [μm]	-	30.9	38.3	-	39.5	38.0	16.0
	$L_{43,SFM}$ [μm]	-	34.0	40.8	-	41.4	41.0	14.7
4.3 l	$L_{43,exp}$ [μm]	27.7	32.5	36.5	-	30.7	15.3	-
	$L_{43,SFM}$ [μm]	31.1	33.3	36.3	-	35.7	13.7	-
12 l	$L_{43,exp}$ [μm]	30.5	38.7	41.4	26.2	11.9	-	-
	$L_{43,SFM}$ [μm]	30.0	36.1	36.8	33.4	9.4	-	-

Continuous experiments (0.01M, 11 min, od)

	[rpm]	100	250	500	750	1000	1500	2000
0.3 l	$L_{43,exp}$ [μm]	-	25.0	29.7	-	33.0	30.0	26.7
	$L_{43,SFM}$ [μm]	-	27.4	34.7	-	35.8	33.1	21.2
4.3 l	$L_{43,exp}$ [μm]	20.0	20.8	22.1	-	-	19.3	-
	$L_{43,SFM}$ [μm]	18.9	19.2	20.4	-	19.5	11.8	-
12 l	$L_{43,exp}$ [μm]	18.5	20.5	20.4	-	18.0	11.0	-
	$L_{43,SFM}$ [μm]	18.0	19.2	20.1	16.8	10.9	-	-

A7.1 Design drawings and dimensions of semibatch reactors

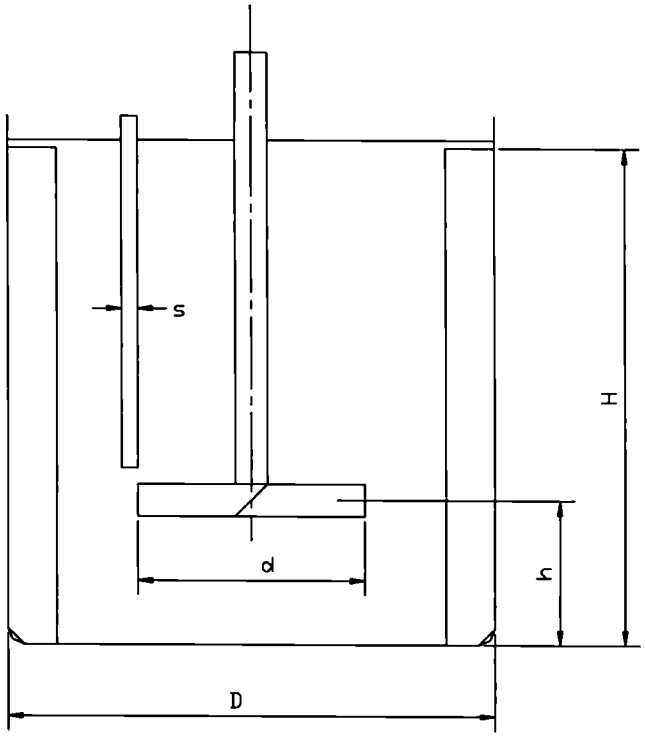

Semibatch reactor with 45^0-pitched blade turbine

Dimensions on different scales

Scale	d [mm]	D [mm]	h [mm]	H [mm]	s [mm]
1 l	40	105	35	110	5
5 l	65	180	60	190	8.5
25 l	110	300	100	320	15

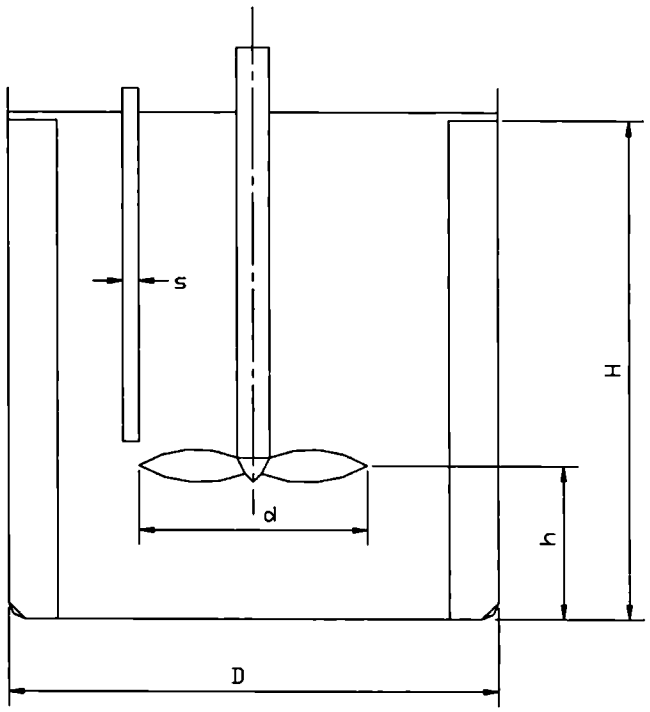

Semibatch reactor with marine-type impeller

A7.2 Experimental and modelling results for volume mean size L_{43} (semibatch mode of operation)

Semibatch experiments (CaOx, reference conditions)

	[rpm]	100	250	500	750	1000	1500	2000
1 l	$L_{43,exp}$ [μm]	11.7	25.0	25.5	-	14.1	10.0	8.1
	$L_{43,SFM}$ [μm]	24.7	23.2	25.9	-	11.1	9.3	8.4
5 l	$L_{43,exp}$ [μm]	11.9	25.1	19.8	-	14.0	11.9	-
	$L_{43,SFM}$ [μm]	14.6	24.7	22.3	-	12.5	8.4	-
25 l	$L_{43,exp}$ [μm]	20.0	22.5	14.1	11.5	-	-	-
	$L_{43,SFM}$ [μm]	18.8	20.3	11.7	8.4	-	-	-

Semibatch experiments (CaOx, marine-type impeller)

	[rpm]	100	250	500	750	1000	1500	2000
1 l	$L_{43,exp}$ [µm]	7.9	14.2	24.0	-	25.1	19.8	16.1
	$L_{43,SFM}$ [µm]	-	17.4	25.4	-	27.3	21.4	16.4
5 l	$L_{43,exp}$ [µm]	7.8	13.2	22.8	-	24.8	16.3	-
	$L_{43,SFM}$ [µm]	-	16.6	26.1	-	26.2	15.6	-
25 l	$L_{43,exp}$ [µm]	11.3	19.9	19.9	15.3	15.0	-	-
	$L_{43,SFM}$ [µm]	13.2	17.3	21.1	17.8	15.2	-	-

Semibatch experiments (CaOx, feed point position close to surface)

	[rpm]	100	250	500	750	1000	1500	2000
1 l	$L_{43,exp}$ [µm]	8.8	13.5	18.1	-	13.0	9.9	7.8
	$L_{43,SFM}$ [µm]	9.7	11.8	18.4	-	12.1	6.5	-
5 l	$L_{43,exp}$ [µm]	9.2	15.1	17.9	-	12.3	10.5	-
	$L_{43,SFM}$ [µm]	10.0	12.7	19.4	-	9.7	5.7	-
25 l	$L_{43,exp}$ [µm]	12.5	14.5	11.3	7.0	-	-	-
	$L_{43,SFM}$ [µm]	10.8	13.7	9.8	6.8	-	-	-

Semibatch experiments (CaOx, high feed rate)

	[rpm]	100	250	500	1000	1500
1 l	$L_{43,exp}$ [µm]	12.9	15.5	18.3	12.2	8.6
	$L_{43,SFM}$ [µm]	11.5	14.2	16.6	9.2	6.4
5 l	$L_{43,exp}$ [µm]	10.0	16.5	16.7	10.9	9.9
	$L_{43,SFM}$ [µm]	11.3	14.4	15.4	9.7	6.6
25 l	$L_{43,exp}$ [µm]	12.2	15.3	12.4	-	-
	$L_{43,SFM}$ [µm]	11.8	15.3	10.5	-	-

Semibatch experiments ($CaCO_3$, reference conditions)

	[rpm]	100	250	500	1000	1500	2000
1 l	$L_{43,exp}$ [μm]	14.9	32.2	26.5	16.0	11.7	9.8
	$L_{43,SFM}$ [μm]	12.3	22.2	19.5	13.0	10.3	8.9
5 l	$L_{43,exp}$ [μm]	24.6	38.0	21.5	14.4	13.1	-
25 l	$L_{43,exp}$ [μm]	39.9	31.5	22.2	-	-	-
	$L_{43,SFM}$ [μm]	28.3	21.7	15.6	-	-	-